# Hydrodynamic Design Structural Analysis and Optimization of Marine Propeller Blade

**M.L.Pavan Kishore**

Mechanical Engineering
**National Institute of Technology Rourkela**

# Hydrodynamic Design Structural Analysis and Optimization of Marine Propeller Blade

*Dissertation submitted to the*

***National Institute of Technology Rourkela***

*in partial fulfilment of the requirements*

*of the degree of*

***Doctor of Philosophy***

*in*

***Mechanical Engineering***

*by*

***M.L.PavanKishore***

(Roll Number: 511ME117)

*under the supervision of*

***Prof. R.K.Behera***


June 2016

Department of Mechanical Engineering

**National Institute of Technology Rourkela**

Mechanical Engineering

**National Institute of Technology Rourkela**

June 23, 2016

# Certificate of Examination

Roll Number: 511ME117

Name: M.L.Pavan Kishore

Title of Dissertation: Hydrodynamic Design Structural Analysis and Optimization of marine Propeller Blade

We the below signed, after checking the dissertation mentioned above and the official record book (s) of the student, hereby state our approval of the dissertation submitted in partial fulfilment of the requirements of the degree of Doctor of Philosophy in Mechanical Engineering at National Institute of Technology Rourkela. We are satisfied with the volume, quality, correctness and originality of the work.

---

*R.K.Behera*
Principal Supervisor

---

*T.Roy*
Member (DSC)

---

*H.Roy*
Member (DSC)

---

*P.Robin Davis*
Member (DSC)

---

Name of the
Examiner

---

*D.R.K.Parhi*
Chairman (DSC)

Mechanical Engineering

**National Institute of Technology Rourkela**

---

**Prof. /Dr. R.K.Behera**

Associate Professor

June 23, 2016

# Supervisor's Certificate

This is to certify that the work presented in this dissertation entitled *"Hydrodynamic Design Structural Analysis and Optimization of marine Propeller Blade"* by "*Mr.M.L.Pavan Kishore"*, Roll Number 511ME117, is a record of original research carried out by him under my supervision and guidance in partial fulfilment of the requirements of the degree of *Doctor of Philosophy* in *Mechanical Engineering*. Neither this dissertation nor any part of it has been submitted for any degree or diploma to any institute or university in India or abroad.

*R.K.Behera.*

*Dedicated to my Parents*

*and*

*Wife*

# Declaration of Originality

I M.L.Pavan Kishore, Roll Number 511ME117 hereby declare that this dissertation entitled "Hydrodynamic Design Structural Analysis and Optimization of marine Propeller Blade" is my original work carried out as a doctoral student of NIT Rourkela and, to the best of my knowledge, it contains no material previously published or written by another person, nor any material presented for the award of any other degree or diploma of NIT Rourkela or any other institution. Any contribution made to this research by others, with whom I have worked at NIT Rourkela or elsewhere, is explicitly acknowledged in the dissertation.Works of other authors cited in this dissertation have been duly acknowledged under the section "Bibliography". I have also submitted my original research records to the scrutiny committee for evaluation of my dissertation. I am fully aware that in case of any non-compliance detected in future, the Senate of NIT Rourkela may withdraw the degree awarded to me on the basis of the present dissertation.

June23, 2016 *M.L.Pavan Kishore*

NIT Rourkela

# Acknowledgment

I extend my deep sense of indebtedness and gratitude to Dr. R.K.Behera for kindly providing me an opportunity to work under his supervision and guidance. With keen interest, invaluable guidance, immense help have helped for the successful completion of the thesis.

It is a great pleasure for me to acknowledge and express my appreciation of my well-wishers Mr. J.Ramachandra (Scientist-E), Prof. J.Srinivas, Prof A.V.Asha, Prof. T.Roy ,Prof H.Roy,Prof P.Robin Davis and friends Mr.Alok Ranjan Biswal, Mr.Sudhansu Meher, Mr.Subramanyam (Scientist-B), Mr.Reddappa for their understanding, relentless support and encouragement during my research work.

I am grateful to our director Prof. Sunil Kumar Sarangi, and Head of the Department Mechanical Engineering Prof. S.S. Mohapatra, for their active interest and support.I am also thankful to the staff members of Mechanical Engineering Department, National Institute of Technology, Rourkela for providing all kind of possible help throughout the completion of this research work.

I am greatly indebted to my parents, my in-laws, to my wife N.Lasya Priya, sister M. Leela Kalpana and brother-in-law K.Ravisekhar (Scientist-D), my brother M. Madhu Pradeep and sister-in-law Sirisha Pradeep for extending their loving support throughout. Lastly, I am thankful to my other family members for their moral support in completion of the present dissertation.

June23, 2016 M.L.Pavan Kishore

NIT Rourkela Roll Number: 511ME117

# Abstract

There are many problems to be addressed in the design of marine propeller blade. Among these, the foremost is the efficiency of the propeller. The design of ship propeller involves a number of competing variables including the rake, pitch distribution and blade surface area. The propeller design also aims at achieving high propulsive efficiency at low levels of noise and vibration with reduced cavitation. All of these factors affect vessels top speed, fuel efficiency, and handling. A thorough understanding of propeller dynamics is necessary to design an efficient and reliable propeller blade. Numerical models are commonly used for the dynamic characterization of propeller blades, due to the difficulties of performing full-scale measurements. In contrast, the current research focuses on the hydrodynamic design of a Wageningen B-series four bladed propeller used for marine applications. The analyses presented in this thesis have been divided into three main phases.

In the first phase, the hydrodynamic design of Wageningen B-series four bladed marine propeller is carried out, to determine the suitability and applicability of propeller blade for underwater conditions is done by

1) Open water characteristics determination,
2) Cavitation inception point determination for metallic propeller blade.

The prevailing conditions applied for evaluating these hydrodynamic characteristics are taken from reference and validated with standard series data.

In the second phase of the research, Strength determination of both metallic and composite propeller (E-glass epoxy material) are determined in terms of its stress and free vibration characteristics. Numerical analyses are carried out using suitable numerical methods for the deflection calculations and to determine the stress distribution in the blade foot and the blades at operational load conditions. A modal vibrational analysis for prediction of vibration response was also conducted for the blade, because the composite blades tend to deform more than that of metallic one and the deformation can be used in the analysis of hydrodynamic performance. Experiments are performed to compare the results with that obtained from the numerical analysis.

In the last phase Structural optimization of composite propeller was done both for non-hybrid and hybrid composites, (comprises a series of combination of Glass fiber reinforced plastic and Carbon reinforced plastic GFRP & CFRP), using the mid-surface as reference and meshed with shell elements to find out the optimum ply stacking sequence for Interlaminar shear stresses and deflection minimization and operational efficiency improvement of composite propeller blade compared to metallic one. The obtained final

stacking sequence of the composite propeller was evaluated by varying the number of layers in steps the Interlaminar shear stresses are calculated, and the results are compared with the metallic propeller. The following basic data are used for analysis and the main points performed during the works are given below.

1. The open water characteristics are predicted computationally on the basis of a validated small sized propeller where the delivered power ($P_D$), the advanced coefficient ($V_a$), and the propeller revolution (N) are known.
2. The cavitation inception point for the metallic propeller is determined which can be used for structural analysis.
3. The Aluminum propeller blade is replaced with E-glass epoxy material blade and structural analyses for both the materials are carried out.
4. An optimum stacking sequence for composite material blade varied with non-hybrid and hybrid materials are determined.
5. Finally, a comparison has been made with metallic and composite materials in terms of their strength behavior.

***Keywords: B-Series; Cavitation; Composite materials; Design phases of Optimisation; Fibre reinforced plastic; Metallic propeller; Modal Analysis; Optimized stacking sequence; Ply Stacking Sequence; Static analysis; Strength Estimates; Stress Analysis; Wageningen Propeller Blade.***

# Contents

# List of Figures

# List of Tables

# Nomenclature

| | |
|---|---|
| $\rho$ | Density |
| $u,v,w$ | Flow components of velocity |
| $\lambda$ | Bulk viscosity coefficient |
| $\mu$ | Coefficient of dynamic viscosity |
| $K_T$ | Thrust coefficient |
| $K_Q$ | Torque coefficient |
| $\eta_0$ | Open water efficiency |
| $J$ | Advanced coefficient |
| $V_a$ | Advanced velocity |
| $N$ | Rotational speed of propeller (rpm) |
| $T$ | Thrust |
| $Q$ | Torque |
| $P_D$ | Power delivered |
| $D$ | Diameter of propeller |
| $Z$ | Number of blades |
| P/D | Pitch to diameter ratio |
| t/D | Thickness to diameter ratio |
| $A_E/A_0$ | Expansion ratio |
| $\xi$ | Rake angle |
| t | Thickness at root |
| C/D | Chord-diameter ratio of the root section |
| $t_0/D$ | Blade thickness fraction |
| $D_m$ | Diameter of model propeller |
| $G_f$ | Rigidity modulus for fiber |
| $G_m$ | Rigidity modulus for matrix |
| $X_t$ | Allowable tensile stress in the principal x (or 1) direction of the material |
| $X_c$ | Allowable compressive stress in the principal x (or 1) direction of the material |
| $\sigma_1$ | Stress along I principal plane |
| $\sigma_2$ | Stress along II principal plane |
| $Ds$ | Diameter of ship propeller |
| $V_{as}$ | Advanced velocity for ship propeller |
| $V_{am}$ | Advanced velocity for model propeller |
| $J_s$ | Advanced coefficient for ship propeller |
| $J_m$ | Advanced coefficient for model propeller |
| $n_s$ | Rotational speed of ship propeller |
| $n_m$ | Rotational speed of model propeller |
| g | Acceleration due to gravity |
| $l$ | Duct length |
| $\upsilon_m$ | Coefficient of kinematic viscosity for model propeller |
| $\upsilon_s$ | Coefficient of kinematic viscosity for ship propeller |
| $T_m$ | Thrust for model propeller |
| $T_s$ | Thrust for ship propeller |
| $P_{Dm}$ | Power delivered for model propeller |
| $P_{Ds}$ | Power delivered for ship propeller |
| $\rho_m$ | Density for model propeller |
| $\rho_s$ | Density for ship propeller |
| $E_f$ | Elastic modulus for fiber |
| $E_m$ | Elastic modulus for matrix |
| $V_f$ | Volume fraction for fiber |
| $V_m$ | Volume fraction for matrix |
| $\mu_f$ | Poisson's ratio for fiber |
| $\mu_m$ | Poisson's ratio for matrix |
| $[B]$ | Strain-displacement matrix |
| D | Stress-strain relation matrix |
| U | Strain energy |
| $E$ | Elastic modulus |
| C | Chord |
| $\varpi$ | Non dimensional frequency |

| | | | |
|---|---|---|---|
| $\sigma_{12}$ | Shear Stress along 1-2 principal plane | $\omega$ | Natural frequency |
| $Y_t$ | Allowable tensile stress in the principal y (or 2) direction of the material | a | Length of the plate |
| $Y_c$ | Allowable compressive stress in the principal y (or 2) direction of the material | b | Width of the plate |
| $\gamma_{1z}$ | Interlaminar shear stress along 1st principal plane | $h$ | Thickness of the plate |
| $\gamma_{2z}$ | Interlaminar shear stress along 2nd principal plane | T | Single force replacing the effect of thrust on each blade |
| $M_Q$ | Bending moment due to torque | ε | Strain |
| $M_T$ | Bending moment due to thrust | P | Absolute Pressure |
| $\Omega$ | Propeller rate of revolution | $P_V$ | Vapour pressure |
| $I$ | Moment of inertia | $P_0$ | Atmospheric pressure |
| $y$ | Distance from neutral axis | | |
| I/y | Section modulus | | |
| $\theta$ | Pitch angle | | |
| $\phi$ | Pre-twist angle | | |
| $M_N$ | Normal Bending moment | | |
| $\sigma$ | Design stress | | |
| $[N]$ | Shape function | | |
| $[K]$ | Stiffness matrix | | |
| $[M]$ | Mass matrix | | |

| | |
|---|---|
| SDB | Soviet Developed board |

# Abbreviations

| | |
|---|---|
| RANS | Reynolds average Navier stokes equation |
| PDE | Partial Difference Equation |
| FEM | Finite element method |
| CFRP | Carbon fiber reinforced plastic |
| GFRP | Glass fiber reinforced plastic |
| GA | Genetic algorithm |
| CRP | Contra rotating propeller |
| PADS | Propeller automated design system |
| RNG | Renormalization group theory |
| SIMPLE | Semi implicit method for pressure linked equations |
| BT | Bend-Twist |
| FRP | Fiber reinforced plastic |
| FSDT | First order shear deformation theory |
| B | Bending |
| T | Twisting |
| CB | Combined bending |
| EB | Edgewise bending |
| VLM | Vortex Lattice Method |
| HYBRIDCOMP1 | Hybrid composite1 |
| HYBRIDCOMP2 | Hybrid composite 2 |
| Hybridcomposite1 | CFRP properties applied at $[\pm 45°]$ and GFRP applied at $[0°, 90°]$ |
| Hybridcomposite2 | GFRP properties applied at $[\pm 45°]$ and CFRP applied at $[0°, 90°]$ |

# Chapter 1

# Introduction

## 1.1 Background

Today, conventional marine propellers remain the standard propulsion mechanism for surface ships and underwater vehicles. In general, the propeller is that component of the ship which converts the engine power into the driving force of the ship. The modifications of basic propeller geometries into water jet propulsors and alternate style thrusters on underwater vehicles have not significantly changed to determine and analyse propeller performance. However, the propellers are required to generate adequate thrust to propel a vessel at some design speed ensuring some “reasonable” propulsive efficiency. Considerations are made to match the engine’s power and shaft speed, as well as the size of the vessel and the ship’s operating speed, with an appropriately designed propeller. The above conditions specified are interdependent, and knowledge on desired operating speed for a given vessel is required, however, the complexity of the flow field in which the propeller must operate efficiently will lead a designer to layout a propeller to overcome most of the dilemma. Another difficulty which arises during propeller action is the variation of inflow, which has a great influence on propellers. Hence, the range of design is restricted for designers.

The study of propeller action and design is complex especially the manufacturing of marine propellers requires a highly specialized procedure. Normally a propeller fitted to the stem of the ship where it operates in water that has been disturbed by the ship as it moves ahead. The performance of the propeller is thus affected by the ship to which it is fitted so that the same propeller will perform slightly differently "behind" different ships. Therefore, one wishes to determine the intrinsic performance characteristics of a propeller, unaffected by the ship to which it is fitted; it is necessary to make the propeller operate in undisturbed or "open" water.

The performance characteristics of a propeller usually refer to the variation of its thrust, torque, and efficiency with its speed of advance and revolution rate in open water.It is difficult to determine the characteristics of a full-size propeller either in "open" water or "behind" the ship by varying the speed of the advance and the revolution rate over a range and measuring the thrust and torque of the propeller. Therefore, recourse is to be done to experiment with models of the propeller and the ship in which the thrust and torque of the model propeller are measured conveniently over a range of speed of advance and revolution rate. However, before one embarks upon model experiments, it is essential to know the conditions under which the quantities measured on the model can be applied to the full-size ship. These conditions are obtained from the "laws of similarity" between a model and its prototype.

### 1.1.1 Aims and Objectives of this Research

In the present investigation, some literature published so far have been surveyed, reviewed and analysed. Most of the researchers studied the effect of cavitation on the propeller blades. However, in actual practice, in addition to cavitation, determination of stresses and deflections, vibrational behavior, and optimization also plays a crucial role in evaluating the performance and strength criteria of propeller blades. Some information is available for determination of the stresses and deflections, vibrational behaviour but this is not exhaustive for real applications. Therefore an attempt has been made to investigate the hydrodynamic behavior and structural analysis of propeller blades systematically. The process has been planned in seven phases so that the results can have practical utility.

The phases of the process plan for the present investigation are as follows:

- Open water characteristics determination of metallic propeller
- Cavitation inception point determination of metallic propeller
- Stress estimation of metallic propeller using Burrill method
- Linear static analysis for stress and deflection determination for both metallic and composite propeller
- Free vibration analysis for both metallic and composite propeller
- Laminate Stacking Sequence Optimization of composite propeller
- Stress and vibrational analysis for optimized stacking sequence

The design of blade geometry being more complex involve many controlling parameters. The design and analysis of such complex 3D blades with conventional formulas will give less accurate values. In such cases, numerical analysis (Finite Element Analysis) gives comparable results with experimental values.

3- Bladed 4-Bladed 5-Bladed

Figure 1.1: Metallic Propeller Blades

In the first stage of the research B-series, Wageningen four bladed propellers were designed and developed. Using the design parameters the hydrodynamic characteristics are determined for the blade for practical applicability in open water conditions. Following the hydrodynamic characteristics, the cavitation inception for the propeller blade is determined using the commercially available software FLUENT 6.23.The determination of cavitation inception point specifies the maximum operating speed of propeller used for propeller design.

In the second stage, the cavitation pressures developed over the surface of the propeller are transferred from the fluid to structure for analysing the deflections and stresses of the metallic propeller. The metal propellers used to cause vibration and noise during its operation, to avoid it; conventional isotropic materials are replaced with composite materials. Glass fiber reinforced plastic (GFRP) material woven with fiber orientation angles are used $(0°\ 45°\ -45°\ 90°)$ as the composite material. Strength analysis is carried out for both metallic and composite propeller. For composite propeller by varying the number of layers, the interlaminar shear stresses are determined.

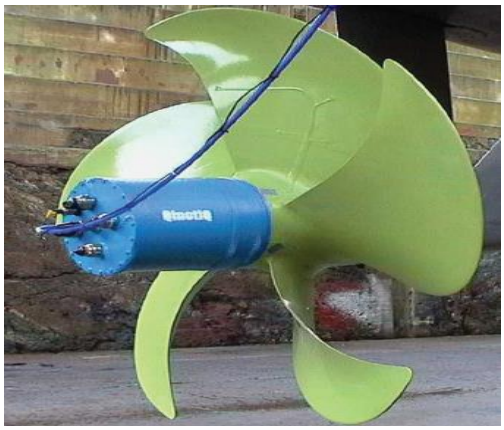

Figure 1.2: Composite Propeller employed for marine application

In the third stage, the free vibration characteristics of both metallic and composite propeller blade are carried out. Blades are the critical components of the ship, the study on their dynamic characteristics is important and fundamental. Due to the dynamic stiffening and spin softening effects caused by inertia forces**,** centrifugal and hydrodynamic forces, etc., dynamic properties of marine propeller blades can be altered considerably. For efficient performance and operating conditions, the design of blades aims at finding out the vibrational characteristics.Reduction in vibration is a very important parameter for successful design of blade structure which may promote to achieve other design goals such as low cost and high stability level.

In the fourth stage of the investigation the structural optimization of composite propeller blade was carried out for both hybrid (combination of GFRP and CFRP) and non-hybrid composites using finite element method based software Optistruct.

In the last stage of investigation with optimized stacking sequence attained for hybrid and non-hybrid composites from structural optimization scheme the suitability of the composite material in replacement of the parent, the material is done for practical applications.

Finally, suitable numerical methods are used to solve the theoretical and experimental expressions developed. Useful conclusions are drawn from the numerical results of respective sections. The numerical results are validated by using the experiments on blades in the corresponding sections. Both the numerical and experimental results are compared, and good agreements are obtained.

## 1.2 Outline of the Thesis

The processes as outlined in this thesis are broadly divided into seven chapters. The current chapter is the first one which deals with the introductory aspect of the thesis. The second chapter contains up-to-date information on literature surveyed on various aspects of hydrodynamic design, cavitation, stress analysis, vibration analysis and optimization of propeller blades. The third chapter of this project deals with the computational fluid dynamics and cavitation concepts of the propeller blade. Chapter 3 is divided into two different sections. These are entitled as;

1. Computational fluid dynamics for fluid flow simulation on propeller blades and
2. Effect of cavitation on propeller blades.

The fourth chapter describes the theoretical method and numerical analysis of stress and vibrational behavioural characteristics of propeller blade through finite element method. The analyses have been presented in four separate sections. They are outlined as;

1. Finite element method and Fibre reinforced plastics
2. Mathematical modelling of propeller blade using Shell elements
3. Propeller blade strength estimates
4. Deformation and vibrational analysis

Chapter 5 deals with the structural optimization of marine propeller blade using finite element method based solvers. Numerical simulations are performed for single propeller blade through a set of operations to obtain topology and stacking sequence optimization as the outcome. The design phases involved in optimizing a structure are outlined as;

1. Optimization Scheme
2. Free size optimization
3. Composite size optimization
4. Composite shuffle optimization

Chapter 6 deals with validation exercises relating to results obtained for theoretical numerical and experimental analysis. These validation exercises are sorted out chapter wise. They are outlined as;

1. Bend-twist coupling and its effect on cavitation inception of the composite marine propeller.
2. Comparison of Beam and Plate theories for free vibrations of metal matrix composite pre-twisted blades.
3. Vibration characteristics of initially twisted rotating shell type composite blades

Chapter 7 represents the detailed discussions on the results obtained from the theoretical, numerical and experimental analysis of Chapters-3, 4, 5 and 6. The last chapter deals with concluding remarks drawn from the discussions and applications along with the scope for further work.

# Chapter 2

# Literature Review

A literature survey was taken up to review the present status of research in the field of theoretical analysis of hydrodynamic design, strength estimation and structural optimization of marine propeller blades.Due to the extended literature the review focuses only on the most important and relevant works**.**The papers collected could be classified broadly into the determination of open water characteristics and cavitation on marine propeller blades. From a structural point of view, the strength estimation of the propeller blade is carried out using theoretically and experimentally studies. To validate the results obtained from these studies either experimental or theoretical or both is carried out by using numerical analysis. Additionally, vibrational analysis of marine propeller blades is also considered which are important in structural optimization.

## 2.1 Hydroelastic Analysis and Fluid Structure Interaction

A moving ship experiences resisting forces produced from the water which must be overcome by thrust produced using some mechanism. In the earlier days, consisted of manually operated oars which gave place in turn to sails & then mechanical devices such as jets, paddle wheels & propellers of many different forms came into existence. Propellers more particularly propeller blades are complex shapes which require the right hydrodynamic surfaces, most of the CAD tools will handle these complex shapes and surfaces. The performance of propellers operating in underwater conditions depends on th thrust and torque determined accurately in the design stage. In general, the efficiency of propulsion system mainly depends upon its propeller performance, force, torque, open water efficiency & its principal parameters to be determined. The hydrodynamic aspects including the thrust deduction, wake, characteristics of the propeller are of importance. Owing to the fact, that the analysis of flow dynamics is a complex, and difficult process for prediction, recent simulations for these types of interactive effects has shown that CFD can provide valuable insight into the flow field generated by a propeller

including forces and moments due to rotating blades. To evaluate the hydro-elastic behavior of flexible propellers using fluid-structure interactions, various researchers used analytical, experimental and numerical methods.

The simple method for assessment of marine propeller hydrodynamic performance is to graph propeller coefficients against advance coefficient (J). The classical blade element theory of propellers is used to determine the propeller characteristics and the force distribution acting on the propeller. The finite element method used to determine the resulting deformation of the propeller blades. Using the systematic propeller series, the design of marine propeller was done by Ekinci [1] who employed empirical relations for design and prediction of B-series type bladed propeller for 3-different cases of loading conditions.

Burrill's method [2] employs Goldstein factors in determining induced velocities for calculating propeller performance in open water conditions. Burrill &Young [3] computed open water propeller efficiency and behind body propeller efficiency for single and twin screw ships, using several definitions of advanced coefficients.

Felli et al. [4] investigated experimentally the flow around a propeller in open water channel with uniform flow conditions. Mihaela [5] used CFD technology to analyze the flow field and physical parameters acting on the propeller body simultaneously. The Navier-stokes equation is applied to the solver to take into account for nonlinearity especially when dealing with turbulent shock and break waves.

Miyata [6] and Subhas [7] reported that CFD estimation of marine propellers thrust and torque performance with different rotational speed are ideal with minor differences compared to experimental results. Callewas et al. [8] carried an open water experimental model for a series of the marine propeller and made a comparison with numerical study while Brandt et al. [9] investigated performance test for 79 propellers which nearly fits into the range of 9 to 11m in diameter. Thrust and torque were measured over a range of propeller speeds normally from 1500 to 7500 rpm, depending upon the propeller diameter. Furthermore Benini [10] illustrated the complementation of combined blade–element momentum theory for light and moderately loaded propellers.

Weick [11-12] determined hydrodynamic characteristics of conventional metallic propellers of various sizes using cavitation and tunnel test.Kerwin [13] and other researchers carried out the analysis of propellers subjected to inviscid or fully viscous fluids by boundary layer method and linearized or exact/partially linearized methods.

Valentine [14] used the "Reynolds average Navier-Stokes equation [RANS]" to estimate the fluid flow field conditions and predict the flow characteristics of the propeller blade. He considered the effects of turbulence flow in flow characteristics with an assumption of no slip at boundary conditions.

Kerwin [15] developed a numerical procedure and computer program for the lifting surface design of sub-cavitation propellers. The procedure includes a careful treatment of the effect of radial-induced velocities on blade-section design and provides for the independent specification of the pitch angle of trailing vorticity. Numerical results demonstrate the importance of including radial-induced velocities for propeller blades having significant skew, rake, and a non- uniform radial pitch distribution. In the case of visualization of flow pattern around merchants ship propeller CFD based lifting surface line theory for the first step is commonly used by Streckwall [16].

The viscous RANS equation solution was used by Kim [17] to analyze the flow pattern around the ship propellers. The ship propeller design [SPD] software code was prepared by Ghassemi [18-22] and employed for various propulsors such as propeller-rudder system, a highly skewed propeller, and a contra-rotating propeller. This code employs the BEM including the boundary layer theory to determine the hydrodynamic analysis of marine propeller. Young [23] used a coupled Boundary element method and finite element method for numerical analysis of flexible composite propellers in the uniform and wake flow. The fluid-structure interaction analysis of flexible composite marine propellers subject to hydrodynamic and inertial loads was also presented by Young [24].

Young and Savander [25] performed numerical analysis for large-scale surface piercing propellers**.** Dymarksi [26] used "Solaga" computer program for computation of open water characteristics and cavitation phenomena. Prakash et al. [27] used CFD simulation software FLUENT to obtain open water characteristics of B-series propeller; they used "Ranse and potential flow simulation program" for prediction of hull-propeller interaction effects [28].Using this coupled analysis scheme of Vortex Lattice

Method(VLM) and RANSE solver an optimization scheme for propeller was developed [29].

Lin [30] and Mulcahy [31] carried out a comprehensive work on the hydro-elastic tailoring of the flexible Composite propeller. A coupled structural fluid flow analysis was performed by Blasques et al. [32] to evaluate the hydro-elastic behavior of a composite marine propeller. Das et al. [33] carried out CFD analysis of contra-rotating propeller. Das et al. [34] and Banerjee [35] carried out analysis on the study of hull-propeller interaction. The study of propeller noise was done by Krishna [36]. Krasinikov [37] used RANS method for numerical prediction of unsteady forces acting on the podded and open propellers operating in oblique flow conditions.

Chattopadhyay et al. [38] used the classical blade element theory in an optimization procedure for improving the performance of a high-speed rotor. For the purpose of structural analysis, they used the finite element method. Chazly [39] performed static and dynamic analysis of a wind turbine blade.

For computation of stress deflection patterns and eigenvalues of the metallic blade, a triangular bending element was used. Bernard [40] presented a numerical investigation of cavitating flows using the mixture model, implemented in the FLUENT 6.2 commercial code. Sridhar et al. [41] predicted the frictional resistance offered by a ship in motion, using FLUENT 6.0 and these results are validated by experimental results.

Chang [42] applied finite element volume CFD method in conjunction with the standard $K-\varepsilon$ turbulence model to calculate the flow pattern and performance parameters of a DTNSRDC P4 119 marine propeller in a uniform flow. Caja [43] has calculated open water flow patterns and performance coefficients for DTRC 4119 propeller using FINFLO code. The flow patterns were predicted by $K-\varepsilon$ turbulence model and suggested a better prediction of tip vortex flow which requires a more sophisticated turbulence model.

Salvatore et al. [44] performed computational analysis by using Insean-PFC propelle flow code developed by CNR Insean. Kimura et al. [45], Takashi et al. [46] and Choong et al. [47] are examples of CFD applications for predicting marine propeller performance characteristics. However, a number of experiments is to be carried out to know the open

water characteristics, flow velocity field in the propeller wake and prediction of cavitation in uniform flow conditions.

## 2.2 Cavitation

The process of beginning of cavitation is called "Cavitation Inception." In general, cavitation occurs when the local absolute pressure is less than local vapor pressure for the fluid medium. In fluid power applications, the evaporation pressure is reached when the flow velocity is increased sufficiently [48-52].Pure water can withstand considerable low pressure (i.e. negative tension) without undergoing cavitation. For the cavitation inception "the inception pressure" is assumed to be equal to the vapor pressure ($P_v$) at the sea. Cavitation inception is of direct importance to Navy vessels, because of the sudden increase in noise levels causes to trouble from stealth point of view at the onset of cavitation.

As cavitation plays an important role in the better efficiency of the propeller at higher speeds, so the cavitation inception point is to be found out for the propeller by performing flow analysis under open water conditions. Euler was the first who reported the possibility of cavitation on a particular design of water wheel in 1754. Reynolds wrote a series of papers on engine-racing in a screw-propelled steamer and introduced cavitation (INA, 1873) in accordance with the knowledge of nowadays . Barnaby reported over speeding characteristics of 27 knots Torpedo boat destroyer HMS Daring in its trials in 1893.

Parsons built the world's first cavitation tunnel to observe the phenomena in model scale and tested the propellers of his famous world's first steam turbine boat "Turbinia" in 1895. This small tunnel kept in working order still at the City Museum in Newcastle upon Tyne, UK. Parsons also constructed a larger tunnel 15 years later in which he could test 12 inch diameter propeller models. Randle [53] predicted the thrust and torque performance for Two Propeller Blades using CFD. Numerical computations of the flow around two typical propeller blades have carried out and compared with the equivalent measurements obtained for the open water thrust and torque performance characteristics of the two propellers. Wienken [54] presented on a method to predict cavitation inception using Large-Eddy Simulation and its application to the Flow Past a Square Cylinder in which cavitation inception around axisymmetric bodies are explained. Lingjiu [55] made his paper

on cavitation study on a marine propeller using RNG K- Є turbulence model and validated with experimental results. Same turbulence model is applied in the project. Kuiper [56] predicted the tip vortex cavitation on a new level, considered for the non-cavitating case; new physical concepts are developed, and some of their results are presented. Simulations by Watanabe [57] were made with steady and unsteady cavitating models around a marine propeller using a RANS CFD code, and he concluded that the present approach could complete the model experiments for actual propeller cavitating propeller design procedures. The predicted values of thrust and torque in uniform flow were in good agreement with the measurements in both cavitating and non-cavitating conditions. Several useful scaling laws, which are based on empirical relations or physical observations are suggested by Arakeri [58] with some general aspects of cavitation inception in flowing situation. Dekanski et al. [59] generated geometry for given operating conditions by using the partial differential equation [PDE] method approach. Standard techniques of surface representation, such as B-spline interpolation, require a large number of control points to achieve this. The PDE method approaches the representative of the blade as a boundary valued problem which ensures that a fair surface is generated and secondly that a small set of design parameters is needed**.**

## 2.3 Strength of Propeller Blades

### 2.3.1 Stress estimates on Propeller Blades

The strength requirements of propellers indicate that not only the blades be sufficiently robust to withstand long periods of arduous service without suffering failure or permanent distortion, but also that the elastic deflection under load should not alter the geometrical shape to such an extent as to modify the designed distribution of loading.The first approach to strength problem was made by Taylor [60] who considered a propeller blade as a cantilever rigidly fixed at the boss. The stresses were evaluated following the theory of simple bending by assuming a cylindrical section of the blade. Such sections are having straight faces and curved backs. The greatest tensile stress was calculated to occur at the trailing edge and the greatest compressive stress at the center of the back. This method being the simplest of all is still widely used for simple and conventional propeller geometries, with narrow blades. But the method is suspect when applied to propellers

with wide blades and width comparable to the length.Therefore Conolly [61] addressed the problem of wide blades and tried to combine both theoretical and experimental investigations**.** The author carried out the measurements of deflection and stresses on model blades subjected to simulated loads with an aim to develop a theoretical model calibrated against the laboratory experiments. This model was validated by measurements of pressure and stress distribution on the blades with experimental results obtained for a full-scale ship propeller operated at sea based conditions. From the results, it was concluded that wide blades are subjected to tensile stress on the face and compressive stress of similar magnitude on the back side. It was pointed out that the accuracy of the prediction from the model depends on the accuracy of working load determined. Sontvedt [62] studied the application of finite element methods for frequency response to improve the frozen type of hydrodynamic loading. The thin shell element of the triangular type and the super parametric shell element are used in the finite element model; it presents the realistic and dynamic stresses in marine propeller blades. Stresses and deformation calculated for ordinary geometry and highly skewed propellers are compared with experimental results.

### 2.3.2 Propeller Blade Failure

Lee et al. [63] investigated the main sources of propeller blade failures and resolved the problem systematically. A FEM analysis is carried out to determine the blade strength in prototype and full-scale condition. The range of safety factor for the propeller under study is determined as well. Jourdian [64] recognized that the failure of un-numerous blades is due to fatigue, which cannot be taken into account in a conventional static strength calculation. When comparing to Conolly [61], improvements were taken on the structural model and also in the wake pattern loading. The feasibility of a dynamic analysis combined with an improved knowledge of fatigue resistance of the material results in a reliable cure for this situation. In general three-dimensional solid elements of the results directly compared with the measured values. The correlation is made between model and full-scale results. The radial stresses have been chosen as typical for the stress situation at each point.

### 2.3.3 Hub-Blade interaction in Propeller Strength

The finite element method is used for calculating the stresses in propeller blade and hub separately. In the blade stress calculation, the hub is assumed to be rigid. On the other hand, the blade is completely ignored if hub strength is considered. Beek [65] studied the interference between the stresses conditions in both parts. Strong tools are available to shift the disturbing boundary conditions from the blade root to the hub-shaft interface and obtain reliable information about the blade root loading and its resolution in the hub. Detailed experimental data, obtained in strain gauge measurements on a full-scale blade, proved the validity of the chosen element type and for application on propeller blades. Finite element calculations of propeller blade stress for a blade clamped to an assumed rigid hub give reliable results over the whole blade except for the very close vicinity of the clamped section. Results of comparative calculations show the strong influence of the hub elastically on the stress distribution in the blade root section. It is noticed that special attention must be paid in hub blade transition for highly skewed blades.

### 2.3.4 Experimental Setup

Stickle [66] used the distribution of thrust and torque along the radius of the blade to compare the actual performance of a propeller with calculated performance. The energy losses in the wake of the propeller as obtained from experimental measurements are discussed. A method of determining these losses from the total thrust and torque of the complete propeller is given. A method permits an analysis of the effects of propeller solidity on the axial and rotational losses of the propeller to be made from the total thrust and torque. The rotational energy loss may be increased many times by the use of a propeller with poor torque distribution which makes it possible to show a large increase in efficiency by the use of counter-rotating propellers that have poor torque distribution. Thrust force obtained from the power-velocity formula is applied on 0.7R to 0.75R region for analysis purpose. Castellini [67] described the vibration measurements on blades of a propeller rotating in water with tracking laser vibrometer. In some cases, component failures are caused principally by vibrating related fatigue stress. Monitoring of component vibration can play an important role in preventing failures due to fatigue. Dynamic and hydrodynamic excitations are mainly the variation of wake upstream. The aim of work is to perform an analysis of the vibration behavior of a propeller rotating in water. In their work, a system

for the tracking of rotating objects has been developed to perform vibration measurements. A tracking laser scanning vibrometer has been used for measuring the vibration of a map of points on the object surface during the complete circular motion. A comparison has been found with the static analysis in water and air for the same propeller.

### 2.3.5 Composite material

Colclough et al. [68] studied the advantages of a composite propeller blade made of a fibre reinforced plastic material with the same propeller made with different materials. The three basic problems encountered in the use of propeller on hovercraft are erosion, corrosion, and noise. When the velocity of a propeller is at a certain maximum speed then the noise is the major problem when it is operating in shallow water or fine suspension of sand and sea water, corrosion is the important problem to be handled. To reduce the noise of propeller, the propeller tip speed should be lowered and to retain its effectiveness, the propeller must be larger, so a large slow running propeller made of corrosion resistant materials would reduce all the problems. To achieve this property, the composite propeller blade with a fiber reinforced plastic has been developed. To evaluate the different properties of propeller blade made of fiber reinforced plastic the author considered different stresses like tensile, compressive, shear and fatigue.

Russel [69] developed a method of blade construction employing CFRP in a basic load carrying spar with a GFRP outer shell of airfoil form. Full-scale blade specimens have been fatigue tested in various modes. Other tests such as bird impact trials have been carried out. Comparisons have been made between the measured vibratory strains and the fatigue test results. The only problem encountered concern the leading edge erosion protection.

Leyens et al. [70] discussed two different materials and design approaches for the purpose of reduced weight and increased strength and stiffness, namely local reinforcement of the Titanium fan blades by using Silicon Carbide Fiber Titanium matrix composites and by partly replaced the bulk titanium fan blade by fiber reinforced plastic (Hybrid concept). The author found that Titanium matrix composites significantly improve the mechanical properties of the fan blades while the Hybrid blades can contribute to considerable weight savings.

Lin [71] discussed the stacking sequence optimization of laminated composite structures using a genetic algorithm with local improvement. In this study, a local improvement is inserted into a standard Genetic Algorithm (GA), and the real calculation, by finite element analysis.

Lin et al. [72] carried out stress calculations for a fiber reinforced composite thruster blade. The composite blade is constructed using multiple layers of braided fiber in a thick shell skin layer. The core is filled with foam type material and uses shear webs for internal supports. The objective of their work is to explore the rotating blade hydrodynamic design constraints of a typical composite blade by performing a 3-D element- stress analysis.

Two salient features are exhibited in the numerical result of composite blade stress calculations. First minimum deflection at the tip of a composite blade can be quite large compared to that of an isotropic metal blade using the same blade form. Secondly, throughout the maximum thickness tensile stress in the skin layer thickness direction could become critical for higher loadings. The composite blade can provide not only a means of weight savings but also can have excellent structural stiffness and strength properties through proper geometric and material design.

### 2.3.6 Use of Contra-rotating Propeller

Praefke et al.[73] proposed three different propulsion arrangements (1) Conventional twin screw arrangement (2) An unconventional twin screw arrangement with staggered propeller plans and with the propeller disks nearly touching and (3) A counter rotating propeller arrangement with the forward propeller conventionally driven and the aft propeller driven by a downstream pod.

The hull lines for all three arrangements are designed and optimized these using CFD methods. In the counter rotating propeller due to the specified arrangement several mechanical and operational advantages are achieved, if the number of blades is equal on forward and aft propeller the numbers of excitation frequencies are small. If the numbers of blades on forward and aft propeller are not identical, then different shaft speeds must be required. Therefore, the choice of some blades directly influences the load distribution between forward and aft propeller. From all these CFD methods and modal tests performed on these three types of propellers, it can be concluded that counter rotating propeller

arrangement offers substantial saving in power without generating unduly high vibration excitation levels.

Nithiyama et al. [74] mainly concentrated on the development of contra- rotating propellers to bulk carrier. The Contra Rotating Propeller [CRP] has been practical use on torpedoes small boats and airplane, but it has not been adopted for large merchant ships. He concluded that the CRP propeller is more useful when compared with the conventional propeller in cases of cavitation, pressure fluctuations, noise and stopping performance. The energy saving amount of the CRP ship was 15% in comparison with the conventional propeller ship.

## 2.4 Free Vibration Analysis of Propeller Blade

Blades are the critical components of the ship and the study on their dynamic characteristics is important and fundamental. Due to the dynamic stiffening and spin softening effects caused by gravities, centrifugal and hydrodynamic forces, etc., dynamic properties of marine propeller blades can be altered considerably. The design of blades depends on many factors such as strength, durability, vibration, cost, etc. For efficient performance and operating conditions, the design of blades aims at finding out the vibrational characteristics. Reduction in vibration is a very important parameter for successful design of blade structure which may promote to achieve other design goals such as low cost and high stability level. With the rapid advancements in material technology variations in design and operating conditions of blades changed a lot, these variations resulted in positive impacts for enhancing the performance and altering the prices.

Depending upon the application of the field of use wide range of materials is used for blades. However, many factors such as operating equipment, corrosion resistance, rigidity, weight, fatigue resistance, appearance have an impact on blade materials. The necessity of these factors made to adopt materials such as composite widely used in structures. Thus, the vibrational analysis of marine blades has received much attention and sufficient references to literature are available with the Eigen frequency problems.

The starting solution for a simple stationary blade are obtained from classical Euler-Bernoulli [75] beam with the cantilever boundary conditions for bending vibration and St Venant's non-circular rod for torsion vibration [75-76]. The solution of cantilever blade

can be obtained by applying classical approach using simplified conditions for solving the differential equation of motion are Ward [77], Wrinch [78], Meyer [79] on tapered beams and Sutherland [80] on the effects of shear and rotary inertia. Power series of a solution of blade natural frequencies have been obtained by Taylor [81] for the case of uniform and completely tapered beam.

Using the Galerkin method Rao [82] obtained the formula for the fundamental flexural frequency of a tapered cantilever beam with rectangular cross section. Considering the effect of pre-twist on the blade Dunholter [83] considered the static displacements and natural frequencies of pre-twisted beams. White [84] employed Greens functions to derive the conditions of orthogonality for a uniform pre-twisted blade performing the bending vibrations. Diprima [85] solved the equations of motion of a pre-twisted cantilever blade by Rayleigh-Ritz method to determine the frequencies and amplitude ratios.

Carnegie [86] described an experimental method to determine the centers of flexural and torsion of aerofoils cross sections. Houbolt [87] derived the equation of motion for a pre-twisted cantilever beam with asymmetrical airfoils and suggested Rayleigh-Ritz method for their solution. Barten et al. [88] used finite element method to study thin stationary blades.

Ahmad et al. [89] followed similar analysis for thick blades and this was extended to rotating blades by Bossak et al. [90]. The implementation of fiber reinforced composite materials to the application of blades continues to increase, since it is important to explore the potential benefits that can be designed into the physics of these materials. Vibration is often critical to the successful operation of engineering structures which are composed of composite materials for example propeller blades, helicopter rotor, wind turbine blades, automatic and aerospace panels.

A single freestanding blade may be considered as a cantilever beam with a rectangular cross section. The vibration characteristics of such blade are always coupled between the two bending modes in the flap wise and chordwise directions and the torsion mode. Leissa et al. [91] were the first ones to investigate the free vibration characteristics of cantilevered twisted beams and plates as a three-dimensional vibrational problem.

Kielb et al. [92] presented a comprehensive review of structural dynamics aspects of pre-twisted beams following the same path of lines and presented a very comprehensive summary of the analytical work performed in the area of twisted plates. The equation related to twisting plates is much more complex than corresponding Euler and Timoshenko beam formulations. An early analytical model to calculate the natural frequencies of a cantilever beam was suggested by Southwell et al. [93] based on Rayleigh energy theorem which defines a simple equation relating the fundamental frequency to that of rotating frequency of a beam.

Friedmann et al. [94] have formulated the discretization of linear equations of motion of blade by the Galerkin method and considered the problem of aeroelasticity based on the finite element method of variable order. Sivaneri et al. [95] , Thakkar et al. [96] treated Hamilton's principle as a variational principle for the rotor blades analysis. Silva et al. [97] considered the nonlinear effects in the motion of rotors.The vibration of the blades was taken into account to determine the geometric nonlinearity effects and to carry out the dynamic stability analysis.Ramamurti et al. [98] studied rotating twisted plates by using finite element method with two different shape functions.

Murthy et al. [99] studied rotating pre-twisted and tapered plates by finite element method with triangular shell elements having three nodes with 18 degrees of freedom respectively. Leissa et al. [100] studied cylindrical shells with camber and twist on the shallow shell theory by Ritz method. Recently Tsuji et al. [101] studied rotating thin twisted plates by the Rayleigh-Ritz method. Hu et al. [102] studied the rotating thin cylindrical panels with a twist on general shell theory. Lo et al. [103] in their analysis simplified the nonlinear problem by assuming the blade to be rigid everywhere except at the root and presented the solution in the phase plane.

Boyce et al. [104] used Rayleigh-Ritz and Southwell methods to determine the upper and lower bounds of natural frequencies of turbine blade vibrating perpendicular to the plane of rotation. Schihansl et al. [105] investigated the stiffening effect of the centrifugal forces on the first mode frequency of a rotating cantilever blade by the use of successive approximation. Hirsch et al. [106] considered the effect of non-rigid supports.

Horway et al. [107] considered hinged ends and Niordson [108] considered the effect of loosely hinged supports on the natural frequencies of rotating blades. Garland et al. [109]

considered the case of a cantilever blade and used the Rayleigh-Ritz method to determine the frequencies and mode shapes .

### 2.4.1 Composite Material

The implementation of fiber reinforced composite materials to the application of blades continues to increase, since it is important to explore the potential benefits that can be designed into the physics of these materials. Vibration is often critical to the successful operation of engineering structures which are composed of composite materials for example propeller blades, helicopter rotor, wind turbine blades, automatic and aerospace panels. The first established work on pre-twisted composite plates was carried out by Qatu et al. [110] to determine the natural frequencies of stationary plates using laminated shallow theory using Ritz method. Bir [111] provided preliminary design method based on the theory of Euler-Bernoulli theory on layup structures, and it was found that the layup sequence obtained by this method did not meet the requirements of actual strength at the root area through analyzing the finite element model.

Kumar [112] stated that Finite Element Analysis offers satisfactory results with additional ability to calculate regional mode and the natural frequency with fracture locations during external loading condition. Free vibration analysis of laminated composite beams has been conducted by a significant amount of research.

Alejandro [113] analyzed the basic vibration mode of composite layup structure of wind turbine blades with the normal operating conditions by transforming complex geometric blade model into equivalent beam model using the VABS calculating program. Liu Wang-yu [114] studied the influence of fiber angle of the layup blade on strength through the finite element model of the blade and combined the response surface methodology, and results showed that when layup angle is near $45^\circ$ it can get higher stability strength. Stacking sequence of a laminated cylindrical shell is optimized based on the natural frequency by Shakeri et al. [115].

Yildirim [116] studied the out of plane free vibration problems of symmetric ply laminated beams using the cross transformation method. Khedir [117] has studied free vibrations of cross-ply laminated beams with arbitrary boundary conditions. Investigations on the natural frequency modes of graphite epoxy cantilever plate and shells were carried

out by Crawley [118] and Wang [119]. Shaw [120] analyzed the free vibrations of rotating composite plates. Most of these structural components can be approximated as laminated composite beams analyzed by Kapuria [121].

## 2.4.2 Material of the Blade

**Propeller Blade shape optimization**

Cho [122] developed a numerical optimization technique to determine the optimum propeller blade shape for efficiency improvement. The method satisfied the constraints of the constant power coefficient and activity factor. The design variables are the twisted angle and chord length, in this study a lifting line and lifting surface theory are used for calculation of objective functions to optimize the blade shapes of propellers. The present method showed good agreement with other numerical schemes for the straight bladed propeller. The optimization code is validated by comparing the results with other numerical schemes.

Dai et al. [123] discussed preliminary propeller design strategy, numerical optimization, knowledge-based systems and geometric algorithms in general and in specific as applied to the design of a particular propeller. A Propeller Automated Design System [PADS] has been developed using the ENGINEOUS software as a design synthesis of applying artificial intelligence, and numerical optimization of the design using PADS are presented and compared with the baseline design.

Latorre [124] interested in the development of efficient, high strength outboard propellers; the cupped propeller with a bent trailing edge has achieved some success.Likewise, a raised bar called an interceptor or spoiler on the propeller blade trailing edge has been discussed. The results indicate the feasibility of the outboard propeller with a spoiler. It presents a 3 part design study which examines the range of available outboard propellers, the optimum size of the outboard propeller and the capacity of predicting the influence of the spoiler on the outboard propeller performance.

## 2.4.3 Design and model evaluation of a new propeller

Kim [125] and Blake [126] developed a new design and presented extensive model test results for a highly skewed, five-blade, fixed pitch propeller. The main objective of

work is to increase cargo carrying capacity by about 50%. A new propeller design was required to provide the increased thrust but with cavitation performance comparable to or better than that of the existing. The design process and powering and cavitation test results are discussed in detail. A comparison of cavitation performance between the existing design and the new propeller is presented. The most important results from the cavitation tests are the cavitation extent on the new propeller is much less than on the original propeller.

# Chapter 3

# Flow Simulation of Marine Propeller Blade Using Computational Fluid Dynamics

## 3.1 CFD Analysis

### 3.1.1 Introduction

Computational Fluid Dynamics (CFD) is the science of predicting fluid flow, heat transfer, mass transfer, chemical reactions (e.g., combustion) and related phenomena by solving mathematical equations that govern these processes using a numerical algorithm on a computer. This technique is very powerful and spans a wide range of industrial and non-industrial applications.

### 3.1.2 Governing Equations of Fluid Flow

The governing equations of fluid flow represent mathematical statements of the laws of conservation of physics.Each individual governing equation represents a conservation principle. The fundamental equations of fluid dynamics are based on the following universal laws of conservation.

1) Conservation of mass
2) Conservation of momentum and
3) Conservation of energy

### 3.1.3 Continuity Equation

The equation based on the principle of conservation of mass is called continuity equation. The laws of conservation of mass applied to a fluid passing through an infinitesimal, fixed control volume yield the following equation of continuity,

$$\frac{\partial \rho}{\partial t}+\frac{\partial(\rho u)}{\partial x}+\frac{\partial(\rho v)}{\partial y}+\frac{\partial(\rho w)}{\partial z}=0 \tag{3.1}$$

$$\frac{\partial \rho}{\partial t} + \nabla.\left(\rho \overline{V}\right) = 0 \tag{3.2}$$

Where 'ρ' is the fluid density and $\overline{V}$ is the velocity vector field. For an incompressible flow, the density of each fluid element remains constant [127] .

### 3.1.4 Momentum Equations

The equations based on the laws of conservation of momentum or on the principle of momentum, state that, the net force acting on fluid mass is equal to the change in momentum of flow per unit time in that direction. The Navier-Stokes equations in conservative form can be written as [127]

$$\frac{\partial(\rho u)}{\partial t} + \frac{\partial\left(\rho u^2\right)}{\partial x} + \frac{\partial(\rho uv)}{\partial y} + \frac{\partial(\rho uw)}{\partial z} = -\frac{\partial p}{\partial x} + \frac{\partial \tau_{xx}}{\partial x} + \frac{\partial \tau_{yx}}{\partial y} + \frac{\partial \tau_{zx}}{\partial z} + \rho f_x \tag{3.3}$$

$$\frac{\partial(\rho v)}{\partial t} + \frac{\partial(\rho uv)}{\partial x} + \frac{\partial\left(\rho v^2\right)}{\partial y} + \frac{\partial(\rho vw)}{\partial z} = -\frac{\partial p}{\partial y} + \frac{\partial \tau_{xy}}{\partial x} + \frac{\partial \tau_{yy}}{\partial y} + \frac{\partial \tau_{zy}}{\partial z} + \rho f_y \tag{3.4}$$

$$\frac{\partial(\rho w)}{\partial t} + \frac{\partial(\rho uw)}{\partial x} + \frac{\partial(\rho vw)}{\partial y} + \frac{\partial\left(\rho w^2\right)}{\partial z} = -\frac{\partial p}{\partial z} + \frac{\partial \tau_{xz}}{\partial x} + \frac{\partial \tau_{yz}}{\partial y} + \frac{\partial \tau_{zz}}{\partial z} + \rho f_z \tag{3.5}$$

Unsteady Convective Pressure Diffusive Source (according to Newton's Law of Viscosity), are

$$\tau_{xy} = \tau_{yx} = \mu\left(\frac{\partial v}{\partial x} + \frac{\partial u}{\partial y}\right) \tag{3.6}$$

$$\tau_{xz} = \tau_{zx} = \mu\left(\frac{\partial w}{\partial x} + \frac{\partial u}{\partial z}\right) \tag{3.7}$$

$$\tau_{yz} = \tau_{zy} = \mu\left(\frac{\partial v}{\partial z} + \frac{\partial w}{\partial y}\right) \tag{3.8}$$

$$\tau_{xx} = \lambda\left(\nabla.\overline{V}\right) + 2\mu\frac{\partial u}{\partial x};\ \tau_{yy} = \lambda\left(\nabla.\overline{V}\right) + 2\mu\frac{\partial v}{\partial y};\ \tau_{zz} = \lambda\left(\nabla.\overline{V}\right) + 2\mu\frac{\partial w}{\partial z} \tag{3.9}$$

Where u,v,w represents the displacements in cartensian coordinate system. $\rho$ is the density of fluid. $\tau_{xy}, \tau_{xz}$ and $\tau_{yz}$ represent the shear stresses.

After rearranging the above term one can obtain

$$\lambda = -\frac{2}{3}\mu \tag{3.10}$$

The Navier-Stokes equations form the basis upon which the entire science of viscous flow theory has been developed. In general, the continuity and energy equations are also included in the Navier-Stokes equation.

## Reynolds averaged Continuity equation

For an incompressible fluid (water) considered here, the continuity equation from the conservation of mass principle is given as

$$\frac{\partial u_i}{\partial x_i} = 0 \tag{3.11}$$

in which $u_i$ is the i$^{th}$-component of the velocity vector .

$$\frac{\overline{\partial u_i}}{\partial x_i} = \frac{\partial \overline{u_i}}{\partial x_i} = 0$$

$$\frac{\partial u_i'}{\partial x_i} = 0 \tag{3.12}$$

The above two equations are the continuity equation for the mean velocity and the continuity equation for its fluctuating part respectively.

## Reynolds averaged Momentum equation

The momentum equation in conservation form can also be represented by eqn (3.3) through (3.5).Decomposing the dependent variables in the conservation equations into time-averaged (obtained over an appropriate time interval) and fluctuating components, the equation [127] becomes:

$$\frac{\partial(\rho U)}{\partial t}+\operatorname{div}(\rho UU)=-\frac{\partial \rho}{\partial x}+\operatorname{div}(\mu \operatorname{grad} U)+\left[-\frac{\partial\left(\rho \overline{u'^2}\right)}{\partial x}-\frac{\partial\left(\rho \overline{u'v'}\right)}{\partial y}-\frac{\partial\left(\rho \overline{u'w'}\right)}{\partial z}\right]+S_{Mx} \tag{3.13}$$

$$\frac{\partial(\rho V)}{\partial t}+\operatorname{div}(\rho VU)=-\frac{\partial \rho}{\partial y}+\operatorname{div}(\mu \operatorname{grad} V)+\left[-\frac{\partial\left(\rho \overline{u'v'}\right)}{\partial x}-\frac{\partial\left(\rho \overline{v'^2}\right)}{\partial y}-\frac{\partial\left(\rho \overline{v'w'}\right)}{\partial z}\right]+S_{My} \tag{3.14}$$

$$\frac{\partial(\rho W)}{\partial t}+\operatorname{div}(\rho WU)=-\frac{\partial \rho}{\partial z}+\operatorname{div}(\mu \operatorname{grad} W)+\left[-\frac{\partial\left(\rho \overline{u'w'}\right)}{\partial x}-\frac{\partial\left(\rho \overline{v'w'}\right)}{\partial y}-\frac{\partial\left(\rho \overline{w'^2}\right)}{\partial z}\right]+S_{Mz} \tag{3.15}$$

Comparison of these equations with conservation equations indicates that, in the case of the turbulent flow, there is an additional stress term, $-\rho u'_i u'_j$ . This additional stress is called the Reynolds stress. There are nine such stresses present in the time- averaged momentum equations, out of which six are unknown.

$$-\rho \overline{u_i' u_j'}=\begin{bmatrix} -\rho \overline{u_1' u_1'} & -\rho \overline{u_1' u_2'} & -\rho \overline{u_1' u_3'} \\ -\rho \overline{u_2' u_1'} & -\rho \overline{u_2' u_2'} & -\rho \overline{u_2' u_3'} \\ -\rho \overline{u_3' u_1'} & -\rho \overline{u_3' u_2'} & -\rho \overline{u_3' u_3'} \end{bmatrix} \tag{3.16}$$

Whereas, there are ten unknowns (namely, three components of the velocity $\overline{u}_i$ , pressure, $\overline{p}$ and six components of the Reynolds stress $-\rho \overline{u}_i' \overline{u}_j'$ .Hence the system is not closed. This problem is known as the closure problem of turbulence.

Therefore Reynolds equations cannot be solved directly because the new apparent turbulent stresses are new unknowns. To proceed further, it is necessary to find additional equations involving the unknowns or make assumptions regarding the relation between the new apparent turbulent quantities and the time-mean variables. This is known as the closure problem, which is handled through turbulence modelling.

## 3.2 Turbulence Modelling

### The RNG k-ε turbulence model:

Transporting the Equations (3.13 to 3.15) for the RNG $k-\omega$ Model one can write

$$\frac{\partial}{\partial t}(\rho k)+\frac{\partial}{\partial x_i}(\rho k u_i)=\frac{\partial}{\partial x_j}(\alpha_k \mu_{eff}\frac{\partial}{\partial x_j})+G_k+G_b-\rho\varepsilon-Y_M+S_k \quad (3.17)$$

$$\frac{\partial}{\partial t}(\rho\varepsilon)+\frac{\partial}{\partial x_i}(\rho\varepsilon u_i)=\frac{\partial}{\partial x_j}(\alpha_\varepsilon \mu_{eff}\frac{\partial\varepsilon}{\partial x_j})+C_{1\varepsilon}\frac{\varepsilon}{k}(G_k+C_{3\varepsilon}G_b)-C_{2\varepsilon}\rho\frac{\varepsilon^2}{k}-R_\varepsilon+S_\varepsilon \quad (3.18)$$

In the above equations,

k= Turbulent kinetic energy

ε = Specific Dissipation Rate

$\tilde{G}_k$ = production of turbulence kinetic energy

$G_b$ = generation of turbulence kinetic energy due to buoyancy

$\alpha_k, \alpha_\varepsilon$ = inverse effective Prandtl numbers for $k$ and $\varepsilon$ and

$S_k, S_\omega$ =user-defined source terms

$Y_M$ represents the contribution of the fluctuating dilatation incompressible turbulence to the overall dissipation rate. The terms $k$ *and* $\varepsilon$ values are used to compute Reynolds stress tensor.

### Numerical Methods in CFD

A numerical solution of a differential equation consists of a set of numbers from which the distribution of the dependent variables 'Φ' can be constructed. In this sense, a numerical method is akin to a laboratory experiment, in which a set of instrument readings enables us to establish the distribution of the measured quantity in the domain under investigation. The numerical analyst and the laboratory experiment both must remain context with only a finite number of numerical values as the outcome, although this number can, at least in principle, be made large enough for practical purposes.

There are three important methods in CFD,

1. Finite Difference Method (FDM)
2. Finite Volume Method (FVM) and
3. Finite Element Method (FEM)

For the present analysis, FVM is used

**Finite Volume Method**

Some weighted residual equations can be generated by dividing the calculation domain into sub-domain (or) control volume, and setting the weighting function to be unity over one sub-domain at a time and zero everywhere else. This variant of the method of weighted residuals is called the sub-domain method (or) finite volume method. It implies that the integral of the residuals over each control volume must become zero. In the control volume formulation, the calculation domain is divided into some non-overlapping control volumes. The differential equation is integrated over each control volume. The appropriate form of the conservation statement for the control volume (namely, that the time rate of increase of energy stored in the volume is equal to the net rate at which energy is conducted into the volume) can be represented mathematically as,

$$\iiint_{R} \rho C \frac{\partial T}{\partial t} dR + \oiint_{S} q n ds = 0 \tag{3.19}$$

The first term in this equation, an integral over the control volume, represents the time rate of increase in the energy stored in the volume. The second term, an integral over the surface of the volume, represents the net rate at which energy is conducted out through the surface of the volume. For a 2D problem, the volume employs a unit depth. In two dimensions, we can represent ends as (idy-jdx) for an integration path around the boundary in a counterclockwise direction. This surface integral on the right, representing the net flow of heat out through the surface of the volume, can be evaluated as

$$\oint_{S} \left( q_x dy - q_y dx \right) \tag{3.20}$$

Where $q_x$ and $q_y$ are components of the heat flux in the x and y directions, respectively. The conservation statement then becomes

$$\iiint_R \rho C \frac{\partial T}{\partial t} dR + \oiint_S (q_x dy - q_y dx) = 0 \quad (3.21)$$

## Solution Algorithm for Pressure-Velocity Coupling in Steady Flows

The convection of a scalar variable Φ, where Φ represents flow properties like u, v, w, p, T, ρ etc., depends on the magnitude and direction of the local velocity field.To develop the solution, the velocity field must be known. Transport equations for each velocity component (momentum equations) can be derived from the general transport equation by replacing the variable Φ by u, v and w respectively. The velocity field must satisfy the continuity equation. The pressure gradient term forms the main momentum source term in many engineering applications. If the pressure gradient is known the process of obtaining discretized equations for velocities from the momentum equations is similar for any other scalar quantity. In this algorithm, the convective fluxes per unit mass through the cell faces are evaluated from so-called guessed velocity components. If the pressure field is known, the discretization of velocity equations and the subsequent solution procedure is similar to that of a scalar equation.

### General Procedure for Algorithms

The steps involved for the present algorithm are

1. Guess the pressure ($P_o$) at each grid point
2. Solve the momentum equations to find the velocity components ($U_0, V_0$).
3. Solve the pressure-correction equation to find 'p' at each grid point
4. Replace the previous intermediate values of pressure and velocity with the new corrected values and return to the original step. Repeat the step until the step converges.

### Simple Algorithm

The acronym SIMPLE stands for a semi-implicit method for pressure linked equations. The algorithm developed by Patankar [128] is essentially a correct guess procedure for the calculation of pressure on the staggered grid arrangement. The method can be explained by considering the two-dimensional laminar steady flow equations in Cartesian coordinates. To initiate the simple calculation process a pressure field P* is guessed. Discretised momentum equations are solved using the guessed pressure field to yield velocity

components U* and V*. The correction $P_1$ is the difference between the correct pressure field P and the Guessed pressure field P*, so that

$$P = P^* + P_1 . \tag{3.22}$$

Similarly, velocity corrections $U_1$ and $V_1$ to relate correct velocities U and V to the guessed velocities $U^*$ and $V^*$ are given by

$$\begin{aligned} U &= U^* + U_1 \text{ and} \\ V &= V^* + V_1 \end{aligned} \tag{3.23}$$

Substitution of the correct pressure field P into the momentum equations (3.3-3.5) yields the correct velocity field (u, v).

**Finite Volume Solver**

FLUENT is a state-of-the-art computer program for modelling fluid flow and heat transfer in complex geometries. FLUENT provides complete mesh flexibility solution for flow problems with unstructured meshes that can be generated about complex geometries with relative ease. Supported mesh types include 2D triangular/quadrilateral, 3D tetrahedral/hexahedral/pyramid/wedge and mixed (hybrid) meshes. FLUENT also allows grid adaption to refine or coarsen grid based on the flow solution.

This solution-adaptive grid capability is particularly useful for accurately predicting flow fields in regions with large gradients, such as free shear layers and boundary layers. In comparison to solutions on structured or block-structured grids, this feature significantly reduces the time required to generate a high-quality grid. Solution adaptive refinement makes it easier to perform grid refinement studies and reduces the computational effort required to achieve a desired level of accuracy since mesh refinement is limited to those regions where greater mesh resolution is needed. The complete CFD analysis for open water characteristics is shown through a flow chart (Fig.3.1)**.**

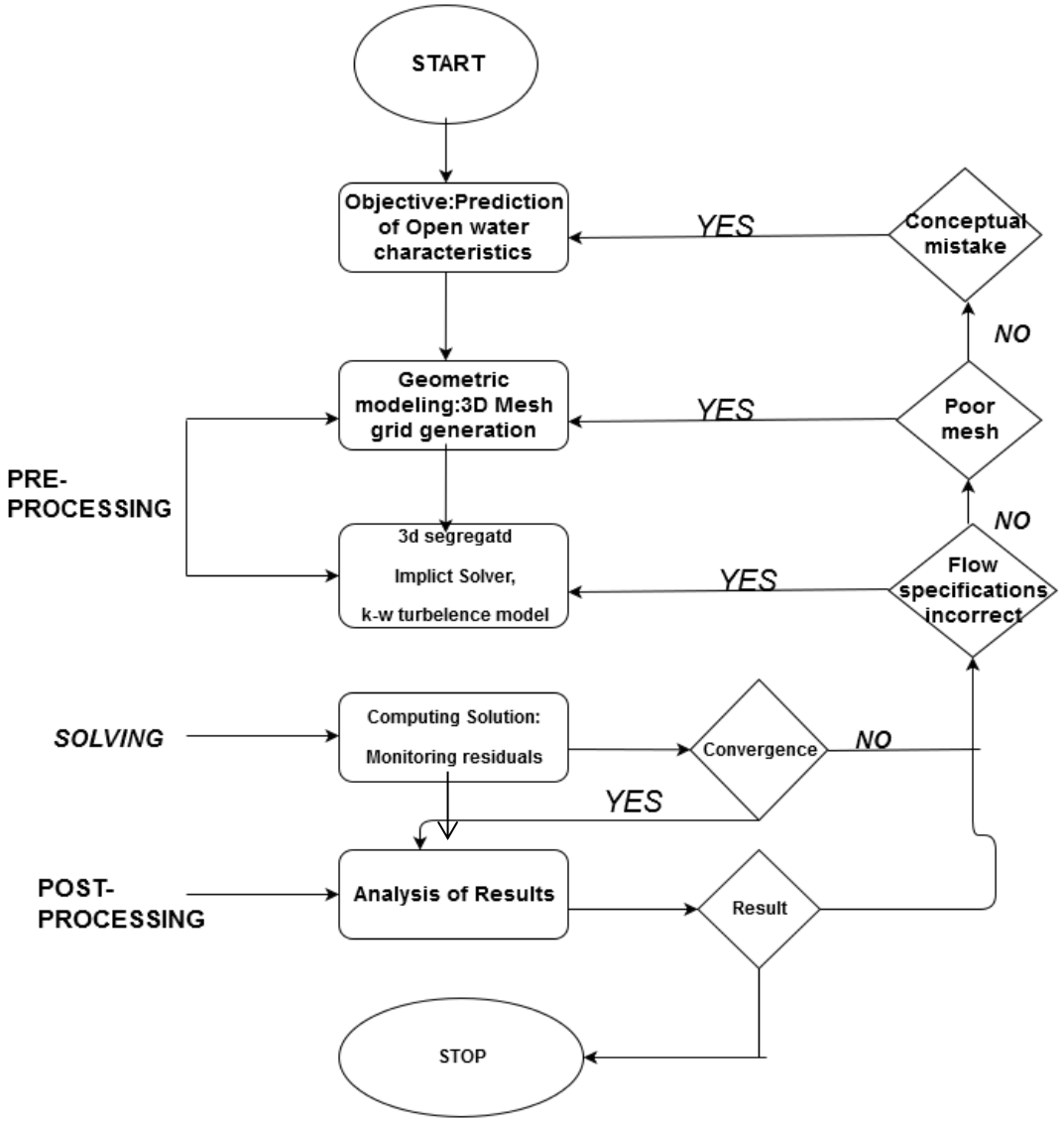


Figure 3.1: Flow Chart showing complete CFD analysis for open water characteristics

## 3.3 Flow simulation of propeller blade

In the numerical simulations of the aerofoil-shaped blades, the numerical method is used to simulate physical problems with the use of governing equations. The numerical method can be used to investigate design approaches without creating a physical model and can be a valuable tool to understand conceptual properties of new mechanical designs. By using simulation instead of doing lab experiments, one may acquire results faster and with less expense. An important aspect in the use of CFD method is to understand the simplifications in software and know the limitations of the computed results. Though the

CFD software uses well known governing equations, severe simplifications are made regarding grid representing geometries.

### 3.3.1 Approximations and Model preparation

In the present study, the numerical study for Wageningen B-series propeller blade is conducted using FLUENT solver. The following procedures are employed to carry out the CFD simulation.

1. The B-series propeller blade geometry was acquired as coordinate vertices, and it is imported into the CATIA software.
2. Some minor adjustments were made to this in order to correct the geometry and make it valid as a CFD model.
3. It creates the working environment where the object is simulated. An important part in this creating is the mesh surrounding the object. This needs to be extended in all directions to get the physical properties of the surrounding fluid – in this case moving water.
4. The mesh and edges must also be grouped in order to set the necessary boundary conditions effectively.

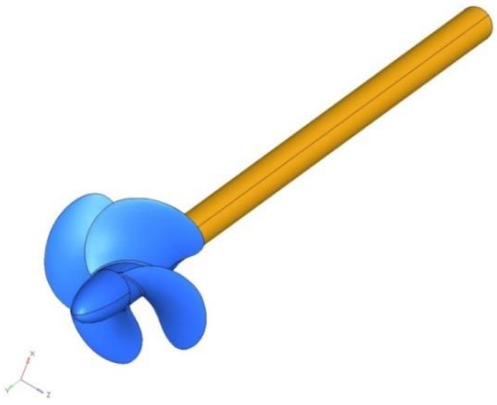

Figure 3.2: Geometric model for CFD analysis

### 3.3.2 Meshing

An environment consisting of two squares and one semicircle (known as far-field) surrounds the B-series propeller. The mesh is constructed to be very fine at regions close to the aerofoil and with high energy and coarser, farther away from the aerofoil. For this aerofoil, a structured quadratic mesh was used. Due to limitations in the FLUENT

software, the mesh has to be fine in certain regions far away from the aerofoil**.** A fine mesh implies a higher number of calculations which in turn makes the simulation longer to execute. For the B-series propeller, the very front has an edge grid distributed with increasing distance between nodes starting from very small sizes. From the point of maximum thickness on the aerofoil to the very back, an even number of points is distributed on the aerofoil surface.

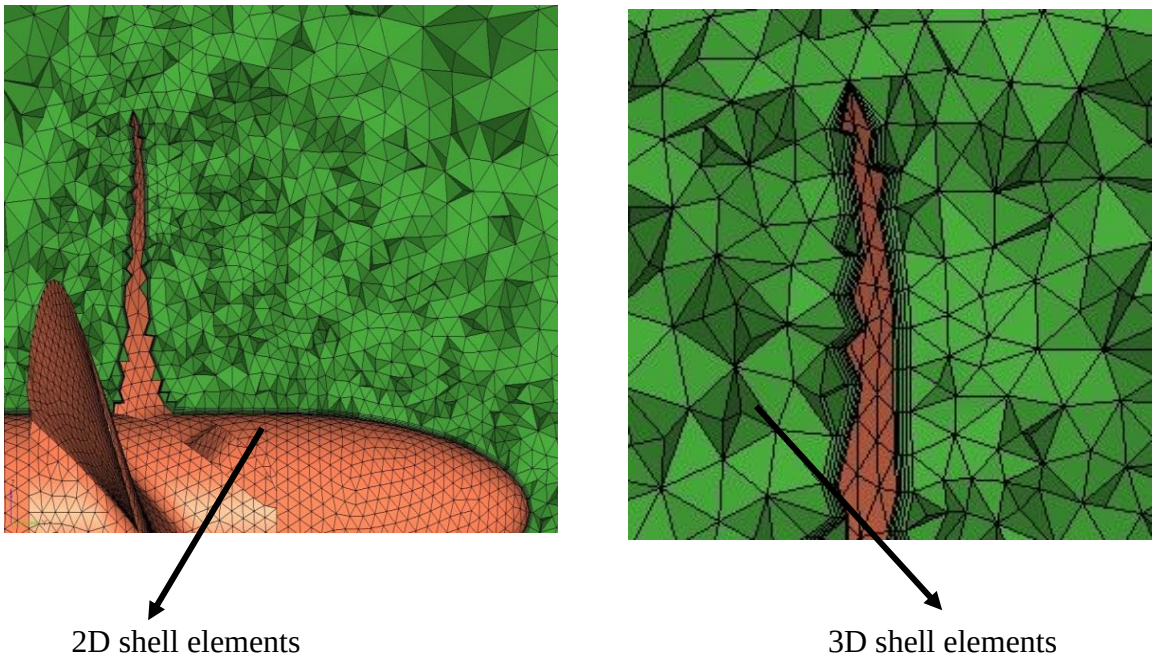


Figure 3.3: Prism layers around the Blades with close view

**Grid Generation.**

Fairing caps and shaft are added to the propeller for CFD analysis as shown in Figure 3.2. The 2D and 3D shell elements for farfield and blade are shown in Figure 3.3**.** The flow domain is required to be discretized to convert the partial differential equations into series of algebraic equations as shown in Figure 3.4. This process is called grid generation.

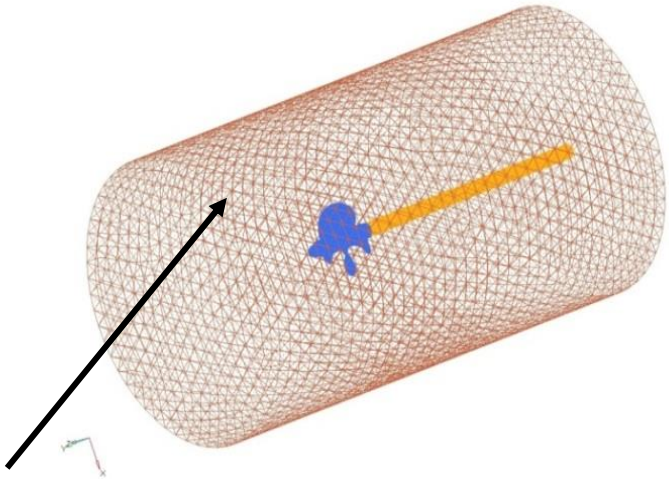

Shell elements

Figure 3.4: Grid over the entire domain

### 3.3.3 Setting boundary conditions

Assigning properties to the different geometries is vital to make the simulation work. In this case, the mesh boundaries were set to the x and y velocity components, and the end boundary to the property "pressure-outlet" to simulate the zero gauge pressure. The continuum is chosen as fluid and the properties of water are assigned to it. A moving reference frame is assigned to fluid with a rotational velocity (800, 900, 930, 1000, 1100, 1200, 1300, 1400, 1500, 1600, 1700, 1800, 1900, 2000 rpm etc). The wall forming the propeller blade, hub and shaft was assigned a relative rotational velocity of zero with respect to adjacent cell zone. A uniform velocity 6.12m/s was imposed at the inlet. At the outlet outflow boundary condition was set. The far boundary (far field) was taken as inviscid wall and assigned an absolute rotational velocity of zero. All boundary zones are shown in Figure 3.5.

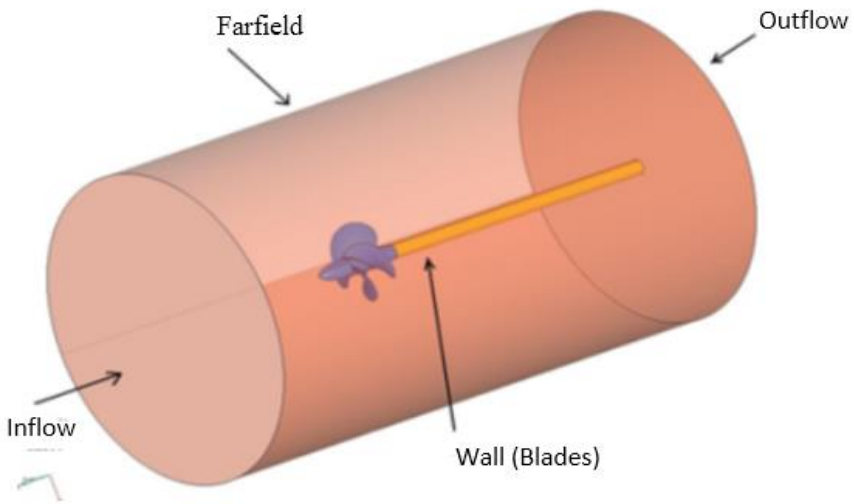


Figure 3.5: Boundary conditions

### 3.3.4 Setting up of FLUENT

The geometries and mesh were imported into FLUENT; the system and environment properties are set. FLUENT has single precision as default, but for these simulations, an accurate solution is requested. The residuals for the different turbulence model variables were set to 8-10, and the iteration max counts to 20000. The simulation process could also be halted or stopped if the $C_L$ or $C_D$ seemed to have stabilized properly.

### 3.3.5 Viscosity Models

Considering vortex shedding and boundary layer separation for propeller blade, this simulation will have to deal with turbulent flows. The chaotic nature of turbulent flow makes it very expensive to compute velocities for all points in space. RANS is opposite to DNS, which is the direct analytic simulation of the governing equations and uses a statistical and averaged approach to find the flow behavior. The reason for using RANS models is that small vortices –in turn, are very expensive to solve and are removed by averaging the flow. The crucial point is to select a viscous model, with FLUENT having several options. There are fundamental differences between the different models, and may be used for different types of flows. In the present study, the viscous models RNG K-Є is used.

### 3.3.6 Flow Solution and Solver Settings

The FLUENT 6.3.2 code was used to solve the three-dimensional viscous incompressible flow. The blade geometry and its specifications are shown in Table 3.1and Table 3.2 shows the solver setting.

Table 3.1: Specifications of Propeller blade

| Propeller | Soviet Developed Board (SDB) |
|---|---|
| Principal Dimensions | Propeller Diameter (D) = 0.212m |
| Domain size | Cylindrical domain of length 1.484m (7D), diameter 0.848m (4D). |
| Mesh count | ~0.55 million tetrahedral and prism cells. |

Table 3.2: Solver settings

| Pressure Link | SIMPLE |
|---|---|
| Pressure | Standard |
| Discretization scheme for convective fluxes and turbulence parameters | First order upwind |
| Turbulence model | RNG K-Є |
| Near Wall Treatment | Standard wall functions |
| Solver | Steady |
| Operating Pressure | 101325 Pa |
| Vapour pressure | 1720 Pa at 15°C |

### 3.3.7 Methodology used in Present analysis:

**Calculation of load on propeller**

The objective of the present CFD analysis is to find the vapour pressure (cavitation inception) around the blade for different values of rotational speed, then the pressures obtained from CFD solution are used as load input for static analysis to exploit the bending and twisting(BT) for (deformed) geometry carried for next CFD simulation. Finally, open water characteristics of a marine propeller ($K_T$, $K_Q$, $\eta_0$) for different values of advance coefficients (J) are presented.

**Creation of model geometry and grid**

The domain was considered three times of the diameter in upstream, four times to the diameter in downstream and two times the diameter in the radial direction. Three-dimensional unstructured tetrahedral grid with prism layers on blades was generated to discretise the domain.

**Selection of solver and physical models**

Three-dimensional segregated implicit solvers were used in the present analysis. The RNG k-ω turbulence model in addition to the continuity and momentum equations were used as governing equations. Boundary conditions used in the present analysis are inlet and far field as velocity inlet, outlet as outflow and blade with caps as walls. For fluid domain, moving rotational reference frame was considered to make the problem steady.

**Computing and monitoring the solution**

The discretized conservation equations were solved iteratively at different values of advance coefficients (J). The solution allowed to converge "when changes in solution variables from one iteration to the next and are negligible ($\leq 0.0001$)".

**Examine and save the results**

After computing and monitoring, it is required to examine the results to review the solution and extract useful data (forces and moments).These results were compared with experimental findings or with standard series data. In the present analysis, only final solution results are presented. To arrive at these results, different boundary conditions and grids have been considered for revision.

## 3.4 Cavitation on Marine Propeller Blade

### 3.4.1 Introduction

When an object moves rapidly through the water, the pressure in the liquid adjacent to the body drops in proportion to the square of local flow velocity. If the local pressure drops below the vapour pressure of surrounding liquid, small pockets or cavities of vapour are formed. As the flow slows down behind the object, these little cavities collapse with explosive force. Cavitation occurs when the minimum pressure on the surface of the hydrofoil falls below vapour pressure. Water, free of dissolved gas can sustain considerable tensile stress, but the air content of near-surface sea water is sufficiently high for vaporization to occur as soon as the vapour pressure is reached.

The inception of cavitation on hydrofoil is a basic phenomenon in hydrodynamics which refers to the appearance of vapour phase when liquid flows around a hydrofoil. For thin hydrofoils at a moderate angle of attack, the first occurrence of cavitation is closely

related to the minimum pressure near the leading edge. Under these conditions, the inception of cavitation marks the establishment of a relatively large separated flow of vapour on the upper surface near the leading edge commonly referred to as sheet cavitation. Once sheet cavitation is developed, pressure on the upper surface of the hydrofoil is higher than the non-cavitating flow. This in turn, limits the hydrofoils maximum lift, increases drag and changes the pitching moment, which may also be responsible for propeller noise and vibration as well as efficiency drop and material erosion. The typical design objective is to delay cavitation to higher angles of attack in order to widen the performance of propeller's blades.

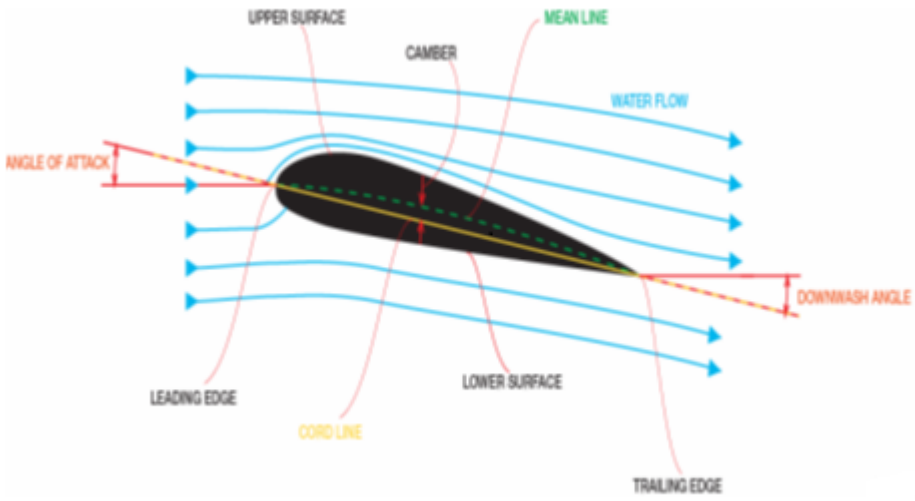


Figure 3.6: Description of hydrofoil

Minimum pressure coefficient ($C_{pmin}$) is used to measure and correlate cavitation inception. For a given hydrofoil at a fixed angle of attack, cavitation inception index ($\sigma_i$) tends to increase with flow Reynolds's number. Various studies provided the cavitation inception index at various angles of attack. Increasing the angle of attack up to the stall angle at a fixed Reynolds's number also causes to increase in cavitation inception index. Cavitation inception is dependent on various effects such as surface roughness, cavitation nuclei and transport of non-condensable gases.

Self-twisting composite marine propellers, when subject to hydrodynamic loading, will not only automatically bend but also twist due to passive bend–twist (BT) coupling characteristics of FRP composites. To exploit the BT coupling effects of self-twisting propellers, CFD methodology is proposed, formulated and implemented. Optimized and

tested lay-up sequences are applied for the propeller. Results from literature show that the self-twisting propeller produced the same performance as the rigid propeller at the design flow condition, and it produced better performance than the rigid propeller at off-design flow conditions, including behind a spatially varying wake. These BT (deflections) indirectly cause the change of angle of attack for the corresponding hydrofoil sections. Thus changes in the angle of attack from BT coupling characteristics of composites should be in such a way to raise the cavitation inception speed. However, this idea can't be applicable for a metal propeller which can be considered as rigid, due to its negligible bend and twist. The local pressure P and local velocity V at any point on the surface of a hydrofoil (propeller blade) are related to the static pressure $P_o$ (atmospheric + water head) and dynamic pressure $q=\frac{1}{2}\rho v^2$ of the uniform flow by Bernoulli's equation.

$$P+\frac{1}{2}\rho V^2 = P_0 + q \tag{3.24}$$

$$P-P_0 = \frac{1}{2}\rho V^2 - \frac{1}{2}\rho v^2 = \frac{1}{2}\rho V^2\left(1-\frac{v^2}{V^2}\right) \tag{3.25}$$

From the above equation the local pressure coefficient is defined as:

$$C_p = (P-P_0)/q = 1-(v/V)^2 \tag{3.26}$$

For non-cavitating flow

$$\sigma_i = -C_{p\min} < \frac{P_o - e}{q} = \sigma \quad \text{(p has dropped to e)} \tag{3.27}$$

$\sigma$ = Cavitation number (a function of the flow conditions)

$\sigma_i$ =Cavitation index (a characteristic of the foil section shape, i.e. its resistance to cavitation)

e = Function of temperature, e =$1.72*10^3$ N/$m^2$

To avoid cavitation on a given foil section, a cavitation "bucket diagram" is plotted for section $\sigma_i$ against the section lift coefficient $C_L$ (Fig 3.7)**.** The three branches of the curve define a bucket within which the sections will not cavitate.

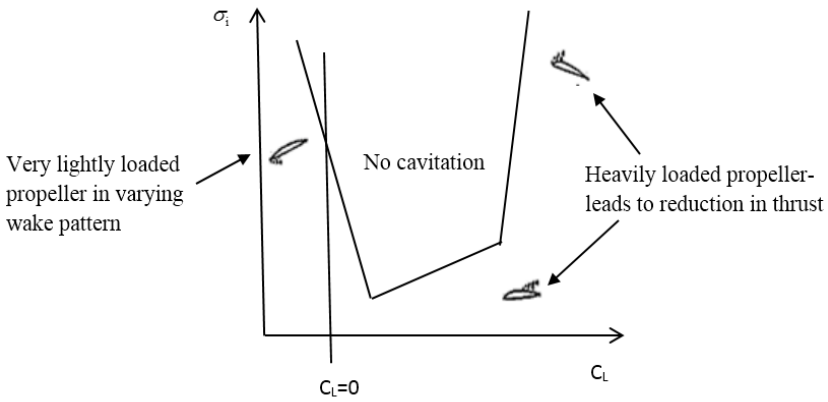


Figure 3.7: Typical cavitation bucket diagram

Each bucket is made up of three curves. The left-hand curve is the boundary between sub-cavitating operation and cavitation from the underside of the leading edge of the section. The right-hand curve is the boundary for cavitation to occur from the upper surface of the section near the leading edge. The lower curve i.e. the bottom of the 'bucket' is the boundary for cavitation to occur from the mid back position on the low -pressure side of the foil, at an angle of incidence around the ideal value. Inside the 'bucket' is the range of cavitation free operation. The width of the bucket defines the range of angles of incidences free from cavitation. Tip vortex cavitation occurs when the thrust of the blades is high enough for the pressure in the tip vortices to drop to vapour pressure. As thrust loading increases, cavitation spreads down the back of the blades. Cavitation occurs when the local absolute pressure is less than local vapour pressure for the fluid medium. The critical measurement for cavitation performance is the cavitation inception point which is the condition for which cavitation is first observed anywhere on the back as shown in Figure 3.8. At this instant, the cavitation number is referred to as incipient or critical cavitation number.

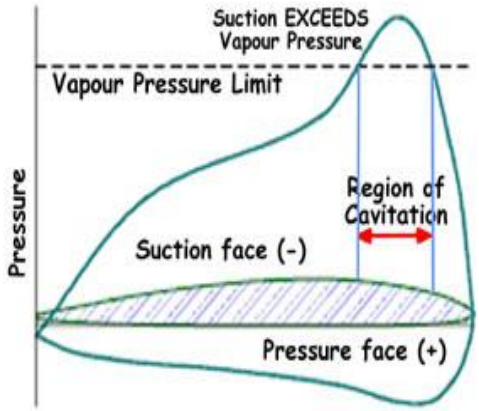


Figure 3.8: Cavitation inception on the suction face.

Cavitation inception is of direct importance to Navy vessels, because of the sudden increase in noise levels at the onset of cavitation, however, on the other side with slightly different conditions cavitation inception causes erosion and radiated pressure fluctuations.

The critical measurement for cavitation performance is the cavitation inception point determination (i.e. cavitation number) with prevailing conditions over which cavitation is first observed any where on the propeller. Typically the inception cavitation number as a function of $K_t$ or J is plotted for a given propeller which defines the cavitation-free operation boundary. This boundary typically has a bucket shape which is referred to as the cavitation bucket.

## 3.5 Comparison with Previous Studies

### 3.5.1 Bend-twist coupling and its effect on cavitation inception of composite marine propeller

In this section, the open water characteristics of a marine propeller blade are determined and compared with the Reference. The aim is to evaluate the suitability and applicability of designed propeller for underwater applications. As per the Reference [129] a metallic propeller blade was designed and modelled using high-end modelling software Catia V5R20 and Solidworks. The tetrahedral mesh for carrying out numerical computing in FLUENT is done using Hypermesh 11.0 software.

The blade, shaft, cap, inlet outlet and fluid domain are meshed with shell elements. The solid mesh is created between wall, shaft, inlet, outlet and far field.With the data taken from reference [129] the thrust and torque values are computed for the developed propeller using FLUENT software. From the values of torque and thrust the thrust coefficient, torque coefficient and open water efficiency for the designed propeller are determined and compared [129].The three dimensional solid model of four blade propeller is shown in the Figure 3.9

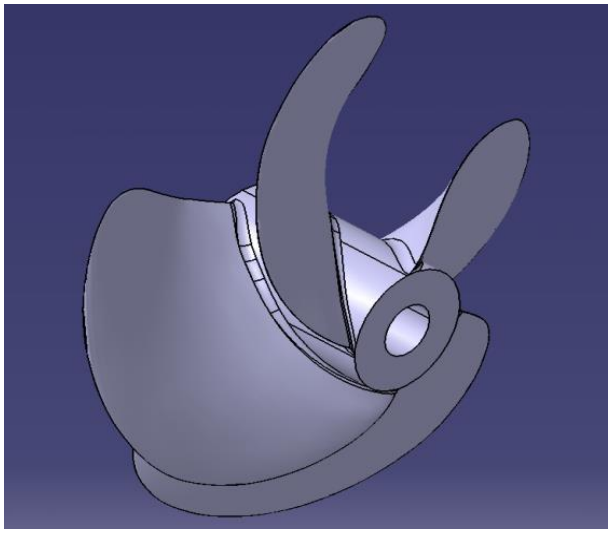

Figure 3.9: Three dimensional model of propeller

## 3.5.2 Flow Solution and Solver Settings

The FLUENT 6.3.26 code was used to solve the three-dimensional viscous incompressible flow.The blade geometry and its specifications along with its solver settings are shown in Table 3.3 and 3.4.

Table 3.3: Propeller specification Details

| Propeller | Soviet Developed Board (SDB) |
|---|---|
| Principal Dimensions | Propeller Diameter (D) = 0.205m |
| Domain size | Cylindrical domain of length 1.435m (7D), diameter 0.82m (4D). |
| Mesh count | 5.5 lakh tetrahedral and prism cells. |

Table 3.4: Solver settings

| Pressure Link | SIMPLE |
|---|---|
| Pressure | Standard |
| Discretization scheme for convective fluxes and turbulence parameters | First order upwind |
| Turbulence model | RNG K-Є |
| Near Wall Treatment | Standard wall functions |
| Solver | Steady |
| Operating Pressure | 140 kPa |
| Vapour pressure | 1.72kPa |

### 3.5.3 Results

The difference of pressure on the face and back of the propeller blade results in thrust. To develop propulsion factors thrusts, torque, the speed of rotation, the speed of hull are to be determined either using propulsion test or analysis package. The propulsion factors represented in terms of non-dimensional coefficients, Thrust coefficient ($K_T$), Torque coefficient ($K_Q$), and Advanced coefficient (J) are to be used for determination of open water Efficiency ($\eta_0$).

These non-dimensional terms expressing the general performance characteristics are

$$\text{Advanced coefficient (J)} = \frac{V_a}{n * D}$$

$$\text{Thrust coefficient } (K_T) = \frac{T}{\rho * n^2 * D^4}$$

$$\text{Torque coefficient } (K_Q) = \frac{Q}{\rho * n^2 * D^5}$$

$$\text{Open water Efficiency } (\eta_0) = \frac{J}{2 * \pi} * \frac{K_T}{K_Q}$$

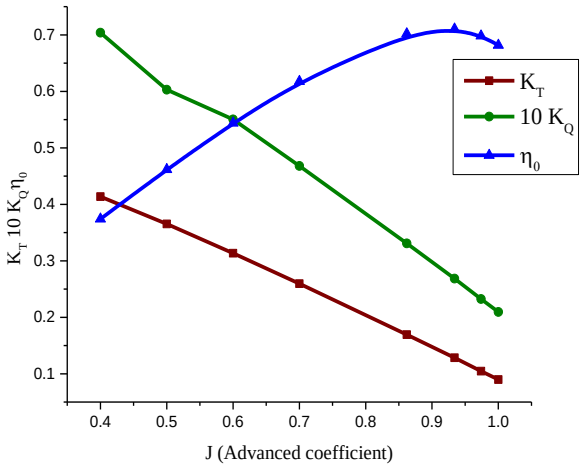


Figure 3.10: Computation of KT, KQ and Open water efficiency (η0) using CFD analysis

The above values of thrust coefficient ($K_T$), toque coefficient ($K_Q$) and open water efficiency ($\eta_o$) are plotted against advance coefficients (J) to get the open water characteristics as shown in the Figure 3.10. The comparison of calculated and reference values of non-dimensional terms are listed in the Tables 3.5-3.7.

Table 3.5: Open water characteristics results obtained from CFD analysis

| Advanced Coefficient (J) | Advanced velocity $V_a$ (m/s) | Rotational speed N (rpm) | Thrust T (N) | Torque Q(N-m) | Thrust Coefficient ($K_T$) | Torque Coefficient ($10K_Q$) | Open water efficiency $\eta_o$ |
|---|---|---|---|---|---|---|---|
| 1.00 | 3.83 | 1120 | 55.21 | 2.642 | 0.0897 | 0.2094 | 0.6817 |
| 0.97 | 3.83 | 1150 | 67.80 | 3.085 | 0.1046 | 0.2324 | 0.6982 |
| 0.93 | 3.83 | 1200 | 90.51 | 3.882 | 0.1283 | 0.2685 | 0.7104 |
| 0.86 | 3.83 | 1300 | 140.14 | 5.615 | 0.1693 | 0.3309 | 0.7021 |
| 0.70 | 3.83 | 1600 | 325.90 | 12.05 | 0.2595 | 0.4680 | 0.6177 |
| 0.60 | 3.83 | 1800 | 535.91 | 19.28 | 0.3135 | 0.5504 | 0.5439 |
| 0.50 | 3.83 | 2200 | 899.32 | 31.77 | 0.3653 | 0.06297 | 0.4617 |
| 0.40 | 3.83 | 2800 | 1590.79 | 55.50 | 0.4136 | 0.7039 | 0.374 |

Table 3.6: Comparison of Thrust, Torque and Advanced coefficient values with Reference[129]

| Advanced Velocity $V_a$ (m/s) | Rotational speed N (rpm) | Advanced Coefficient (J) | | Thrust T (N) | | Torque Q (N-m) | |
|---|---|---|---|---|---|---|---|
| | | Ref [129] | Present | Ref [129] | Present | Ref [129] | Present |
| 3.83 | 1200 | 0.93 | 0.93 | 90.51 | 90.51 | 3.88 | 3.882 |
| 3.83 | 1600 | 0.70 | 0.70 | 324.92 | 325.91 | 12.01 | 12.05 |
| 3.83 | 1800 | 0.62 | 0.60 | 498.17 | 535.91 | 17.29 | 19.28 |
| 3.83 | 2200 | 0.51 | 0.50 | 854.58 | 899.32 | 30.24 | 31.77 |
| 3.83 | 2800 | 0.40 | 0.40 | 1587.42 | 1590.79 | 55.38 | 55.50 |

Table 3.7: Comparison of predicted and reference [129] values of KT, KQ, $\eta_0$

| Advanced coefficient (J) | | Thrust Coefficient ($K_T$) | | Torque Coefficient ($10K_Q$) | | Efficiency ($\eta_0$) | |
|---|---|---|---|---|---|---|---|
| Ref [128] | Present | Ref [129] | Present | Ref [129] | Present | Ref [129] | Present |
| 0.93 | 0.93 | 0.128 | 0.128 | 0.268 | 0.268 | 0.711 | 0.710 |
| 0.70 | 0.70 | 0.259 | 0.259 | 0.466 | 0.468 | 0.619 | 0.617 |
| 0.62 | 0.60 | 0.313 | 0.313 | 0.531 | 0.550 | 0.586 | 0.543 |
| 0.51 | 0.50 | 0.360 | 0.365 | 0.621 | 0.629 | 0.470 | 0.461 |
| 0.40 | 0.40 | 0.425 | 0.413 | 0.721 | 0.703 | 0.351 | 0.374 |

Figure 3.11 shows that there is a good degree of agreement of results between the calculated and standard values from the Reference [129].

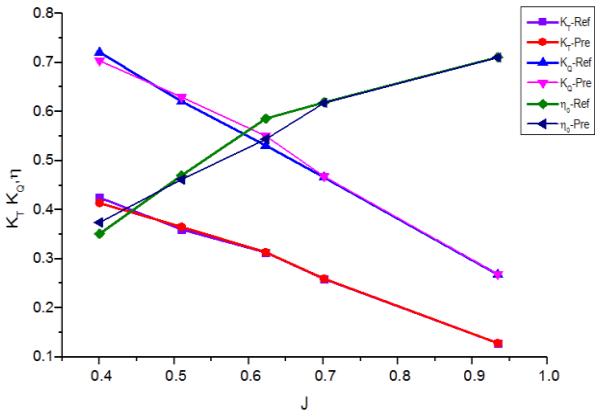


Figure 3.11: Comparison of Thrust, Torque, Open water efficiency and Advanced coefficient values with Reference [129]

Pressure distribution on the surface of blades is shown in Figure 3-12. The front and back are experiencing high and low pressures respectively. The maximum pressure is obtained on both faces of the blade.

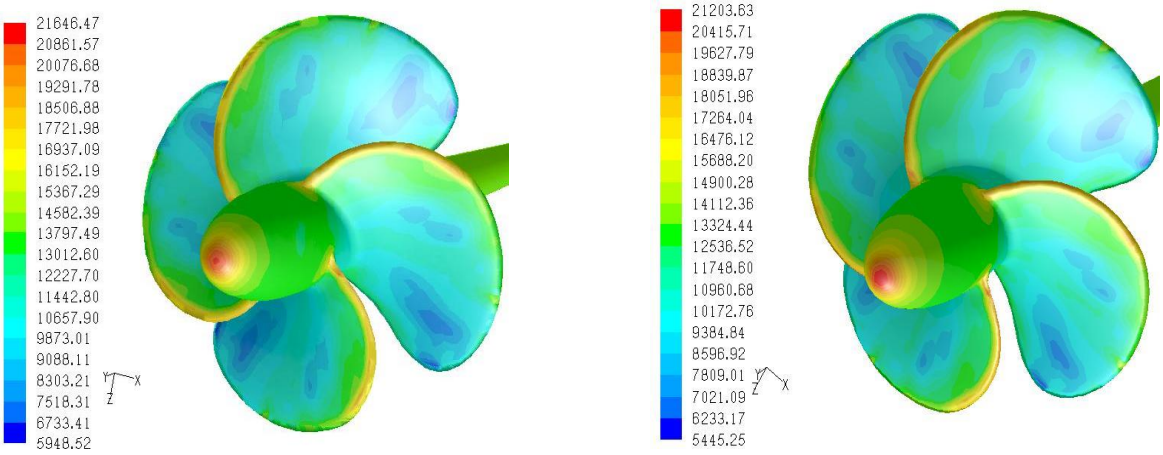


(a):at N=1100 rpm & J=1.01 (b):at N=1150 rpm & J=0.974

Figure 3.12: Absolute pressure contours on blade surface (Pa)

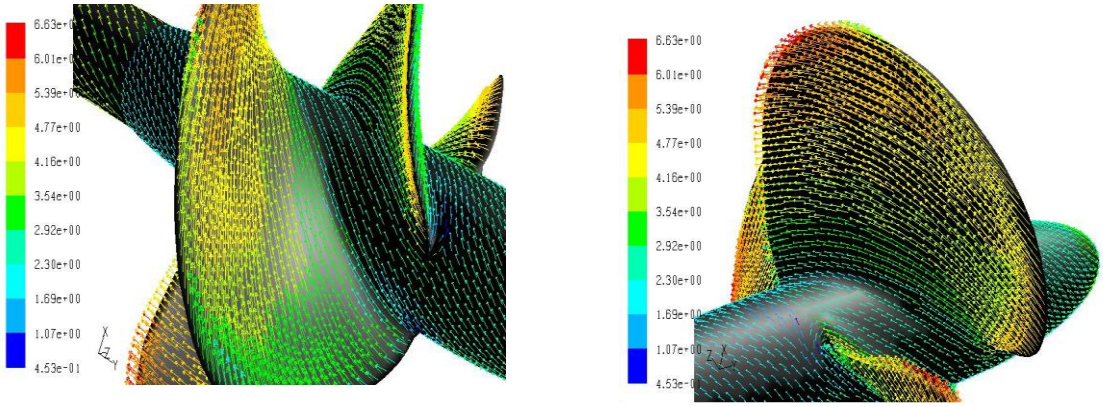


Figure 3.13: Relative velocity vectors at blade surface for $V_a$= 3.83 m/s, and J=0.934

CFD analysis for rotational speed=1100 rpm and advanced velocity=3.83m/s and relative velocity distribution at N=1200 rpm and J=0.9341 around the blade surface are shown in Figures 3.13 and 3.14. Figure 3.13 shown above represents that there is no flow separation near the blade surface section, which was expected as the propeller was a well-designed standard one.

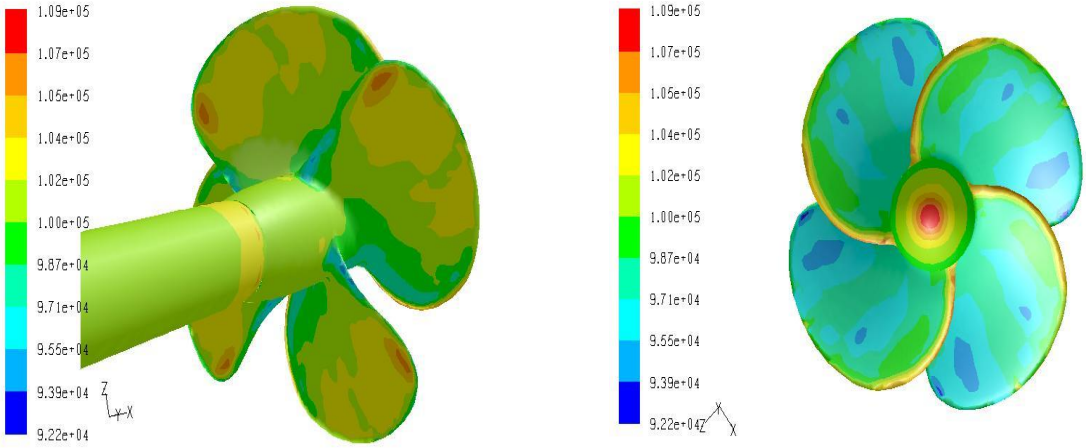


Figure 3.14: Absolute pressure (Pa) on face and back of propeller at J= 0.9341 and N=1200 rpm

### 3.5.4 Discussions

In this study the open water characteristics are predicted computationally by a validated small sized propeller where the delivered powers ($P_D$), the advanced velocity ($V_a$), and the propeller revolution (N) are known.

The following conclusions are obtained from this comparative analysis.

1. Maximum open water efficiency is 71.04%. This value is obtained exactly at operating conditions J=0.934, $V_a$=3.83 m/s and N=1200 rpm, which shows that the computational results are up to the mark.
2. With a variation of thrust coefficient from 0.0897 to 0.3135 and Torque coefficient from 0.2094 to 0.5504, the advanced coefficient (J) varies from 1.00 to 0.6. Computational results obtained from FLUENT software are in good agreement with the reference [128]. Further experiments can be done to validate the numerical results obtained for better reliability.
3. More research work can be conducted for the refinement of mesh and more particularly an improved way of combining the blade and hub of propeller inside the block. For attaining closed form of results tetrahedral element mesh is replaced with hexahedral elements.
4. Further trials can be conducted over varying advanced velocities and rotational speed, to have conclusive results in comparison with experimental results. This

additional analysis provides more amount of information for enhancement of open water efficiency and distribution of pressure over the blades.

## 3.6 Numerical Analysis

### 3.6.1 Hydro dynamic Design for modelling of Wageningen B-series propeller

The complexity of the flow field in which a propeller must operate efficiently will be a challenging task for the designers. Moreover to design a propeller with a variation of inflow conditions influencing the propeller action cost reduction factors and fuel consumption also play an important role in evaluating the efficiency of vessels. The two major factors contributing to the successful design of propulsion systems are performance level and consistency improvements.

With the two factors taken into consideration, the basic data required for the creation of aerofoil shaped profiles are collected from the Reference [130] represented in two-dimensional form, from which the three dimensional geometry of the complete set of blades is generated. In its original form, the two-dimensional data defines a section similar to that of the shape of an aerofoil wing. The cross section is defined by intervals located along the span and varying in length, maximum thickness and maximum camber. The type of series selected is a B-series Wageningen propeller with four blades attached to the hub. The model details required for modelling of propeller blade are specified as below.

### 3.6.2 Data for B-series propeller blade [130]

| | | |
|---|---|---|
| Type of series | : | Wageningen B screw series propeller |
| Delivered power ($P_D$) | : | 648KW |
| Advance speed ($V_A$) | : | 15m/s |
| Propeller rate of rotation (N) | : | 380 rpm |
| Propeller diameter (D) | : | 2.12m |
| Number of blades (Z) | : | 4 |
| Blade area ratio ($A_E/A_0$) | : | 0.70 |
| P/D Ratio | : | 0.9 |

The design parameters for modelling propeller blade are calculated (Table 3.8) and their corresponding notations are shown below.

$A_r$, $B_r$ = the constants in the equation for t/D

a = distance between leading edge and generator line at r

b = distance between leading edge and location of maximum thickness

c = chord length of blade section at radius r

t = maximum blade section thickness at radius r

Table 3.8: Design Parameters for Modelling of Propeller Blade

| $r/R$ | $\frac{c}{D}*\frac{Z}{(A_E/A_0)}$ | $a/c$ | $b/c$ | $t/D = A_r - B_r Z$ | |
|---|---|---|---|---|---|
| | | | | $A_r$ | $B_r$ |
| 0.2 | 1.662 | 0.617 | 0.350 | 0.0526 | 0.0040 |
| 0.3 | 1.882 | 0.613 | 0.350 | 0.0464 | 0.0035 |
| 0.4 | 2.050 | 0.601 | 0.351 | 0.0402 | 0.0030 |
| 0.5 | 2.152 | 0.586 | 0.355 | 0.0340 | 0.0025 |
| 0.6 | 2.1877 | 0.561 | 0.389 | 0.0278 | 0.0020 |
| 0.7 | 2.144 | 0.524 | 0.443 | 0.0216 | 0.0015 |
| 0.8 | 1.970 | 0.463 | 0.479 | 0.0154 | 0.0010 |
| 0.9 | 1.580 | 0.351 | 0.500 | 0.0092 | 0.0005 |
| 1.0 | 0.000 | 0.000 | 0.000 | 0.0030 | 0.000 |

### 3.6.3 Design parameters for Scaled Propeller

For studying the performance of a propeller, indeed studying hydrodynamic phenomena in general, the laws of similarity and method of dimensional analysis provide the conditions under which a model must be made to operate so that its performance will faithfully reflect the performance of the prototype.

From the Condition of geometrical similarity, we have

$$\lambda = \frac{D_M}{D_S} \tag{3.28}$$

Further from the condition of kinematic similarity, we have

$$\frac{V_{AS}}{V_{AM}} = \frac{\pi n_s D_S}{\pi n_M D_M} \text{ and} \tag{3.29}$$

$$J_S = J_M$$

(3.230)

Further the Condition of kinetic (dynamic) similarity, we can write

$$F_n = \frac{V}{\sqrt{gL}} \quad , R_n = \frac{VL}{\upsilon} \quad , E_n = \frac{p}{\frac{1}{2}\rho V^2} \tag{3.30}$$

Where $F_n$ = Froude number, $R_n$ = Reynolds number, $E_n$ = Euler's number

### 3.6.4 Laws of similarity

A full size ship propeller of diameter (D) operating at a speed of advance ($V_{AS}$) and revolution rate ($n_s$) has been considered. Pressure at the centre of the propeller is ($P_s$) and correspondingly the speed of advance, revolution rate and pressure of a model propeller of diameter ($D_{MS}$) operate so that the laws of similarity are satisfied. The laws of similarity require that the advance coefficient (J), the Reynolds number ($R_n$), the Froude number ($F_n$) and the Euler number ($E_n$) for the ship propeller and the model propeller be the same.

The model scale is given by:

$$\lambda = \frac{D_M}{D_S} \tag{3.31}$$

For equal Reynolds number for both model and ship propeller one can write

$$\frac{V_{AM} D_M}{\upsilon_M} = \frac{V_{AS} D_S}{\upsilon_S} \tag{3.32}$$

Neglecting other factors causing disturbances between model and ship propeller one can write

$$V_{AM} = \lambda V_{AS} \tag{3.33}$$

For equal advanced coefficients

$$\frac{V_{AM}}{n_M D_M} = \frac{V_{AS}}{n_S D_S}$$
$$n_M = n_S \frac{V_{AM}}{V_{AS}} \frac{D_S}{D_M} \text{ and} \quad (3.34)$$

$$n_M = n_S \lambda^2 \quad (3.35)$$

Similarly for equal Froude number the thrust coefficients are given by

$$T_M = T_S \left(\frac{n_M}{n_S}\right)^2 \left(\frac{D_M}{D_S}\right)^4 \text{ and}$$
$$T_M = T_S \lambda^{-3} \quad (3.36)$$

With above equations taking into consideration following dimensions are determined for scaled model propeller.

Power developed for model propeller is

$$P_{DM} = P_{DS} * \frac{\rho_M}{\rho_S} * \lambda^{-3.5} = 648 * \frac{1000}{1025} * 6^{-3.5} = 632.195 * 6^{-3.5} = 1.194 \quad (3.37)$$

Speed of model propeller is

$$n_M = n_S * \lambda^{0.5} = 380 * 6^{0.5} = 930.806 \text{ rpm} \quad (3.38)$$

Advanced velocity for model propeller is found as

$$V_{aM} = V_{aS} * \lambda^{-0.5} = 15 * 6^{-0.5} = 6.123 \text{ m/s} \quad (3.39)$$

The design parameters for full and reduced scale model are shown in the Table 3.9

Table 3.9: Design Parameters for Full and Reduced scale model

| Design parameter | Full Model | Scaled Model(1/6th) |
|---|---|---|
| Power (kW) | 648 | 1.19 |
| Advanced velocity (m/s) | 15 | 6.123 |
| Diameter (m) | 2.12 | 0.35 |
| Pitch diameter ratio | 0.9 | 0.9 |
| Expansion ratio | 0.7 | 0.7 |
| Number of blades | 4 | 4 |
| Speed (rpm) | 380 | 930.80 |

## 3.7 Numerical modelling of propeller

Modelling of the propeller is done using the software CATIA V5 R 17. To develop a full-scale model of the blade, it is necessary to have sections of the propeller at various radii. These sections are drawn and rotated through their respective pitch angles. Then all rotated sections are projected onto right circular cylinders of respective radii as shown in Figure 3-15. By using multi-section surface option, the blade is modelled. Figure 3-15 shows constructions of hydrofoils by joining of points on the surface of the blade.Finally, a surface model is made into solid by closing all the surfaces edges and filling the volume between the surfaces with solid. The final model is as shown in Figure 3-16.

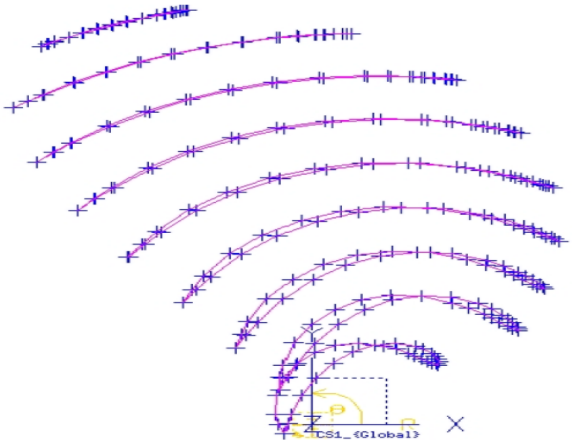

Figure 3.15: Construction of hydrofoils by joining of points on surface of the blade

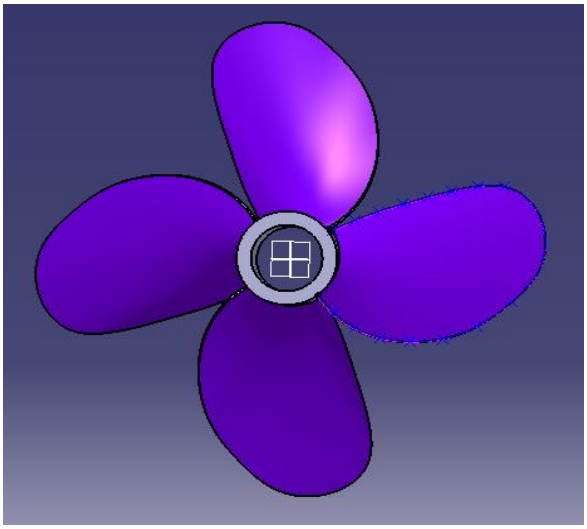

Figure 3.16: Final solid model of propeller

## 3.8 Results and discussions of propeller for improving cavitation inception speed

The numerical/ CFD results obtained for the propeller blade are used for improving cavitation inception speed as described below.

### 3.8.1 Open water characteristics

The open water characteristics of a propeller are usually given in terms of the advance coefficient (J), the thrust coefficient ($K_T$), the torque coefficient ($K_Q$) and the open water efficiency ($\eta_0$). These values are given in Table 3.10 and Table 3-11, and a plot has been made between $K_T$, $K_Q$ and $\eta_0$ as functions of J for open water efficiency ( $\eta_0$ ) shown in the Figure 3.17.A propeller normally operates between zero and 100 percent slip conditions. For both conditions, the open water efficiencies $\eta_0$ is zero. The maximum value of $\eta_0$ occurs at an effective slip ratio between 10 and 20 percent and for values of J greater than that corresponding to the maximum $\eta_0$ it falls sharply to zero. Open water tests of propellers can be performed either in a cavitation tunnel or a towing tank. Although the test procedure applied to obtain open water characteristics of a propeller in a cavitation tunnel is different from those in a towing tank, these characteristics are the same used in the analysis of the propulsion tests and the estimation of the required power. In a cavitation tunnel, the procedure is applied as follows: The range of measurements should cover tested propeller operating range in terms of the advance coefficient (J), such that the advance coefficient, (J) should be varied in between 0 to 1. In general, for the open water characteristics, determination through the tunnel tests velocity is kept constant while the propeller rate of rotation n (rps), increases or vice versa. In each run, the water velocity, propeller rotation, thrust, torque values are recorded. If any cavitation occurrence on the propeller blades is observed, it will be recorded.

### 3.8.2 Performance Coefficients of Propeller blade

The performance coefficient of propeller blade are written below.

Advance Coefficient $$J = \frac{V_a}{n.D} \tag{3.40}$$

Thrust Coefficient $$K_T = \frac{T}{\rho.n^2.D^4} \quad (3.41)$$

Torque Coefficient $$K_Q = \frac{Q}{\rho.n^2.D^5} \quad (3.42)$$

Efficiency $$\eta = \frac{J}{2*\pi*\frac{K_T}{K_Q}} \quad (3.43)$$

Cavitation number $$\sigma_n = \frac{P_o - P_v}{\frac{1}{2}*\rho*v_a^2} \quad (3.44).$$

Pressure coefficient $$C_p = \frac{P - P_v}{\frac{1}{2}*\rho*v_a^2}, \quad (3.45)$$

Where T=thrust, n=speed in rps, $P_0$ =absolute pressure, $P_v$ = vapour pressure, $\rho$ =density of water and $V_a$ = advanced velocity.

The performance of propeller is conventionally represented in terms of non-dimensional coefficients, i.e., thrust coefficient ($K_T$), torque coefficient ($K_Q$), efficiency **(η),**cavitation number $(\sigma_n)$ and pressure coefficient $(C_p)$ listed in 3.8.2, and their variation with advance coefficients (J). Initially computational results are validated for a small sized propeller with better satisfaction. The test facility is suitable for small sized propellers only.Hence, validation is made on a small propeller and then a similar procedure is followed considering the former one as proof for further larger propellers' simulation. The complete computational solution for the flow was obtained using the FLUENT software. The software also estimated thrust and torque from the computational solutions for different rotational speeds (rps) of the propeller. These were expressed in terms of $K_T$& $K_Q$. The estimated thrust and torques are given in Table 3.11 and Table 3.14

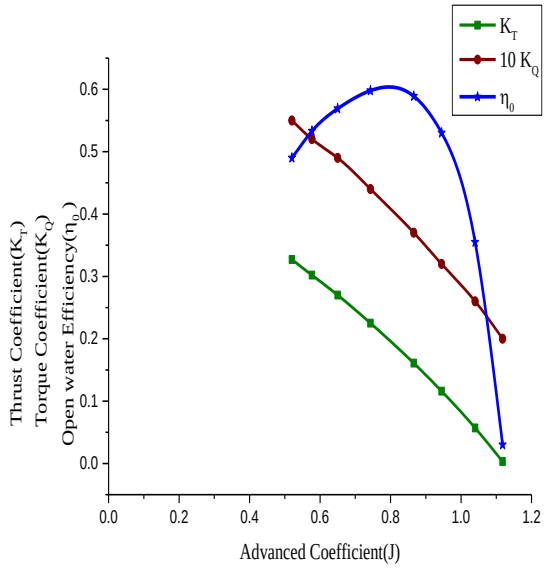


Figure 3.17: Open water characteristics for modelled propeller (with change in Speed)

Table 3.10: Open Water Characteristics of modelled Propeller (with change in Speed)

| Rotational Speed n(rps) | Advanced Velocity $V_a$ (m/s) | Advanced Coefficient (J) | Thrust T (N) | Torque $\tau$ (N-m) |
|---|---|---|---|---|
| 33.33 | 6.12 | 0.520 | 5642.62 | 335.79 |
| 30.00 | 6.12 | 0.577 | 4225.31 | 258.93 |
| 26.66 | 6.12 | 0.650 | 2982.85 | 191.14 |
| 23.33 | 6.12 | 0.743 | 1906.76 | 132.56 |
| 20.00 | 6.12 | 0.866 | 1001.08 | 82.62 |
| 18.33 | 6.12 | 0.945 | 607.39 | 60.60 |
| 16.66 | 6.12 | 1.040 | 246.98 | 40.37 |
| 15.50 | 6.12 | 1.118 | 12.954 | 27.04 |
| 15.00 | 6.12 | 1.155 | -91.612 | 21.77 |
| 13.33 | 6.12 | 1.300 | -398.05 | 4.02 |

Table 3.11: Comparison of modelled and B-series data values of KT, KQ, ηo

| Advanced Coefficient (J) | Thrust Coefficient ($K_T$) | Torque Coefficient( $K_Q$) | Open water efficiency ($\eta_{o)}$ |
|---|---|---|---|
| 0.520 | 0.327 | 0.055 | 0.490 |
| 0.577 | 0.302 | 0.052 | 0.533 |
| 0.650 | 0.270 | 0.049 | 0.569 |
| 0.743 | 0.225 | 0.044 | 0.598 |
| 0.866 | 0.161 | 0.037 | 0.589 |
| 0.945 | 0.116 | 0.032 | 0.530 |
| 1.040 | 0.057 | 0.026 | 0.355 |
| 1.118 | 3.472e-3 | 0.020 | 0.030 |
| 1.155 | -0.026 | 0.017 | -0.270 |
| 13.33 | -0.144 | 4.134e-3 | -7.205 |

Table 3.12: Comparison of modelled and standard-series data values of KT, KQ, ηo

| Advanced Coefficient (J) | Thrust Coefficient ($K_T$) | | Torque Coefficient ($K_Q$) | | Open water efficiency ($\eta_o$) | |
|---|---|---|---|---|---|---|
| | present | B-series data [131] | present | B-series data [131] | present | B-series data [131] |
| 0.866 | 0.161 | 0.072 | 0.037 | 0.016 | 0.589 | 0.625 |
| 0.743 | 0.225 | 0.103 | 0.044 | 0.018 | 0.598 | 0.670 |
| 0.650 | 0.270 | 0.134 | 0.049 | 0.021 | 0.5695 | 0.641 |
| 0.577 | 0.302 | 0.185 | 0.052 | 0.030 | 0.533 | 0.566 |
| 0.520 | 0.327 | 0.303 | 0.055 | 0.046 | 0.490 | 0.545 |

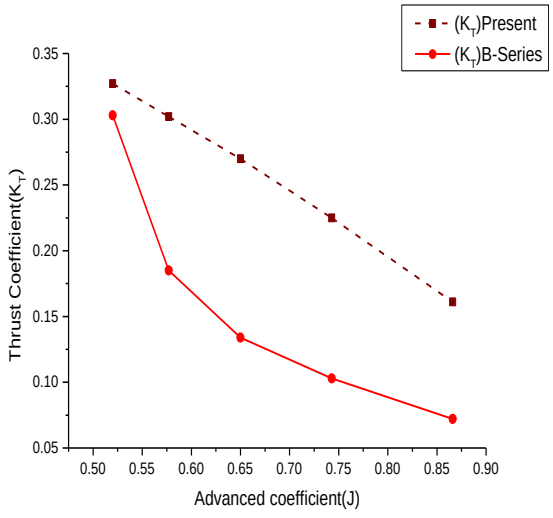


a)Thrust Coefficient ($K_T$) comparison

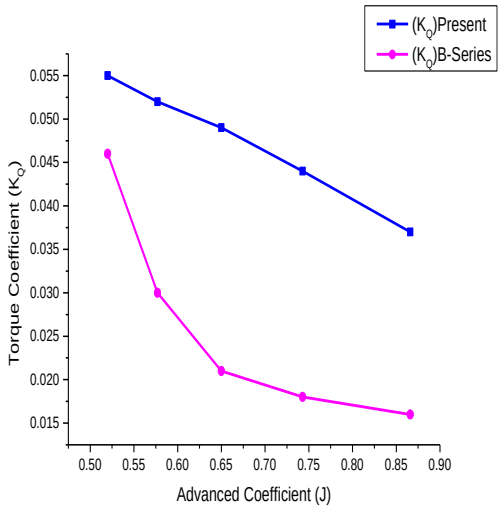


b) Torque Coefficient ($K_Q$) comparison

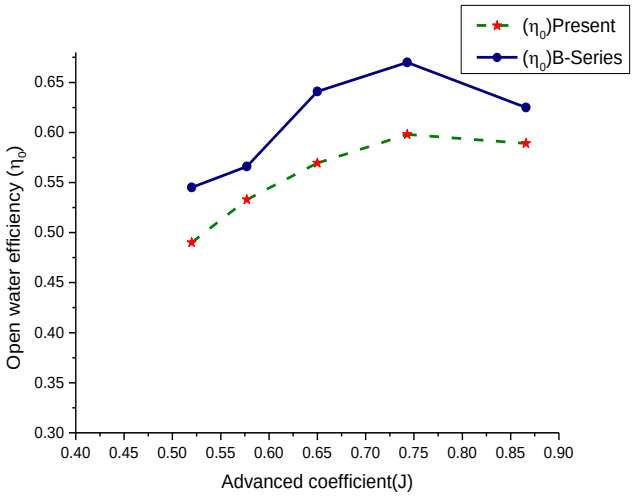


c) Open water efficiency ($\eta_O$) comparision

Figure 3.18: Comparison of open water characterstics for modelled propeller vs. B- series data

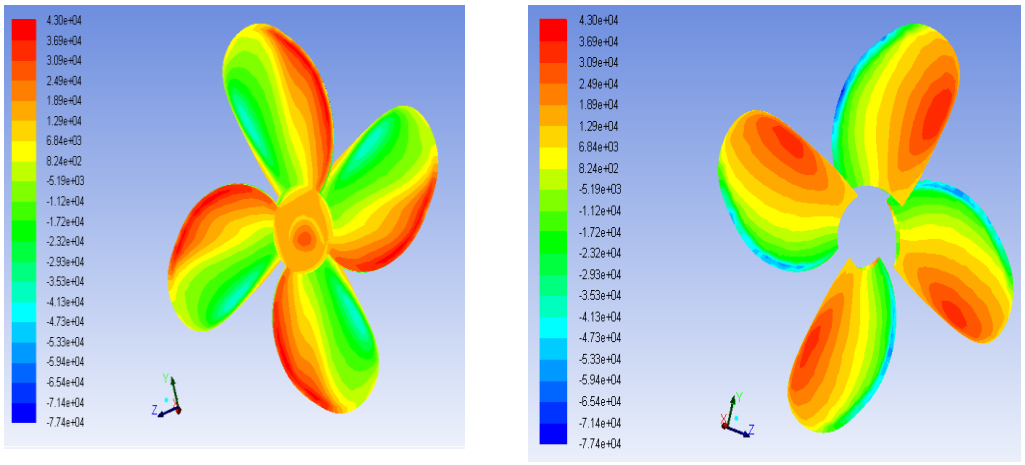

(a): $V_a$= 6.12 m/s and N=930 rpm (b):$V_a$= 6.12 m/s and N=930 rpm

Figure 3.19: Absolute pressure contours (Pa) on Front and Rear surfaces of propeller blade at $V_a$= 6.12 m/s and N=930 rpm

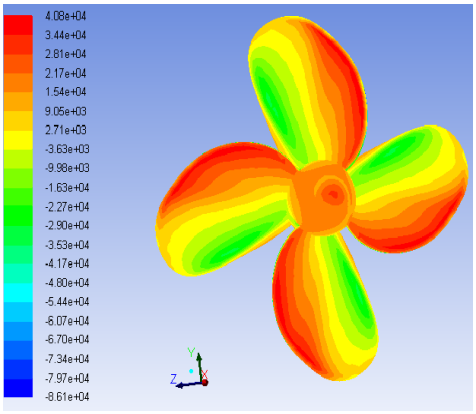

(a) $V_a$=6.12m/s and N=800 rpm

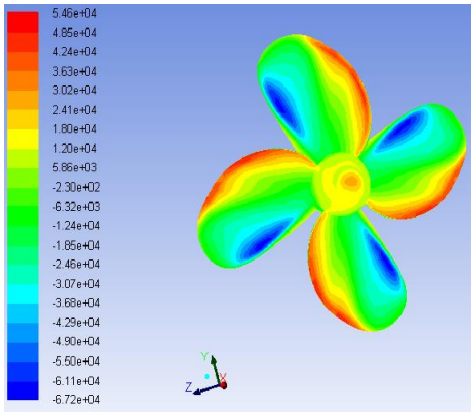

(b): $V_a$=6.12m/s and N=1200 rpm

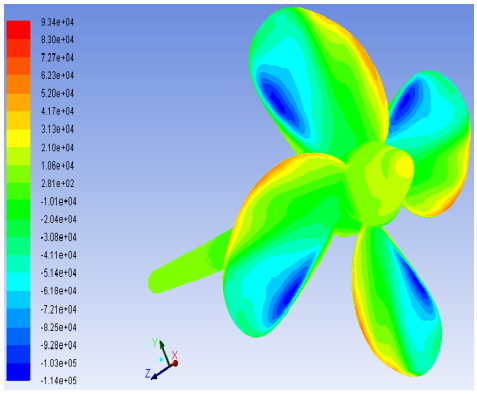

(c): $V_a$ = 6.12m/s and N=1600 rpm

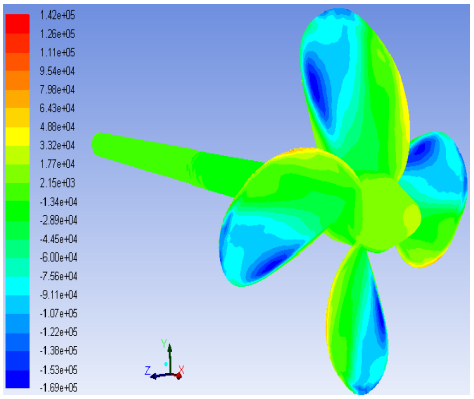

(d): $V_a$= 6.12m/s and N=2000 rpm

Figure 3.20: Absolute pressure contours (Pa) on face of propeller blade at $V_a$ =6.12m/s and N=800, 1200, 1600, 2000 rpm

Table 3.13: Open Water Characteristics of B-Series Propeller (with change in Velocity)

| Rotational Speed n (rps) | Advanced Velocity $V_a$ (m/s) | Advanced Coefficient (J) | Thrust T (N) | Torque $\tau$ (N-m) |
|---|---|---|---|---|
| 15.5 | 2.0 | 0.365 | 1383.72 | 81.91 |
| 15.5 | 2.5 | 0.456 | 1299.28 | 76.61 |
| 15.5 | 3.0 | 0.548 | 1167.34 | 71.08 |
| 15.5 | 3.5 | 0.639 | 1019.35 | 65.34 |
| 15.5 | 4.0 | 0.731 | 859.35 | 59.40 |
| 15.5 | 4.5 | 0.822 | 687.96 | 52.98 |
| 15.5 | 5.0 | 0.913 | 501.05 | 46.02 |
| 15.5 | 5.5 | 1.005 | 296.60 | 38.17 |
| 15.5 | 6.0 | 1.096 | 70.46 | 29.33 |
| 15.5 | 6.12 | 1.118 | 12.95 | 27.04 |

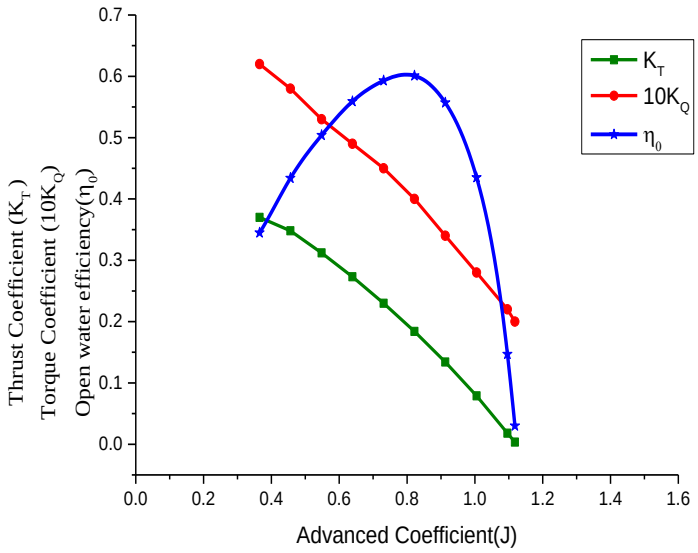


Figure 3.21: Open water characteristics for modelled propeller (with change in Velocity)

Table 3.14: Computational Estimation of $K_T$ , $K_Q$, $\eta_0$

| Advanced Coefficient (J) | Thrust Coefficient ($K_T$) | Torque Coefficient ($K_Q$) | Open water efficiency ($\eta_o$) |
|---|---|---|---|
| 0.365 | 0.370 | 0.062 | 0.345 |
| 0.456 | 0.348 | 0.058 | 0.434 |
| 0.548 | 0.312 | 0.053 | 0.504 |
| 0.639 | 0.273 | 0.0496 | 0.5595 |
| 0.731 | 0.230 | 0.045 | 0.593 |
| 0.822 | 0.184 | 0.040 | 0.601 |
| 0.913 | 0.134 | 0.034 | 0.557 |
| 1.005 | 0.079 | 0.028 | 0.435 |
| 1.096 | 0.018 | 0.022 | 0.147 |
| 1.118 | 3.373e-3 | 0.020 | 0.030 |

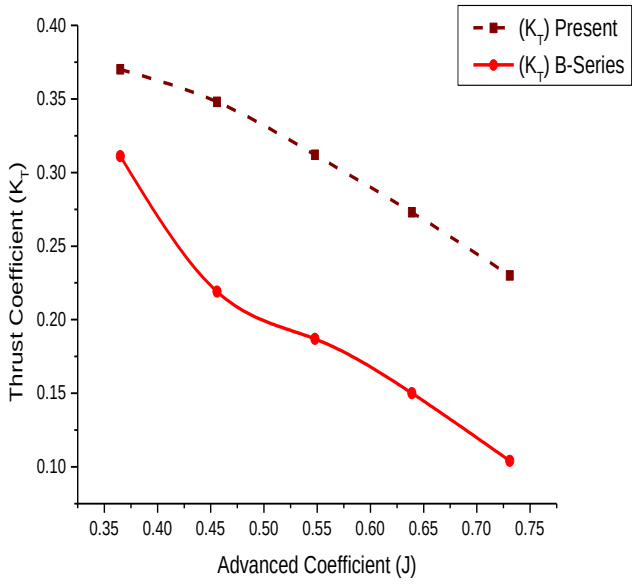


a) Thrust Coefficient (KT) Comparison

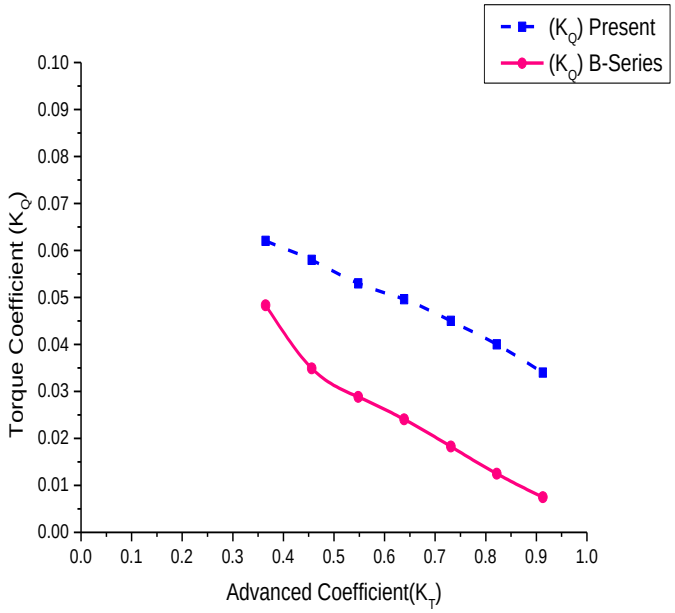


b) Torque Coefficient (KQ) Comparison

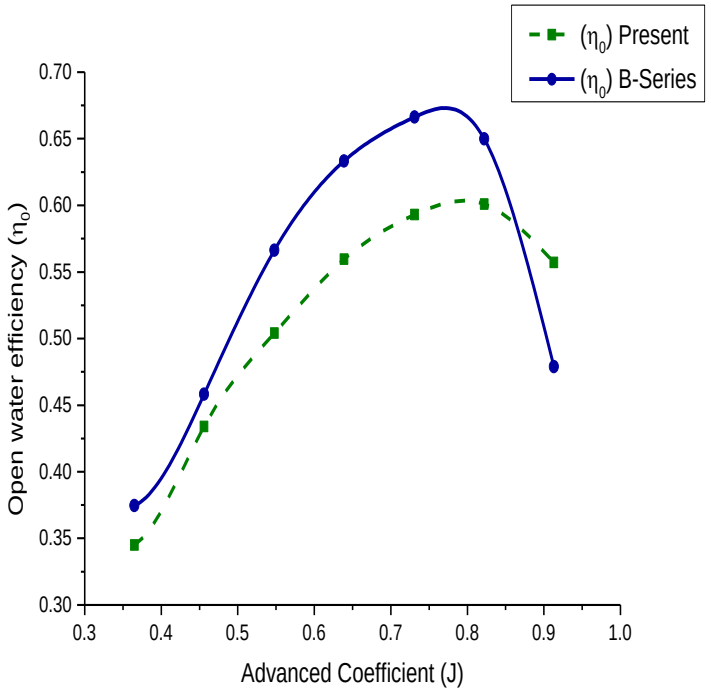


c) Open water efficiency ($\eta_O$) comparision

Figure 3.22: Comparison of modelled propeller vs. B-series Data

Table 3.15: Comparison of Predicted and B-series Data values of $K_T$, $K_Q$,$\eta_O$

| Advanced Coefficient (J) | Thrust Coefficient($K_T$) | | Torque Coefficient($K_Q$) | | Open water efficiency($\eta_o$) | |
|---|---|---|---|---|---|---|
| | present | B-series data [131] | present | B-series data [131] | present | B-series data [131] |
| 0.365 | 0.370 | 0.311 | 0.062 | 0.0483 | 0.345 | 0.3747 |
| 0.456 | 0.348 | 0.219 | 0.058 | 0.03486 | 0.434 | 0.4581 |
| 0.548 | 0.312 | 0.187 | 0.053 | 0.0288 | 0.504 | 0.5664 |
| 0.639 | 0.273 | 0.150 | 0.0496 | 0.02407 | 0.5595 | 0.6332 |
| 0.731 | 0.230 | 0.104 | 0.045 | 0.01826 | 0.593 | 0.6664 |
| 0.822 | 0.184 | 0.061 | 0.040 | 0.01245 | 0.601 | 0.6498 |
| 0.913 | 0.134 | 0.0246 | 0.034 | 0.00747 | 0.557 | 0.4788 |

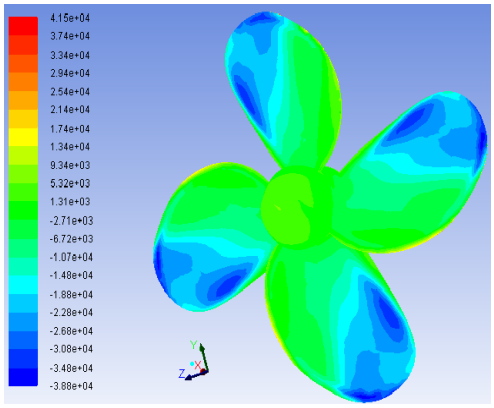


(a): N=930 rpm and $V_a$ =2m/s

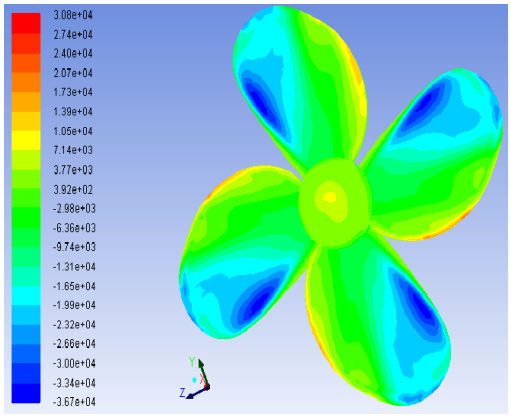


(b): N=930 rpm and $V_a$ =3m/s

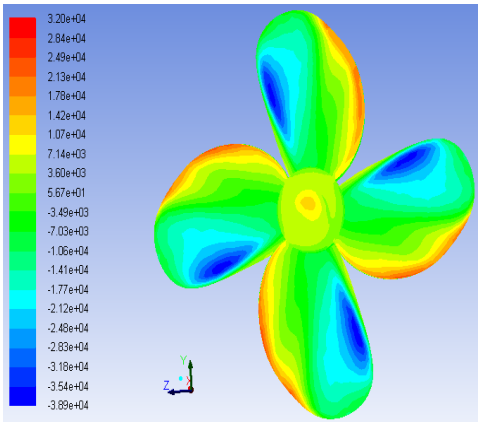


(c): N=930 rpm and $V_a$ =4m/s

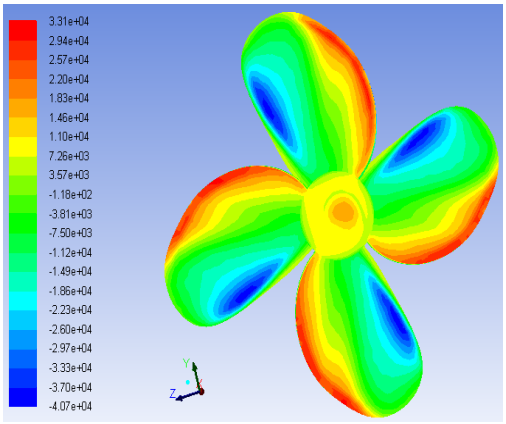


(d): N=930 rpm and $V_a$ =5m/s

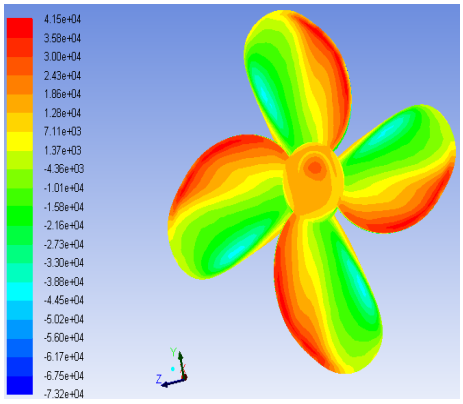


(e): N=930 rpm and $V_a$ =6.12m/s

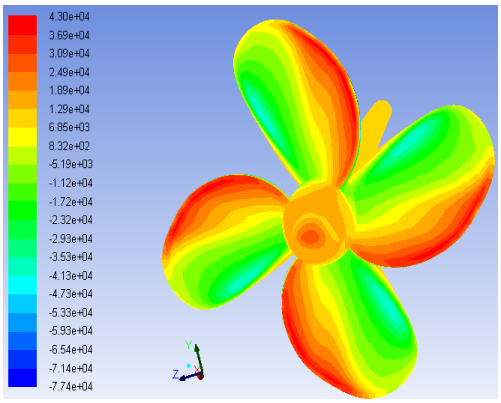


(f) N=930 rpm and $V_a$ =6.12m/s

Figure 3.23: Absolute pressure contours (Pa) for N=930rpm and $V_a$=2 to 6.12m/s

This Figure 3.24 shows that there is no flow separation near the blade surface section, which was expected as the propeller was a well-designed standard one.

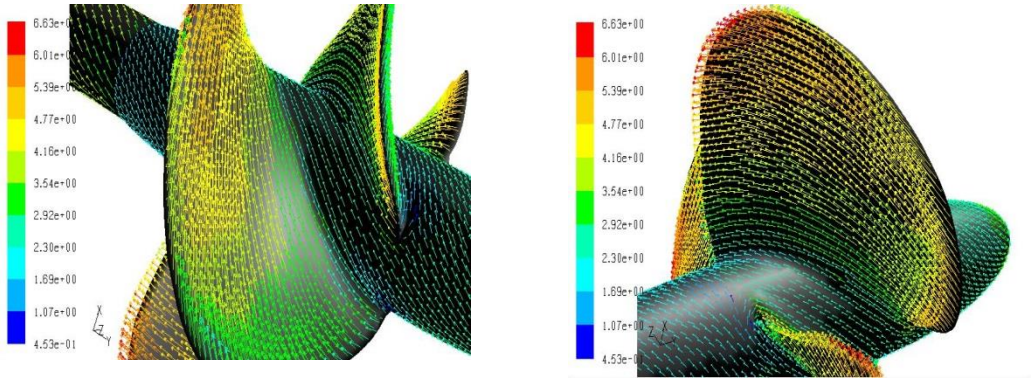

Figure 3.24: Relative velocity vectors for N=1200rpm $V_a$= 6.12m/s and J=0.934

## 3.9 Cavitation Inception point determination

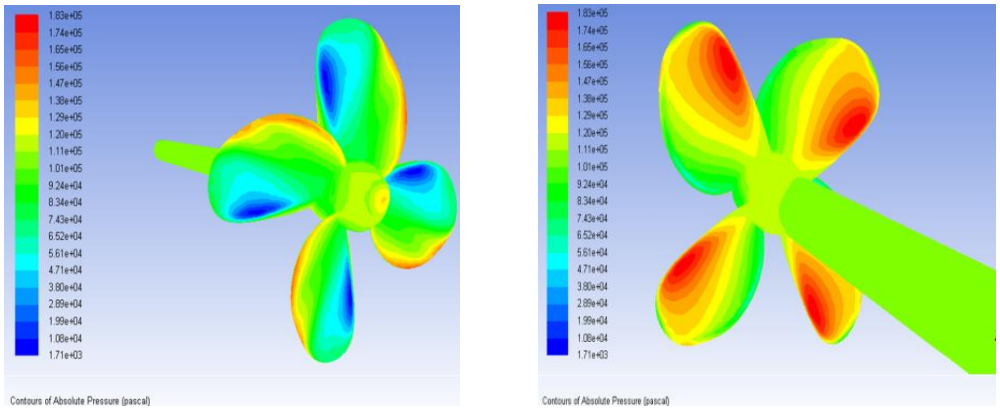


Figure 3.25: Absolute pressure (Pa) on face and back of propeller at J=0.4483 and N=1490rpm

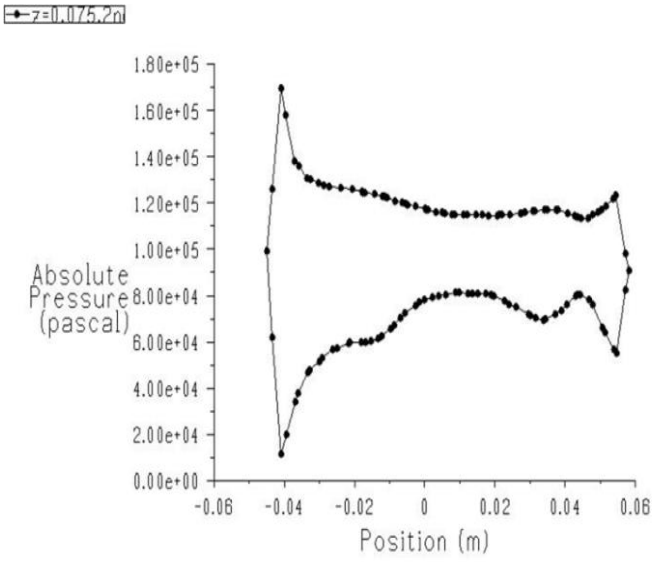


Figure 3.26: Absolute pressure distribution plot at $\frac{r}{R_p}$ =0.73 and N=1490 rpm

## 3.10 Discussions

Flow through B-series propeller was computed using FLUENT 6.3 software.The purpose of this simulation is to obtain the open water characteristics of the propeller for advanced ratio 0.2 to 1.4.The variation of thrust coefficient $(K_T)$ , torque coefficient $(K_Q)$ and open water efficiency $(\eta_0)$ with respect to advanced coefficient (J) are shown in Figure 3.24. Figure 3.18 to Figure 3.24 it emerges that the results obtained for the modelled B-series propeller are close to the standard B-series data in concern with prediction of $K_T, K_Q$ and $\eta_0$. "Figure 3.18 to Figure 3.24 refer to various features of the solution obtained using the data presented in Table 3.10 to Table 3.15".

At J=0.4222 minimum absolute pressure on blade is$1.71x10^3$ Pa, which is less than the vapour pressure $1.72x10^3$ Pa [132]. This is the stage at which cavitation is just started which is the point of cavitation inception. The pressure distribution over the blade under cavitating conditions are shown in Figures 3.25 and 3.26. At this cavitation inception speed, a finite element analysis is performed for determining the deformations and corresponding stresses. The material properties of Aluminium and composite with layup sequence are taken from the standard Reference to satisfy the overall repetitions. The repetitive CFD and finite element analysis are to be continued up to the point when the pressure difference between two successive CFD iterations is less than 10% of maximum pressure obtained at cavitation inception point.

# Chapter 4

# Strength Evaluation of Marine Propeller Blade

## 4.1 Introduction

Virtually every phenomenon in nature, whether biological, geological or mechanical can be described with the aid of the laws of physics, regarding algebraic, differential or integral equations relating various quantities of interest. With the rapid advancement of technology, the complexity of the problem to be dealt by a design engineer is also increasing. This scenario demands speedy, efficient and optimal design from an engineer. To keep pace with the development and ensure better output, the engineer today is resorting to numerical methods. For problems involving complex shapes, material properties, and complicated boundary conditions, it is difficult and in many cases intractable to obtain analytical solutions, for example the determination of stress distribution in a pressure vessel with oddly shaped holes with numerous stiffeners subjected to mechanical, thermal, and aerodynamic loads. Finding the concentration of pollutants in sea water or in the atmosphere and simulating weather in an attempt to understand and predict the mechanics of formation of tornadoes and thunderstorms, are a few examples of many important practical problems. While the derivation of the governing equations for these problems is not unduly difficult their solution by exact methods of analysis is a formidable task. In such cases, approximate methods of analysis provide alternative means of finding solutions. Most of the numerical methods provide approximate but acceptable solutions to such problems.Among these; the finite difference methods, finite element methods and variation methods such as the Rayleigh-Ritz and Galerkin methods are more frequently used.

## 4.2 Fiber Reinforced Plastic Materials

### 4.2.1Overview

Fiber reinforced composite material consists of fibres of high strength and modulus embedded in or bonded to the matrix. In this form both fibres and matrix retain their physical and chemical identities, yet they produce a combination of properties that cannot be achieved with either of the constituents acting alone. In general, fibres are the principal load-carrying members, while the surrounding matrix keeps them in desired location, and orientation acts as a load transfer medium between them and protects them from environmental damages due to elevated temperatures and humidity. Thus, even though the fibres provide reinforcement for the matrix, the latter also serves some useful functions in a fiber reinforced composite material.

The most common form in which fiber reinforced composites are used in structural applications is called a laminate stacking, a number of thin layers of fibres and matrix and consolidating them into desired thickness. Fiber orientation in each layer and stacking sequence of various layers can be controlled to generate a wide range of physical and mechanical properties of the composite laminate.Each layer may differ from the other in.

1. Relative volumes of the constituent materials.
2. The form of the reinforcement used as continuous or discontinuous fibres, woven or non-woven reinforcement.
3. The orientation of fibres with respect to the common reference axis.

One of the most important factors for determining the properties of composites is the relative proportion of the matrix and reinforced materials. The relative proportionate can be given as the weight fractions or the volume fractions. The weight fractions are easier to obtain during fabrication or by one of the experimental methods after fabrication. The volume fractions are exclusively used in the theoretical analysis of composite materials.

### 4.2.2 Fiber

Fibers are the principal constituents of a fiber reinforced composite material. They occupy the largest volume fraction in a composite laminate and share the major portion of the load acting on a composite structure. Proper selection of the type, amount, and

orientation of fibers is very important since it influences the following characteristics of a laminate.

- Specific gravity
- Tensile strength and modulus
- Compressive strength and modulus
- Fatigue strength as well as fatigue failure mechanisms
- Damping
- Electrical and thermal conductivities
- Cost

Carbon fibers are commercially available with a variety of tensile modulus ranging from 207 GPA on the low side to 1035 GPA on the high side. Among the advantages of carbon fibers are their exceptionally high strength to weight ratios, very low coefficient of linear thermal expansion and high fatigue strengths. The disadvantages are their low impact resistance and high electrical conductivity.

### 4.2.3 Matrix

The role of matrix in a fiber reinforced composite material is

- To transfer stresses between the fiber
- To provide a barrier against an adverse environment
- To protect the surface of the fiber from mechanical abrasion

The matrix plays a minor role in load carrying capacity. The matrix has a major influence on interlaminar shear as well as in-plane shear properties of the composite. Interlaminar shear strength is important in design under bending loads. In-plane shear strength is important under torsion loads. The matrix provides lateral support against the possibility of fiber buckling under compressive loads. Among the matrix materials epoxies are used because of commercial availability, and ease of processing.

The advantages of epoxies over other matrices are

- Wide variety of properties available
- Absence of volatile materials during cure
- Low shrinkage during cure

- Excellent resistance to chemicals and solvents
- Excellent adhesion to fibers

The disadvantages are relatively high cost and curing time.

The stress-strain curve of the composite is shown in Figure 4.1.The stress-strain curve for a composite lies in between the stress-strain curves of the fibers and matrix. The actual location of the composite stress, strain curve will depend on the relative volume fraction of the constituents. If the fiber volume fraction is high, the composite stress-strain curve will be close to the fiber stress-strain curve. On the other hand the composite stress–strain curve may be closer to the matrix stress-strain curve for a higher matrix volume fraction.

## 4.3 Elastic Properties of a Lamina (Equations of Rule of Mixture)

**The elastic properties of unidirectional angle ply lamina are stated below.**

(a) Unidirectional continuous fiber $0^o$ lamina

Longitudinal modulus = $E_{11} = E_f V_f + E_m V_m$ (4.1)

Major Poisson's ratio = $\upsilon_{12} = \upsilon_f V_f + \upsilon_m V_m$ (4.2)

Transverse Modulus = $E_{22} = \dfrac{E_f E_m}{E_f V_M + E_M V_F}$ (4.3)

Minor Poisson's ratio = $\upsilon_{21} = \dfrac{E_{22}}{E_{11}} \upsilon_{12}$ (4.4)

Shear Modulus = $G_{12} = \dfrac{G_f G_m}{G_f \upsilon_m + G_m \upsilon_f}$ (4.5)

The equations define the elastic properties in the material coordinate system and these are known as the equations of rule of mixture, except for the one for $\upsilon_{21}$.

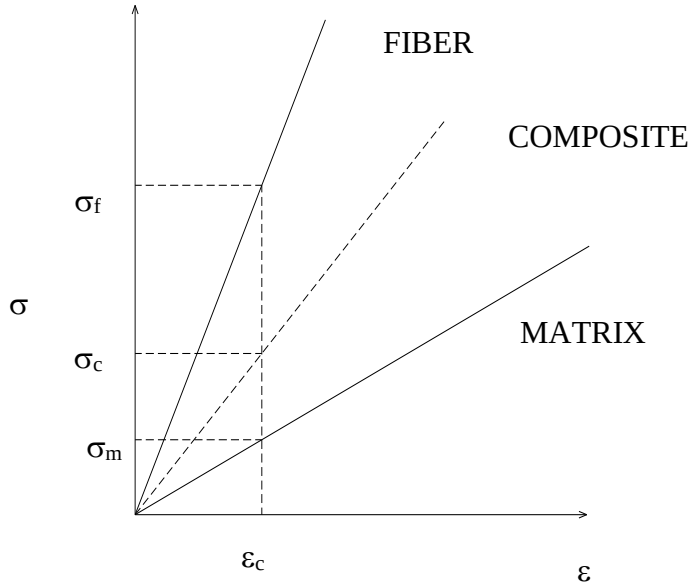


Figure 4.1: Stress –Strain Diagram for a hypothetical composite

**(b) Unidirectional Continuous Fiber Angle-Ply Lamina**

The given equations are obtained from the plane stress transformation and valid in the global coordinate system for any fiber angle, θ. The equations give the effective elastic properties in the global coordinate system.

The elastic modulus matrix E is composed of a number of sub matrices

$$E = \begin{bmatrix} A & B & 0 \\ B & D & 0 \\ 0^T & 0^T & H \end{bmatrix} \tag{4.6}$$

Where A relates to extensional stiffness, D relates bending stiffness; B is the coupling stiffness and H relates to transverse shear stiffness matrices**.** For a layer from $z_{min}$ to $z_{max}$.

$$A = \int_{z_{min}}^{z_{max}} \bar{Q}\, dz = (z_{max} - z_{min})\bar{Q}$$

$$B = \int_{z_{min}}^{z_{max}} \bar{Q}\, z\, dz = \frac{1}{2}(z^2{}_{max} - z^2{}_{min})\bar{Q}$$

$$D = \int_{z_{min}}^{z_{max}} \bar{Q}\, z^2\, dz = \frac{1}{3}(z^3{}_{max} - z^3{}_{min})\bar{Q}$$

$$H = \int_{z_{min}}^{z_{max}} \bar{Q}_s\, dz = (z_{max} - z_{min})\bar{Q}_s \quad (4.7)$$

Where z is the throughout the thickness, $\bar{Q}$ is the reduced stiffness matrix that relates in-plane stresses to in-plane strains, and $\bar{Q}_s$ is the reduced stiffness matrix that relates out-of-plane shear stresses to transverse shear strains. Both $\bar{Q}$ and $\bar{Q}_s$ are defined in the shell finite element local axes, and not the layer material axes. The layer material axes are rotated by angle θ with respect to the element local axes. For a layer with orthotropic material properties, $E_{11}, E_{22}, \upsilon_{12}, G_{12}, G_{13}$ and $G_{23}$ the in-plane elastic modulus matrix in the material axes are given by

$$Q = \begin{bmatrix} Q_{11} & Q_{12} & 0 \\ Q_{12} & Q_{22} & 0 \\ 0 & 0 & Q_{66} \end{bmatrix} \quad (4.8)$$

Where

$$Q_{11} = \frac{E_{11}}{1 - \upsilon_{12}^2 (E_{22}/E_{11})} \quad (4.9)$$

$$Q_{12} = \frac{\upsilon_{12} E_{22}}{1 - \upsilon_{12}^2 (E_{22}/E_{11})} \quad (4.10)$$

$$Q_{22} = \frac{E_{22}}{1 - \upsilon_{12}^2 (E_{22}/E_{11})} \quad (4.11)$$

and $Q_{66} = G_{12}$ (4.12)

The out of plane shear elastic modulus matrix in the material axes is

$$Q_s = \begin{bmatrix} Q_{55} & 0 \\ 0 & Q_{44} \end{bmatrix} \tag{4.13}$$

Where

$$Q_{44} = k_s G_{23} \tag{4.14}$$

$$Q_{55} = k_s G_{13} \tag{4.15}$$

In equations (4.14) and (4.15) $k_s$ represent shear correction factor. The shear correction factor makes an allowance for the non-constant distribution of out-of-plane shear stresses. The present method of incorporating this factor is only approximate with $k_s$ = 5/6.After transformation from the material axes to the shell local axes one can write

$$Q = \begin{bmatrix} \bar{Q}_{11} & \bar{Q}_{12} & \bar{Q}_{13} \\ \bar{Q}_{21} & \bar{Q}_{22} & \bar{Q}_{23} \\ \bar{Q}_{31} & \bar{Q}_{32} & \bar{Q}_{31} \end{bmatrix} \tag{4.16}$$

where

$$\begin{aligned}
\bar{Q}_{11} &= Q_{11}m^4 + Q_{22}n^4 + 2m^2n^2(Q_{12} + 2Q_{66}) \\
\bar{Q}_{12} &= m^2n^2(Q_{11} + Q_{22} - 4Q_{66}) + (m^4 + n^4)Q_{12} \\
\bar{Q}_{16} &= \left[ Q_{11}m^2 - Q_{22}n^2 - (Q_{12} + 2Q_{66})(m^2 - n^2) \right] mn \\
\bar{Q}_{22} &= Q_{11}n^4 + Q_{22}m^4 + 2m^2n^2(Q_{12} + 2Q_{66}) \\
\bar{Q}_{26} &= \left[ Q_{11}n^2 - Q_{22}m^2 + (Q_{12} + 2Q_{66})(m^2 - n^2) \right] mn \\
\bar{Q}_{66} &= \left( Q_{11} + Q_{22} - 2Q_{12} \right) m^2n^2 + Q_{66}(m^2 - n^2)^2
\end{aligned} \tag{4.17}$$

and

$$\begin{aligned}
\bar{Q}_{44} &= Q_{44}m^2 + Q_{55}n^2 \\
\bar{Q}_{45} &= \left( Q_{55} - Q_{44} \right) mn \\
\bar{Q}_{55} &= Q_{55}m^2 + Q_{44}n^2
\end{aligned} \tag{4.18}$$

Where m = cos θ and n = sin θ. The elastic modulus matrices for both layers must be summed to form the elastic modulus matrix for the shell. Equations (4.16) through (4.18) are used to obtain Equations (4.19) to (4.22).

$$\frac{1}{E_{XX}} = \frac{\cos^4\theta}{E_{11}} + \frac{\sin^4\theta}{E_{22}} \left[ \frac{1}{G_{12}} - \frac{2\upsilon}{E_{11}} \right] \sin^2\theta \cos^2\theta \tag{4.19}$$

$$\frac{1}{E_{yy}} = \frac{\sin^4\theta}{E_{11}} + \frac{\cos^4\theta}{E_{22}}\left[\frac{1}{G_{12}} - \frac{2\upsilon}{E_{11}}\right]\sin^2\theta\cos^2\theta \tag{4.20}$$

$$\upsilon_{xy} = E_{xy}\left[\frac{\upsilon_{12}}{E_{11}}\left(\sin^4\theta + \cos^4\theta\right)\right] - \left[\frac{1}{E_{11}} + \frac{1}{E_{22}} - \frac{1}{G_{12}}\right]\sin\theta\cos\theta \tag{4.21}$$

$$\frac{1}{G_{xy}} = 2\left[\frac{2}{E_{11}} + \frac{2}{E_{22}} + \frac{4\upsilon_{12}}{E_{11}} - \frac{1}{G_{12}}\right]\sin^2\theta\cos^2\theta + \frac{1}{G_{12}}\left[\sin^4\theta + \cos^4\theta\right] \tag{4.22}$$

## 4.4 Classical Lamination Theory

There is only a single classical lamination theory (CLPT)**.** Classical lamination theories make the following assumption regarding the behaviour of the lamina.

1. The lamina is perfectly bonded together.
2. The bonds are infinitesimally thin, and no lamina can slip relative to another.
3. The linear variation of strain through the laminate thickness is assumed.
4. Deformation in the X-Y plane of the plate at any point C at a distance z in the normal direction to plate middle surface is

$$\begin{aligned} U &= U_0 + z\theta_y \\ V &= V_0 - z\theta_x \end{aligned} \tag{4.23}$$

Where U, V, W are the displacements along the X, Y and Z directions**,** $U_0$,$V_0$ are the membrane displacements in the element coordinate system, and $\theta_x, \theta_y$ are the rotations.

The strain-displacement-middle surface strain and curvatures relationship are given by:

$$\begin{Bmatrix} \varepsilon_x \\ \varepsilon_y \\ \upsilon_{xy} \end{Bmatrix} = \begin{Bmatrix} \dfrac{\partial U_0}{\partial x} \\ \dfrac{\partial V_0}{\partial y} \\ \dfrac{\partial U_0}{\partial y} + \dfrac{\partial V_0}{\partial x} \end{Bmatrix} + z\begin{Bmatrix} \dfrac{\partial \theta_y}{\partial x} \\ -\dfrac{\partial \theta_x}{\partial y} \\ \dfrac{\partial \theta_y}{\partial y} - \dfrac{\partial \theta_x}{\partial x} \end{Bmatrix} = \begin{Bmatrix} \varepsilon^0{}_x \\ \varepsilon^0{}_y \\ \upsilon^0{}_{xy} \end{Bmatrix} - z\begin{Bmatrix} \chi_x \\ \chi_y \\ \chi_{xy} \end{Bmatrix} \tag{4.24}$$

Where $\varepsilon^0, \chi'$ are the middle surface strains and curvatures respectively.

The stress resultants for an N-layer laminate are obtained by integration of the stresses in each lamina through the laminate thickness as:

$$\begin{Bmatrix} N_x \\ N_y \\ N_{xy} \end{Bmatrix} = \int_{-\frac{t}{2}}^{\frac{t}{2}} \begin{Bmatrix} \sigma_x \\ \sigma_y \\ \tau_{xy} \end{Bmatrix} dz = \sum_{k=1}^{N} \int_{z_{k-1}}^{z_k} \begin{Bmatrix} \sigma_x \\ \sigma_y \\ \tau_{xy} \end{Bmatrix}_k dz \tag{4.25}$$

$$\begin{Bmatrix} M_x \\ M_y \\ M_{xy} \end{Bmatrix} = -\int_{-\frac{t}{2}}^{\frac{t}{2}} \begin{Bmatrix} \sigma_x \\ \sigma_y \\ \tau_{xy} \end{Bmatrix} dz = -\sum_{k=1}^{N} \int_{z_{k-1}}^{z_k} \begin{Bmatrix} \sigma_x \\ \sigma_y \\ \tau_{xy} \end{Bmatrix}_k z dz \tag{4.26}$$

$$\begin{Bmatrix} N_x \\ N_y \\ N_{xy} \end{Bmatrix} = \sum_{k=1}^{N} [G]_k \left[ -\int_{z_{k-1}}^{z_k} \begin{Bmatrix} \varepsilon^0{}_x \\ \varepsilon^0{}_y \\ \upsilon^0{}_{xy} \end{Bmatrix}_k dz \right] - \left\{ \int_{z_{k-1}}^{z_k} \begin{Bmatrix} \chi_x \\ \chi_y \\ \chi_{xy} \end{Bmatrix} z dz \right\} \tag{4.27}$$

$$\begin{Bmatrix} M_x \\ M_y \\ M_{xy} \end{Bmatrix} = \sum_{k=1}^{N} [G]_k \left[ -\int_{z_{k-1}}^{z_k} \begin{Bmatrix} \varepsilon^0{}_x \\ \varepsilon^0{}_y \\ \upsilon^0{}_{xy} \end{Bmatrix}_k z dz \right] - \left\{ \int_{z_{k-1}}^{z_k} \begin{Bmatrix} \chi_x \\ \chi_y \\ \chi_{xy} \end{Bmatrix} z^2 dz \right\} \tag{4.28}$$

Where $[G]_k$ is the material matrix transformed from the laminate coordinate system into the lamina coordinate system. This relation can be written in the following form used to describe shell elements.

$$\begin{bmatrix} F \\ M \end{bmatrix} = \begin{bmatrix} A & B \\ B & D \end{bmatrix} \begin{Bmatrix} \varepsilon^0 \\ \chi \end{Bmatrix} \tag{4.29}$$

Equation (4.16) is valid only for thin-walled structures, i.e. beams, plates and shells.

Where

$$\begin{aligned} [A] &= \sum_{k=1}^{N} [G_k](z_k - z_{k-1}) \\ [B] &= \frac{1}{2} \sum_{k=1}^{N} [G_k]\left(z^2{}_k - z^2{}_{k-1}\right) \\ [D] &= \frac{1}{3} \sum_{k=1}^{N} [G_k]\left(z^3{}_k - z^3{}_{k-1}\right) \end{aligned} \tag{4.30}$$

F and M are the vectors of normal forces and bending/twisting moments (equation (4.16)), and the corresponding [A],[B],[D] are named in composite element literature as the membrane, membrane coupling, and bending matrices, respectively.

The normal forces F, bending moments M and the transverse shear forces Q are related to the middle surface strain, curvatures and transverse shear strains by the following equation.

$$\begin{bmatrix} F \\ M \\ Q \end{bmatrix} = \begin{bmatrix} TG_1 & T^2G_4 & 0 \\ T^2G_4 & \frac{T^3}{12}G_2 & 0 \\ 0 & 0 & T_SG_3 \end{bmatrix} \begin{Bmatrix} \varepsilon^0 \\ \chi \\ \gamma \end{Bmatrix} \tag{4.31}$$

Where

$$A = TG_1, B = T^2G_4 \text{ and } D = \frac{T^3}{12}G_2$$

$$\{Q\} = \begin{Bmatrix} Q_x \\ Q_y \end{Bmatrix} = \text{Transverse shear resultants}$$

$$\{\gamma\} = \begin{Bmatrix} \gamma_x \\ \gamma_y \end{Bmatrix} = \textbf{T}\text{ransverse shear strains}$$

T =Nominal plate thickness

$T_s$ = Effective transverse shear material thickness

$G_3$ = Effective transverse shear material matrix

Equivalent thermal properties are determined as follows:

$$\begin{Bmatrix} \alpha_{\varepsilon_0} \\ \alpha_\chi \\ \alpha_{\chi\varepsilon_0} \end{Bmatrix} = \begin{Bmatrix} T\alpha_1 \\ \frac{T^3}{12}\alpha_2 \\ T^2\alpha_3 \end{Bmatrix} = \begin{bmatrix} A & B & 0 \\ B & D & 0 \\ 0 & 0 & T_SG_3 \end{bmatrix}^{-1} \begin{Bmatrix} G\alpha_{\varepsilon_0} \\ G\alpha_\chi \\ G\alpha_{\chi\varepsilon_0} \end{Bmatrix} \tag{4.32}$$

The following coefficients are used to determine equivalent thermal properties:

$$\begin{aligned}
\left\{G\alpha_{\varepsilon_0}\right\} &= \sum_{k=1}^{N}\left[G\right]_k \left\{\alpha\right\}_k \left(z_k - z_{k-1}\right) \\
\left\{G\alpha_{\chi}\right\} &= \frac{1}{3}\sum_{k=1}^{N}\left[G\right]_k \left\{\alpha\right\}_k \left(z^3{}_k - z^3{}_{k-1}\right) \\
\left\{G\alpha_{\chi\varepsilon_0}\right\} &= \frac{1}{2}\sum_{k=1}^{N}\left[G\right]_k \left\{\alpha\right\}_k \left(z^2{}_k - z^2{}_{k-1}\right)
\end{aligned} \tag{4.33}$$

These coefficients are used to calculate the equivalent thermal properties as follows:

$$\begin{aligned}
\left\{\alpha_{\varepsilon_0}\right\} &= \left[A\right]^{-1}\left\{G\alpha_{\varepsilon_0}\right\} \\
\left\{\alpha_{\chi}\right\} &= \left[D\right]^{-1}\left\{G\alpha_{\chi}\right\}
\end{aligned} \tag{4.34}$$

Where $\left\{\alpha_{\varepsilon_0}\right\}$ , $\left\{\alpha_{\chi}\right\}$ and $\left\{\alpha_{\chi\varepsilon_0}\right\}$ are the membrane, bending, and membrane bending coupling equivalent thermal properties. The thermal expansion relationships in the shell element formulation take the following form.

$$\alpha_{\varepsilon_0} = T\alpha_1, \alpha_{\chi} = \frac{T^3}{12}\alpha_2 \text{ and } \alpha_{\chi\varepsilon_0} = T^2\alpha_3 \tag{4.35}$$

Where $\alpha_1, \alpha_2$ and $\alpha_3$ are the thermal expansion inputs on the materials.

The terms $G_1, G_2$ and $G_4$ are defined by the following integrals;

$$\begin{aligned}
G_1 &= \frac{1}{T}\int\left[G_e\right]dz \\
G_2 &= \frac{1}{T}\int z^2\left[G_e\right]dz \\
G_4 &= \frac{1}{T^2}\int(-z)\left[G_e\right]dz
\end{aligned} \tag{4.36}$$

The limits on the integration are from the bottom surface to the top surface of the laminated composite. The reduced stiffness matrix [$G_e$] has the following form for isotropic materials

$$\left[G_e\right]_l = \begin{bmatrix}
\frac{E}{1-\upsilon^2} & \frac{\upsilon E}{1-\upsilon^2} & 0 \\
\frac{\upsilon E}{1-\upsilon^2} & \frac{E}{1-\upsilon^2} & 0 \\
0 & 0 & \frac{E}{2(1+\upsilon)}
\end{bmatrix} \tag{4.37}$$

For orthotropic materials, the matrix, [G e], is written as follows

$$[G_e]_0 = \begin{bmatrix} \frac{E_1}{1-\upsilon_{12}\upsilon_{21}} & \frac{\upsilon_{12}E_2}{1-\upsilon_{12}\upsilon_{21}} & 0 \\ \frac{\upsilon_{21}E_1}{1-\upsilon_{12}\upsilon_{21}} & \frac{E_2}{1-\upsilon_{12}\upsilon_{21}} & 0 \\ 0 & 0 & G_{12} \end{bmatrix} \tag{4.38}$$

Here, $\upsilon_{12}E_2=\upsilon_{21}E_1$ to satisfy the requirement that the reduced stiffness matrix be symmetric . In general, the analyst may supply element properties with respect to a particular orientation, which does not necessarily correspond to the principal material axes. In this case, the analyst must also supply the value of the angle, q or material coordinate system that orients the element material axis relative to the side $G_1$-$G_2$ of the element. The program into the element modulus matrix through the relation then transforms the material elastic modulus matrix

$$[G_e]=[U]^t[G_m][U] \tag{4.39}$$

Where

$$[U]=\begin{bmatrix} \cos^2\theta & \sin^2\theta & \cos\theta\sin\theta \\ \sin^2\theta & \cos^2\theta & -\cos\theta\sin\theta \\ -2\cos\theta\sin\theta & 2\cos\theta\sin\theta & \cos^2\theta-\sin^2\theta \end{bmatrix} \tag{4.40}$$

The finite element model of a structure composed of composite materials requires the evaluation of the reduced stiffness matrix for each plate element of the model.The characteristics of the composite media are totally contained in these matrices.

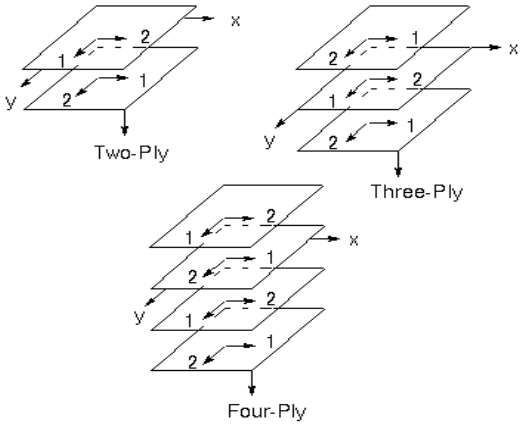


Figure 4.2: Exploded view of three cross- ply laminated plates

To illustrate the evaluation of these matrices, one can consider the cross-ply laminates of Figure 4.2. In this portion of the discussion, the three configurations shown in Figure 4.1 are assumed to be represented by a single quadrilateral plate element and the coordinate axes shown are coincident with the element coordinate axes. Then, if it is assumed that each lamina of the n-ply laminates is of thickness *T/n*, where *T* is the total thickness of each of three configurations the matrices of elastic moduli may be evaluated from the following relations:

$$[G_1]=\frac{1}{T}\left\{\int_{-(\frac{T}{2})}^{-\frac{T}{2}+\frac{T}{n}}[G_e]_1\,dz+\int_{-\frac{T}{2}+\frac{T}{n}}^{-\frac{T}{2}+\frac{2T}{n}}[G_e]_2\,dz+\ldots\ldots+\int_{-(\frac{T}{2})+\frac{(n-1)T}{n}}^{\frac{T}{2}}[G_e]_n\,dz\right\} \tag{4.41}$$

$$[G_2]=\frac{1}{T}\left\{\int_{-(\frac{T}{2})}^{-\frac{T}{2}+\frac{T}{n}}[G_e]_1\,z^2dz+\int_{-\frac{T}{2}+\frac{T}{n}}^{-\frac{T}{2}+\frac{2T}{n}}[G_e]_2\,z^2dz+\ldots\ldots+\int_{-(\frac{T}{2})+\frac{(n-1)T}{n}}^{\frac{T}{2}}[G_e]_n\,z^2dz\right\} \tag{4.42}$$

$$[G_4]=\frac{1}{T^2}\left\{\int_{-(\frac{T}{2})}^{-\frac{T}{2}+\frac{T}{n}}[G_e]_1\,(-z)dz+\int_{-\frac{T}{2}+\frac{T}{n}}^{-\frac{T}{2}+\frac{2T}{n}}[G_e]_2\,(-z)dz+\ldots\ldots+\int_{-(\frac{T}{2})+\frac{(n-1)T}{n}}^{\frac{T}{2}}[G_e]_n\,(-z)dz\right\} \tag{4.43}$$

These relations reflect the assumption that the xy-plane of the element coordinate system is coincident with the geometric middle plane of the laminate.The xy-plane of the element coordinate system is defined in the mean plane of the element so that any offset

between the mean plane of the connected grid points and the geometric middle plane of the laminate would be reflected in the integration limits of the preceding relations.It may be noted that $IT^3/12$ in the evaluation, [$G_2$], i.e. the value $(12*I/T^3)$ will be assigned the default value of 1.0 on the plate element property entry. The matrix of elastic moduli for transverse shear $[G_3]_m$ is defined as a $2\times2$ matrix of the form.

$$[G_3]_m = \begin{bmatrix} G_{12} & G_{13} \\ G_{13} & G_{23} \end{bmatrix} \tag{4.44}$$

$G_{12}$ is associated to the in- plane shear stress, at the same time $G_{13}$ and $G_{23}$ are related to the transverse shear stresses**.** The corresponding matrix transformed into an element coordinate system is given by

$$[G_3]_e = [w]^T [G_3]_m [w] \tag{4.45}$$

$$\text{where } [w] = \begin{bmatrix} \cos\theta & \sin\theta \\ -\sin\theta & \cos\theta \end{bmatrix}$$

The mean value of the transverse shear modulus G of the laminated composite is defined in terms of the transverse shear strain energy U, through the depth and $V_F$ is the shear force**.**

$$U = \frac{1}{2}\frac{V_F^{\,2}}{\bar{G}T} = \frac{1}{2}\int \frac{(\tau(z))^2}{G(z)} dz \tag{4.46}$$

A unique mean value of transverse shear strain is assumed to exist for both the x and y components of the element coordinate system, but for ease of discussion, only the evaluation of an uncoupled x component of the shear moduli will be illustrated here.From Eq. (4.33) the mean value of the transverse shear modulus may be written in the following form

$$\frac{1}{\bar{G}_x} = \frac{T}{V_x^{\,2}} \sum_{i=1}^{N} \int_{z_{i-1}}^{z_i} \frac{(\tau_{zx}(z))^2}{(G_x)_i}\, dz \tag{4.47}$$

Where $\bar{G}$ is an "average" transverse shear coefficient used by the element code and $(G_x)_i$ is the local shear coefficient for layer i. To evaluate Eq. (4.34), it is necessary to obtain an expression for $\tau_{zx}(z)$ which can be accomplished by assuming that the x and y components

of stress are decoupled from one another. This assumption allows the desired equation to be deduced through an examination of a beam of unit cross-sectional width.

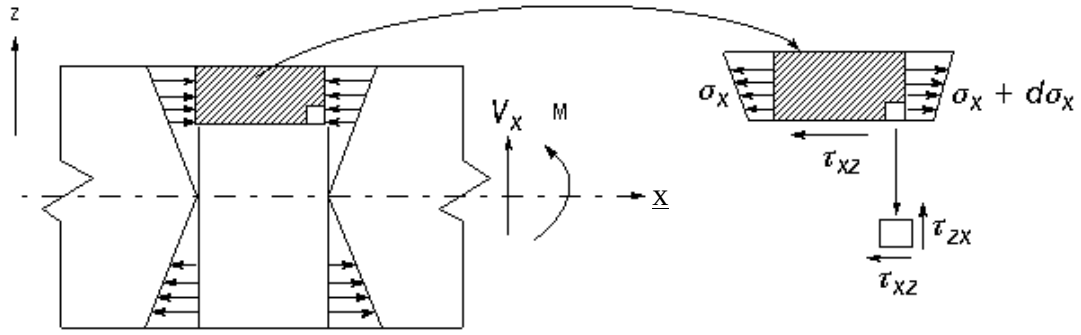


Figure 4.3: Cross –sectional beam of unit length

The equilibrium conditions in the horizontal direction and for total moment are

$$\frac{\partial \tau_{xz}}{\partial z} + \frac{\partial \sigma_x}{\partial x} = 0 \tag{4.48}$$

$$V_x + \frac{\partial M_x}{\partial x} = 0 \tag{4.49}$$

Now, if the location of the neutral surface is denoted by *zx* and $\rho$ is the radius of curvature of the beam, the axial strain $\varepsilon_x$ may be expressed in the form

$$\sigma_x + \frac{E_x(\bar{z}_x - z)}{(\rho)} = 0 \tag{4.50}$$

Eq.(4.50) may be differentiated with respect to x combined with Eqs. (4.48, 4.36 and 4.49). In a region of constant $E_x$ the result may be integrated to yield the following expression

$$\tau_{xz} = C_i + \frac{V_x}{(\overline{EI})_x}(\bar{z}_x\, z - \frac{z^2}{2})E_{xi} \qquad z_{i-1} \le z \le z_i \tag{4.51}$$

Eq.(4.51) is particularly convenient to use in the analysis of n-ply laminates because sufficient conditions exist to determine the constants $C_i$ (i = 1, 2... n) and the "directional bending center"($z_x$).For example, consider the following laminated configuration

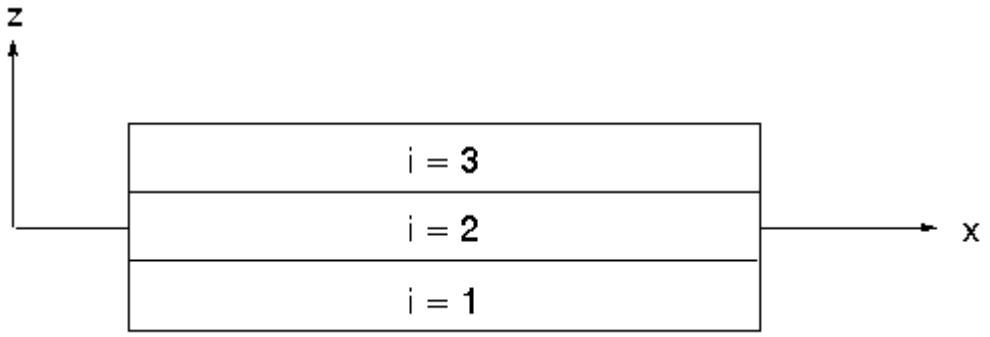


Figure 4.4: Stacking sequence of layers

At the bottom surface (i= 1, $z = z_0$ , and $\tau_{xz} = 0$)

$$C_1 = \frac{-V_x}{(\overline{\overline{EI}})_x}\left[(\bar{z}_x\, z_0 - \frac{z_0^{\,2}}{2})\right]E_{x1} \tag{4.52}$$

and for the first ply at the interface between plies i = 1 and i = 2 ($z = z_1$)

$$\boldsymbol{(\tau_{xz})_1 = \frac{V_x}{(\overline{\overline{EI}})_x}\left[(\bar{z}_x(z_1 - z_0) - \frac{1}{2}(z^2{}_1 - z^2{}_0)\right]E_{x1}} \tag{4.53}$$

At this interface between plies i = 1 and i = 2,

$$(\tau_{xz})_2 = C_2 + \frac{V_x}{(\overline{\overline{EI}})_x}\left[\bar{z}_x z_1 - \frac{z^2{}_1}{2}\right]E_{x2} \tag{4.54}$$

at $z = z_1$ ; $(\tau_{xz})_2 = (\tau_{xz})_1$

$$C_2 = (\tau_{xz})_1 - \frac{V_x E_{x2}}{(\overline{\overline{EI}})_x}\left[\bar{z}_x z_1 - \frac{z^2{}_1}{2}\right] \tag{4.55}$$

Then, in the ply, $z_1 < z < z_2$, the shear stress is:

$$\boldsymbol{(\tau_{xz})(z) = (\tau_{xz})_1 - \frac{V_x E_{x2}}{(\overline{\overline{EI}})_x}\left[\bar{z}_x(z - z_1) - \frac{1}{2}(z^2 - z_1{}^2)\right]} \tag{4.56}$$

In general for any ply, $z_{i-1} < z < z_i$, the shear stress is:

$$\tau_{xz}(z) = (\tau_{xz})_{i-1} - \frac{V_x E_{xi}}{(\overline{\overline{EI}})_x}\left[\bar{z}_x(z - z_{i-1}) - \frac{1}{2}(z^2 - (z_{i-1})^2)\right] \tag{4.57}$$

At any ply interface, $z_i$, the shear stress is therefore

$$\left(\tau_{xz}\right)_i = \frac{V_x}{(\overline{EI})_x}\sum_{j=1}^{i} E_{xj}T_j\left[\bar{z}_x - \frac{1}{2}(z_j + z_{j-1})\right] \tag{4.58}$$

where $T_j = z_j - (z_{j-1})$

Note that the shear stress at the top face,$(\tau_{xz})_n$, is zero and therefore

$$\left(\tau_{xz}\right)_n = \frac{V_x}{(\overline{EI})_x}\left[\bar{z}_x\sum_{j=1}^{n} E_{xj}T_j - \sum_{j=1}^{n} E_{xj}T_j\frac{(z_j + z_{j-1})}{2}\right] = 0 \tag{4.59}$$

Eq.(4.59) proves that if $\bar{z}_x$ is the bending center, the shear stress at the top surface must be zero. Substituing the Eq. (4.57) into Eq. (4.58) and performing integration, a better form of Eq. (4.59), for this purpose is:

$$\left(\left(\tau_{xz}(z)\right)\right)_i = \frac{V_x E_{xi}}{(\overline{EI})_x}\left[f_{xi} + \bar{z}_x\left(z - z_{i-1}\right)\frac{1}{2}\left[z^2 - \left(z_{i-1}\right)^2\right]\right] \tag{4.60}$$

Where $f_{xi} = \frac{1}{E_{xi}}\sum_{j=1}^{i-1} E_{xj}T_j\left[z_x - \frac{(z_j + z_{j-1})}{2}\right]$

Substituting Eq. (4.60) into Eq. (4.51) and after a considerable effort of integrating the results we obtain

$$\frac{1}{\bar{G}_x} = \frac{T}{(\overline{EI})^2_x}\sum_{i=1}^{N}\frac{1}{G_{xi}}R_{xi} \tag{4.61}$$

Where $R_{xi} = \left(E_{xi}\right)^2 T_i\left[\begin{array}{l}\left[\left\{f_{xi} + \left(\bar{z}_x - z_{i-1}\right)T_i - \frac{1}{3}T_i^2\right\}\right]f_{xi} \\ + \left\{\frac{1}{3}\left(\bar{z}_x - 2z_{i-1}\right) - \frac{1}{4}T_i\right\}\bar{z}_x T_i^2 + \left\{\frac{1}{3}z^2{}_{i-1} + \frac{1}{4}z_{i-1}T_i + \frac{1}{20}T_i^2\right\}T_i^2\end{array}\right]$

This expression for the inverse shear modulus for the x-direction may be generalized to provide for the calculation of each term in the $2\times 2$ matrix of shear moduli.

$$\left[G_{kl}\right] = \left[\frac{T}{\left(\overline{EI}\right)^2_{kk}}\sum_{i=1}^{n}\left[G^i{}_{kl}\right]^{-1}R_{ki}\right]^{-1} \tag{4.62}$$

Where k= 1, 2 *l*= 1, 2

The moduli for individual plies are provided through user input because, in general, $G_{12} \neq G_{21}$ will be used for the coupling terms. Finally

$$[G_3] = \begin{bmatrix} \bar{G}_{11} & (\bar{G}_{12})_{avg} \\ (\bar{G}_{12})_{avg} & \bar{G}_{22} \end{bmatrix} \tag{4.63}$$

Considering for a single layer element. For this case let

$z_{i-1} = -T/2, \bar{z} = 0, f_0 = 0$ and $EI = ET^3/12$ .Evaluating Eq. (4.49) we obtain

$$R_i = E^2T^5\left[\frac{1}{12} - \frac{1}{8} + \frac{1}{20}\right] = \frac{E^2T^5}{120} \text{ and} \tag{4.64}$$

$$\frac{1}{\bar{\bar{G}}} = \left[\frac{(12)^2 T}{E^2T^6}\right] * \left[\frac{E^2T^5}{120G_1}\right] = \frac{6}{5G_1} \tag{4.65}$$

This provides the correct factor for a non-uniform shear distribution in a plate.

## 4.5 Failure Indices

In the analysis of isotropic materials, strength is independent of the orientation of the body under load and one may compare the largest computed principal stress with an allowable stress to establish the integrity of the structure.Laminated composites are anisotropic materials and may exhibit unequal properties in tension and compression. Thus, the strength of these orthotropic laminates is a function of body orientation relative to the imposed stresses.

The evaluation of the matrices of material moduli for laminated composites provides sufficient information to determine the actual stress field sustained by the material, the determination of structural integrity will depend on the definition of an allowable stress field. The basic ingredient of this definition is the establishment of a set of allowable stresses or strengths of the principal material directions.

### 4.5.1 Hill's theory

The failure index of Hill represents an analytical expression for an ellipse in the $\sigma_1\sigma_2$ plane. This original expression for failure was subsequently modified to that shown on the left-hand side of the expression by Tsai (Equation (4.66)) and hence this failure theory is sometimes known as the Tsai-Hill Theory.

$$\frac{\sigma_1^2}{X^2}-\frac{\sigma_1\sigma_2}{X^2}+\frac{\sigma_2^2}{Y^2}+\frac{\tau_{12}^2}{S^2}=FI \tag{4.66}$$

Where X is allowable stress in 1-direction

Y is allowable stress in 2-direction

S is allowable stress in shear

$X= X_t$ if $\sigma_1$ is positive

or $X=X_c$ if $\sigma_1$ is negative

and similarly for Y and $\sigma_2$. For the interaction term $\sigma_1\sigma_2/X^2$ , $X = X_t$ if $\sigma_1\sigma_2$ is positive or $X = X_c$ if $\sigma_1\sigma_2$ is negative. Hill's theory is used for materials that have the same strength in tension and compression.

A plot of the above equation obtained by setting the failure index to 1 on the $\sigma_1\sigma_2$ planes yields an ellipse and is the anisotropic yield criterion of Hill (modified later by Tsai, and hence also sometimes known as the Tsai-Hill theory). Therefore, if the failure index so calculated is less than 1, the ply stresses are inside the yield ellipse, and the ply is said to be "safe"; conversely, if the failure index is greater than 1, the ply stresses are outside the yield ellipse and the ply has failed.

### 4.5.2 Tsai-Wu theory

The Tsai-Wu tensor polynomial theory is valid for both orthotropic and anisotropic materials. The only limitation is the plane stress state for orthotropic material (Eq. (4.67)).

The coefficient $F_{12}$ is experimentally determined from test specimens under biaxial loading. This inconvenience along with the constraint that $F_{12}$ satisfies a stability criterion of the form creates some complication in the use of this theory.

$$\left[\frac{1}{X_t}-\frac{1}{X_c}\right]\sigma_1+\left[\frac{1}{Y_t}-\frac{1}{Y_c}\right]\sigma_2+\frac{\sigma_1^2}{X_tX_c}+\frac{\sigma_2^2}{Y_tY_c}+\frac{\sigma_{12}^2}{S}+\frac{\sigma_1\sigma_2}{X_tX_c}=FI \tag{4.67}$$

$$\left[\frac{1}{X_tX_c}\right]\left[\frac{1}{Y_tY_c}\right]-F_{12}^2\geq 0 \tag{4.68}$$

**Tensor Polynomial theory of Tsai-Wu:**

The theory of strength for anisotropic materials proposed by Tsai and Wu specialized to the case of an orthotropic lamina in a general state of plane stress is

$$F_1\sigma_1+F_2\sigma_2+F_{11}\sigma^2{}_1+F_{22}\sigma^2{}_2+2F_{12}\sigma_1\sigma_2+F_{66}\sigma^2{}_{12}=1 \tag{4.69}$$

Where

$$F_1=\left[\frac{1}{X_t}-\frac{1}{X_c}\right];F_2=\left[\frac{1}{Y_t}-\frac{1}{Y_c}\right];F_{11}=\frac{1}{X_tX_c};F_{22}=\frac{1}{Y_tY_c};F_{66}=\frac{1}{S^2} \tag{4.70}$$

And $F_{12}$ is to be evaluated experimentally. The magnitude of $F_{12}$ is, however, constrained by the following inequality called a "stability criterion"

$$F_{11}F_{22}-F_{12}^2\geq 0. \tag{4.71}$$

The necessity of satisfying the stability criterion, together with the requirement that $F_{12}$ be determined experimentally by a combined stress state, poses difficulties in the use of this theory. Narayanaswami and Adelman[133] have suggested that $F_{12}$ be set to zero and that use of Hoffman's theory or Tensor Polynomial theory with $F_{12}=0$ is a preferred alternative to the experimental determination of $F_{12}$.The analyst may provide a value of $F_{12}$ to be used in the Tsai-Wu failure index if he wishes.

## 4.5.3 Hoffman's theory

The Hoffman's theory for an orthotropic and anisotropic lamina in a general state of plane stress is given by Eq.(4.72).The failure index is obtained by evaluating the left-

hand side of the above equation. This theory takes into account the difference in tensile and compressive allowable stresses by using linear terms in the equation.

$$\left[\frac{1}{X_t}-\frac{1}{X_c}\right]\sigma_1+\left[\frac{1}{Y_t}-\frac{1}{Y_c}\right]\sigma_2+\frac{\sigma_1^2}{X_tX_c}+\frac{\sigma_2^2}{Y_tY_c}+\frac{\sigma_{12}^2}{S}-\frac{\sigma_1\sigma_2}{X_tX_c}=1 \tag{4.72}$$

### 4.5.4 Maximum Strain Theory

The midplane strains and curvatures are available in the element coordinate system. From these, the stresses and strains in each lamina along the fiber direction and transverse direction can be calculated quite easily.

$X_t, X_c$ are allowable strains in tension and compression, respectively, in the longitudinal direction.Moreover, $Y_t, Y_c$ are allowable strains in tension and compression, respectively, in the transverse direction.$S$ is the allowable strain for in-plane shear.

The Failure Index is calculated using the following relations;

$\frac{\varepsilon_1}{Y_t}$ (or $\frac{\varepsilon_1}{X_c}$ if $\varepsilon_1$ is compressive)

$\frac{\varepsilon_2}{Y_t}$ (or $\frac{\varepsilon_2}{X_c}$ if $\varepsilon_2$ is compressive) and $\left|\frac{\gamma_{12}}{S}\right|$

The failure index is given by

$$\text{Failure Index} = \text{Max}\left[\left[\frac{\varepsilon_1}{Y_t}\right],\left[\frac{\varepsilon_2}{Y_t}\right],\left[\left|\frac{\gamma_{12}}{S}\right|\right]\right] \tag{4.73}$$

In addition, the user needs to be informed which mode of failure index is critical; i.e., longitudinal (1), transverse (2), or shear (12). Thus, in the output for failure indices, the values 1, 2 or 12 is printed alongside the FP value to indicate the critical direction. There is no change in the way the failure index is calculated for interlaminar shear stresses. It is quite possible that for the maximum strain theory, the user may wish to specify Lamina stress allowable instead of strain allowable. In this case, the failure indices are calculated using

$\frac{\varepsilon_1 * E_{11}}{X_t}$ (or $\frac{\varepsilon_1 * E_{11}}{X_c}$ if $\varepsilon_1$ is compressive)

$\frac{\varepsilon_2 * E_{22}}{X_t}$ (or $\frac{\varepsilon_2 * E_{22}}{X_c}$ if $\varepsilon_2$ is compressive) and

$\frac{|\gamma_{12}| * G_{12}}{S}$

The failure index= $\text{Max}\left[\left[\frac{\varepsilon_1 * E_{11}}{X_t}\right], \left[\frac{\varepsilon_2 * E_{22}}{Y_c}\right], \left[\frac{|\gamma_{12}| * G_{12}}{S}\right]\right]$ (4.74)

## 4.6 Interlaminar Shear Stress and Strains:

Classical lamination theory which utilizes the plane stress assumption does not account for inter laminar stresses. As a result, this theory cannot be used to predict the magnitude of these stresses. High values of these inter laminar stresses can lead to failures that are unique to composite materials. An approximate technique is used to calculate the interlaminar shear stresses. The basic assumption in this approximate technique is that the x and y components of stress are decoupled from one another. The interlaminar shear stress is calculated using classical lamination theory. The interlaminar shear strains are calculated by

$$\gamma_{1z} = \frac{\tau_{1z}}{G_{1z}} \text{ and } \gamma_{2z} = \frac{\tau_{2z}}{G_{2z}} \quad (4.75)$$

## 4.7 Propeller Blade Strength Estimates

It is quite normal to make propeller blades as thin as possible in part to save expensive material and unnecessary weight and in part because thinner blades result in better performance, provided the sections are correctly chosen. In general, propellers normally operate in non-uniform wake flow and possibly in non-steady flow with the loads acting on the blade varying cyclically as the propeller rotates. In such circumstances blade failure is always due to fatigue, unless some accident arises/occurs to cause loadings in excess of normal service requirement. The origination of fatigue due to hydrodynamic pressure causes the crack to occur on the face of the propeller blade resulting in higher tensile

stresses. Mostly the blades crack across the width near the boss with the crack starting close to the mid chord.

### 4.7.1Preliminary estimates of Blade Root thickness

The design of the blade can be based on the selection of nominal mean design stress due to the average blade loading in one revolution at a steady speed, with the propeller absorbing full power. The stress level must be chosen so that the stress fluctuations about this mean level do not give rise to cracking.

The normal stress level has to be chosen in relation to the following:

1. The degree of non-uniformity in wake flow
2. Additional loading due to ship motions
3. Special loadings due to backing and maneuvering
4. The percentage of service life spent at full power
5. The required propeller service life
6. The degree of approximation of the analysis used

In practice, the mean nominal blade stress is chosen empirically on the basis of service experience with the different ship types and materials such as those from various resources included.

### 4.7.2 Method of Estimating Propeller Stresses

Simplified methods are available for predicting the blade root stress with which the propeller blade is related and simple cantilever and beam theory is applied. The structural shell theories using finite element methods may be used to predict the detailed stress distributions for the propeller blades [134] . These methods will be used in conjunction with the computational fluid dynamics techniques including vortex lattice or panel methods, to determine the distribution of hydrodynamic pressures acting on the blades. Hydro elastic techniques can relate the deflections from the finite element analysis back to the CFD analysis illustrated schematically as shown in Figure 4.5.

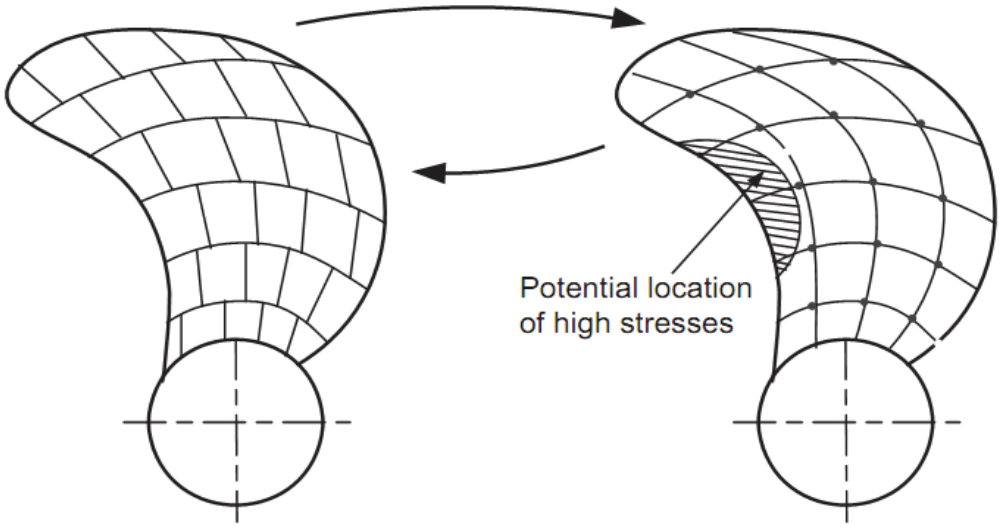


Figure 4.5: CFD methods distribution of loading FEA methods distribution of deflections and stresses

The vortex lattice /panel methods are used for highly skewed propellers coupled with a finite element stress analysis (FEA), such methods provide local stresses but are computer intensive. A simple bending theory applies to the blade root sections which are commonly used as a final check.

### 4.7.3 Propeller Blade strength calculations using Simple Beam theory

In this method of calculation, the blade is considered as a simple cantilever for which the stresses can be calculated by beam theory. The method takes into the account the stresses due to the following

1. Bending moments associated with the thrust and torque loading
2. Bending moments and direct tensile loads due to centrifugal action

**Bending Moments due to Thrust Loading**

At a section of radius $r_0$ the bending moment due to thrust is shown in the Figure 4.6. The equation for bending moment [134] is given as

$$M_T(r_0) = \int_{r_0}^{R} (r - r_0) \frac{dT}{dR} dr \qquad (4.76)$$

$$M_T(r_0) = \int_{r_0}^{R} r \frac{dT}{dR} dr - r_0 T_0 \qquad (4.77)$$
$$= T_0 \bar{r} - T_0 r_0 = T_0 (\bar{r} - r_0)$$

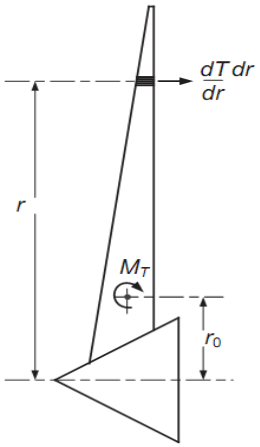


Figure 4.6: Bending moments due to thrust

Where $T_0$ is the thrust of that part of the blade outboard of $r_0$ and $r$ is the centre of thrust from the center line. $M_T$ is about an axis perpendicular to shaft centre line and blade generator.

**Bending Moments due to Torque Loading**

The bending moment due to torque about an axis parallel to shaft center line at radius $r_0$ is shown in Figure 4.7**.** The bending moment $M_Q$ is writen as

$$M_Q = \int_{r_0}^{R} (r - r_0) \frac{dF_Q}{dr} dr \qquad (4.78)$$

$$\text{Since } \frac{dQ}{dr} = r \frac{dF_Q}{dr} \qquad (4.79)$$

Hence

$$M_Q = \int_{r0}^{R} \left(1 - \frac{r_0}{r}\right) \frac{dQ}{dr} dr = Q_0 - r_0 \int_{r0}^{R} \frac{1}{r} \frac{dQ}{dr} dr \qquad (4.80)$$

$$Q_0 - \frac{r_0}{\bar{r}} Q_0 = Q_0 (1 - \frac{r_0}{\bar{r}}) \qquad (4.81)$$

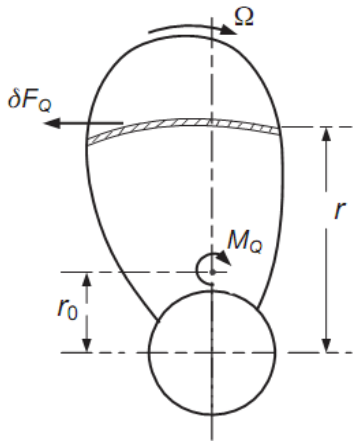


Figure 4.7: Moments due to Torque loading

Where $Q_0$ is the torque due to blade outboard of $r_0$ and $\bar{r}$ is the center of torque load from the center line.

**Forces and Moments due to Blade rotation**

Bending moments due to rotation arise when blades are raked, shown in the Figure 4.8. Let the tensile load L (r) is the load arising due to centripetal acceleration and A (r) is the local blade cross sectional area. The change in L (r) across an element $\delta r$ at radius r is given by the following:

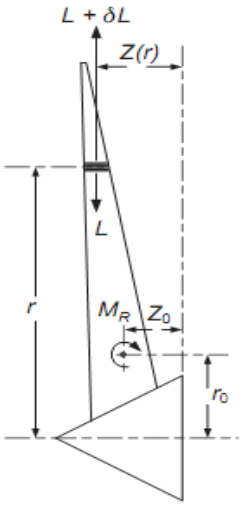


Figure 4.8: Moments due to Blade rotation

$$\delta L = \left[\rho A(r)\delta r\right] r\,\Omega^2 \tag{4.82}$$

Where $\rho$ is the metal density, $\left[\rho A(r)\delta r\right]$ is the mass and

$$\frac{dL}{dr} = \rho\,\Omega^2\, r\, A(r) \tag{4.83}$$

Since L(r) = 0 at the blade tip, then at $r = r_0$

$$L(r_0) = \rho\,\Omega^2 \int_{r_0}^{R} r A(r)\, dr \tag{4.84}$$

It is convenient to assume that the area A is proportional to r and that A (r) varies from A=0 at the tip. If the centre of gravity of the blade section is raked about the generator line by a distance Z(r) then the elementary load from contributes to a bending moment about the same axis as the thrust moment $M_T$ is given by

$$M_R(r_0) = \int_{r_0}^{R} \left[Z(r) - Z(r_0)\right] \frac{dL}{dr}\, dr = \rho\,\Omega^2 \int_{r_0}^{R} \left(Z - Z_0\right) r\, A(r)\, dr \tag{4.85}$$

or

$$M_R(r_0) = \rho\,\Omega^2 \int_{r_0}^{R} \left[r\, Z(r)\, A(r)\, dr\right] - \rho\,\Omega^2\, Z(r_0) \int_{r_0}^{R} r\, A(r)\; dr \tag{4.86}$$

$$M_R(r_0) = \rho\,\Omega^2 \left\{ \int_{r_0}^{R} r\, Z(r)\, A(r)\, dr - Z(r_0)\, L(r_0) \right\} \tag{4.87}$$

Writing the above equation in more reliable useful form and for a radius ratio r/R=0.2,as follows:

$$M_{R0.2} = \int_{0.2R}^{R} m(r).r.\Omega^2 Z'(r).dr \tag{4.88}$$

Where $Z'$ is $(Z\text{-}Z_0)$ and $r_0$ is assumed to be 0.2R.

The centrifugal force can be written as

$$F_c = \int_{0.2R}^{R} m(r)\, r\, \Omega^2 dr \tag{4.89}$$

where $m(r) = \rho A(r) = \text{mass / unit radius}$

**Resolution of Bending Moments**

The primary bending moments $M_T$, $M_Q$ and $M_R$ must be resolved into bending moments about the principal axes of the propeller blade section shown in Figure 4.6 and 4.7. The direction of these principal axes depends on the precise blade section shape, and the pitch angle of the section datum face at the radius $r_0$ .Of the two principal axes shown A-A and B-B (Figure 4.9) the section modulus (I/y) is least about the axis A-A, leading to the greatest tensile stress in the middle of the blade face at P and the largest compressive stress at Q shown in Figure 4.9.

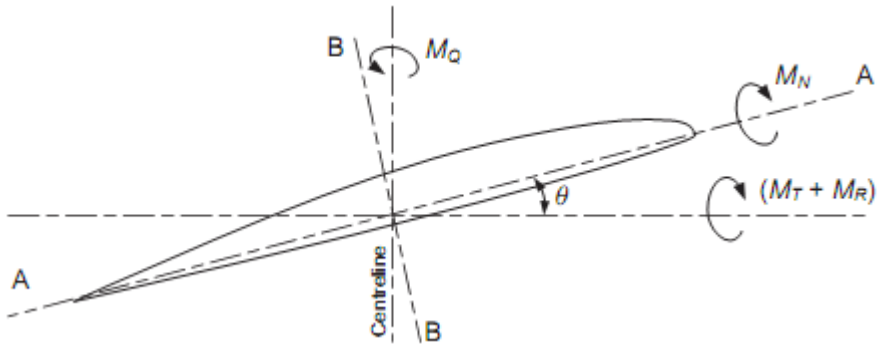


Figure 4.9: Resolution of bending moments

The equation for the pitch angle is given by

$$\theta = \tan^{-1}\left(\frac{P/D}{\pi x}\right) \tag{4.90}$$

The significant bending moment from the blade strength point of view is thus

$$M_N = (M_T + M_R)\cos\theta + M_Q \sin\theta \tag{4.91}$$

The above equation is used in computing the blade bending stress.

**Properties of Blade Structural Design**

Usually the structural modulus should be obtained for a plane section A-A as shown in Figure 4.9.In practice, cylindrical sections $A' - A'$ are used in defining the blade-geometry(Figure 4.10) and a complex drawing procedure is needed to derive the plane sections. Since pitch angle reduces as the radius increases a plane section assumes an S-shape with the nose is drooping and the tail lifting ( Figure 4.9).

Compared with the other approximations inherent in the simple beam theory method, the error involved in calculating the section modulus from a cylindrical section rather than a plane section is not significant. Common practice is to use cylindrical sections and to assume that the principal axis is parallel to the pitch datum line.

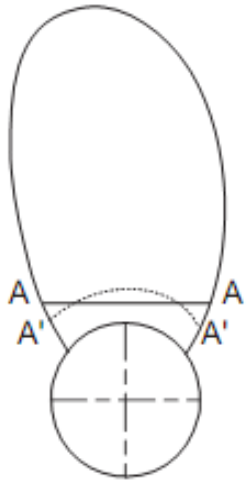


Figure 4.10: Blade Geometry

Typical values of I/y are as follows:

Aero foil I/y= $0.095ct^2$

Round back I/y= $0.112ct^2$

Typical values of the area at the root are as follows:

A = 0.7ct to 0.72ct

Where c is the chord and t is the thickness

An approximation to the root chord ratio at 0.2R based on the Wageningen series [134] is as follows:

$$\left(\frac{c}{D}\right)_{0.2R} = 0.416 \times BAR \times \frac{4}{Z} \tag{4.92}$$

Where Z is the number of blades.

Blade thickness fraction $t_0/D$ at the centreline for the Wageningen series together with the approximate estimates of $t_0/D$ at 0.2R, 0.7R and 0.75R are taken from the reference [134].

Finally the design stress is

$\sigma =$ direct stress + bending stress

$$\sigma = \frac{F_c}{A} + \frac{M_N}{I / y} \tag{4.93}$$

## 4.8 Preliminary Results for Propeller Blade Strength Estimates

Propellers operate in a non-uniform wake flow and possibly in an unsteady flow where the blades are subjected to cyclic loads due to rotation.Under these conditions the failure of blades is due to fatigue, until unless some accident may arises (e.g. grounding) to cause loadings in excess of normal service requirements.The following section 4.8.1 defines the necessary parameters required for strength estimates of propelle blade.

### 4.8.1 Selection of Parameters for Propeller Blade Strength Estimates

For scaled Model the following parameters are selected.

| | | |
|---|---|---|
| Number of blades (Z) | = | 4 |
| Pitch diameter ratio (P/D) | = | 0.9 |
| Expansion ratio ($A_E/A_0$) | = | 0.7 |
| Speed of revolution (N) | = | 1490 rpm |
| Advanced velocity ($V_a$) | = | 6.12 m/s |
| Power developed ($P_D$) | = | 1.194 Kw |
| Chord(C) | = | 0.0949 m |
| Maximum chord ($C_{max}$) | = | 0.119 m |
| Thickness of blade at tip (t1) | = | 0.001m |
| Thickness at root (t) | = | 0.0121m |
| Chord-diameter ratio of the root section (C/D) | = | 0.268 |
| Blade thickness fraction ($t_0/D$) | = | 0.034 |

Thickness-chord ratio of the root section (t/C) = 0.127

Max-chord diameter ratio of the propeller ($C_{max}$/D) = 0.338

Rake angle ( $\xi$ ) = $10^0$

Density of the material ( $\rho_m$ ) = 2700 Kg/$m^3$

## 4.8.2 Burrill Method for determination of stresses in blades

An approximate method for calculating propeller blade stress is done by Burrill[134] . In this method the thrust distribution on each blade can be taken to act at as a point whose distance from the root section is 0.6 times the length of the blade from root to tip and the transverse force on each blade which gives rise to the torque is taken to act at a distance from the root section of 0.55 times the length of the blade. The following calculations are used to determine the thrust, torque, bending moment and the maximum stress developed in the root section of the blade.

The thrust load $P_T = P_D \times \eta$

Where, $P_D$ is the power developed by the propeller and $\eta$ is the mechanical efficiency.

Assuming mechanical efficiency $\eta$ as 0.6, the thrust load is calculated as

$P_T = 1.194 \times 0.64 = 0.7616$ kW

$$\text{Thrust (T)} = \frac{P_T}{V_a} = \frac{0.7616}{6.12} = 124.44\text{N}$$

$V_a$ represent the advanced velocity.

$$\text{Torque (Q)} = \frac{P_D}{2\pi n} = \frac{1.194}{2\pi(1490/60)} = 4.8811\text{N} - \text{m}$$

Bending moment due to thrust $(M_T)$;

Number of blade=4

Diameter of propeller = 0.353 m

$x_0$ = 0.2 m

$$M_T = \frac{T * D}{Z}\left((1 - x_0)\right) * 0.3 = \frac{(124.44 * 0.353)}{4}\left(1 - 0.2\right) * 0.3 = 2.6356\ \text{N} - \text{m}$$

$$M_Q = \left(\frac{Q}{Z}\right)*\left(\frac{0.55*(1-x_0)}{0.55+0.45*x_0}\right) = \frac{(4.811*0.55*0.8)}{4*[0.55*+(0.45*0.2)]} = 0.826\,\text{Nm}$$

Mean thickness of blade from root to tip;

Thickness of blade at tip = 0.001 m

Diameter of propeller = 0.353 m

$t_0/D=0.034$, $t_1/D=0.001/0.353$

$$\bar{t} = 0.5\left[(1-x_0)\frac{t_0}{D}+(1+x_0)\frac{t_1}{D}\right]D = \bar{t} = 0.5*\left[(0.8*0.0343)+(1.2*0.00314)\right]*0.353$$

$$= 5.508*10^{-3}\text{m}$$

$$A_E = 0.7*(\frac{\pi}{4}*0.353^2) = 0.0684\ \text{m}^2$$

$$m_b = 2700*5.508*10^{-3}*\left(\frac{0.0684}{4}\right)*0.75 = 190.762\ \text{Kg}$$

$$\bar{x}_R = \left[0.2+0.32*(1-0.2)\right]*\frac{0.353}{2} = 0.080\ \text{m}$$

$$F_c = 190.762*\left(2*\pi*\left(\frac{1490}{60}\right)^2\right)*0.08 = 371.523\ \text{kN}$$

$$M_R = 371.523*(0.456-0.2)*\frac{0.353}{2}*\tan(10^0+6^0) = 4.813\ \text{kN}-\text{m}$$

$$a = k_2 ct = 0.725*0.268^2*0.1279*0.353^2 = 8.299*10^{-4}\text{m}^2$$

$$\frac{I}{y} = k_3 ct^2 = 0.1*0.268^3*0.1279^2*0.353^3 = 1.385*10^{-6}\text{m}^3$$

$$\tan\varphi = \frac{P}{\pi x_0 D} == \frac{0.9}{\pi*0.2} = 1.4324$$

Or $\varphi = 55.08°$

$$S = \left(\frac{(M_T+M_R)\cos\varphi+M_Q\sin\varphi}{(I/y)}\right)+\left(\frac{F_C}{a}\right)$$

$$S = \frac{(2.6356+(4.813*10^3))\cos 55.08°+(0.8268*\sin 55.08°)}{(1.385*10^{-6})}+\left(\frac{371.523*10^3}{8.299*10^{-4}}\right)$$

$$= 447.672*10^6+1994.806*10^6$$

$$S = \frac{(2.6356 + (4.813*10^{3}))\cos 55.08° + (0.8268*\sin 55.08°)}{(1.385*10^{-6})} + \left(\frac{371.523*10^{3}}{8.299*10^{-4}}\right)$$

$$= 447.672*10^{6} + 1994.806*10^{6}$$

S=2442.47MPa.

Figures 4.11 shows the single meshed propeller blade with hub and corresponding Figure 4.12 shows the single meshed propeller blade with constraints.The three dimensional modelling of propeller blade was done using Catia VR20 and the meshing was done using Hypermesh software 11.0 version.The total number of elements are 3069 and nodes are 6032.

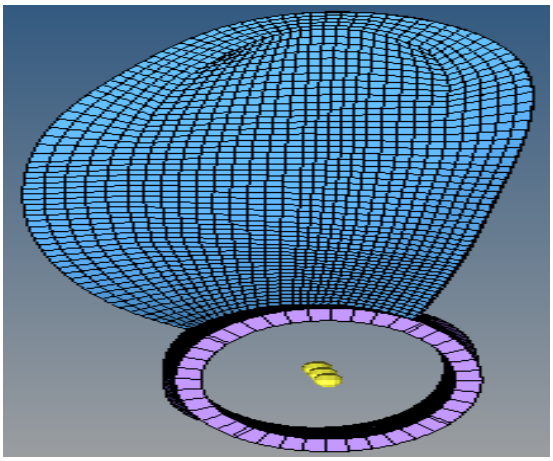

Figure 4.11: Single Meshed Propeller Blade with Hub

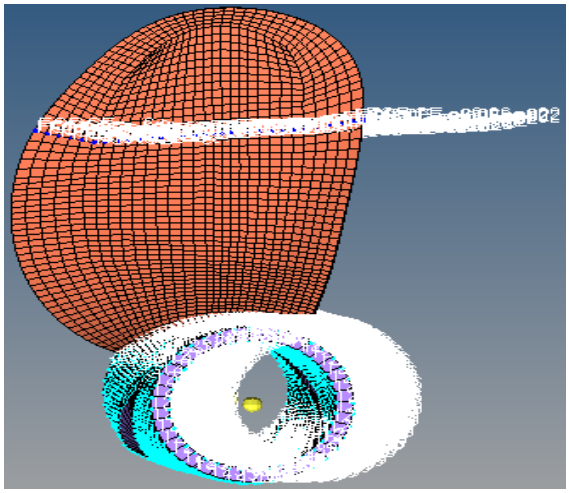

Figure 4.12: Single Meshed Propeller Blade with Constraints

### 4.8.3 Validation of the model

Feed back how the CFD results were obtained.

The hydrodynamic pressures obtained from CFD analysis are taken as input for structural analysis for Aluminum and composite propeller blades. The obtained pressure is mapped on propeller and the corresponding thrust and torque are determined. Since the value of torque is very less compared to thrust it is ignored.The corresponding thrust value is taken as input (Fig 4.12) to determine the maximum stress occur on the blade.

From CFD analysis maximum amount of thrust produced due to rotation of propeller is

$T_{max}$ = 2424.318 N (see Table 4.1)

For a single propeller blade thrust produced is $=T_{max}/Z$

Where Z= number of blades

For a single propeller blade thrust produced is

$T_{single}$ = 2424.318/4

= 606.079 N

This amount of thrust produced is applied uniformly over the blade with cantilever condition applied.

From using ANSYS (APDL) solver, the maximum amount of stress produced

$\sigma_{max}$ =2469.8 Pa.

Table 4.1 : Evaluation of Thrust from CFD analysis

| | Moments (n-m) | | |
|---|---|---|---|
| Zone | Pressure | Viscous | Total |
| wall | 151.79298 | 5.682484 | 157.47546 |
| Net | 151.79298 | 5.682484 | 157.47546 |
| Forces | | | |
| | Forces (n) | | |
| Zone | Pressure | | |
| wall | (2446.9169 -0.061625957 -5.3611352) | | |
| Net | (2446.9169 -0.061625957 -5.3611352) | | |
| Forces - Direction Vector | (1 0 0) | | |
| | Forces (n) | | |
| Zone | Pressure | Viscous | Total |
| wall | 2446.9169 | -22.598426 | 2424.3185 |
| Net | 2446.9169 | -22.598426 | 2424.3185 |

### 4.8.4 Static Analysis of Aluminium Propeller

A thrust of 606.079 N is applied on the face side of the blade in the region between 0.7R and 0.75R (Figure 4.12). The intersection of hub and shaft point's deformations in all directions are fixed. The thrust is produced because of the pressure difference between the face and back sides of propeller blades. This pressure difference also causes rolling movement of the underwater vehicle. This rolling movement is nullified by the forward propeller which rotates in another direction (reverse direction of aft propeller). The propeller blade is considered as a cantilever beam condition. The deformation pattern for the aluminum propeller is shown in the Figure 4.13. The maximum deflection at the free end of the blade was found as 39.399 mm.

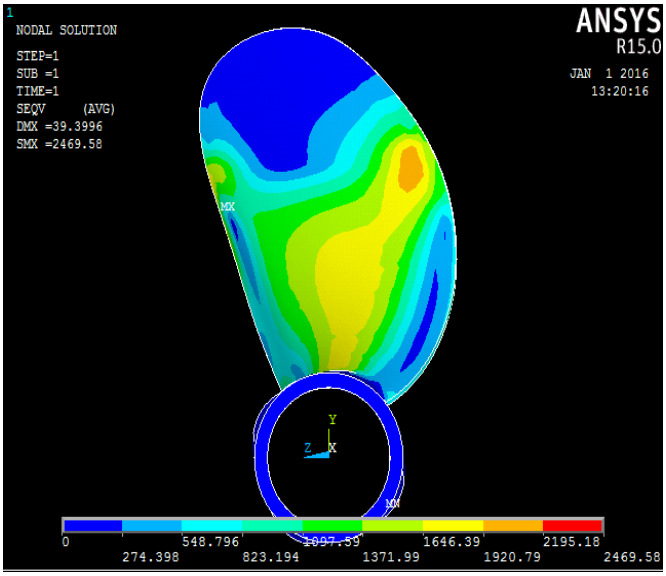


Figure 4.13: von Mises Stress (Pa) for Aluminium Propeller Blade

The von Mises stress on the basis of shear distortion energy theory was also calculated in the present analysis. The maximum von Mises stress induced for the aluminum blade is 2469.58 N/mm$^2$ .The thickness of the blade near the hub is 12 mm and at the tip it is 2 mm. The maximum von Misses stress obtained might be due to the high thrust experienced by the blade at the mid-chord of the hub intersection.The stresses are greatest near the mid-chord of the blade-hub intersection with smaller stress magnitude towards the tip and edges of the blade. Figure 4.13 shows the induced deformations and stresses in Aluminium propeller for a single blade.

# 4.9 Mathematical Modelling of Propeller Blade Using Shell Element

## 4.9.1 Introduction

For the modelling purpose, an SHELL181 element is being selected among the available elements in ANSYS 15.0 element library. Figure 4.14 shows the solid geometry, node locations and the element coordinate system of the SHELL181 element. The element is defined by four nodes (I, J, K, and L). This is a 2D four nodded element with six degrees of freedom per node, and the degree of freedoms of each node are the translations and rotations in the respective axis. It is suitable for thin to moderately thick structures and well suited for linear, large rotation and large strain nonlinear applications. Thin to moderately thick structures can be analysed using this shell element. It can also be used for analysing shells whose thickness change under the nonlinear analysis of plates. This shell element can also be used for analysing layered shell structures. All the analysis is governed by First-order Shear Deformation Theory (FSDT).

## 4.9.2 Mathematical Formulation

Low aspect ratio blades are usually analysed using beam and plate theories. The beam theory is considered to be the simplest of all and needs less computation. In the present analysis, a propeller blade of the considerable chord and thickness is taken into account. The twisted blade characteristics are evaluated using shell element 181 taken from ANSYS library (Figure 4.15). The propeller blade model is developed in ANSYS based on the built-in FSDT kinematics. The displacement field's u, v and w at any point along the x, y and z-axes can be written as follows:

$$\begin{aligned} u(x,y,z) &= u_0(x,y) + z\,\theta_x(x,y) \\ v(x,y,z) &= v_0(x,y) + z\,\theta_y(x,y) \\ w(x,y,z) &= w_0(x,y) + z\,\theta_z(x,y) \end{aligned} \tag{4.94}$$

Where u, v and w represent the displacements of any point along (x, y, z) coordinate. Moreover, $u_0$ , $v_0$ is the in-plane and $w_0$ is the transverse displacement of the mid-plane and $\theta_x$ ,$\theta_y$ are the rotations of the normal to the mid-plane of y and x-axes respectively. Here $\theta_z$ is the higher order term in Taylor's series of expansion. The geometry of two-dimensional laminated composite blades with a positive set of coordinate axis and the middle plane displacement terms are shown in Figure 4.16 .

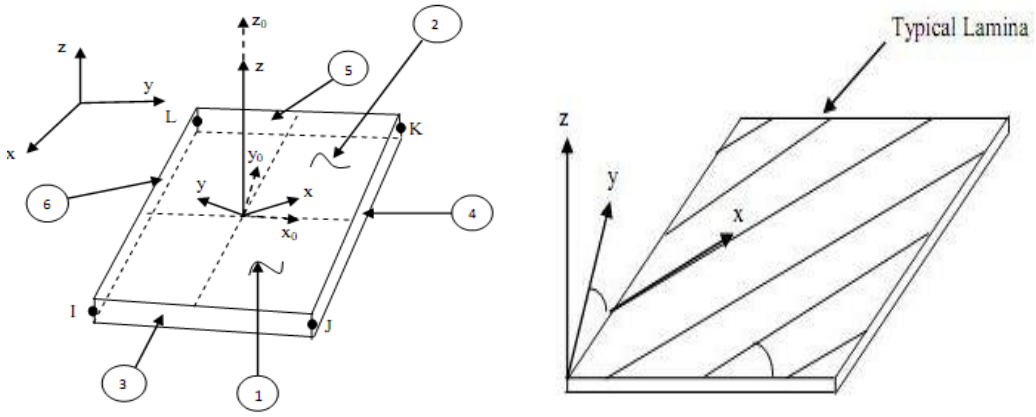


Figure 4.14: Shell 181 element

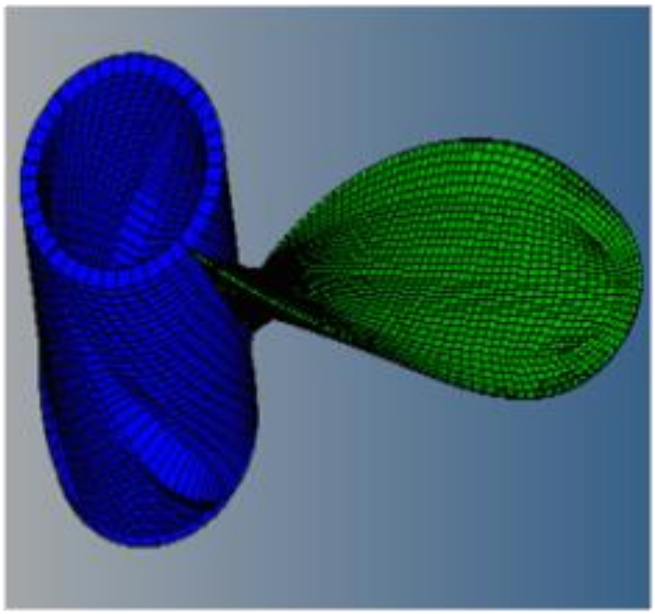

Figure 4.15: Pre-twisted Blade with shell elements

The value of displacements expressed for shape functions is given by

$$\delta = \sum_{i=1}^{j} N_i \delta_i$$
$$\text{where } \delta_i = \begin{bmatrix} u_{0i} & v_{0i} & w_{0i} & \theta_{xi} & \theta_{yi} & \theta_{zi} \end{bmatrix} \quad (4.95)$$

The shape functions for a four-noded element (j=4) in natural coordinates $(\xi,\eta)$ are given by

$$N_1 = \frac{1}{4}(1-\xi)(1-\eta),\ N_2 = \frac{1}{4}(1+\xi)(1-\eta)$$

$$N_3 = \frac{1}{4}(1+\xi)(1+\eta) \text{ and } N_4 = \frac{1}{4}(1-\xi)(1+\eta) \tag{4.96}$$

The vector of strain components are given by

$$\{\varepsilon\} = \{\varepsilon_{xx} \quad \varepsilon_{yy} \quad \varepsilon_{zz} \quad \gamma_{xy} \quad \gamma_{yz} \quad \gamma_{zx}\}^T \tag{4.97}$$

Explicitly one can write $\{\varepsilon\}$ vector as

$$\{\varepsilon\} = \left\{ \frac{\partial u}{\partial x} \quad \frac{\partial v}{\partial y} \quad \frac{\partial w}{\partial z} \quad \frac{\partial u}{\partial y}+\frac{\partial v}{\partial x} \quad \frac{\partial v}{\partial z}+\frac{\partial w}{\partial y} \quad \frac{\partial u}{\partial z}+\frac{\partial w}{\partial x} \right\}^T \tag{4.98}$$

Where $\left\{\frac{\partial u}{\partial x} \frac{\partial v}{\partial y} \frac{\partial w}{\partial z}\right\}$ are the normal strain components and

$$\left[\frac{\partial u}{\partial y}+\frac{\partial v}{\partial x} \quad \frac{\partial v}{\partial z}+\frac{\partial w}{\partial y} \quad \frac{\partial u}{\partial z}+\frac{\partial w}{\partial x}\right]$$

are the shear strain components in inplane and outplane directions.

Now, the in-plane and transverse strain vector for the element can be written as

$$\begin{Bmatrix} \varepsilon_x \\ \varepsilon_y \\ \gamma_{xy} \end{Bmatrix} = \begin{Bmatrix} \varepsilon_{x_0} \\ \varepsilon_{y_0} \\ \gamma_{xy_0} \end{Bmatrix} + z \begin{Bmatrix} K_x \\ K_y \\ K_{xy} \end{Bmatrix} \text{ and } \begin{Bmatrix} \varepsilon_z \\ \gamma_{yz} \\ \gamma_{xz} \end{Bmatrix} = \begin{Bmatrix} \varepsilon_{z_0} \\ \gamma_{yz_0} \\ \gamma_{xz_0} \end{Bmatrix} + z \begin{Bmatrix} K_z \\ K_{yz} \\ K_{xz} \end{Bmatrix} \tag{4.99}$$

Again the deformation components can be written as

$$\begin{Bmatrix} \varepsilon_{x_0} \\ \varepsilon_{y_0} \\ \varepsilon_{xy_0} \end{Bmatrix} = \begin{Bmatrix} \frac{\partial u_0}{\partial x} \\ \frac{\partial v_0}{\partial y} \\ \frac{\partial u_0}{\partial y}+\frac{\partial v_0}{\partial x} \end{Bmatrix} \text{ and } \begin{Bmatrix} K_x \\ K_y \\ K_{xy} \end{Bmatrix} = \begin{Bmatrix} \frac{\partial \theta_x}{\partial x} \\ \frac{\partial \theta_y}{\partial y} \\ \frac{\partial \theta_x}{\partial y}+\frac{\partial \theta_y}{\partial x} \end{Bmatrix} \tag{4.100}$$

$$\begin{Bmatrix} \varepsilon_{z_0} \\ \gamma_{yz_0} \\ \gamma_{xz_0} \end{Bmatrix} = \begin{Bmatrix} \theta_z \\ \frac{\partial w_0}{\partial y} + \theta_y \\ \frac{\partial w_0}{\partial x} + \theta_x \end{Bmatrix} \text{ and } \begin{Bmatrix} K_z \\ K_{yz} \\ K_{xz} \end{Bmatrix} = \begin{Bmatrix} 0 \\ \frac{\partial \theta_z}{\partial y} \\ \frac{\partial \theta_z}{\partial x} \end{Bmatrix} \tag{4.101}$$

The strain vector expressed in terms of nodal displacement vector can be represented as

$$\{\boldsymbol{\varepsilon}\} = [\mathrm{B}]\{\boldsymbol{\delta}\} \tag{4.102}$$

[B] is the strain-displacement matrix containing interpolation functions and their derivatives.

Here the nodal displacement vector is

$$\{\boldsymbol{\delta}\} = \{u_0 \quad v_0 \quad w_0 \quad \theta_x \quad \theta_y \quad \theta_z\}^{\mathrm{T}}. \tag{4.103}$$

The generalized stress-strain relationship on reference plane is given by

$$\{\boldsymbol{\sigma}\} = [\mathrm{D}]\{\boldsymbol{\varepsilon}\} \tag{4.104}$$

Where $\{\boldsymbol{\sigma}\}$ and $\{\boldsymbol{\varepsilon}\}$ are the stress and strain vectors.

$[\mathrm{D}]$ is the constitutive matrix.

The value of strain-displacement matrix $[\mathrm{B}]$ is given by

$$[B]=\sum_{i=1}^{4}\begin{bmatrix}
\frac{\partial N_i}{\partial x} & 0 & 0 & 0 & 0 & 0\\
0 & \frac{\partial N_i}{\partial x} & 0 & 0 & 0 & 0\\
0 & 0 & 0 & 0 & 0 & 1\\
\frac{\partial N_i}{\partial y} & \frac{\partial N_i}{\partial x} & 0 & 0 & 0 & 0\\
0 & 0 & \frac{\partial N_i}{\partial y} & 0 & 1 & 0\\
0 & 0 & \frac{\partial N_i}{\partial x} & 1 & 0 & 0\\
0 & 0 & 0 & \frac{\partial N_i}{\partial x} & 0 & 0\\
0 & 0 & 0 & 0 & \frac{\partial N_i}{\partial y} & 0\\
0 & 0 & 0 & 0 & 0 & 0\\
0 & 0 & 0 & \frac{\partial N_i}{\partial y} & \frac{\partial N_i}{\partial x} & 0\\
0 & 0 & 0 & 0 & 0 & \frac{\partial N_i}{\partial y}\\
0 & 0 & 0 & 0 & 0 & \frac{\partial N_i}{\partial x}
\end{bmatrix} \tag{4.105}$$

The element stiffness and mass matrix can be derived as

$$[K]^e=\int_{-1}^{1}\int_{-1}^{1}\int_{-1}^{1}[B]^T[D][B]|J|d\xi\, d\eta \text{ and}$$

$$[M]^e=\int_{-1}^{1}\int_{-1}^{1}\int_{-1}^{1}[N]^T\rho[N]|J|d\xi\, d\eta \tag{4.106}$$

Where $|J|$ is the Jacobian matrix and $[N]$ is the shape function matrix.

From the given stiffness matrix the deflections in static analysis can be determined as

$$[K]\{\delta\} = \{P\} \tag{4.107}$$

Where $\{\delta\}$ represents the nodal displacement vector.

$[P]$ is the static load vector acting on the nodes.

Equation of motion for the blade can be obtained by using Hamilton's principle.The governing equation of motion for blade can be written as

$$\int_{t_0}^{t_1} (\delta T - \delta U)\, dt = 0 \tag{4.108}$$

The variation instrain energy U and kinetic energy T can be written as

$$\delta U = \int_V \left[ \delta\varepsilon_{xx} E\varepsilon_{xx} + \delta\varepsilon_{yy} E\varepsilon_{yy} + \delta\varepsilon_{zz} E\varepsilon_{zz} + \delta\gamma_{xy} G\gamma_{xy} + \delta\gamma_{yz} G\gamma_{yz} + \delta\gamma_{zx} G\gamma_{zx} \right] dV$$

$$\delta T = -\int_V \rho \left\{ \bar{P}_u \delta u + \bar{P}_v \delta v + \bar{P}_w \delta w \right\} dV \tag{4.109}$$

Using equations (4.96) and (4.95) the equations of motion including damping can be written as

$$[M]\{\ddot{\delta}\} + [C]\{\dot{\delta}\} + [k_e + k_g + k_r]\{\delta\} = \{F_{ext} + F_r\} \tag{4.110}$$

$$[M]\{\ddot{\delta}\} + [C]\{\dot{\delta}\} + [k_e + k_g]\{\delta\} = \{F_{ext}\} \tag{4.111}$$

$$[M]\{\ddot{\delta}\} + [C]\{\dot{\delta}\} + [k_e + k_g]\{\delta\} = 0 \tag{4.112}$$

Where $\ddot{\delta}, \dot{\delta}$ and $\delta$

are the acceleration, velocity and displacement of the blade.

$[M]$ represents the mass matrix. $[C]$ represents the damping matrix. $k_e, k_g$ and $k_r$ are the material, geometric and rotational stiffness matrices.In the absence of damping and external force the equation of motion can be reduced to

$$[M]\{\ddot{\delta}\} + [K]\{\delta\} = 0 \tag{4.113}$$

Knowing the mass and stiffness matrices the natural frequency of the blade can be determined.

## 4.10 Material Properties of Propeller Blade

The propeller blades are made up of aluminium and composite materials. The material properties for aluminium and composite materails are taken from the reference [135].

Table 4.2: Properties of Aluminium Propeller Blade

| Properties | Values |
|---|---|
| Elastic modulus (E) | 69 GPa |
| Shear modulus (G) | 26.12 GPa |
| Density( $\rho$ ) | 2700 Kg/m$^3$ |
| Poisson's ratio( $\upsilon$ ) | 0.334 |

Table 4.3: Properties of Composite propeller Blade

| Properties | E-glass-epoxy | Carbon-epoxy |
|---|---|---|
| Density $\rho$ (Kg/m$^3$) | 2100 | 1580 |
| Longitudinal modulus $E_x$ (GPa) | 39 | 142 |
| Transverse modulus$E_y$ (GPa) | 8.6 | 10.3 |
| In plane shear modulus$G_{xy}$ (GPa) | 3.8 | 7.2 |
| Major Poisson's ratio $\upsilon_{12}$ | 0.28 | 0.27 |
| Major Poisson's ratio $\upsilon_{21}$ | 0.06 | 0.02 |
| Longitudinal Tensile strength $F_{1t}$ (MPa) | 1080 | 2280 |
| Transverse Tensile strength $F_{2t}$ (MPa) | 39 | 57 |
| In-plane shear strength $F_6$ (MPa) | 89 | 71 |
| Longitudinal compressive strength $F_{1c}$ (MPa) | 620 | 1440 |
| Transverse compressive strength $F_{2c}$ (MPa) | 128 | 228 |
| Ultimate longitudinal Tensile strain $\varepsilon_{1t}^{u}$ | 0.028 | 0.015 |
| Ultimate Transverse Tensile strain $\varepsilon_{2t}^{u}$ | 0.005 | 0.006 |

# 1.1 Results and Discussions

## 4.11.1 Static Analysis

Linear static analysis is concerned with the behaviour of elastic continua under prescribed boundary conditions and statically applied loads. The applied load, in this case is the amount of pressure acting on the blades. Clockwise rotating B-series propeller is chosen for FE analysis. The FE analysis is carried out using theoretical and numerical computations. The material properties for aluminium and E-glass epoxy are shown in Tables 4.2 and 4.3.The deformations and stresses are calculated for aluminium alloy (isotropic) and composite propeller (orthotropic material). In composite propeller with two sets of materials and their combination (Hybrid) composites are taken into consideration. For propeller blade analysis, shell element 181 (from ANSYS library) is considered for aluminium and composite propeller material

**Static analysis of Aluminium Propeller Blade**

The pressure obtained from the CFD (cavitation pressures) is distributed equally on front and the rear face side of the blade in the region of root and tip. The intersection of hub and shaft point's deformations in all directions are fixed. The thrust and torque are produced because of the pressure difference between the face and back sides of propeller blades. This pressure difference also causes rolling movement of the underwater vehicle. A 3 D surface model combined with the solid model of the hub is shown in Figure 4.16 using shell element.The pressure applied on the blade is shown in Figure 4.17. The deformation pattern for the aluminium propeller is shown in Figure 4.18. The von Mises stress by shear distortion energy theory is also calculated in the present analysis. The maximum von Misses stress induced for the aluminium blade is 11 $N/mm^2$ as shown in Figure 4.19. The maximum deflection was found as 0.082 mm at the free end (Figure 4.18). The corresponding X,Y and Z-component stresses are shown in Figures 4.20-4.22. Maximum principal stress values for the aluminium propeller are shown in Figure 4.23 to Figure 4.25. The stresses are nearer to the mid-chord of the blade hub intersection, the stresses reduce towards the tip and edges of the blade. Table  shows induced deformations and stresses in aluminium and E-Glass epoxy propeller.

Table 4.4: Deformation and Stress values for Metallic propeller blade

| Parameter | Aluminium |
|---|---|
| Deformation(mm) | 0.082 |
| Von Mises -stress(MPa) | 11.000 |
| I-Principal stress(MPa) | 10.400 |
| II-Principal-stress(MPa) | 3.530 |
| III-Principal-stress(MPa) | 0.037 |
| X-Component (MPa) | 2.250 |
| Y-Component (MPa) | 10.100 |
| Z-Component (MPa) | 7.870 |

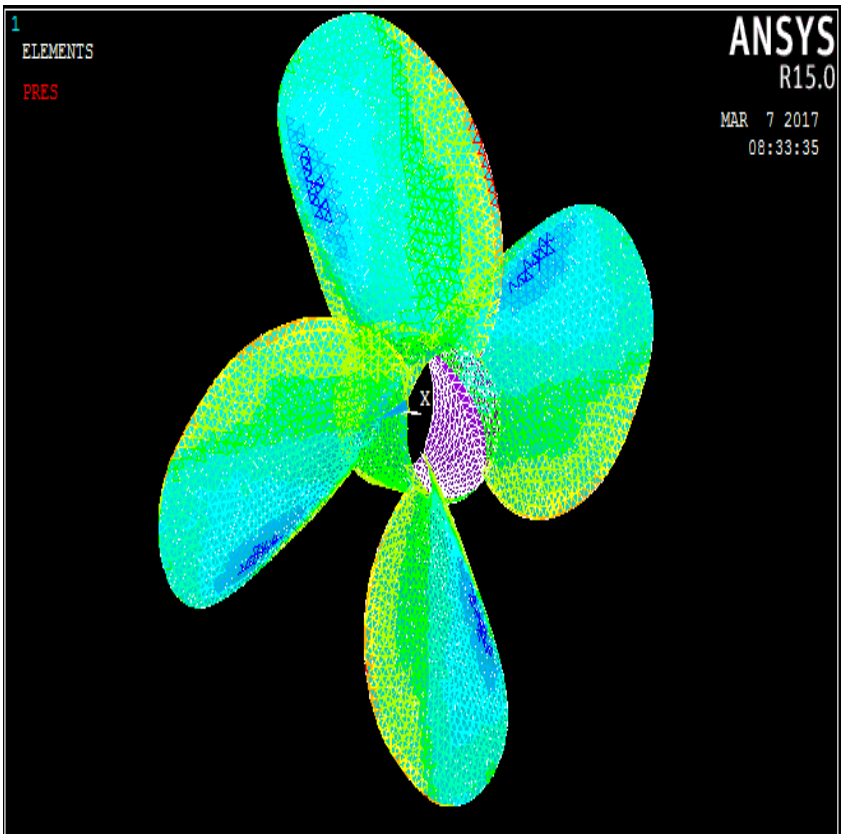


Figure 4.16: Meshed Model

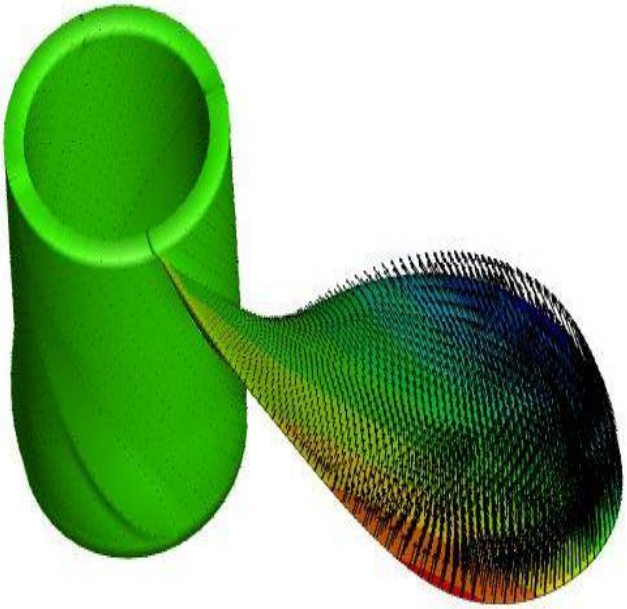

Figure 4.17: Single Blade propeller with Pressure mapping

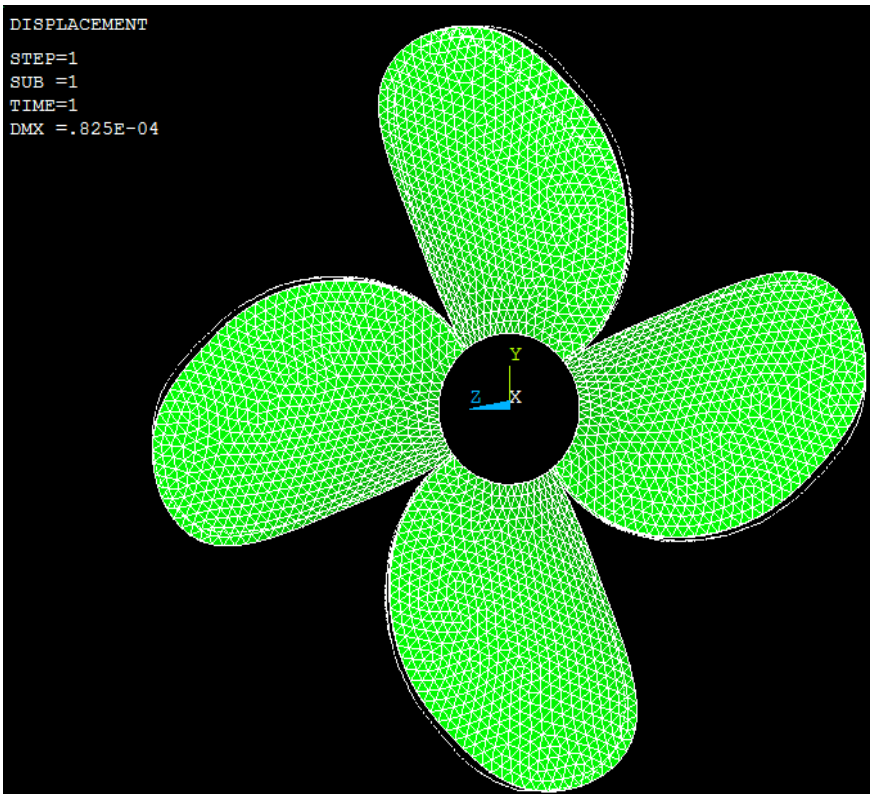


Figure 4.18: Deformed model (mm) of metallic propeller

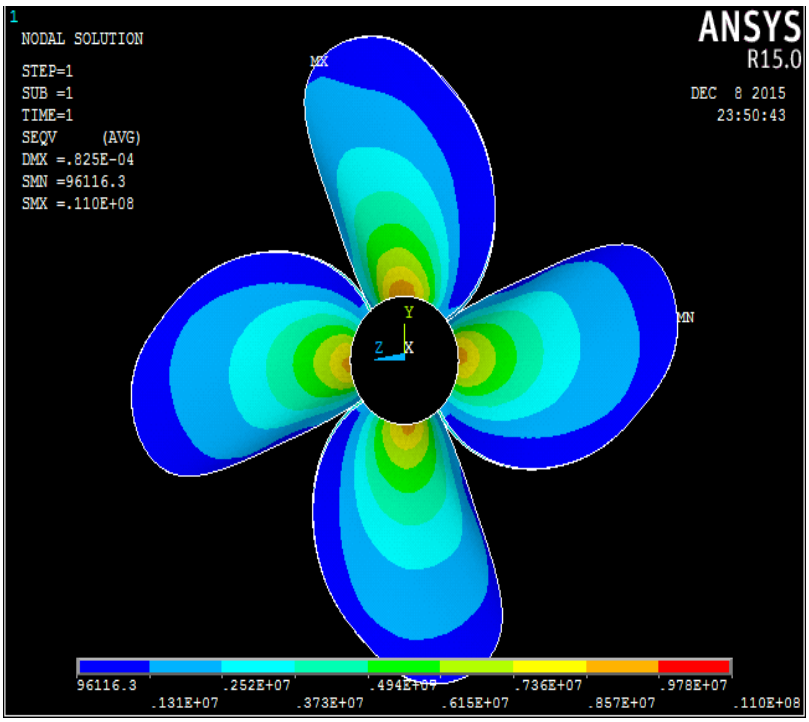


Figure 4.19: von Mises Stress (MPa) of metallic propeller

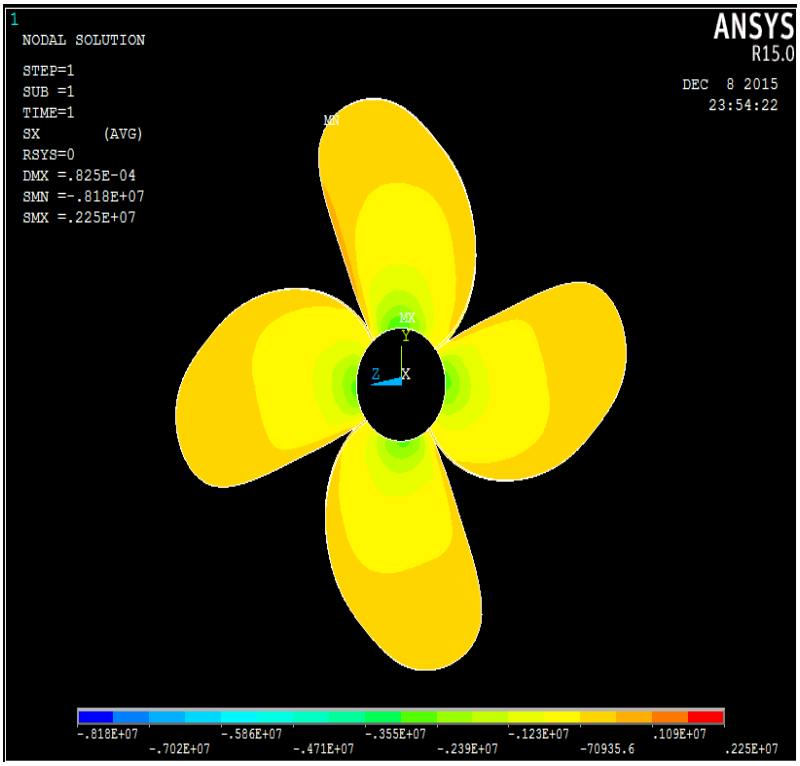


Figure 4.20: X-Component Stress (MPa)

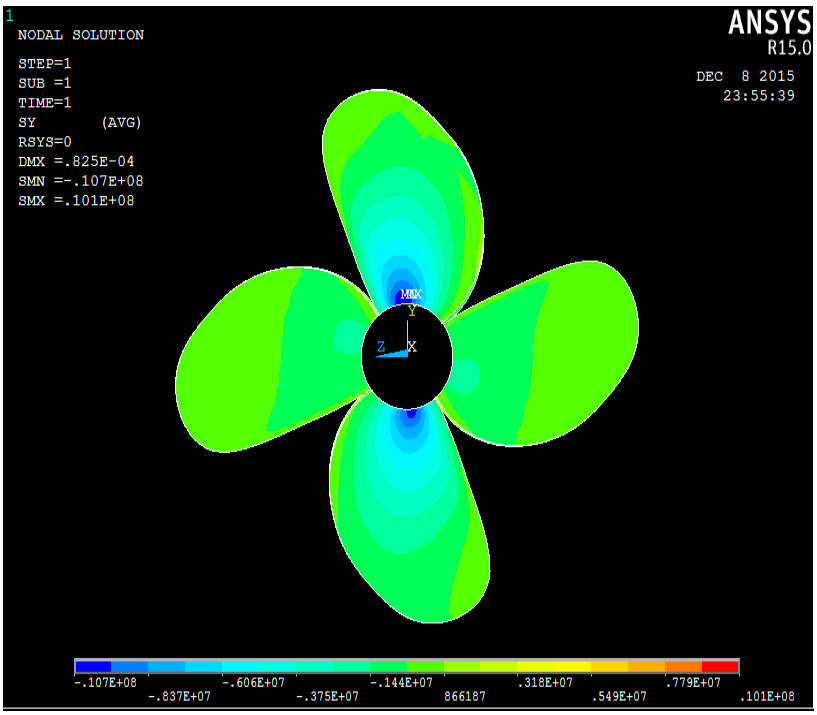


Figure 4.21: Y-Component Stress (MPa)

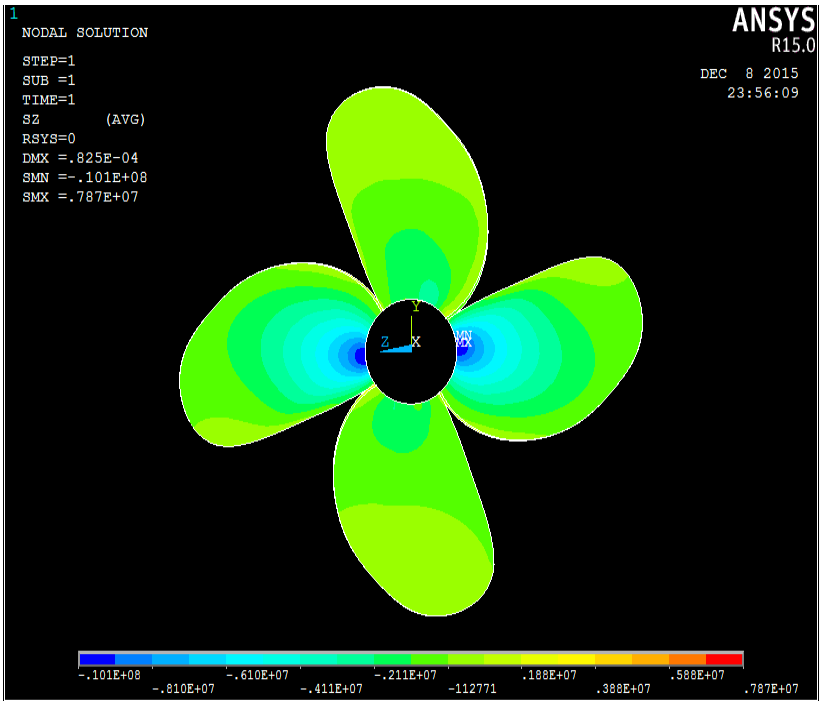


Figure 4.22: Z-Component Stress (MPa)

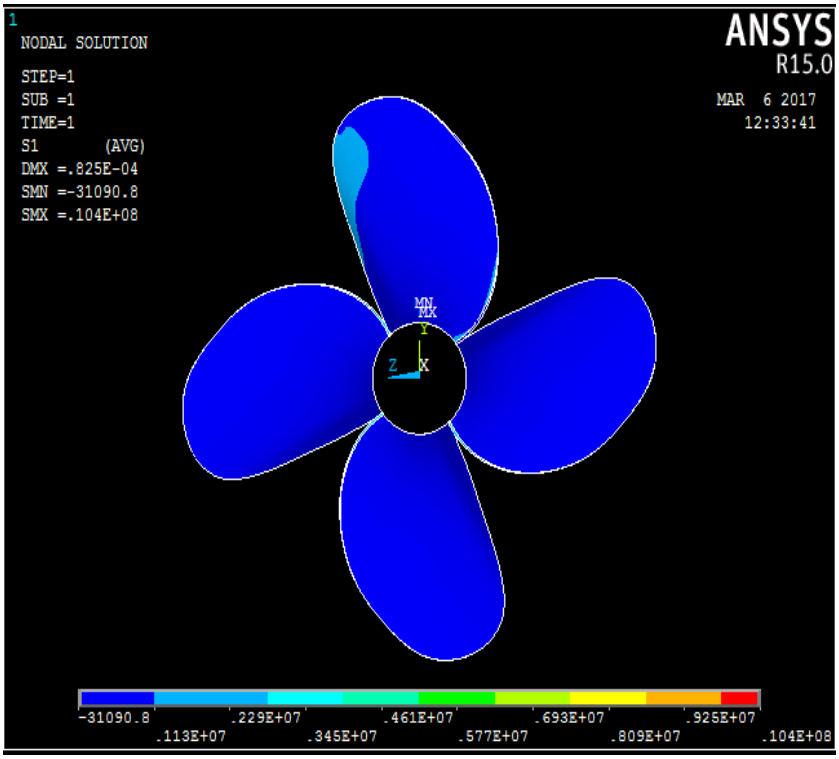


Figure 4.23: I-Principal Stress (MPa)

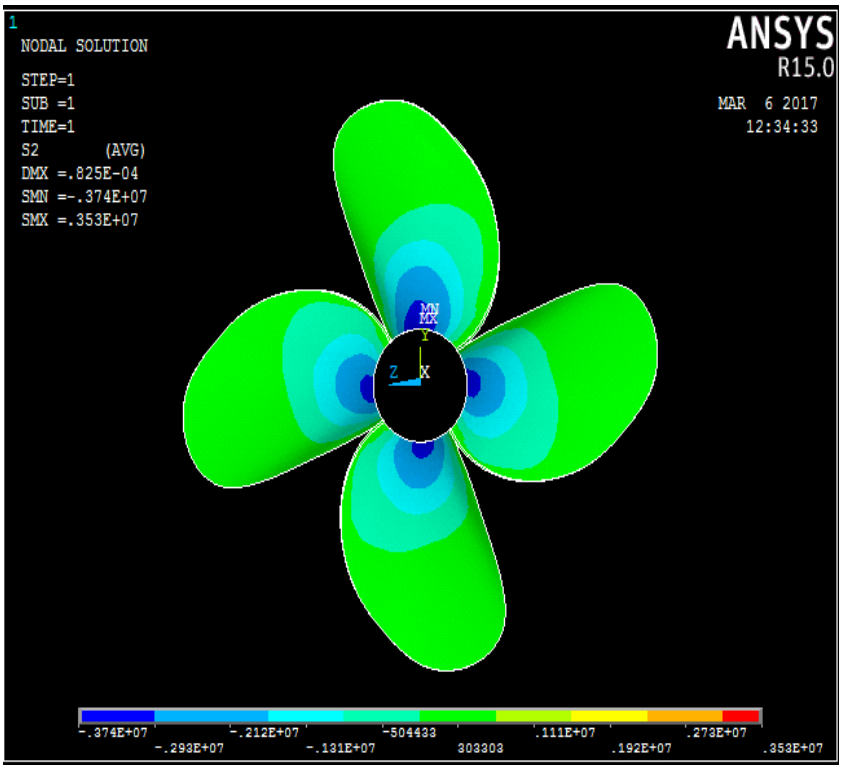


Figure 4.24: II-Principal Stress (MPa)

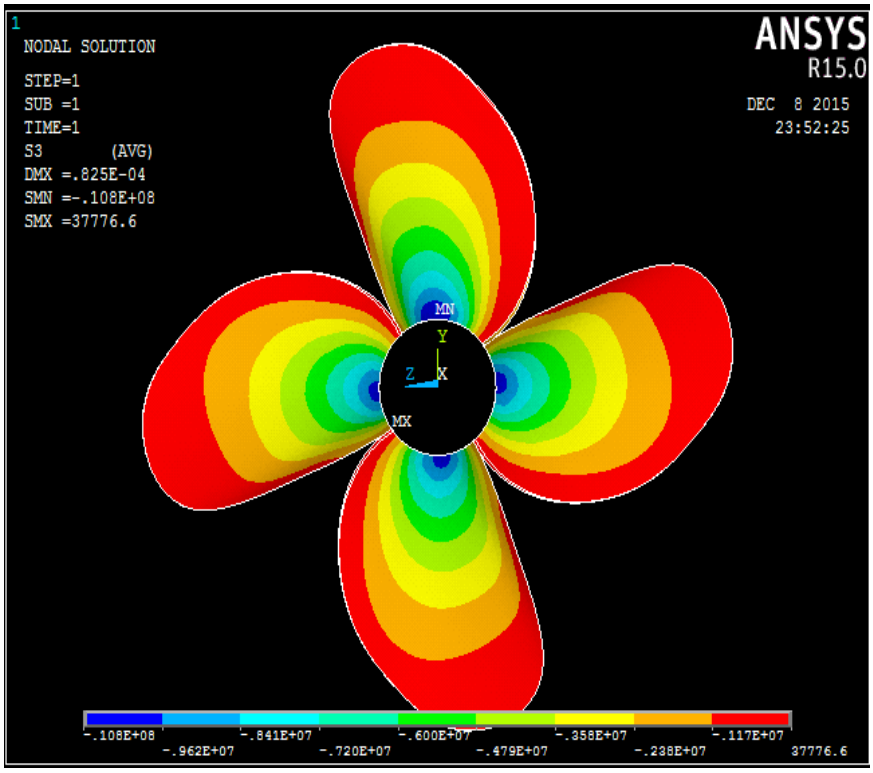


Figure 4.25: III-Principal Stress (MPa)

## 4.11.2 Stress Variations on Composite Propeller Blade

### Linear static analysis of composite propeller

For linear static analysis of composite propeller, E-glass fiber reinforced plastic (GFRP) material is used. For the composite propeller, four cases are considered for static analysis by varying the numbers of layers viz. 2, 4, 6 and 8 to check the bonding strength. Initially, the number of layers is taken as 2, and fiber orientation angle of +45 and -45 with ply stacking sequence $\left(-45°/45°/90°/0°\right)_s$ is given for GFRP material respectively. Interlaminar shear stresses between various layers are plotted. The same procedure is repeated with varying the number of layers, i.e. 4, 6 and 8. The deformation and stress value for E-glass epoxy blade are shown in Table 4.5.

.

Table 4.5: Deformation and Stress values for E-Glass epoxy Blade

| Parameter | E-Glass epoxy |
|---|---|
| Deformation (mm) | 0.327 |
| X-Component (MPa) | 4.870 |
| Y-Component (MPa) | 11.900 |
| Z-Component (MPa) | 9.750 |
| I-Principal stress (MPa) | 13.200 |
| II-Principal-stress (MPa) | 3.760 |
| III-Principal-stress (MPa) | 0.067 |

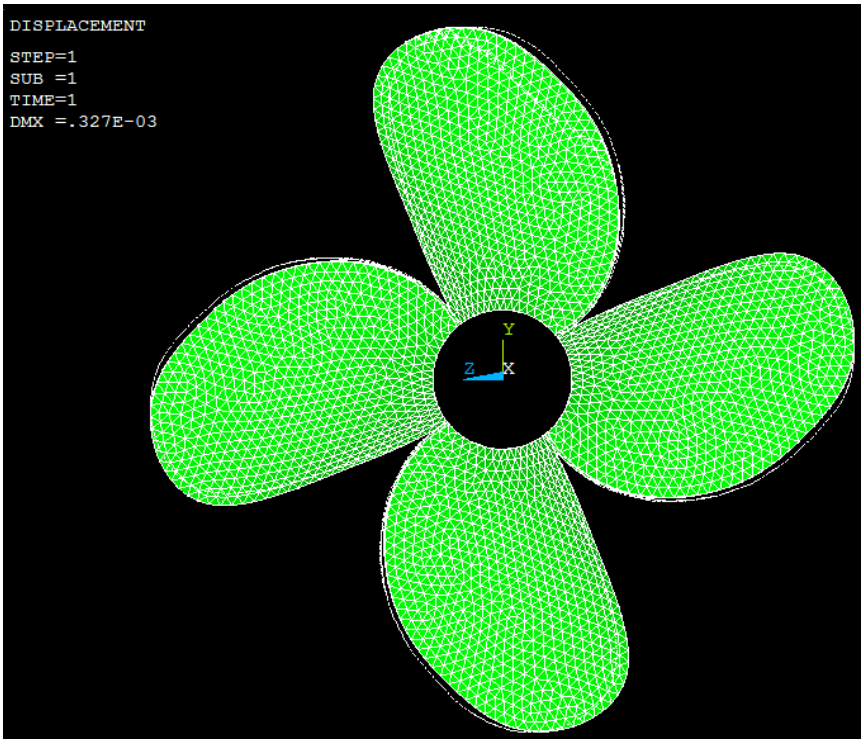


Figure 4.26: Deformed model (mm) of composite propeller

The above figure shows the deformed model of the composite propeller blade.The maximum deformation obtained for the composite propeller blade is 0.327mm, The corresponding component of stresses along X, Y, Z and principal stresses (I, II, III) are represented in the Figure 4.27 to 4.32.

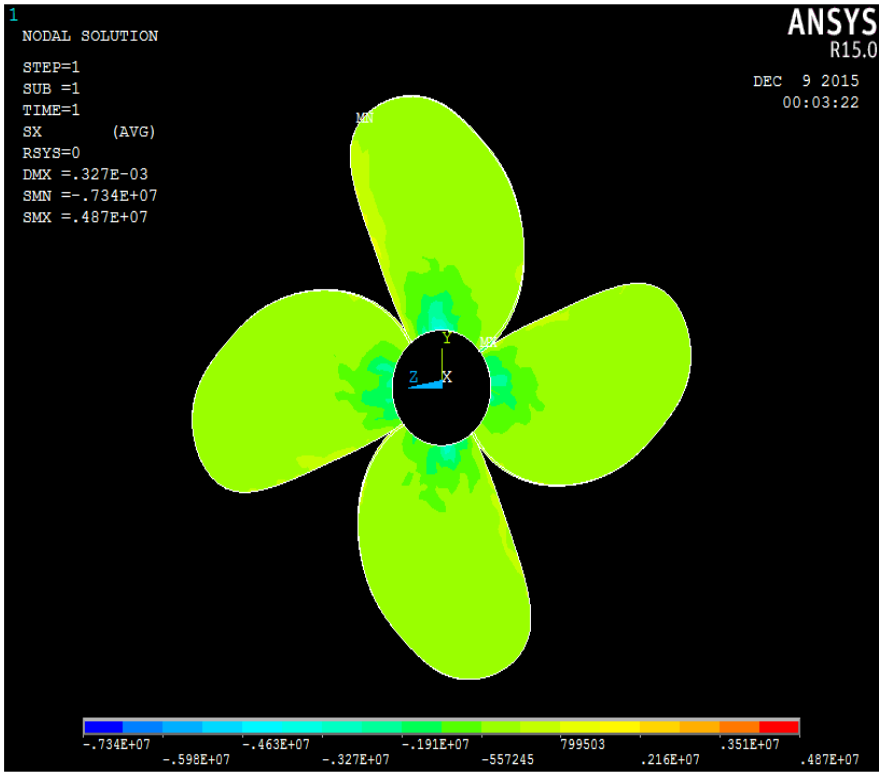


Figure 4.27: X-Component Stress (MPa) of composite propeller

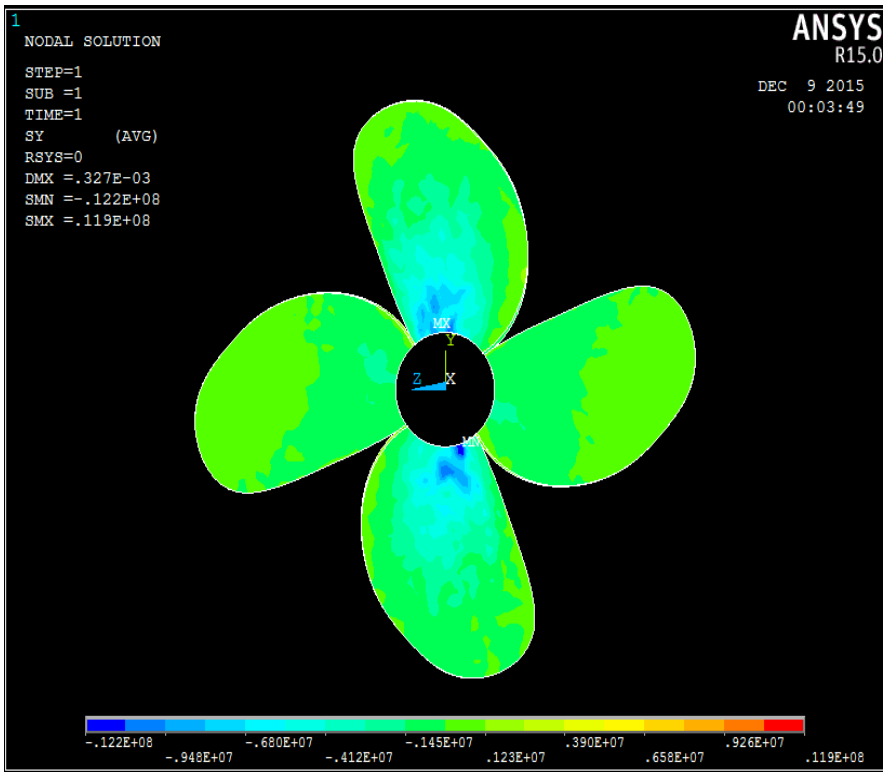


Figure 4.28: Y-Component Stress (MPa) of composite propeller

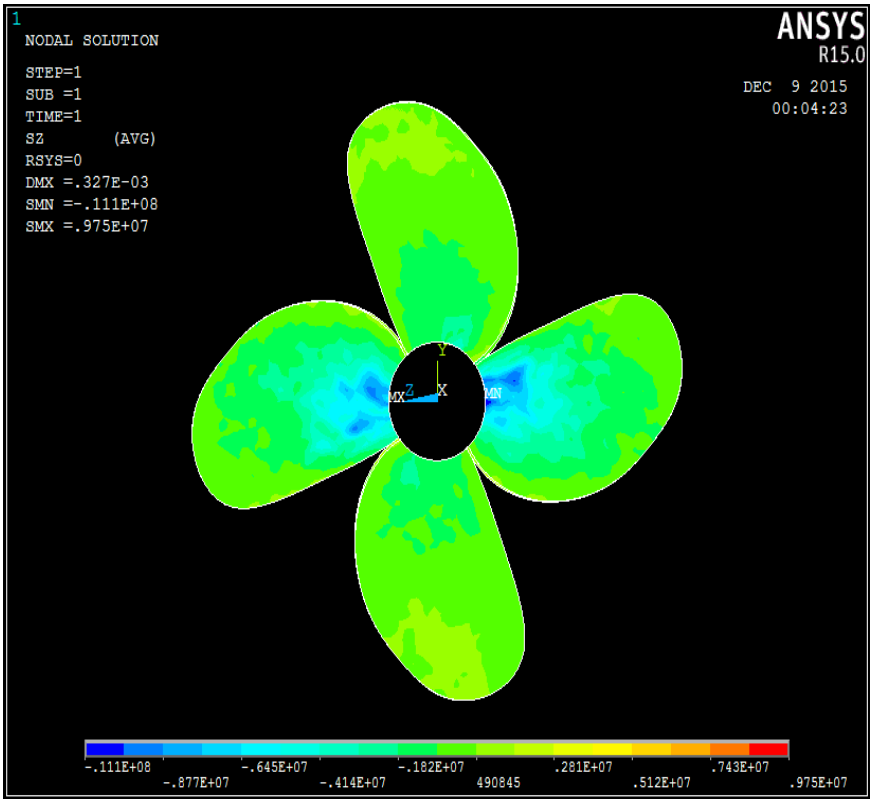


Figure 4.29: Z-Component Stress (MPa) of composite propeller

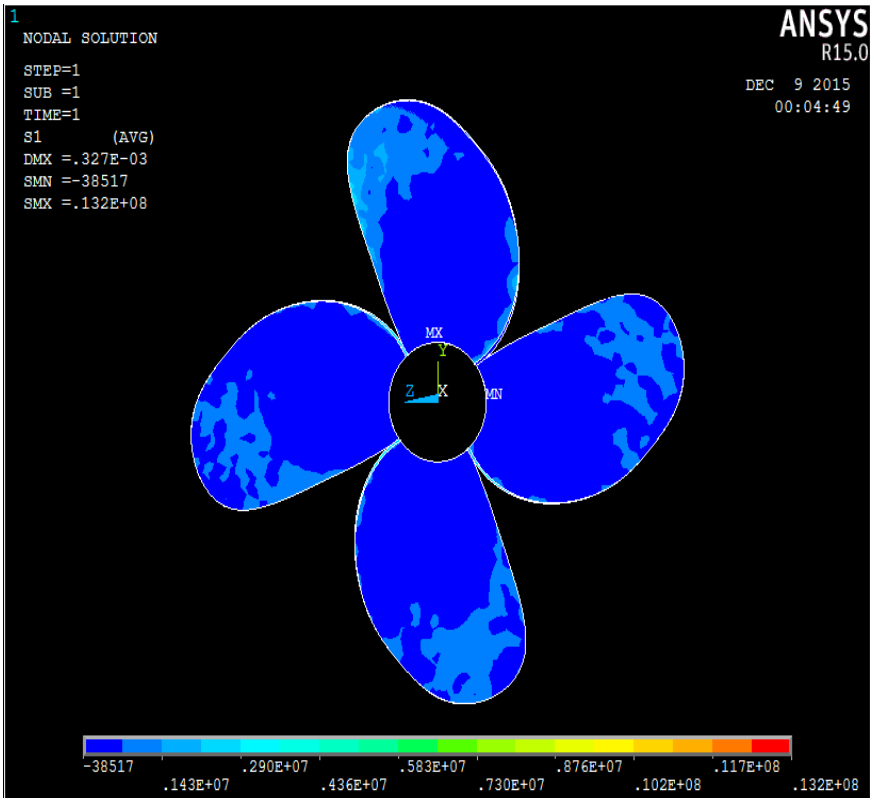


Figure 4.30: I-Principal Stress (MPa) of composite propeller

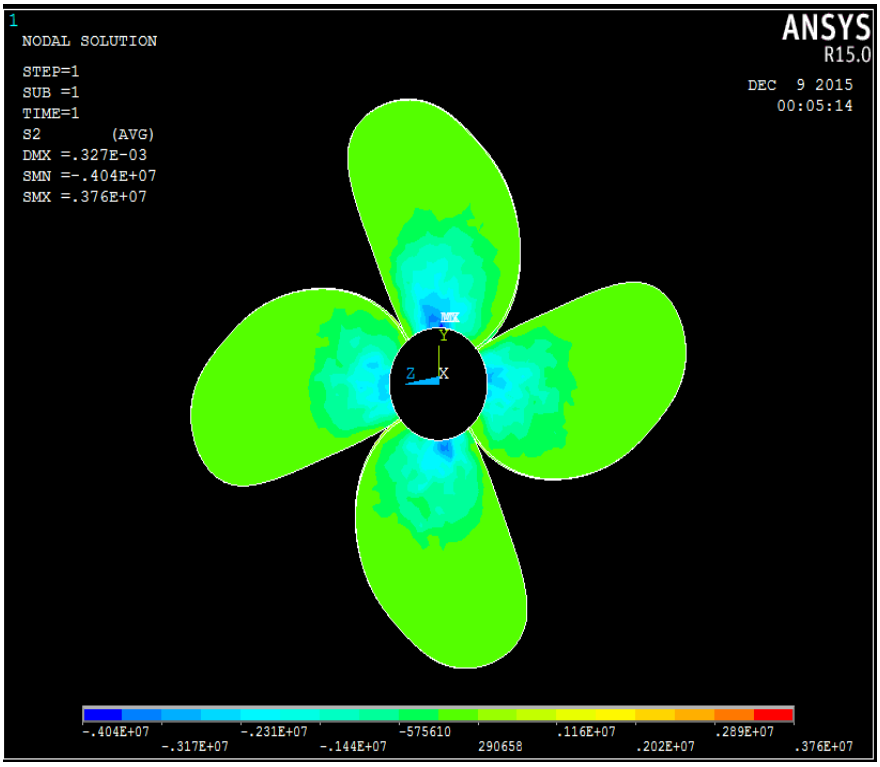


Figure 4.31: II-Principal Stress (MPa) of composite propeller

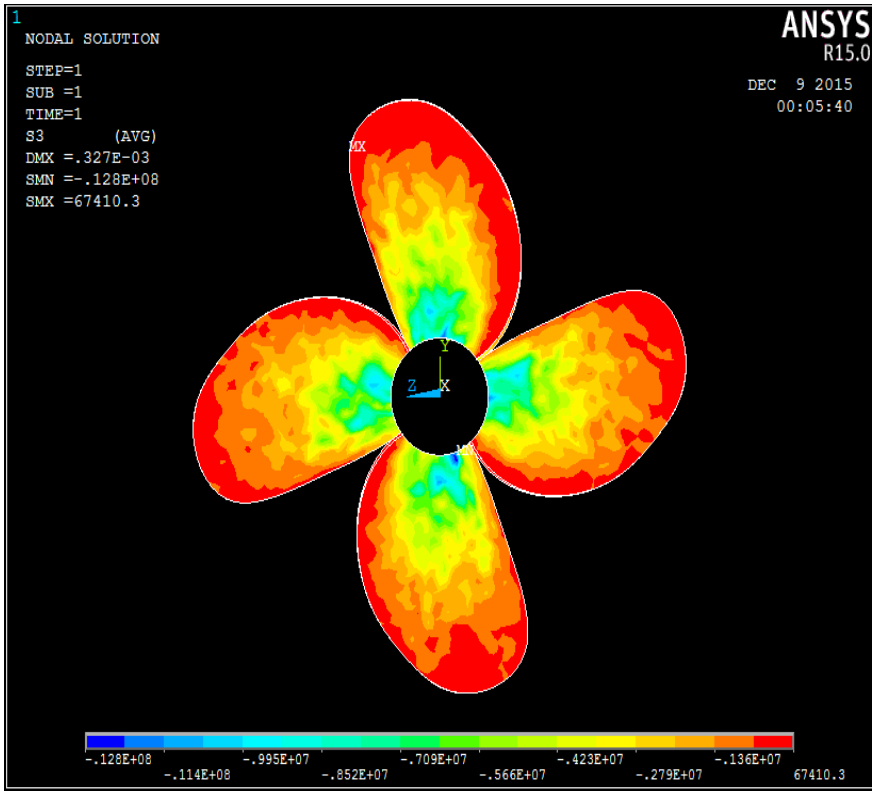


Figure 4.32: III-Principal Stress (MPa) of composite propeller

The interlaminar shear stresses for 2, 4, 6 and 8 layers are represented in Figures 4.33 through 4.36.

Table 4.6: Interlaminar stresses for E-Glass epoxy

| Number of layers | XZ-component (MPa) | YZ-component (MPa) |
|---|---|---|
| 2 | 0.478 | 1.140 |
| 4 | 0.478 | 1.140 |
| 6 | 0.669 | 2.110 |
| 8 | 0.669 | 2.110 |

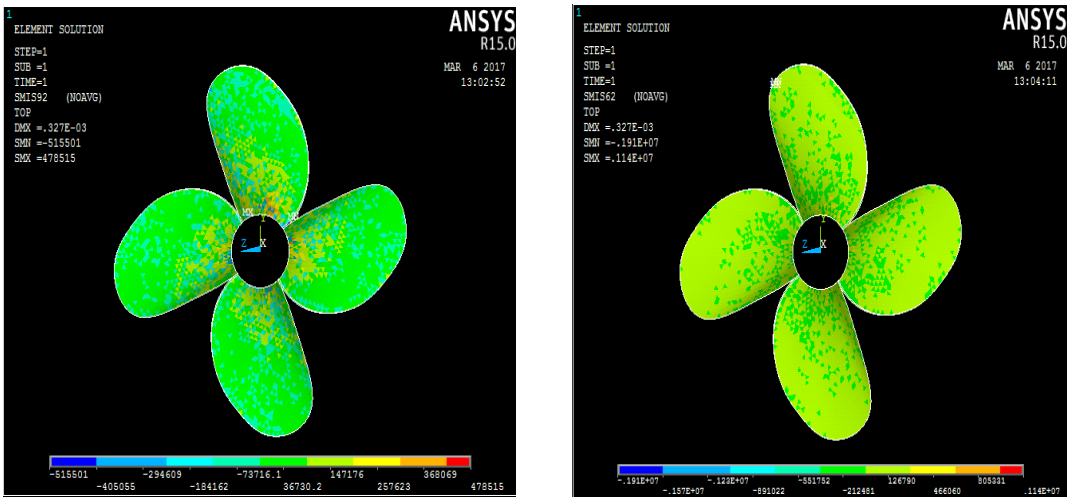


Figure 4.33: Inter laminar shear stress (MPa) for 2 layers along XZ, YZ planes

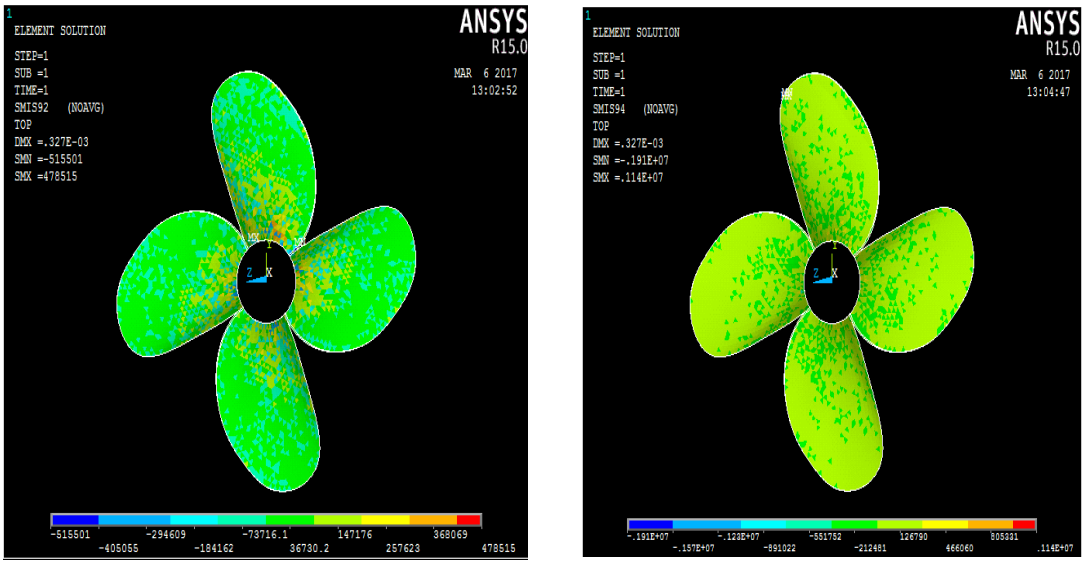


Figure 4.34: Inter laminar shear stress(MPa) for 4 layers along XZ, YZ planes

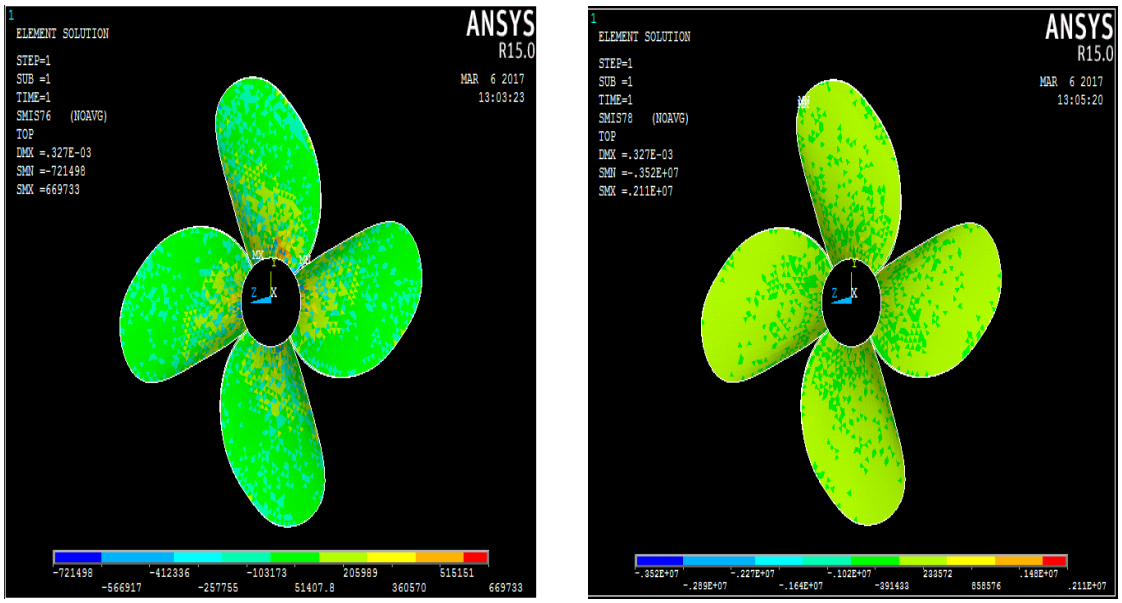


Figure 4.35: Inter laminar shear stress (MPa) for 6 layers along XZ, YZ planes

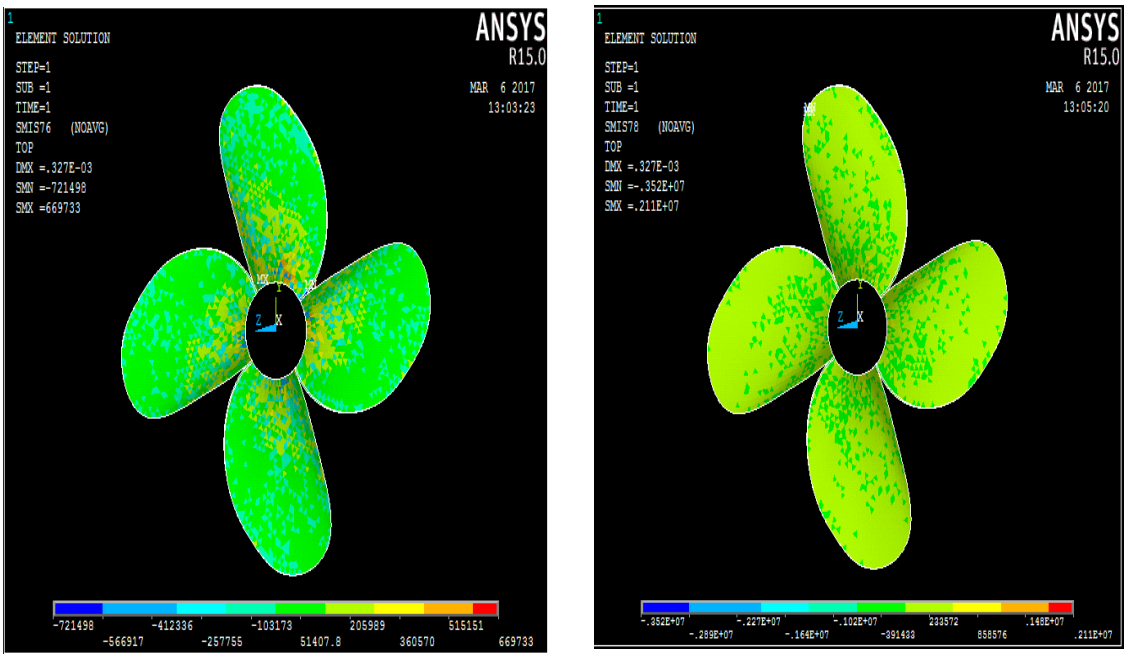


Figure 4.36: Interlaminar shear stress (MPa) for 6 layers along XZ, YZ planes

## 4.12 Discussions

Static analysis is performed on both metallic and composite propellers for pressure loading obtained from CFD analysis, for composite with given lay-up sequence $[-45°/45°/90°/0°]_S$ [136] and material identification. Maximum deflection and stress obtained on Aluminium propeller are 0.082 mm and 11MPa, for the composite propeller is

0.327 mm at the tip as shown in Figure 4.20, to 4.32.The interlaminar shear stress for composite are determined along XZ and YZ planes. The maximum interlaminar shear stress was found to be 2.110 MPa developed along YZ planes shown in Figure 4.35.

### 4.12.1 Results for Free Vibration Analysis

This present chapter deals with the results of the analysis of the vibration characteristics of a homogeneous and fiber reinforced plastic material based pre-twisted propeller blade using the finite element formulation as mentioned in the previous chapter. A set of finite elements consisting of shell elements is used to develop the finite element procedure. The first order shear deformation theory is used to develop the model for twisted blade taking into account for the transverse shear deformation and rotary inertia. The modal characteristics and its corresponding mode shapes for both conventional material Aluminium and E-glass epoxy material are carried out. The numerical results in this chapter are presented as follows:

- Convergence study
- Comparison with previous studies
- Experimental procedure for modal analysis
- Experimental and numerical results

**Convergence study**

The convergence study is done for first three lowest non- dimensional frequencies of free vibration of the twisted isotropic cantilever blade with a pitch angle of 15° for various mesh divisions shown in the Table 4.6. Similarly, the convergence study is then performed for non-dimensional fundamental frequencies of composite twisted cantilever blade for the same pitchangle with different mesh divisions shown in the Table 4.8. From the results plotted in the Table 4.6 and Table 4.7, it is observed that for a mesh division of 10x10 shows the good convergence of the numerical solution for the free vibration of the twisted cantilever blade and this mesh is carried out for further study to idealize the blade in the subsequent vibration analysis.

Table 4.7: Convergence of non-dimensional fundamental frequencies of free vibration of isotropic twisted blades

Span of the blade =0.14455m; Chord of the blade =0.09455m, Thickness of the blade=0.01212m; E=69 GPa, $\upsilon$ =0.334, $\rho$ =2.7 g/cm$^3$ ,Non-dimensional frequency $\varpi = \omega a^2(\sqrt{\rho h / D})$

| Mesh division | Angle of twist | Pitch Angle | Non-dimensional frequency | | | |
|---|---|---|---|---|---|---|
| | | | 1st frequency | 2nd frequency | 3rd Frequency | 4th frequency |
| 4x4 | 0° | 15° | 3.509 | 12.041 | 21.594 | 34.586 |
| 8x8 | | | 3.470 | 11.155 | 19.851 | 23.739 |
| 10x10 | | | 3.447 | 10.993 | 19.274 | 21.316 |
| 20x20 | | | 3.447 | 10.993 | 19.274 | 21.316 |
| 40x40 | | | 3.447 | 10.993 | 19.274 | 21.316 |

Table 4.8: Convergence of non-dimensional fundamental frequencies of free vibration of E-glass epoxy twisted blade with $[-45/45/90/0]_s$ lamination

$E_{11}$=39 GPa, $E_{22}$=8.6 GPa,$G_{12}$=3.8 GPa, $\upsilon_{12}$ =0.28, $\rho$ = 2.1 g/cm$^3$ , Non-dimensional frequency $\varpi = \omega a^2(\sqrt{\rho h / D})$

| Mesh division | Angle of twist | Pitch angle | Non-dimensional frequency | | | |
|---|---|---|---|---|---|---|
| | | | 1st frequency | 2ndfrequency | 3rd frequency | 4th frequency |
| 4x4 | 0° | 15° | 0.113 | 0.813 | 0.915 | 0.978 |
| 8x8 | | | 0.112 | 0.721 | 0.898 | 0.905 |
| 10x10 | | | 0.112 | 0.710 | 0.895 | 0.896 |
| 20x20 | | | 0.112 | 0.710 | 0.895 | 0.896 |
| 40x40 | | | 0.112 | 0.710 | 0.895 | 0.896 |

**Comparison with previous studies**

With the convergence, a study performed the efficiency and accuracy of the present finite element formulation is established by validating with previous studies. The first six lowest non-dimensional natural frequency parameters of isotropic pre-twisted plate type blade obtained by present formulation is compared with those obtained by Nabi and Ganeshan [137] using triangular type element and Kee and Kim [138] using shell type element shown in Table 4.9. The study is concerned with untwisted and twisted plate type with an angle of 0°,30°,45° where the symbols B, T, CB, EB represents the bending, torsion,

chordwise bending and edgewise bending mode shapes. The present results show good agreement with the previous studies mentioned in the literature.

**Vibration characteristics of initially twisted rotating shell type composite blades**

This case study is designed to demonstrate some aspects of the effect of centrifugal action and Coriolis acceleration on the initially twisted shell type structures. Since the vibration analysis of rotating composite blade is the main purpose of this study, from the application point of view, the blades are key structural units in marine, turbo-machinery of the aeronautical and aerospace industries. In this work, initially the present finite element formulation is validated for free vibration of a twisted laminated plate Figure 4.39 For a laminated plate with ply sequence $(90^\circ/90^\circ/0^\circ)$ Figure 4.40 are done by comparing the non-dimensional fundamental frequencies of vibration of graphite epoxy cantilever plates with the results presented by Kee and Kim [138], Jensen and Crawley [139] , as shown in Table 4.11.There exists a good agreement between the results obtained by the present formulation and those presented by the previous investigations.

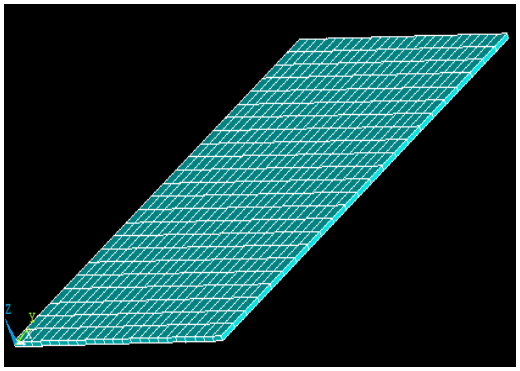

Figure 4.37: Flat type blade with $\phi = 0^0$

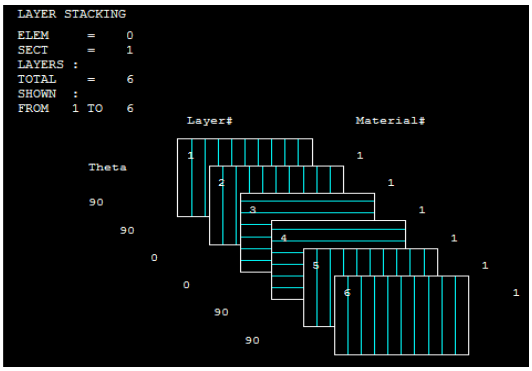


Figure 4.38: Stacking sequence of blade $(90^\circ/90^\circ/0^\circ)_s$

Table 4.9: Comparison of frequency parameters ($\lambda$) of the initially twisted plate type Metallic blade, $\varpi = \omega a^2(\sqrt{\rho h / D})$

| Phi ($\phi°$) | Mode | Present study ($\lambda$) | Reference($\lambda$) [138] | Reference($\lambda$) [137] |
|---|---|---|---|---|
| 0 | 1B | 3.51 | 3.49 | 3.46 |
| | 2B | 21.70 | 22.0 | 21.44 |
| | 1T | 8.47 | 8.51 | 8.53 |
| | 1EB | 44.38 | 45.62 | 46.14 |
| | 1CB | 27.40 | 27.33 | 27.05 |
| 30 | 1B | 3.651 | 3.42 | 3.41 |
| | 2B | 20.62 | 19.51 | 18.88 |
| | 1T | 16.66 | 14.43 | 16.88 |
| | 1EB | 49.70 | 49.48 | 49.60 |
| | 1CB | 27.24 | 27.41 | 27.98 |
| 45 | 1B | 3.08 | 3.35 | 3.36 |
| | 2B | 16.10 | 17.22 | 16.51 |
| | 1T | 19.75 | 20.45 | 22.31 |
| | 1EB | 47.97 | 52.74 | 54.00 |
| | 1CB | 29.42 | 28.76 | 30.40 |

Table 4.10: Comparison of frequency parameters ($\lambda$) of the initially twisted plate type blade (for $\phi = 0^\circ$)

| Phi ($\phi°$) | Mode | Present study | | Reference [138] | Reference [137] |
|---|---|---|---|---|---|
| | | Matlab | ANSYS | | |
| 0 | 1B | 3.475 | 3.51 | 3.49 | 3.46 |
| | 2B | 21.754 | 21.70 | 22.0 | 21.44 |
| | 1T | 8.521 | 8.47 | 8.51 | 8.53 |
| | 1EB | 44.380 | 44.38 | 45.62 | 46.14 |
| | 1CB | 27.556 | 27.40 | 27.33 | 27.05 |

A comparison has been made for frequency parameters ($\lambda$) with the established results by Nabi and Ganeshan [137] and Kee and Kim [138] shown in Table 4.9

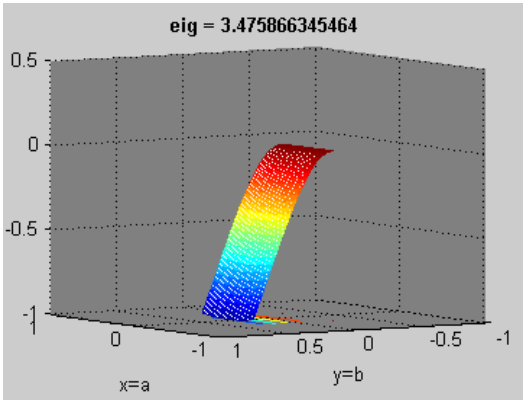


(a):I[st] Bending Mode shape

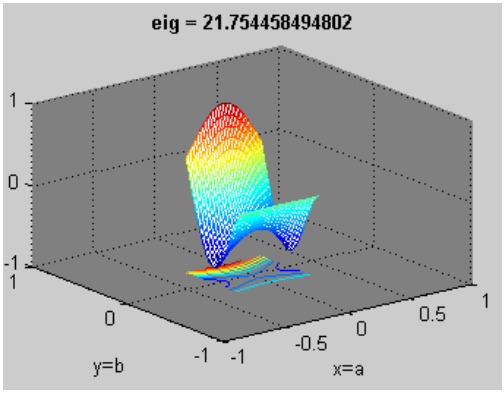


(b): II[nd] Bending Mode shape

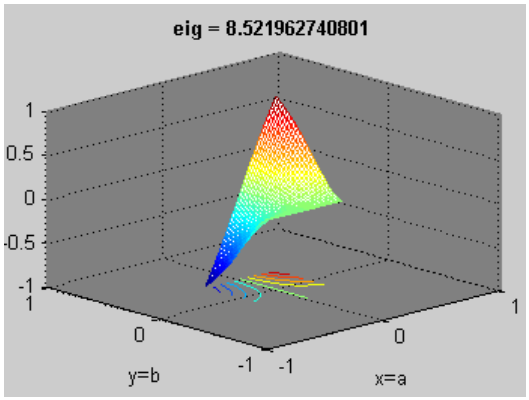


(C): I[st] Twisting mode shape

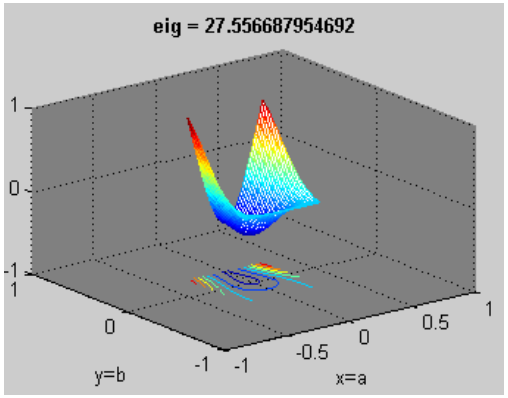


(d): Chord-wise Bending mode shape

Figure 4.39: Mode shapes of MS type Blade ( $\phi = 0^0$ )

The first four mode shapes for plate type metal (Mild Steel) blade is shown in Figure 4.39

Table 4.11: Non-dimensional frequencies of laminated composite plates upon different stacking sequences

| Stacking sequence | Mode no | Present | Reference[138] | Reference[139] FEM Result |
|---|---|---|---|---|
| $[90/90/0]_s$ | 1B | 3.80 | 3.97 | 3.8 |
| | 2B | 23.91 | 25.7 | 23.9 |
| | 1T | 33.76 | 35.9 | 35.1 |
| $[30/30/0]_s$ | 1B | 6.87 | 6.7 | 6.3 |
| | 2B | 37.87 | 40.6 | 37.3 |
| | 1T | 61.63 | 61.5 | 56.9 |
| $[45/45/0]_s$ | 1B | 5.68 | 5.1 | 4.9 |
| | 2B | 32.89 | 32.6 | 30.1 |
| | 1T | 50.29 | 52.6 | 49.4 |

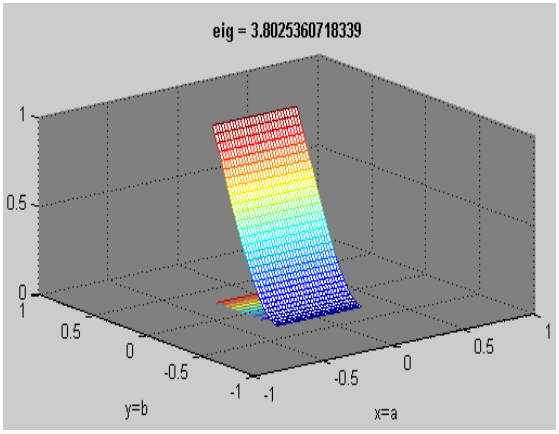


(a): I[st] Bending mode shape

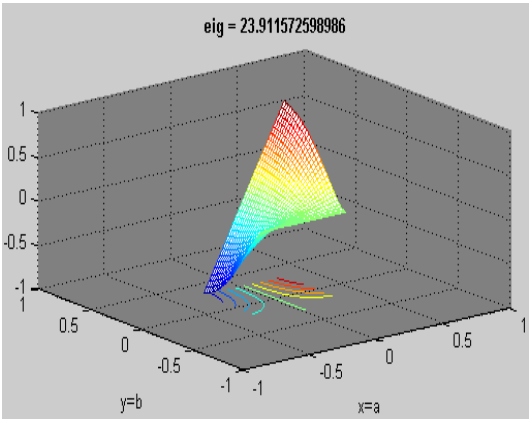


(b): II[nd] Bending mode shape

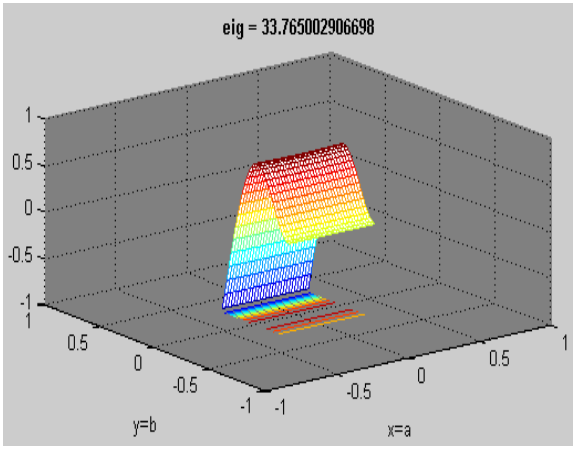


(c) Ist Twisting mode shape

Figure 4.40: Mode shapes for $(90°/90°/0°)_s$ Sequence

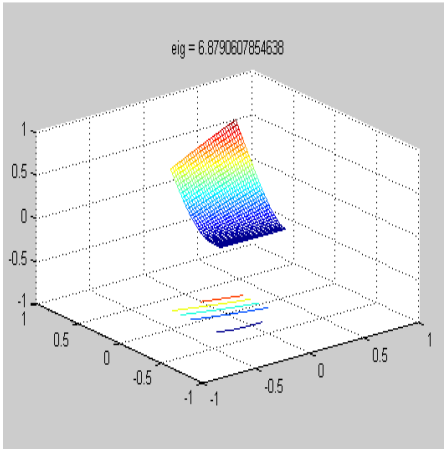


(a): I[st] Bending mode shape

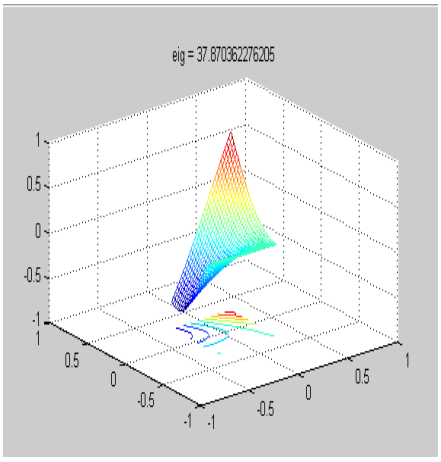


(b): II[nd] Bending mode shape

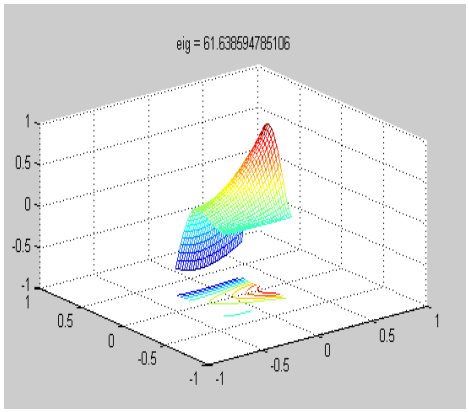


(c) I[st] Twisting mode shape

Figure 4.41: Mode shapes of $(30°/30°/0°)_s$ type Blade

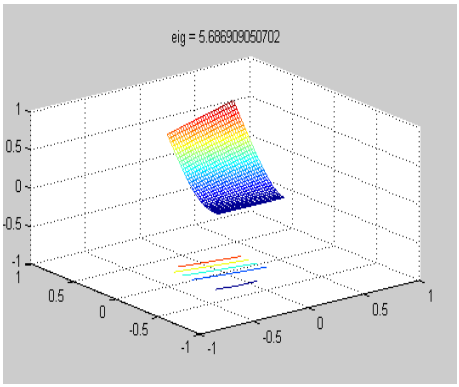


(a): I[st] Bending mode shape

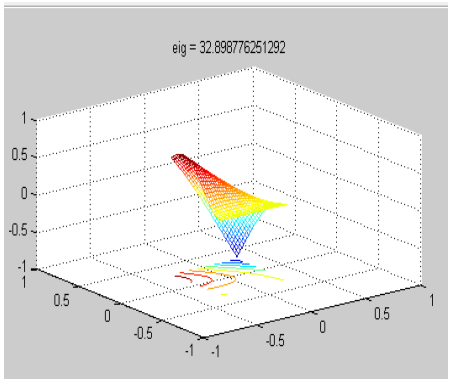


(b): II[nd] Bending mode shape

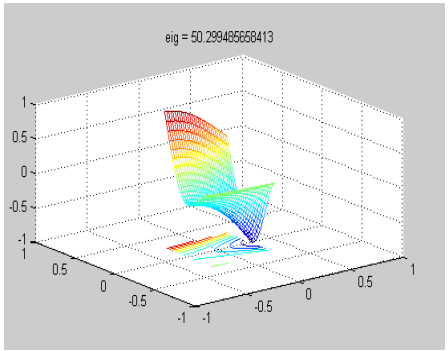


(c) I[st] Twisting mode shape

Figure 4.42: Mode shapes of $(45°/45°/0°)_s$ Composite Blade

As the stacking sequence changes from Figure 4.39 to 4.41, it is noticed that the mode shape changes considerably. To validate the formulation for further studies treating, the

blade to be a moderately thick open cylindrical shell, that includes the transverse shear deformation and rotary inertia, and is oriented arbitrarily with respect to the axis of rotation, to consider the effects of disc radius and setting the angle. For a thick shell, the effect of the transverse shear deformation, as well as rotary inertia is taken into consideration. Generally, Reissener-Mindlin assumptions have been adopted in the development of such elements which enables shell elements to consider the effect of transverse shear deformation in a structure in an average sense by allowing a constant shear strain distribution across the thickness. Although this distribution is not similar to the actual strain field in a plate or shell, it helps to account for the effect of transverse shear force in the analysis of the structure. It has been shown that the accuracy of the frequency is improved by the rotatory inertia terms in the mass matrix for thick shells as well as the inclusion of transverse shear effects in the stiffness matrix.

Kee and Kim[138] used a degenerated shell element based on Reissner–Mindlin's assumptions for finding out the vibration analysis of a rotating composite blade. Leissa and Lee[100] used Shallow shell theory and the Ritz method to determine the frequencies and mode shapes of turbomachinery blades having both camber and twist, rotating with non-zero angles of attack, Olson and Lindberg[140] used doubly-curved shallow shell element of arbitrary triangular shape which includes thickness variations for dynamic analysis of arbitrary shallow shell structures.

Thus, based on the concept of the degenerated shell element with the Reissner–Mindlin's assumptions, the finite element method is used for solving the governing equations. In the numerical study, the effects of various parameters are investigated; initial twisting angles, thickness to radius ratios, layer lamination and fiber Orientation of composite blades. This comparative study also indicates good agreement between the results obtained from the present study and those of Kee and Kim [138], Leissa and Lee[100], Olson and Lindberg[140] shown in the Table 4.12.

Table 4.12: Natural frequencies of open cylindrical shell blade

| Mode No | Present (Hz) | Reference [138] (Hz) | Reference [100] (Hz) | Reference [140] (Hz) | |
|---|---|---|---|---|---|
| | | | | Experimental | Numerical |
| 1 | 80.099 | 85.4 | 85.9 | 85.6 | 86.6 |
| 2 | 130.03 | 139.68 | 137.8 | 134.5 | 139.17 |
| 3 | 247.24 | 251.81 | 248.6 | 259 | 251.30 |
| 4 | 331.72 | 347.77 | 342.9 | 351 | 348.59 |
| 5 | 372.76 | 391.63 | 387.4 | 395 | 393.42 |
| 6 | 581.53 | 564.06 | 531.9 | 531 | 533.37 |
| 7 | 758.99 | 746.84 | 736.6 | 751 | 746.37 |
| 8 | 767.88 | 762.13 | 738.4 | 743 | 752.09 |
| 9 | 815.57 | 792.21 | --- | 790 | 790.1 |
| 10 | 878.92 | 831.04 | --- | 809 | 813.8 |

## 4.13 Experimental procedure for modal analysis

In order to confirm the theoretical formulation developed for the propeller blade, the experimental analysis is carried out at DRDO, Hyderabad, INDIA for the current investigation. For experimental analysis an experimental set-up has been developed in order to measure the vibrational response of cantilever type propeller blade made of both Aluminium and composite materials. The details of the experimental set-up and experimental procedure along with test results are given below.

### 4.13.1 Experimental and Numerical Results

With the validation of the previous studies, further studies are extended to find out the modal characteristics of propeller blade made of conventional material and composite material. The Eigenvalue problem of propeller blade employs a number of modal equations with a finite number of degrees of freedom. Under non-damping and non-external load condition fixed body analysis was carried out to determine the natural frequencies of the blade at its end of the root (hub) with all degrees of freedom are constrained. An aluminium single bladed propeller is taken into consideration for free vibration analysis (Figure 4.43). At the root of the propeller blade all degrees of freedom were constrained as shown by Figure 4.44. The cantilever blade with a span of length 144.5mm, chord 94.55mm, root thickness 12.2mm and tip

thickness 1.1mm, modulus of elasticity E=69GPa,Poisson's ratio $\upsilon = 0.334$, and density $\rho$ =2700kg/m3 are considered for numerical analysis. The first six natural frequencies corresponding first bending, first twisting, second bending, second twisting, chord wise and edgewise bending are listed and compared for cantilever conditions Table 4.14. The corresponding lowest first three fundamental mode shapes for blade are plotted. Further, the lowest first three non- dimensional frequencies for shell and experimental results are presented in Table 4.15: First Mode shape of Aluminium blade, is shown in Figure 4.49.Similarly, results are obtained for an E-glass epoxy blade having the same geometry as that of aluminium blade.

## 4.13.2 Fabrication and Experimentation of Propeller blade

The datum points for the blades (Aluminium and E-glass epoxy) were generated. The surface was made touching all the generated points (Figure 4.45). After modelling the blades and hub they are manufactured. Experiments were performed to find out the natural frequencies and mode shapes. Three accelerometers are used to receive the signal from the blade. The properties of the accelerometers are illustrated in Table 4.13.

Table 4.13: Properties of Accelerometers

| Accelerometer | Parameter |
|---|---|
| Quantity | 3 |
| Weight of accelerometer 1 in gm | 10 |
| Weight of accelerometer 2 in gm | 13 |
| Weight of accelerometer 3 in gm | 12 |
| Type of accelerometer | Integrated Circuit Piezoelectric (ICP) |
| Sensitivity of Accelerometer 1 | 97.8 |
| Sensitivity of Accelerometer 2 | 98.3 |
| Sensitivity of Accelerometer 3 | 99.6 |

The mass of accelerometers are very less compared to the mass of the blades. The vibration amplitudes due to masses of accelerometers have negligible effect. The accelerometers were placed on the surface of the blades. Accelerometer number one was placed on tip of the blade. The second accelerometer was positioned at the mid chord. The third accelerometer was positioned arbitrarily at different locations on the surface of the blade. With the help of a modal hammer a tap was applied on the blade. The vibration responses were recorded with the help of FFT analyser. The corresponding frequency response functions (FRF) are shown in Figures 4.46. The x-coordinate represent the frequency and Y-coordinate represents the amplitude of motion.

The time degrees of freedom(time history) and the synthesized graph were also recorded and presented in Figure 4.46 through 4.47.After placing all the accelerometers at desired locations the time degree of freedom for stabilisation was recorded (Figure 4.48).This gives the final response(the combined output response of all accelerometers) of the combined accelerometer. The fabricated model of the E-glass epoxy blade is shown in figure 4.51.Same procedure as that of metallic propeller blade were repeated for E-glass epoxy blade to find out the vibration response. The results are presented in Figures 4.52 to 4.54.The mode shape of the E-glass epoxy blade is shown in the figure 4.55.

Figure 4.43: Fabricated model of Aluminium single bladed propeller

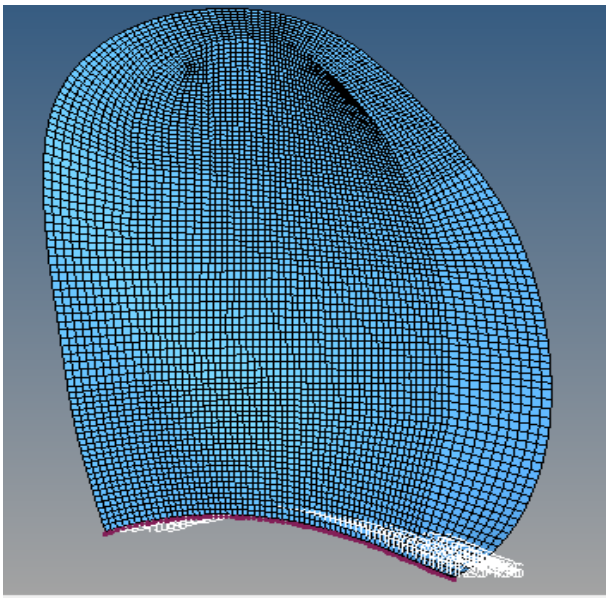

Figure 4.44: Single Surface Propeller with root constrained to all degrees of freedom

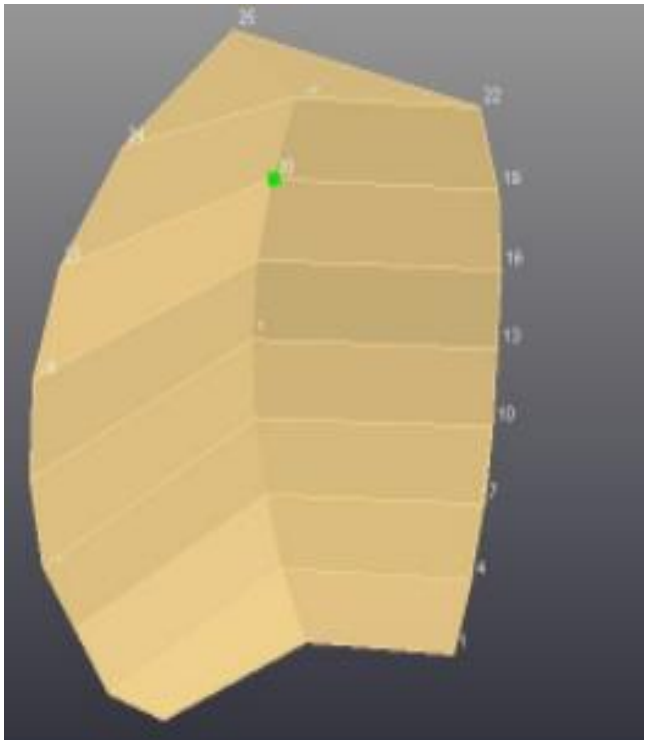

Figure 4.45: Surface generation through coordinates

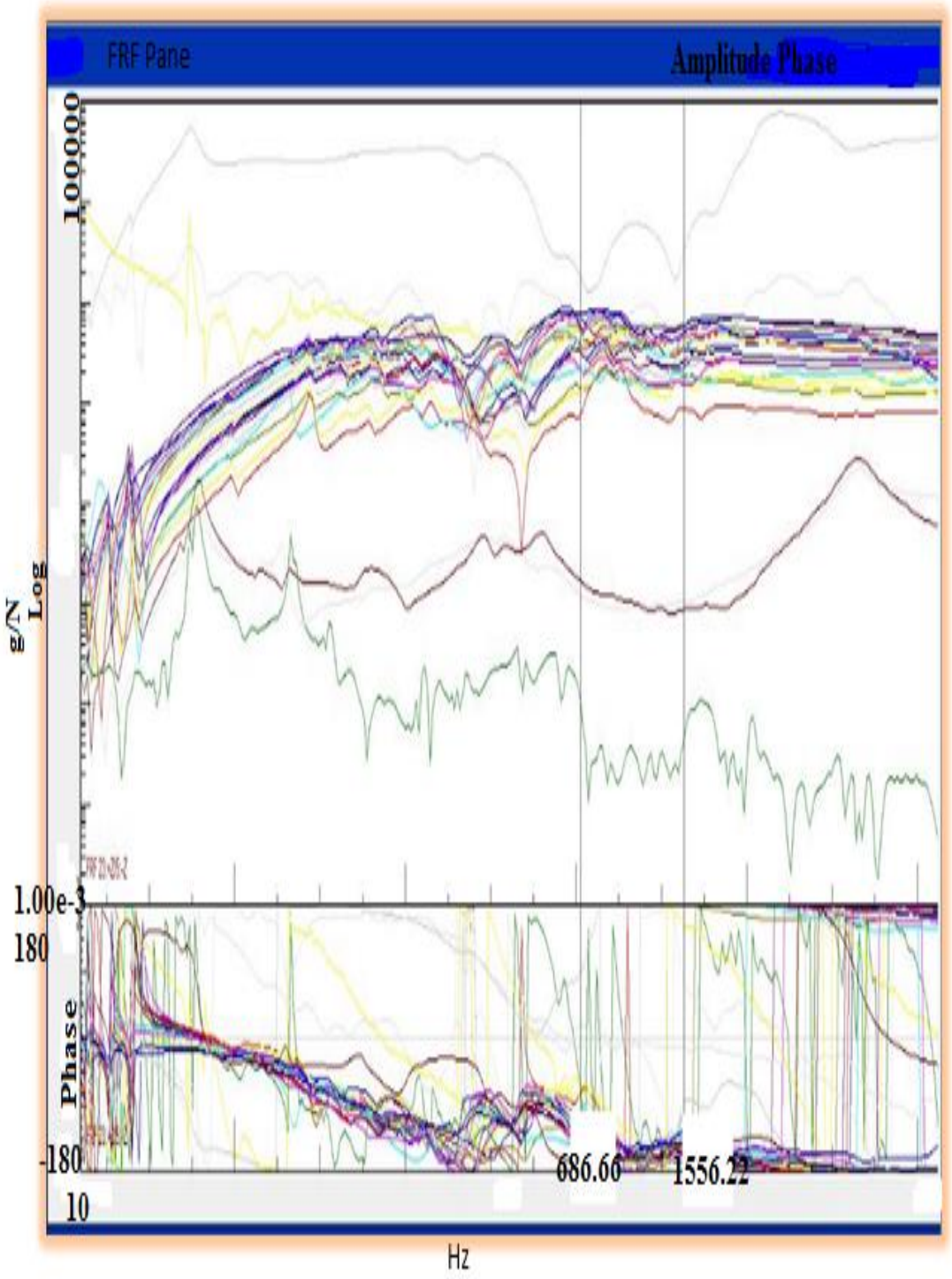


Figure 4.46: Modal data selection for all control points

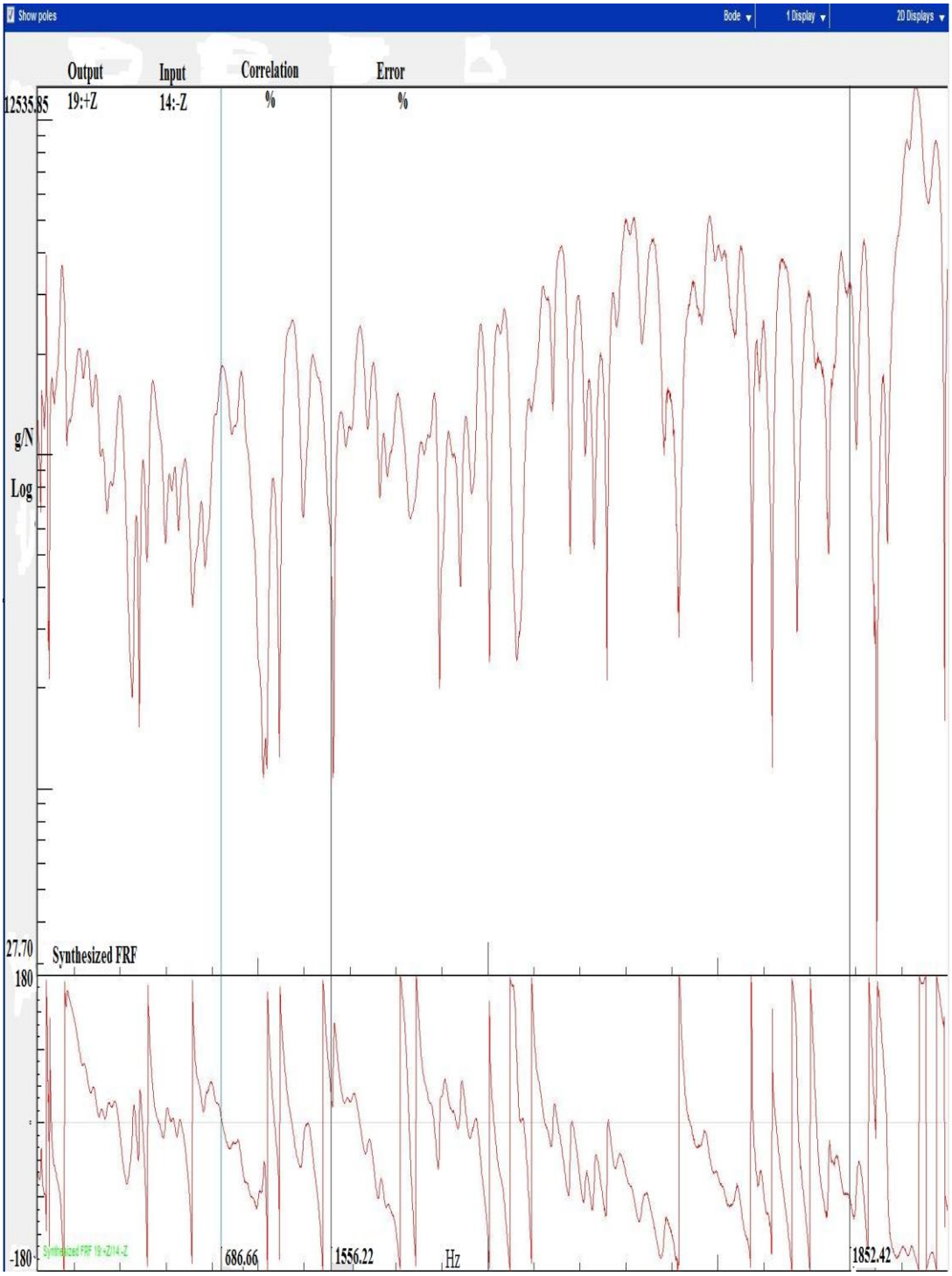


Figure 4.47: Final synthesized FRF

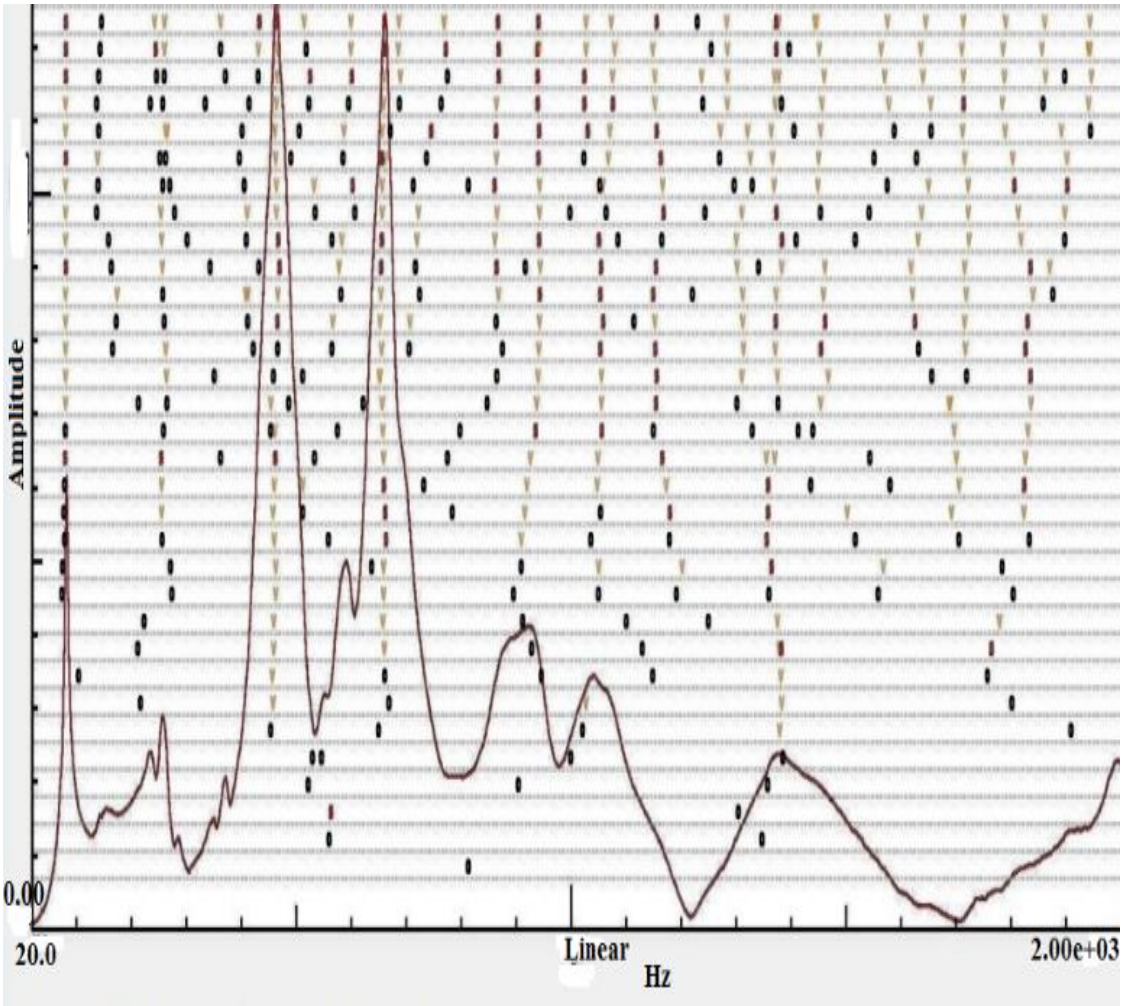


Figure 4.48: Time Degrees of freedom for Stabilization

Table 4.14: Free vibrational-analysis of Aluminium propeller blade

| Mode Number | Theoretical (Hz) | Numerical result (Hz) | | Experimental (Hz) |
|---|---|---|---|---|
| | | ANSYS | Optistruct software | |
| 1 | 487.09 | 671.92 | 676 | 686.662 |
| 2 | 1551.62 | 1527.74 | 1520 | 1556.226 |
| 3 | 2714.85 | 1836.88 | 1830 | 1852.42 |
| 4 | 2974.54 | 2682.97 | 2670 | 2510.72 |
| 5 | 5145.68 | 2774.12 | 2760 | 2740.572 |
| 6 | 7308.62 | 3560.71 | 3550 | 3182.770 |

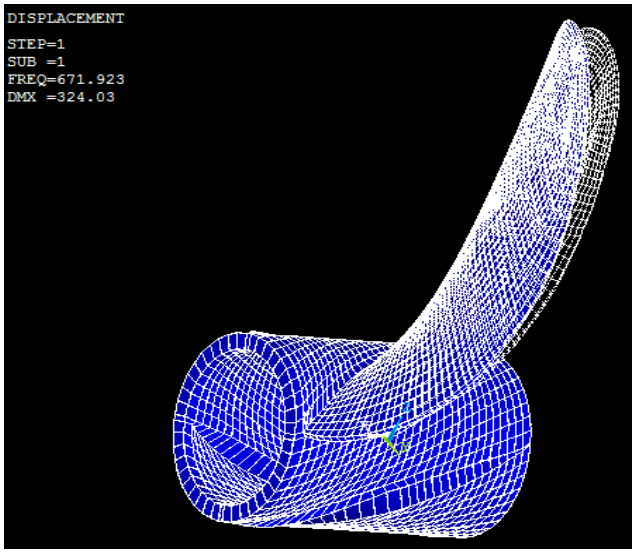


Figure 4.49: First Mode shape of Aluminium blade

Table 4.15: Comparison of Non-dimensional frequencies for Aluminium pre-twisted blade

| Mode Number | Non-dimensional frequency | |
|---|---|---|
| | Shell type element | Experimental result |
| 1 | 3.444 | 4.768 |
| 2 | 10.970 | 10.867 |
| 3 | 19.194 | 12.868 |

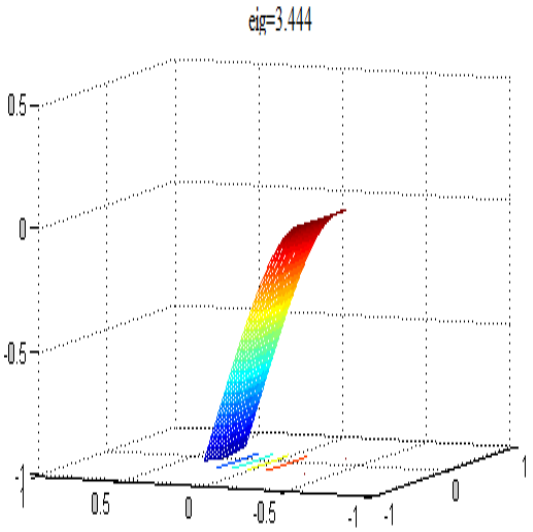


(a): I$^{st}$ Bending mode shape

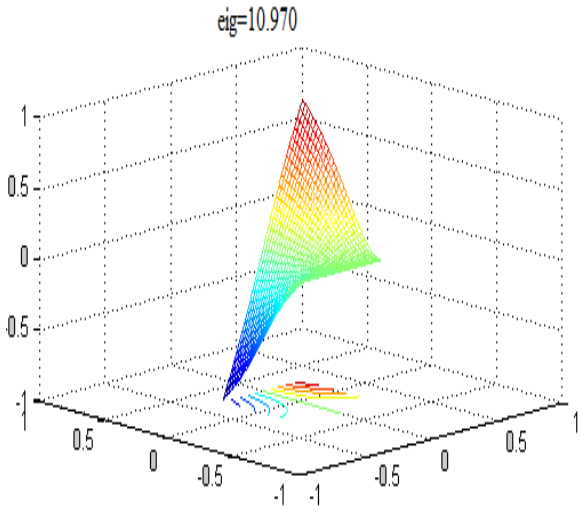


(b): I$^{st}$ Twisting mode shape

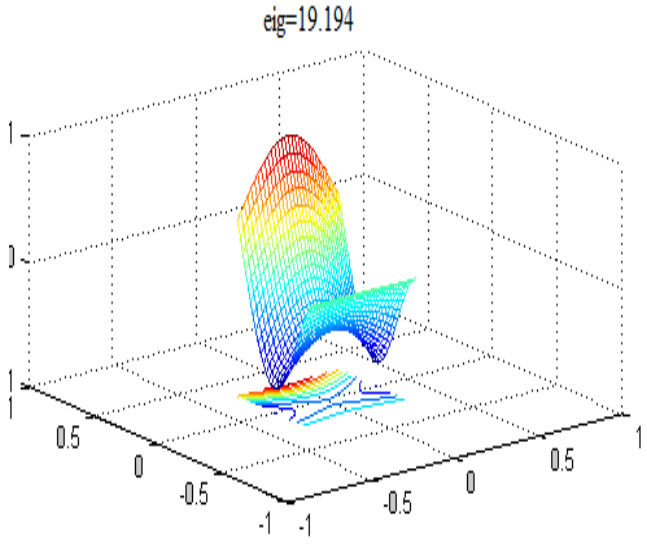


(c) II[nd] Bending mode shape

Figure 4.50: Mode shapes for Aluminium Propeller Blade

Figure 4.51: Fabricated model of E-glass epoxy blade

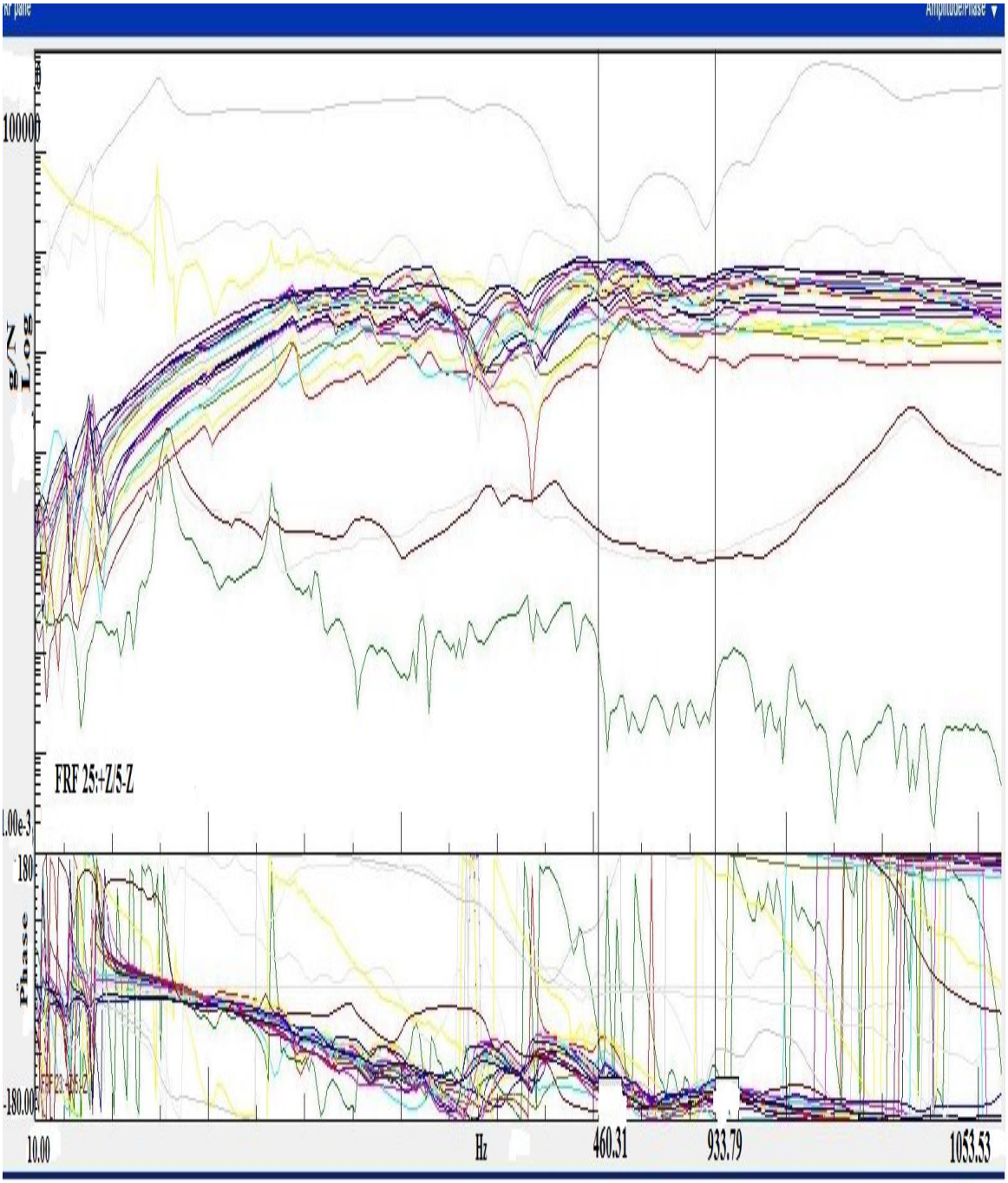


Figure 4.52: Modal data selection for all control points

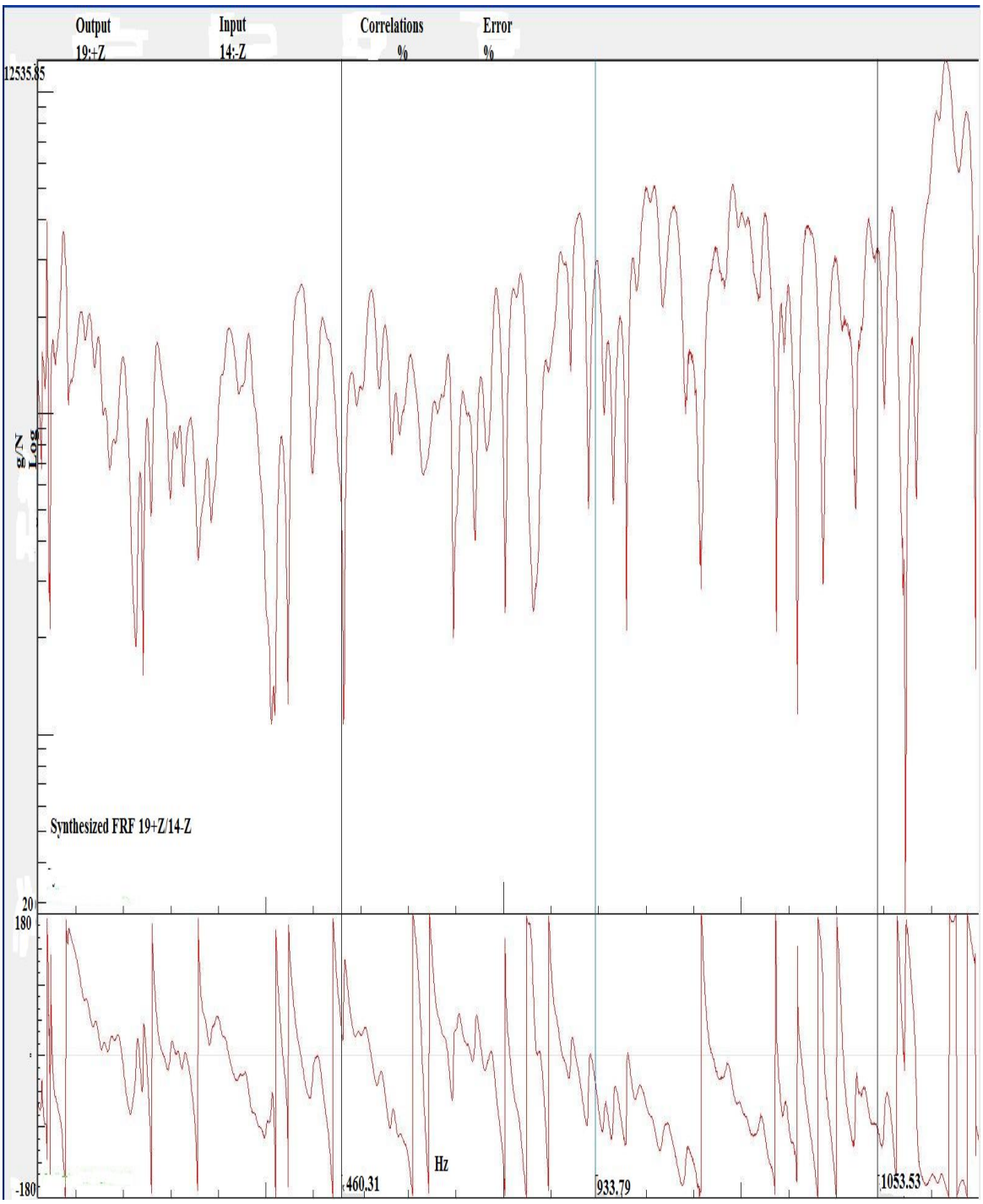


Figure 4.53: Final synthesized FRF

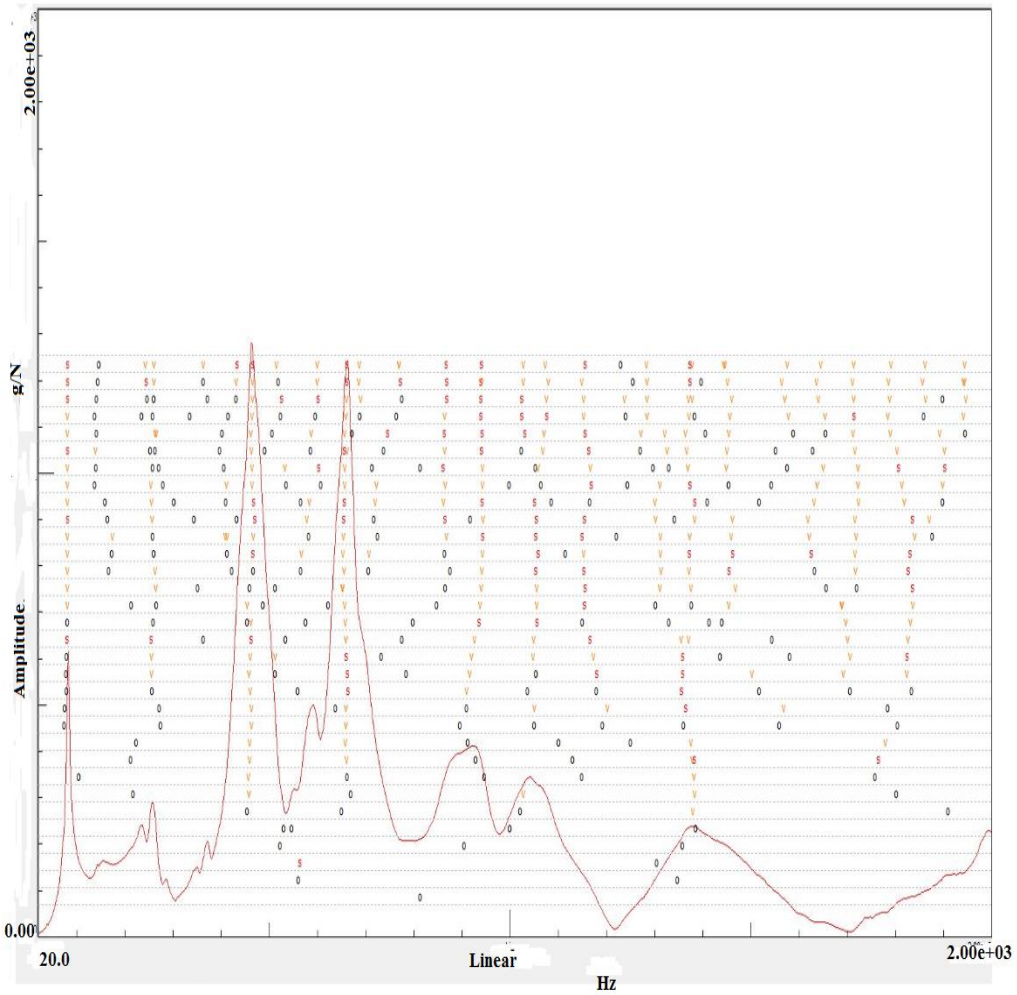


Figure 4.54: Time Degrees of freedom for Stabilization

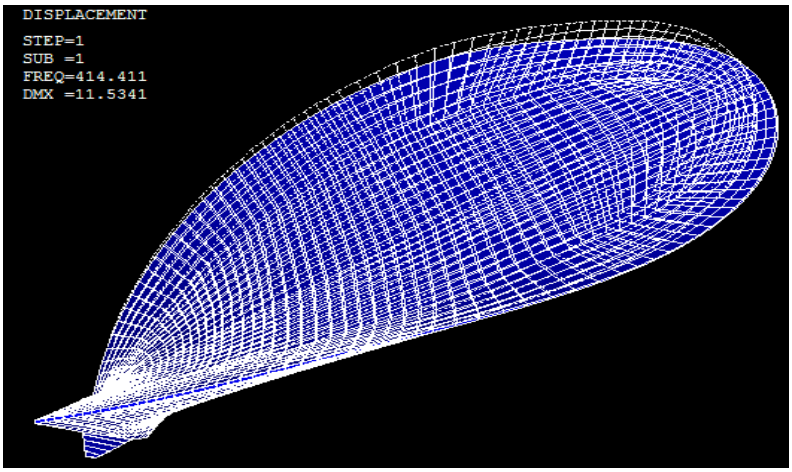


Figure 4.55: First Mode shape of E-glass epoxy blade

Table 4.16: E-Glass Fibre Reinforced Plastic $[-45°/45°/90°/0°]_s$

| Mode Number | Theoretical (Hz) | Ansys (Hz) | Experimental (Hz) |
|---|---|---|---|
| 1 | 319.45 | 414.411 | 460.31 |
| 2 | 1066.8 | 910.27 | 933.799 |
| 3 | 1175.6 | 1065.91 | 1053.53 |
| 4 | 2181.4 | 1542.44 | 1463.253 |
| 5 | 2717.9 | 1642.40 | 1733.561 |
| 6 | 3750.8 | 2030.52 | 2078.420 |

Non-dimensional natural frequency of isotropic plate is given by

$$\varpi = \omega * (b^2) * \sqrt{\frac{12 * \rho * (1 - \upsilon^2)}{E_{11} * h^2}}$$

Where $\varpi$ = Non-dimensional frequency, b=width of the blade , $E_{11}$ =Young's modulus of elasticity, $\rho$ =Density of the material, $\upsilon$ =Poisson's ratio and h=Thickness of the material.

Table 4.17: Numerical results for E-Glass epoxy material type blade

| Mode Number | Non-dimensional frequency | |
|---|---|---|
| | Shell type element | Experimental |
| 1 | 1.054 | 1.518 |
| 2 | 3.520 | 3.080 |
| 3 | 3.879 | 3.474 |

## 4.14 Discussions

In this study, the vibrational characteristics of composite marine propeller made of both metallic and fiber reinforced plastics material of (E-Glass epoxy) are analyzed by developing a mathematical model in the framework of the FSDT using shell type elements. A computer code is developed in MATLAB software to evaluate the vibrational characteristics. Additionally, to support the result ANSYS (APDL) is used. Using a set of the balanced sequence $[-45°/45°/90°/0°]_s$ a comparison has been made between metallic and composite to find out the variation in operating frequencies for the blade. Finally, to validate the result, an experimental investigation has been carried out for both the materials and the corresponding illustrations has been shown in the Figures 4.46 to 4.55.The effects on the non-dimensional fundamental frequencies and frequency ratios of the shell type blade have been discussed in detail.

# Chapter 5

# Structural Optimization Scheme

## 5.1 The Optimization Problem

The main aim of optimization is to determine the best possible solution under given circumstances. The problem of optimization may be defined by either minimization or maximization criteria. The present problem of structural optimization deals with some sort of maximization or minimization, for example, minimization of volume fraction, displacements, stresses or maximization of stiffness, to be able to find out the optimal solution depending upon the set of design variables specified in terms of numerical value. This set of design variables defined on a function is known as "cost function".

In general, the optimization problem is often formulated mathematically as minimization of the cost function (which may be easily converted to maximize by minimizing the negative function), subject to constraints which are expressed as

$$\begin{aligned} &\text{Find } x = \{x_1, x_2, x_3 \ldots\ldots\ldots\ldots x_n\} \\ &\text{minimize } f(x) \\ &\text{subject to } g_i(x) \le 0 \; i = 1, 2, 3, \ldots\ldots\ldots\ldots m \\ &\qquad h_i(x) = 0 \; j = 1, 2, 3, \ldots\ldots\ldots\ldots n \end{aligned} \tag{5.1}$$

Where x vector of design parameter

f(x) cost function

g(x) inequality constraint function

h(x) equality constraint function.

m the number of constraint sets and

n is the number of design parameters

The set of parameters defined above contributes to form a constrained optimization problem. The set of feasible solutions is determined by the constraint sets and the bounds

applied to this design parameter. Each constraint set may be written as a pair of constraint equations. Most of the software handling this optimization problem will take care of these design parameters and bounds along with constraints imposed over the problem.

## 5.2 Single Point Design Optimization Scheme

### 5.2.1 Introduction

The following sections describe a technique for calculating the composite lay-up for a hydro dynamically loaded shape of a B-series composite propeller blade subjected to constraints. The starting point is a target propeller blade shape with a specified hydrodynamic pressure distribution, and the result is the deformed shape of the propeller blade with the optimum composite ply arrangement. The optimization scheme follows a minimization and maximization criteria, where the deformations, volume fractions, and corresponding stress values are subjected to minimization and Eigenvalue frequencies are for maximization. The objective of the Fibre reinforced plastic blade is to minimize its deformation, stresses, and volume fractions and maximize its frequencies. The designed variables and bounds are referred with that of conventional isotropic material. From the composite shuffle optimization scheme the final optimal stacking sequence is determined which maximizes the operational range for the pre-twisted blade consistent with the stress and deflections calculations. The flexibility and strength of the structure may be estimated by using this method which suits for most of the practical applications.

### 5.2.2 Basic Optimization Scheme

It is assumed that the design condition has a desired loaded shape and associated load distribution in the design condition. In addition to the shape, defining the structural model Figure 5.1), there is a shape that occurs which is the solid representation of the model. the external surface or skin (Figure 5.2)). Importantly, displacements are not assumed to be small, and the geometry of the structure may change with load. The aim is to find the optimum composite ply arrangement so that the desired deformed shape will occur at the specified load after the blade undergoes the maximum amount of desired deformations without overstressing. To acheive this, the optimization process outlined in Figure 5.3 is followed.

The steps in the optimization process are:

1. Import the hydro dynamically loaded propeller blade subject to optimization.
2. Assume a uniform distribution of composite material properties.
3. If there are sub-steps, specify those design parameters that are fixed and those that are adjustable.
4. Repeat the following steps:
   a. Calculate the static and dynamic analysis of the targeted propeller blade.
   b. Calculate the objective function of the optimization process, i.e. the determination of optimum ply its deformations, stresses and volume fractions.
   c. Calculate the constraint functions.
   d. Exit the iterative loop if a maximum of the objective function has been found subject to the constraints. Otherwise, adjust the composite material properties, and implicitly the associated stiffness matrix of the arrangement for loading propeller which we seek to maximize its Eigenvalues and minimize structure since details of this procedure depend on the chosen design parameters.
5. If there are sub-steps, and it is not the last sub-step, return to step 2) above in order to change the set of adjustable design parameters.
6. Calculate the final optimized stacking sequence of the propeller blade based on the geometry and loads of the design condition. (To perform above optimization scheme hydrodynamic calculations are not necessarily required.)

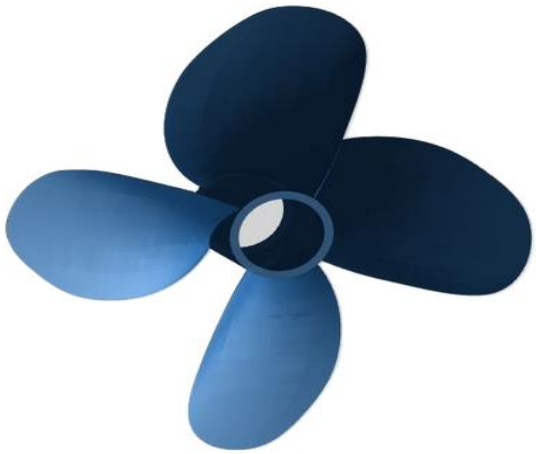

Figure 5.1: Four Bladed Metallic Propeller

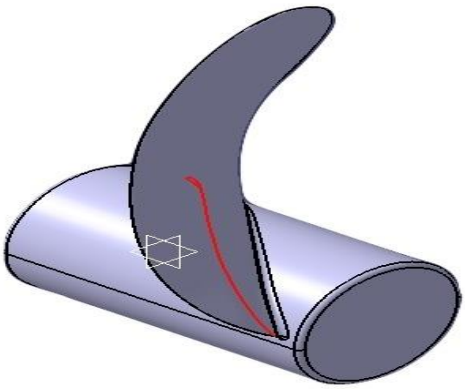

Figure 5.2: Single Bladed Propeller for optimization

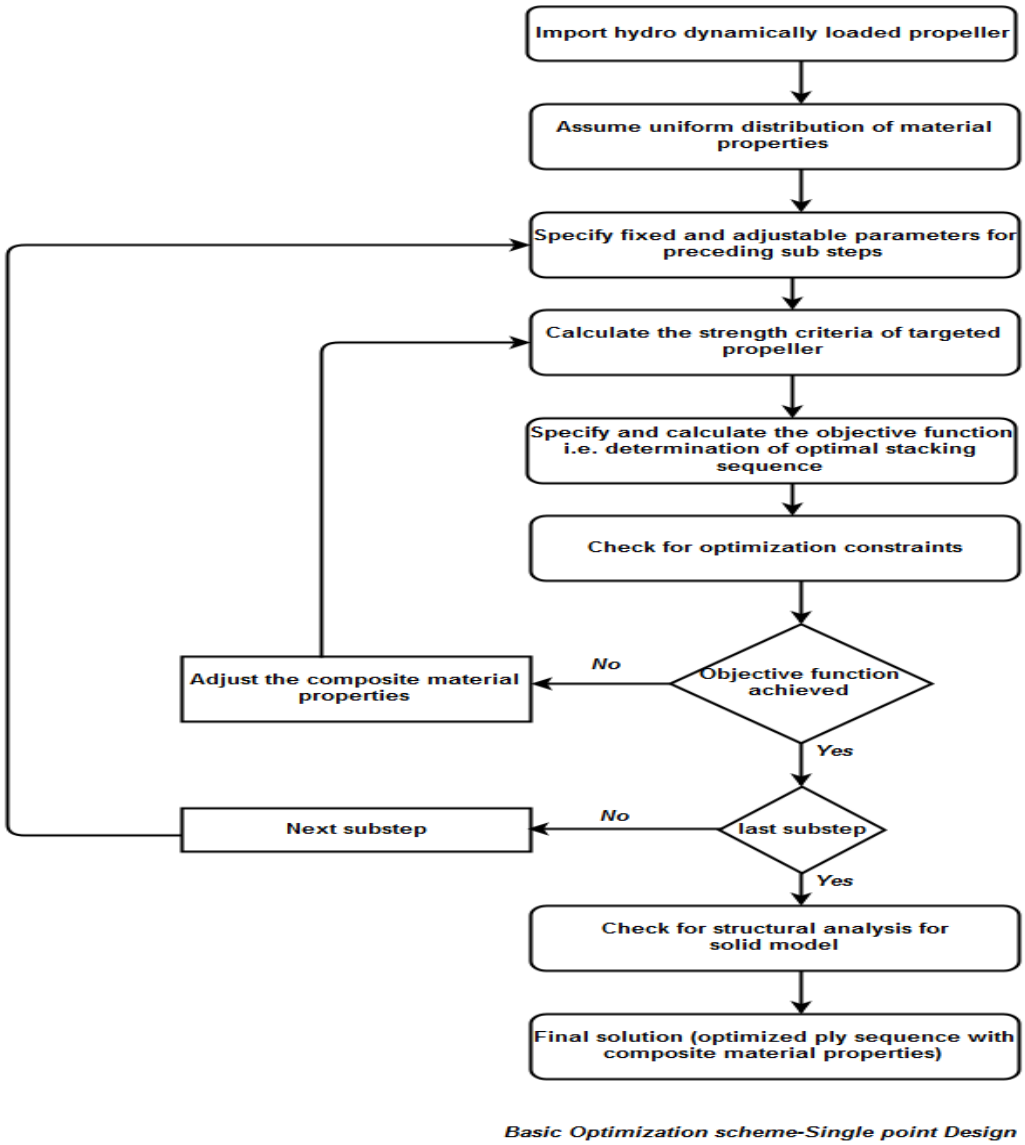


Figure 5.3: Flow chart for Basic design optimization process

### 5.2.3 The Stepwise Approach

The recursive nature of the structural optimization results in the determination of optimum composite ply arrangement for the deformed shape of the propeller. With the design variables varied at the design state, to maximize the operational range, variation between the unloaded and specified design condition stiffness distribution along the blade is altered, even though Optistruct (software) handles the optimization problem with continuous design parameters the discrete nature of the composite material employs some difficulties. The use of stepwise approach reduces the complexity associated with continuous variables.

A preliminary operation to estimate the proportion of plies at different specified angles $[0° \pm 45° 90°]$ with a set of different materials (CFRP and GFRP) are considered, since designing of the blade is done for maximum thickness. The thickness of the structural section is divided into two layers.

Using the set of inputs obtained from the preliminary operation, and constraints bounds set for the structure following sequence of optimization phases, an optimized composite lay-up is defined for the blade. This will be the final optimized lay-up.

The optimized ply lay-up is checked for the test to find the best result that satisfies the design objectives, the results are adjusted until the best lay-up is determined for the designed objectives, only part of the ply angles are adjusted while the other angles for remaining plies are fixed.

The two distinct optimization schemes used for achieving optimal lay-up are

1. By varying the proportions of angles and their corresponding materials.
2. By varying the ply angles as design variables.

The outcome of these two schemes results in same basic design, but the details refer to their design parameters. The selected design parameters are updated for every set of the iterative cycle.

**Objective Function**

The function to be maximized is the operating range of the propeller between the unloaded and loaded states, calculated at various sets of ply arrangements using both hybrid

and non- hybrid composite materials. This must be a positive quantity as the operational frequency of the unloaded blade should be greater than that of the blade in the loaded state.

**Design Parameters**

As mentioned previously, the design parameters are continuous variables that describe the elastic properties of the propeller blade or hydrofoil. Two alternative sets of design parameters are considered in this study:

a) Proportions of two materials with specified elastic properties and ply angles and
b) Discrete ply angles.

Details of the parameters and computations are given below.

**Material Proportions and Ply Angles**

In the present study, the structural section consists of two layers – a bottom layer and a top layer with each layer assumed to consist of a number of plies. Each ply will be made of either one or two specified composite materials, and may be placed at one of a specified set of ply angles. Here the term "composite material" refers to the combination of matrix and fiber in a single ply. The matrix material will probably be the same for both materials so that only the fiber component is different with one fiber usually being substantially stiffer than the other. Two options are considered for the ply angles

1. Fixed ply angles, i.e. the ply angles are not design parameters but are specified.
2. Ply angles are continuous design parameters and are varied by the optimization procedure along with the material proportions.

For the first option, above, the design parameters of the optimization scheme are the proportions of plies at the specified angle and the proportions of plies at the specified angle that consist of the first of the two materials. For the second option, the ply angles are also design parameters in addition to those of the first option.

The proportions of plies at the specified angles are related by

$$\sum_{i=1}^{n_\theta} P_{\theta i} = 1 \tag{5.2}$$

Where $n_\theta$ is the number of possible ply angles, and $P_{\theta i}$ is the proportion of the layer thickness of plies at angle θ. Note that only $n_\theta - 1$ are angles independent.

For example, if, $n_\theta = 5$, where the ply angles are -90°,-45°, 0°, +45° and 90°, only four proportions are independent, so that

$$P_{45} = 1 - P_{-45} - P_0 - P_{-90} - P_{90} \tag{5.3}$$

Also, for each ply angle, a certain proportion, $r_{\theta i}$ of the plies at this angle consist of material 1, and the remainder of material 2. Therefore, the proportion of plies at angle $\theta_i$ that consists of material 1 of the time and the proportion of material 2 is, $P_{\theta i}(1 - r_{\theta i})$. The number of design parameters per layer is, $2n_\theta - 1$. For the previous example with 5 ply angles, there are 9 design parameters per layer: $p_{-90}, p_{-45}, p_0, p_{90}, r_{-90}, r_{-45}, r_0, r_{45}, r_{90}$. If there are a large number of plies, and the plies at the various angles are evenly distributed throughout the thickness of the layer, the elastic modulus matrix of the layer E may be expressed as the weighted combination of the elastic modulus matrices for plying with the two materials at the range of specific ply angles.

$$E = \sum_{i=1}^{n_\theta} p_{\theta i} E_{\theta i}$$

$$E = \sum_{i=1}^{n_\theta} p_{\theta i} \left[ r_{\theta i} E_{\theta i}^1 + (1 - r_{\theta i}) E_{\theta i}^2 \right] \tag{5.4}$$

Where $E_{\theta i}^1$ is the elastic modulus matrix for the layer with material 1 at an angle, $E_{\theta i}^2$ is the similarity matrix for material 2, and $E_{\theta i}$ is the weighted combination of $E_{\theta i}^1, E_{\theta i}^2$ based on the proportion $r_{\theta i}$.

**Discrete Ply Angles**

The design parameters are the ply angles θ, which are discrete so that for any given ply the angle θ may only take up one of some specific angles $\theta_1, \theta_2, \ldots, \theta_n$. The difficulty is that the available optimization software works with continuous variables but not discrete variables. To overcome this problem, it was decided to use "angle numbers" $s_\theta$, which are

real numbers not integers, and are such that specific ranges of these numbers correspond to specific discrete ply angles.

For example, consider the case with three possible ply angles -45°, 0°, and 45° is considered. Take lower and upper bounds for the angle number $s_\theta$ as 1/2 and 3/2 , then values of $s_\theta$ can be related to the ply angles in the following manner:

$$\begin{aligned} \frac{1}{2} \le s_\theta \le \frac{3}{2} \\ \frac{3}{2} \le s_\theta \le \frac{5}{2} \\ \frac{5}{2} \le s_\theta \le \frac{7}{2} \end{aligned} \qquad (5.5)$$

The optimization software works with the angle numbers $s_\theta$, which must be translated to ply angles $\theta$ before computing the elastic modulus matrices of the structure. The effect of this is that the elastic modulus matrix of any given finite element, and therefore the structural stiffness, deformations and the objective function, does not change in a smooth manner with changes in ply angle numbers . Therefore, gradient methods are not suitable for solving the optimization problem, but the Adaptive Response Surface Method has proven to be more useful.

## 5.2.4 Constraints

The constraints for the optimization problem come in two categories: parameter bounds and constraint functions. There are two proposed sets of parameters and the bounds for the two sets will be described separately.

**Material Proportion Parameter Bounds**

The lower and upper bounds of, the $p_{\theta i}$ , the proportion of the layer thickness of plies at angle $\theta_i$, are zero and unity, respectively. If the plies are to be alternated, so that there are no two successive plies with the same angle, the upper bound should be set at 0.5 (this is an approximation if the thicknesses of the plies are different for the various ply angles). As stated above, one of the proportions is not independent and in this case, the bounds must be incorporated as constraint functions. The lower and upper bounds of, the $p_{\theta i}$ , the proportion

of plies at angle θi that consists of material 1 are zero and unity, respectively. For the example with ply angles of -45°, 0° and 45°, and with alternating plies, the parameter bounds are

$$\begin{aligned} &0 \le p_{-45} \le 0.5 \\ &0 \le p_0 \le 0.5 \\ &0 \le r_{-45} \le 1 \\ &0 \le r_0 \le 0.5 \\ &0 \le r_{45} \le 1 \end{aligned} \tag{5.6}$$

and the constraint set for the dependent ply angle proportion is

$$0 \le (1 - p_{-45} - p_0) \le 0.5 \tag{5.7}$$

These are the parameter bounds and constraint set for one layer, and similar constraints are required for both top and bottom layers.

**Ply Angle Constraints**

As noted previously, the ply angles θj for ply j are related to ply angle numbers, which have ranges of $\frac{1}{2}$ about an integer value:

$$\left(i_{\theta j} - \frac{1}{2}\right) \le s_{\theta j} \le \left(i_{\theta j} + \frac{1}{2}\right) \tag{5.8}$$

The integer value $i_{\theta j}$ ranges from 1 to the number of possible ply angles $n_\theta$, and therefore the ply angle numbers range from $\frac{1}{2}$ to $n_\theta + \frac{1}{2}$. Additional constraints must be imposed to incorporate stacking rules. For example, if no two successive plies are to have the same ply angle, the ply angle numbers of any two adjacent plies must differ by unity or more. This can be written as a single constraint

$$\left(n_c - (n_p - 1)\right) = 0 \tag{5.9}$$

Where $n_c$ is the number of times that the ply angle number differs by unity or more between plies, and $n_p$ is a total number of plies. A slightly less stringent constraint is to require the above expression to be satisfied for the plies in each half thickness of the component, but not at the two plies adjacent to the mid-surface.

**Strain Constraints**

Some particular combinations of the design parameters, while minimizing the objective function, may produce a composite lay-up that does not have sufficient strength to resist the applied loads. To provide limits on the strength of the structure during the optimization computations, it is proposed to limit the surface strains to a specified range. For each ply angle θ, the strains are limited, so that at the top and bottom surfaces of the shell

$$\varepsilon_{11\min} \le \varepsilon_{11} \le \varepsilon_{11\max}$$
$$\varepsilon_{22\min} \le \varepsilon_{22} \le \varepsilon_{22\max}$$
$$\gamma_{12} \le \gamma_{12\max} \qquad (5.10)$$

Where $\varepsilon_{11}, \varepsilon_{22}, \upsilon_{12}$, are the in-plane strains in the material directions and $\varepsilon_{11}\min$, $\varepsilon_{11}\max$ $\varepsilon_{22}\min$ $\varepsilon_{22}\max$ and $\gamma_{12\max}$ are limiting strains. The limiting strains are determined for the worst case of all ply materials and include an appropriate factor of safety.

**Shell-Solid Transformation**

The final step in the calculations is to compute the three-dimensional solid body representation of the unloaded structure based on the shape of the shell finite element model. Nodal displacements and rotations are computed for the shell structural model, but the displacements of points on the surface of the blade are required for the calculation of the solid shape of the blade. Each point on the surface has an associated node in the shell mesh, and the surface points and shell nodes are assumed to be connected by rigid links. The spatial relationship between the surface points and shell nodes are determined for the target loaded shape and, except for rigid body rotations, remain the same for the predicted unloaded shape. The relative positions of a surface point and an adjacent shell node are defined by a vector v from the node to the point of the target shape

$$v = x_p - x_m \qquad (5.11)$$

Where $x_p$ and $x_m$ are the coordinates of the surface point and shell mid-surface node, respectively. For the shell node under consideration, displacements u and rotations θ relative

to the unloaded shape are calculated. The shell node coordinates of the unloaded and target shapes are related by

$$x_m = x_{m0} + u \tag{5.12}$$

Where $x_{m0}$ are the coordinates of the unloaded shell mid-surface node. The coordinates of the surface point on the unloaded shape $x_{p0}$ are

$$x_{p0} = x_{m0} + R_{123}^{T}(-\theta)v \tag{5.13}$$

Where R123 is a rotation matrix. Note that the negative of the rotations θ are used to form the rotation matrix. The rotation matrix is

$$R_{123(\phi,\theta,\varphi)} = \begin{bmatrix} c_\theta c_\varphi & c_\theta s_\varphi & -s_\theta \\ s_\phi s_\theta c_\varphi - c_\phi s_\varphi & s_\phi s_\theta s_\varphi + c_\phi c_\varphi & c_\phi s_\varphi \\ c_\phi s_\theta c_\varphi + s_\phi s_\varphi & c_\phi s_\theta s_\varphi - s_\phi c_\varphi & c_\theta c_\varphi \end{bmatrix} \tag{5.14}$$

Where $\phi$ , θ and $\varphi$ are rotations about the x, y and z axes, and $c_\theta$=cosθ, $s_\theta$=sin θ, etc. When the above operation is carried out for all surface points this defines the shell-solid transformation for the unloaded solid shape:

$$c_\theta = T(\theta, s_0) \tag{5.15}$$

**Applied Loads**

Calculations of the Unloaded Shape, above, the loads are the nodal loads of the shell finite element mesh for the target loaded shape. Equivalent nodal loads may be derived from a pressure distribution on the surface of the loaded body. One step in the calculation of the unloaded shape of the body involves computation of the deformations due to the incremental application of the loads to the initially unloaded body. It is important that this computation uses the equivalent nodal loads derived from the pressure distribution on the loaded shape and not the loads derived from the pressures applied to the geometry of the unloaded shape. The hydrodynamic pressure loads on the surface of the blade must be transformed to equivalent nodal loads acting on the shell model of the blade. First, the equivalent point loads acting on points on the blade surface are computed. Then, using static equivalence

relations, these point loads are transformed to point loads and moments acting on the nodes of the shell model.

### 5.2.5 Design phases for Basic Optimization Scheme

Phase 1: Concept design synthesis through free size optimization

Phase 2: Design fine tuning through ply sizing optimization

Phase 3: Detailed design through ply stacking sequence optimization

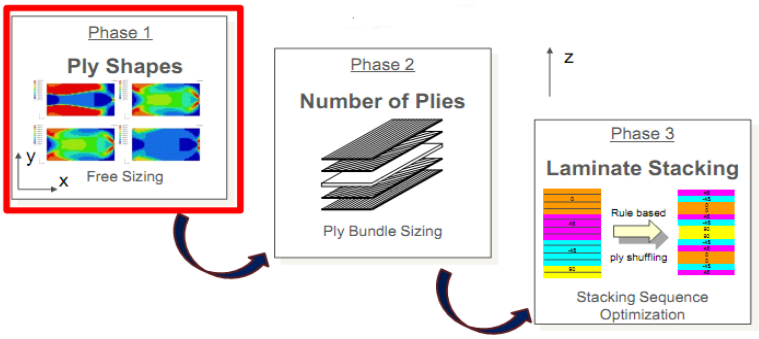


Figure 5.4: Design Phases of optimization for composites

**Phase 1: Concept design synthesis (or) free size optimization**

In the design phase of optimization (Figure 5.4), free size optimization is used to determine the material thickness distribution of the fiber reinforced plastic material blade where multiple load cases are applied to the blade using optistruct solver. Due to large deformation, stresses and inelastic behavior of the structure a non-linear analysis is performed to study the effects of geometric non-linearities**.** The free size optimization done by optistruct optimizes the thickness of every element in the design space to generate an optimum thickness distribution in the structure for the given objective under given constraints. Free size optimization for composite propeller blades is done for all the load cases with an objective of minimizing weight. When the loads are defined in different subcases, optistruct automatically optimizes the blade for all the different loads. All these constraints are not applied at the same point but are distributed at different instances. The optimized blade is optimal for all load cases. The design variable for free size optimization is the thickness of shell elements on the surfaces. The thickness of the blade is allowed to vary between tip to root. In the design phase, a displacement constraint is also used to limit

the value of displacement for the composite blade not to exceed the conventional isotropic materials limit.

**Size Optimization**

Size optimization is an automated mathematical code used to find the optimal design by modifying the structure parameters. In size optimization, design variables such as the shell thickness, structural cross section properties, etc., are modified to solve the optimization problem (Figure 5.5 and 5.6). The objective of size optimization is used to identify the optimal thickness of each ply bundle. The size optimization procedure of structure consists of the following main steps:

1. Define the objective function

   In this case, the optimal ply thickness of each ply bundle is determined

2. Define design variable

   Design variable is defined using a bulk data entry for size optimization thickness of blade is chosen as a design variable.

3. Define design constraint

Design constraints can be defined as lower bound or an upper bound or any response that is dependent on the design variable. The mode shapes along with volume are defined as constraints in the optimization model.

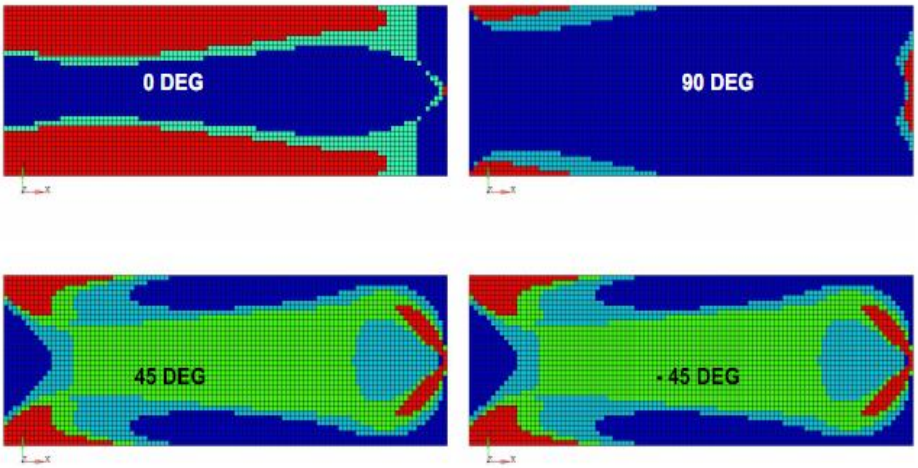


Figure 5.5: Size optimization results per fibre orientation

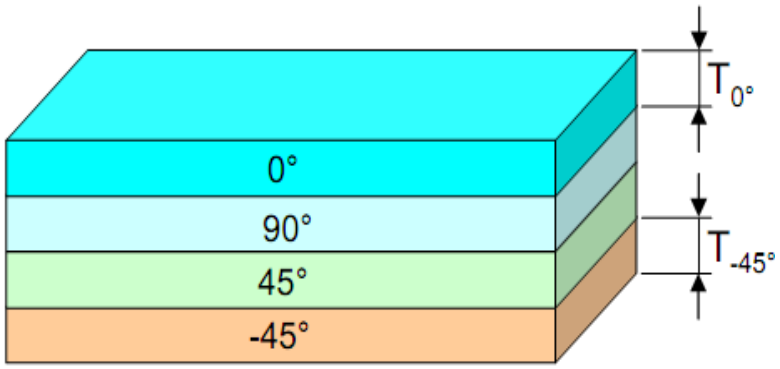


Figure 5.6: Composite laminate with super ply thickness

**Phase 2: Design fine tuning through ply sizing optimization**

Design fine tuning process involves a sizing optimization of the ply bundles generated from phase1 of the design process, with the optimal ply shape established and patch locations identified, the next step follows to fine tune the design for thickness. Phase 2 involves identifying the optimal thickness for each ply bundle. The choice of running the optimization with the thickness as a discrete or continuous is made available, specification of minimum manufacturable ply thickness is done by running a discrete optimization and allowed for a calculated optimal ply bundle thickness to be a multiple of the minimum ply thickness value which helps in calculating the total number of plies required per fiber orientation (Figure 5.7).

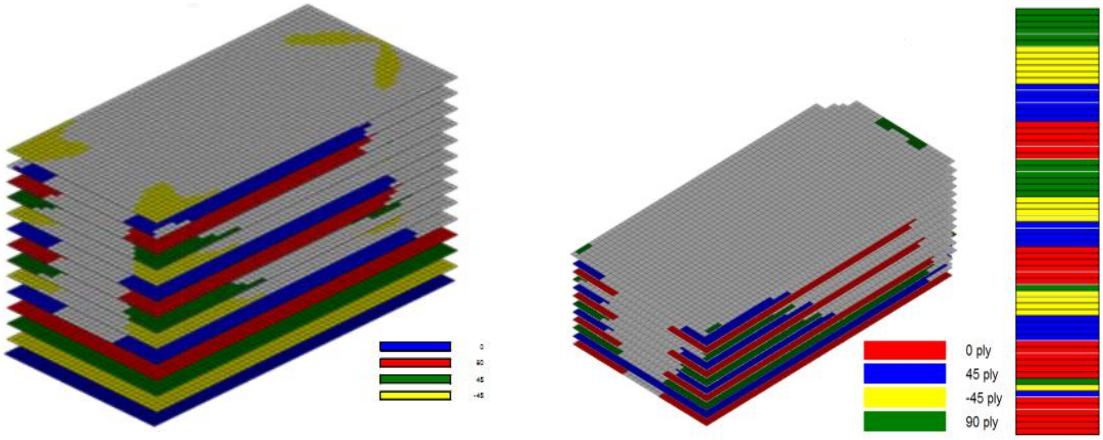


Figure 5.7: Ply-bundle sizing

**Phase 3: Ply stacking sequence optimization**

During shuffling the stacking sequence (Figure 5.8) it is important that the behavioral and design constraints are preserved. Also, it makes clear that the requirement that certain ply book rules are to be applied to guide the stacking of plies based on specific requirements. To control the stacking sequence, some of the rules taken into consideration are

1. Maximum number of successive plies of a particular fibre orientation
2. Pairing of plies
3. Identification of sequence

For this case of optimization problem as previously formulated in the sizing phase and additional ply books rules are applied They are

1. The maximum successive number of plies does not exceed 4 plies.
2. The ply angles $-45 and +45$ are reverse paired.

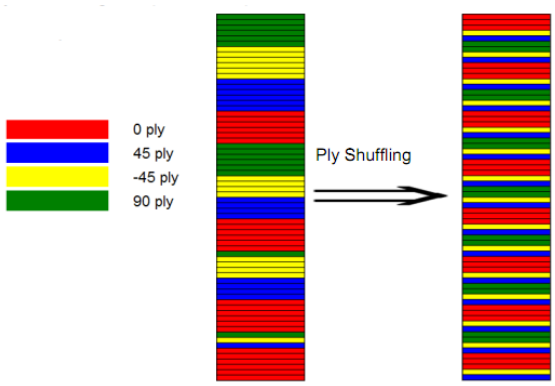


Figure 5.8: Ply-stacking sequence optimization

## 5.3 Results and Discussions

To achieve knowledge and understanding of how optimization can be used in the design process a systematic approach has been evaluated for single marine composite propeller blade. The work was performed as pilot case starting from specifications and limitations and ending up with proposals for the final product. In some of the cases, specifications and limitations were only partly known. The steps to reach a reasonable resulting design using the tools of HyperWorks were to be found out during the work

process. An iterative process using a method of trial-and-error was used. Many of the different approaches led to unsatisfactory results which, although they gave an increased understanding of the problem, will not be presented here. Here the work is described step by step from the definition of the problems to the analysis of the resulting design and an evaluation of the used method.

## 5.4 Problem Definition:

A composite propeller blade is subjected to pressure loads and is fixed on the periphery, to optimize the blade for optimum ply drop off using Free Size Optimization by using ply orientations 0°, 45°/-45° and 90°, each of 1.52 mm super ply thickness (Total Laminate = 12.2 mm thick). Also optimize the thickness of each ply (Composite Size) and the stacking sequence (Shuffling) of all the plies in the laminate. The maximum displacement of the aluminium propeller meshed with shell element is 0.939 mm which is considered as a reference for evaluating the stacking sequence results for composites.

### 5.4.1 Constraints:

Maximum Allowable Displacement is 0.939 mm.

Manufacturable ply thickness = 0.6

45/-45 plies to be balanced

### 5.4.2 Objective:

The component considered is a composite propeller blade whose optimal stacking sequence is to be determined using design driven approach of optimization using optistruct. The blade is subjected to a pressure load and fixed at its root with maximum displacement limited to 0.939mm, and manufacturing ply thickness is 0.6.

To obtain optimized stacking sequence, the optimization scheme follows a three phase approach

Phase 1: Concept design synthesis

Phase 2: Design fine tuning

Phase 3: Ply stacking sequence optimization

By stringing these three operations together, optistruct offers a unique and comprehensive process, for the design and optimization of composite laminates. All the process phases are integrated automatically in the Hyperworks software where the input data generation for a subsequent phase is carried from the previous design phase.

**Phase 1: Concept design synthesis (or) free size optimization**

In the first phase of design optimization, the thickness of each desirable element is stated as a design variable. The application of this step of optimization of composites implies that the design variable is the thickness of each super ply per element. The conceptual design phase identifies the stiffest design possible for the given fraction of the materials. For best results, manufacturing constraints are incorporated through all phases of design automatically.

Design variables: Element thickness of each ply orientation

Objective : Minimize the volume fraction

Constraints: Maximum allowable displacement is 0.939mm

Manufacturing constraints:

1. Ply percentage for 0° and 90° not less than 10% and not more than 60%
2. The manufacturable ply thickness is 0.6mm
3. A balance constraint that ensures an equal thickness distribution for +45°and- 45°s.
4. Balanced sequence followed [-45°/45°/90°/0°]

The full meshed model four bladed Propeller with single surface extracted with pressureloading are depicted in Figure 5.9 and 5.10 respectively.The static displacement and its corresponding von Mises stress are obtained. These are represented in Figure 5.10 and 5.11.The elemental thickness distribution with different ply angles are shown in Figures 5.12 to 5.16.Maximum thickness is obtained for the composite Propeller is obtained for $90^0$ ply angle.

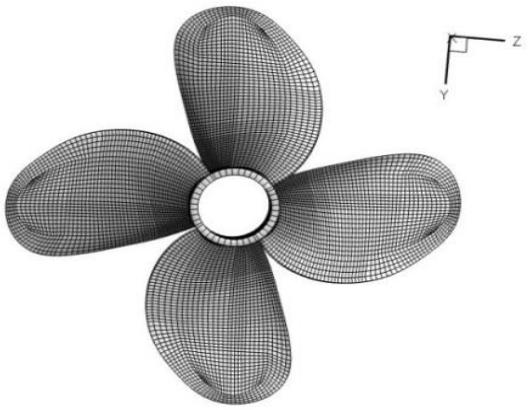


Figure 5.9: Meshed model four bladed propeller

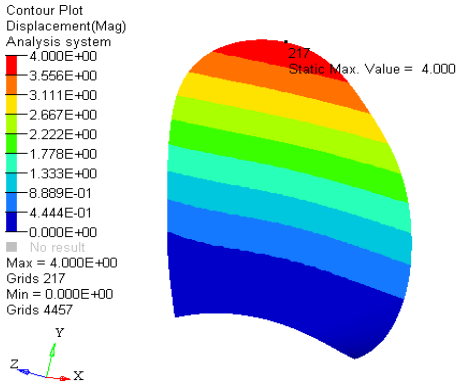


Figure 5.10: E-glass epoxy blade with maximum Static displacement (mm)

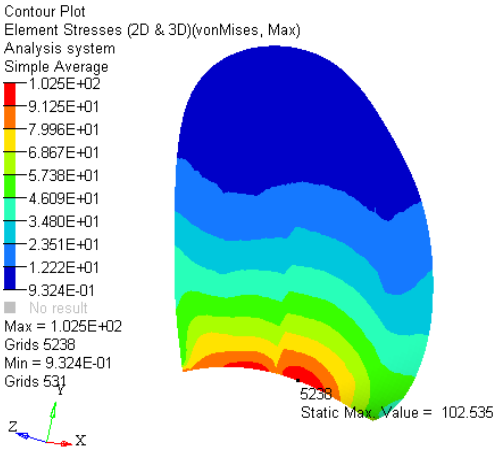


Figure 5.11: E-glass epoxy blade with von Mises stress (MPa)

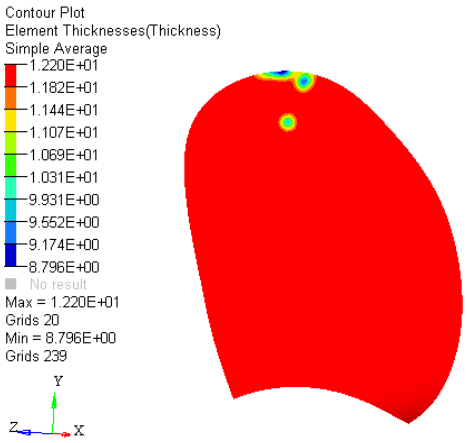


Figure 5.12: Composite Blade with elemental thickness distribution (mm)

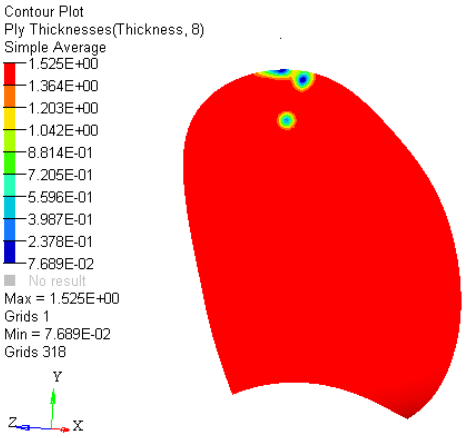


Figure 5.13:E-glass epoxy blade with elemental thickness(mm) distribution for -45° ply angle

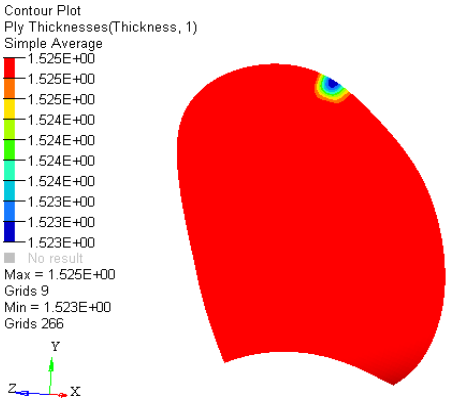


Figure 5.14: E-glass epoxy blade with elemental thickness (mm) distribution for +45° ply angle


Figure 5.15: E-glass epoxy blade with elemental thickness (mm) distribution for +90° ply angle

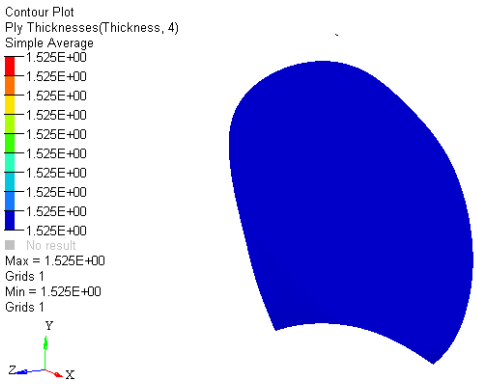


Figure 5.16: E-glass epoxy blade with elemental thickness (mm) distribution for 0° ply angle

**Phase 2: Composite size optimization (Design fine tuning)**

In the second stage of composite size optimization design, fine tuning of the thickness of the optimized ply bundles is done in order to ensure that the design optimization meets the specified requirements. In addition to these requirements Eigenvalue frequencies and composite strains are incorporated into this second phase of optimization stated in terms of performance criteria. Under these assembled conditions load cases as a constraint are added to evaluate the natural frequencies of the structure.

The following are the modifications incorporated into the second phase of optimization.

Design variables: Ply thickness defined in the phase1 is carried over

Objective : Minimize the total designable volume

Constraints : Natural frequencies ($1^{st}$ to $5^{th} \geq 530Hz$)

Composite strains in the fairing $\leq 5000$microstrain

The orientation thickness for E-glass epoxy blade with different ply angles having contour plots are shown in Figure 5.17 through 5.21.For ply angle $0^0$ and $90^0$, the elemental thickness for both the case are same.

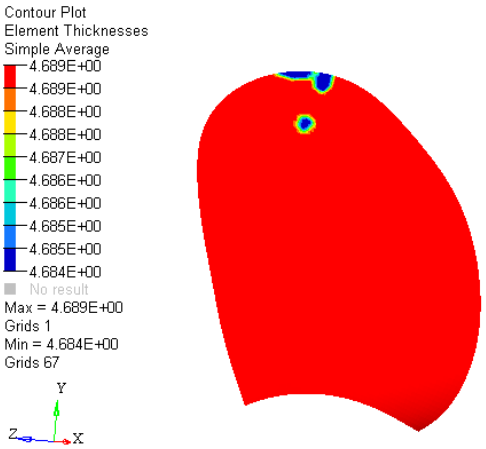


Figure 5.17: Contour plot for elemental thickness (mm) for E-glass epoxy blade in phase 2


Figure 5.18: Contour plot for orientation thickness (mm) for E-glass epoxy blade ply angle -45°

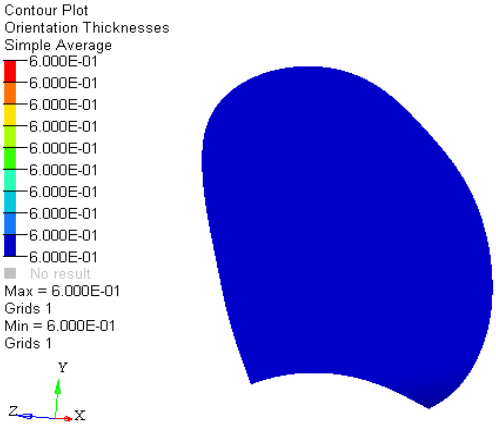


Figure 5.19: Contour plot for orientation thickness (mm) for E-glass epoxy blade ply angle 0°

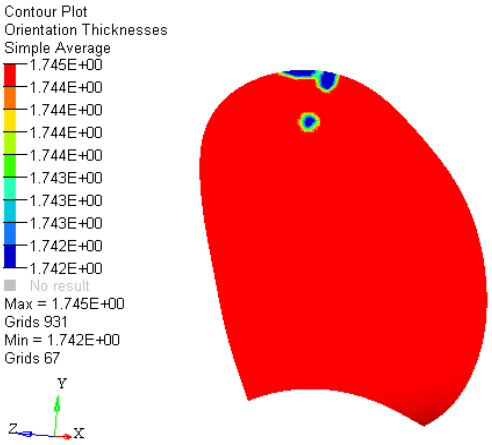


Figure 5.20: Contour plot for orientation thickness (mm) E-glass epoxy blade for ply angle 45°

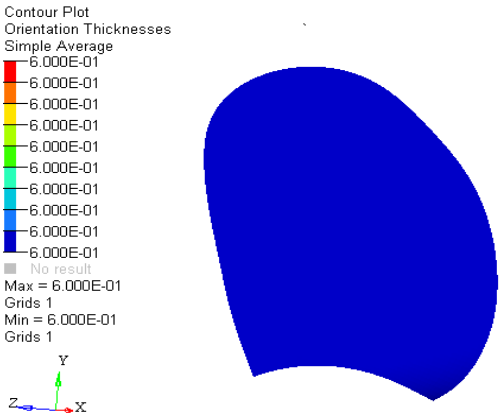


Figure 5.21: Contour plot for orientation thickness (mm) E-glass epoxy blade for ply angle 90°

**Phase 3: Ply stacking sequence/composite shuffling optimization**

The final phase of optimization specifies the optimal stacking sequence to be used. From the previous design phase, ply stacking sequence is carried over to composite shuffling optimization and the stack card is updated automatically. In this phase of design for composite, plies are shuffled to determine the optimal stacking sequence and those design parameters are presented.

Two manufacturing constraints are applied to this phase of optimization

1. The maximum successive number of plies of a particular orientation does not exceed 4 plies.
2. The +45°s and -45°s are reverse plied.

The final optimized stacking sequence for E-glass, Carbon, Hybrid composite1 and Hybrid composite 2 are shown in Figures 5.22 through 5.25.

## 5.4.3 Optimized stacking sequence for Composites

First of all the three phases of optimization are performed.Then the stacking optimization is converged in successive analysis iterations.The optimization history plot Table (5.1 to 5.4) shows the total weighted compliance that has been reduced by reordering the stacking sequence, giving an improvement in structural performance. The plies are coloured orientation, giving an overview of the laminate ply book. The final optimized stacking sequence for E-Glass epoxy, Carbon-epoxy and Hybrid composites are shown in the following Tables 5.1 to 5.4.

## Optimized Stacking Sequence for E-glass epoxy Blade

Table 5.1: Final optimized stacking sequence for E-glass epoxy blade

**Stacking sequence for STACK 1**

| Iteration 0 | Iteration 1 | Iteration 2 | Iteration 3 | Iteration 4 | Iteration 5 |
|---|---|---|---|---|---|
| 11101 | 12101 | 13101 | 14101 | 13101 | 13101 |
| 12101 | 11101 | 17301 | 13101 | 17401 | 17401 |
| 13101 | 14101 | 18301 | 17401 | 18401 | 18401 |
| 14101 | 13101 | 17201 | 18401 | 14101 | 14101 |
| 14102 | 17101 | 18201 | 15101 | 15101 | 15101 |
| 14103 | 18101 | 14101 | 14102 | 14102 | 14102 |
| 15101 | 14102 | 16101 | 14103 | 14103 | 14103 |
| 15102 | 16101 | 17401 | 17301 | 17201 | 17201 |
| 15103 | 17201 | 18401 | 18301 | 18201 | 18201 |
| 16101 | 18201 | 14102 | 17201 | 16101 | 16101 |
| 16102 | 14103 | 14103 | 18201 | 16103 | 16103 |
| 16103 | 16102 | 16103 | 16101 | 16102 | 16102 |
| 17101 | 17301 | 16102 | 16103 | 17101 | 17101 |
| 18101 | 18301 | 15101 | 16102 | 18101 | 18101 |
| 17201 | 15101 | 17101 | 17101 | 12101 | 12101 |
| 18201 | 16103 | 18101 | 18101 | 11101 | 11101 |
| 17301 | 17401 | 12101 | 12101 | 15102 | 15102 |
| 18301 | 18401 | 11101 | 11101 | 15103 | 15103 |
| 17401 | 15102 | 15102 | 15102 | 17301 | 17301 |
| 18401 | 15103 | 15103 | 15103 | 18301 | 18301 |

| Legend |
|---|
| 90.0 degrees |
| 45.0 degrees |
| 0.0 degrees |
| -45.0 degrees |

## Optimized Stacking Sequence for Carbon epoxy Blade

Table 5.2 Final optimized stacking sequence for Carbon epoxy blade

**Stacking sequence for STACK 1**

| Iteration 0 | Iteration 1 | Iteration 2 | Iteration 3 | Iteration 4 | Iteration 5 | Iteration 6 | Iteration 7 |
|---|---|---|---|---|---|---|---|
| 11101 | 12101 | 13101 | 14101 | 14101 | 14101 | 14101 | 14101 |
| 12101 | 11101 | 14101 | 12301 | 12301 | 12301 | 12301 | 12301 |
| 13101 | 17101 | 12301 | 11301 | 11301 | 11301 | 11301 | 11301 |
| 14101 | 18101 | 11301 | 12401 | 12401 | 16401 | 12401 | 12401 |
| 16101 | 13101 | 12401 | 11401 | 11401 | 12401 | 11401 | 11401 |
| 17101 | 12201 | 11401 | 17401 | 17401 | 11401 | 17401 | 17401 |
| 18101 | 11201 | 12201 | 18401 | 18401 | 17401 | 18401 | 18401 |
| 11201 | 17201 | 11201 | 12201 | 12201 | 18401 | 12201 | 12201 |
| 12201 | 18201 | 17301 | 11201 | 11201 | 12201 | 11201 | 11201 |
| 17201 | 16101 | 18301 | 17101 | 17101 | 11201 | 17101 | 17101 |
| 18201 | 12301 | 12101 | 18101 | 18101 | 17101 | 18101 | 18101 |
| 11301 | 11301 | 11101 | 17301 | 17301 | 18101 | 17301 | 17301 |
| 12301 | 17301 | 17101 | 18301 | 18301 | 17301 | 18301 | 18301 |
| 16301 | 18301 | 18101 | 13101 | 17201 | 18301 | 16401 | 16401 |
| 17301 | 16301 | 17401 | 16401 | 18201 | 16301 | 16301 | 16301 |
| 18301 | 12401 | 18401 | 16301 | 13101 | 17201 | 17201 | 17201 |
| 11401 | 11401 | 16401 | 12101 | 16401 | 18201 | 18201 | 18201 |
| 12401 | 16401 | 16301 | 11101 | 12101 | 13101 | 13101 | 13101 |
| 16401 | 17401 | 17201 | 16101 | 11101 | 12101 | 12101 | 12101 |
| 17401 | 18401 | 18201 | 17201 | 16301 | 11101 | 11101 | 11101 |
| 18401 | 14101 | 16101 | 18201 | 16101 | 16101 | 16101 | 16101 |

| Legend |
|---|
| 90.0 degrees |
| 45.0 degrees |
| 0.0 degrees |
| -45.0 degrees |

### Optimized Stacking Sequence for Hybrid composite1

Table 5.3 Final optimized stacking sequence for Hybrid composite1

**Stacking sequence for STACK 1**

| Iteration 0 | Iteration 1 | Iteration 2 | Iteration 3 | Iteration 4 |
|---|---|---|---|---|
| 11101 | 12101 | 12101 | 12101 | 12101 |
| 12101 | 11101 | 11101 | 11101 | 11101 |
| 13101 | 14101 | 15101 | 14101 | 14101 |
| 14101 | 13101 | 14101 | 14102 | 14102 |
| 14102 | 17101 | 14102 | 15102 | 15102 |
| 15101 | 18101 | 17301 | 17301 | 17301 |
| 15102 | 14102 | 18301 | 18301 | 18301 |
| 16101 | 16101 | 17101 | 17201 | 17201 |
| 16102 | 17201 | 18101 | 18201 | 18201 |
| 17101 | 18201 | 17201 | 17101 | 17101 |
| 18101 | 15101 | 18201 | 18101 | 18101 |
| 17201 | 17301 | 15102 | 16102 | 16102 |
| 18201 | 18301 | 17401 | 16101 | 16101 |
| 17301 | 16102 | 18401 | 13101 | 13101 |
| 18301 | 17401 | 16102 | 17401 | 17401 |
| 17401 | 18401 | 16101 | 18401 | 18401 |
| 18401 | 15102 | 13101 | 15101 | 15101 |

| Legend |
|---|
| 90.0 degrees |
| 45.0 degrees |
| 0.0 degrees |
| -45.0 degrees |

### Optimized Stacking Sequence for Hybrid composite2

Table 5.4 Final optimum stacking sequence for Hybrid composite2

**Stacking sequence for STACK 1**

| Iteration 0 | Iteration 1 | Iteration 2 | Iteration 3 | Iteration 4 | Iteration 5 |
|---|---|---|---|---|---|
| 11101 | 12101 | 13201 | 16101 | 13201 | 13201 |
| 12101 | 11101 | 16101 | 13101 | 16101 | 16101 |
| 13101 | 17101 | 13101 | 17101 | 13101 | 13101 |
| 14101 | 18101 | 12201 | 18101 | 17101 | 17101 |
| 15101 | 13101 | 11201 | 15101 | 18101 | 18101 |
| 16101 | 12201 | 17101 | 14101 | 15101 | 15101 |
| 17101 | 11201 | 18101 | 12101 | 14101 | 14101 |
| 18101 | 17201 | 15101 | 11101 | 12101 | 12101 |
| 11201 | 18201 | 14101 | 17201 | 11101 | 11101 |
| 12201 | 14101 | 12101 | 18201 | 17201 | 17201 |
| 13201 | 12301 | 11101 | 13201 | 18201 | 18201 |
| 17201 | 11301 | 17201 | 12201 | 12201 | 12201 |
| 18201 | 17301 | 18201 | 11201 | 11201 | 11201 |
| 11301 | 18301 | 17301 | 17301 | 17301 | 17301 |
| 12301 | 16101 | 18301 | 18301 | 18301 | 18301 |
| 17301 | 12401 | 12301 | 12301 | 12301 | 12301 |
| 18301 | 11401 | 11301 | 11301 | 11301 | 11301 |
| 11401 | 15101 | 17401 | 17401 | 17401 | 17401 |
| 12401 | 17401 | 18401 | 18401 | 18401 | 18401 |
| 17401 | 18401 | 12401 | 12401 | 12401 | 12401 |
| 18401 | 13201 | 11401 | 11401 | 11401 | 11401 |

| Legend |
|---|
| 90.0 degrees |
| 45.0 degrees |
| 0.0 degrees |
| -45.0 degrees |

### 5.4.4 Stress analysis result for Aluminium blade

For Aluminium propeller blade the displacement and von Mises stress are represented in Figures 5.22 and 5.23 .The maximum deflection at the tip of the blade is 0.9395mm.But the stress is maximum near the root of the blade (104.7 MPa).

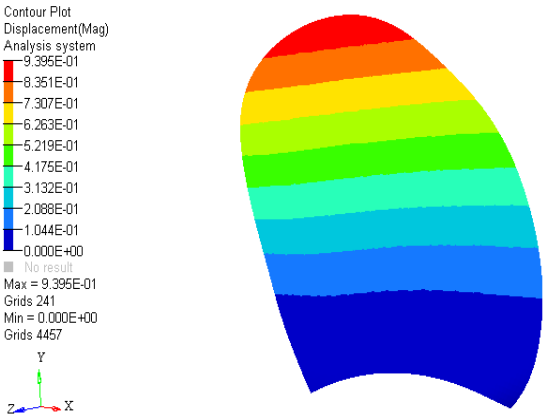


Figure 5.22: Deformed model of Aluminium propeller blade (mm)

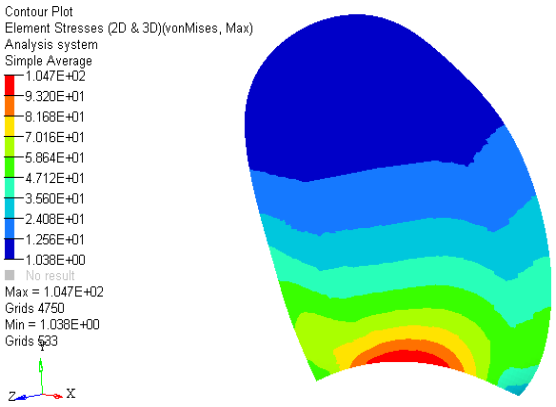


Figure 5.23: Maximum von Mises stress for Aluminium propeller blade (MPa)

Table 5.5 Stress analysis result for composite blade before optimization

| Parameter | Aluminium | E-glass epoxy | Carbon epoxy | Hybrid comp1 | Hybrid comp2 |
|---|---|---|---|---|---|
| Displacement(mm) | 0.939 | 4.000 | 1.471 | 1.828 | 2.833 |
| Von Mises stress (MPa) | 104.70 | 102.720 | 112.304 | 150.700 | 119.004 |
| Major principal (MPa) | 118.30 | 112.20 | 117.602 | 158.120 | 125.701 |
| Minor principal (MPa) | 40.531 | 47.650 | 50.261 | 54.370 | 38.904 |
| X-component (MPa) | 117.42 | 101.50 | 92.750 | 112.200 | 84.225 |
| Y-component (MPa) | 114.93 | 108.65 | 107.010 | 98.304 | 125.520 |
| XY-component (MPa) | 16.911 | 37.570 | 48.391 | 62.910 | 25.810 |
| Maximum shear (MPa) | 39.101 | 42.880 | 53.130 | 71.001 | 48.651 |

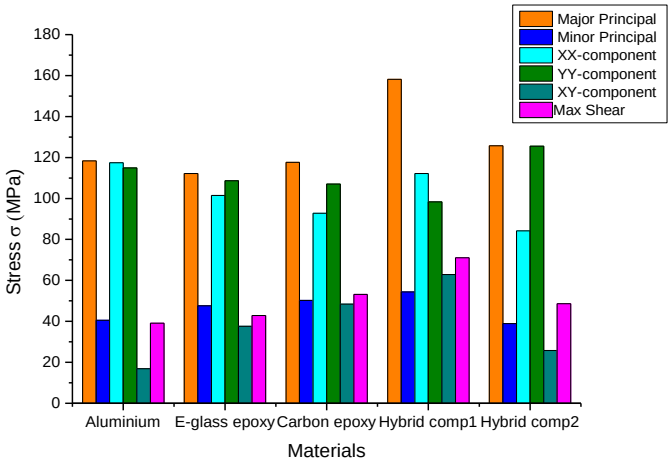


Figure 5.24: Stress comparisons (MPa) between various materials before optimization

Table 5.6 Stress analysis result for composite blade after optimization

| Parameter | Aluminium | E-glass epoxy | Carbon epoxy | Hybrid comp1 | Hybrid comp2 |
|---|---|---|---|---|---|
| Displacement(mm) | 0.939 | 3.882 | 1.315 | 3.602 | 2.485 |
| Von Mises stress(MPa) | 104.70 | 118.000 | 124.000 | 166.500 | 177.900 |
| Major principal (MPa) | 118.30 | 131.400 | 116.100 | 191.201 | 186.600 |
| Minor principal (MPa) | 40.531 | 34.970 | 44.291 | 81.740 | 22.621 |
| X-component (MPa) | 117.42 | 130.801 | 112.021 | 188.000 | 75.081 |
| Y-component (MPa) | 114.93 | 104.900 | 92.590 | 133.204 | 185.404 |
| XY-component(MPa) | 16.911 | 24.700 | 25.541 | 50.761 | 26.661 |
| Maximum shear (MPa) | 39.101 | 48.530 | 50.910 | 56.730 | 83.880 |

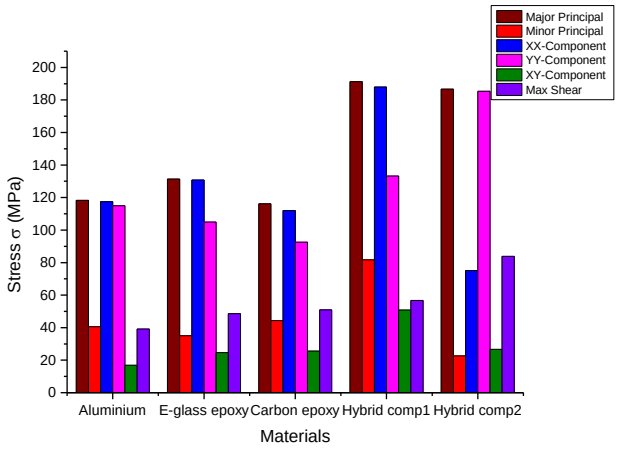


Figure 5.25: Stress comparisons (MPa) between various materials after optimization

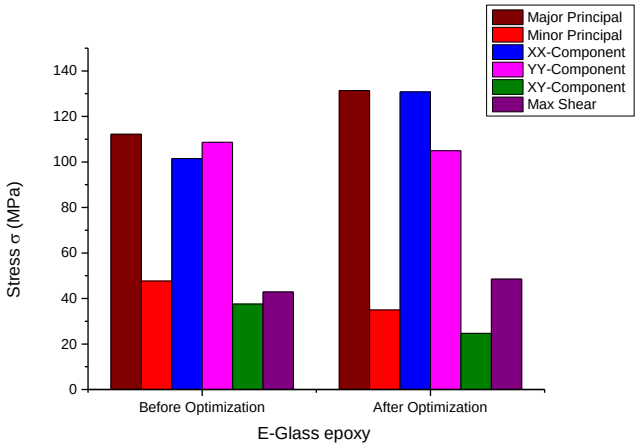


Figure 5.26: E-Glass Stress (MPa) comparison for optimum sequence

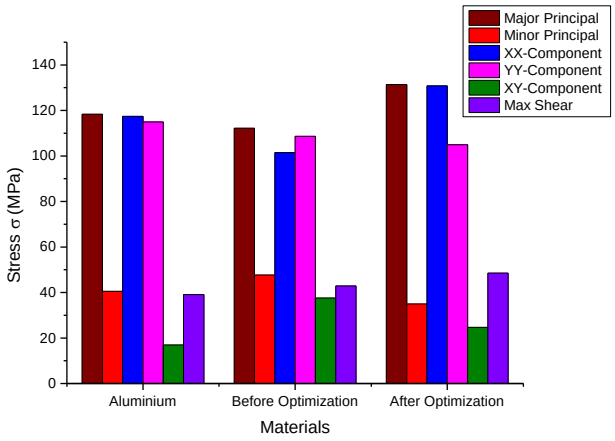


Figure 5.27: Stress Comparison (MPa) between conventional and composite material

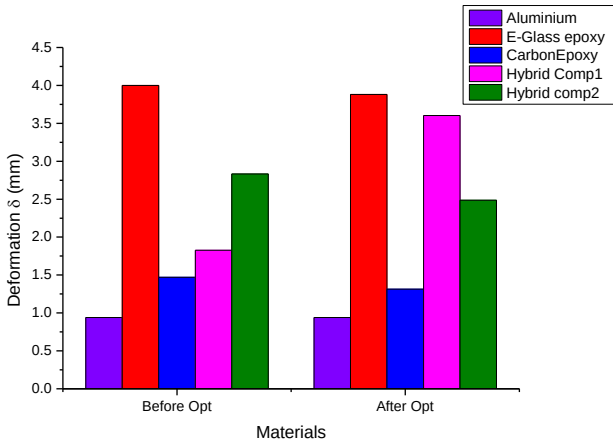


Figure 5.28: Deformation comparison (mm) for conventional and composite materials

Table 5.7 Modal analysis result for composite blade before optimization

| Mode No | Aluminium (Hz) | E-glass(Hz) | Carbon(Hz) | Hybrid comp1(Hz) | Hybrid comp2(Hz) |
|---|---|---|---|---|---|
| 1 | 557.639 | 305.921 | 577.397 | 482.172 | 386.770 |
| 2 | 1857.749 | 1039.598 | 1929.705 | 1519.281 | 1366.999 |
| 3 | 2063.317 | 1202.868 | 2341.177 | 1867.775 | 1589.908 |
| 4 | 3853.943 | 2123.408 | 3968.402 | 3078.867 | 2814.898 |
| 5 | 4943.645 | 2842.821 | 5423.187 | 4469.561 | 3542.176 |
| 6 | 6871.660 | 3770.276 | 7047.436 | 5566.235 | 4686.968 |

Table 5.8 Modal analysis result for composite blade after optimization

| Mode No | Aluminium (Hz) | E-glass(Hz) | Carbon(Hz) | Hybrid comp1(Hz) | Hybrid comp2(Hz) |
|---|---|---|---|---|---|
| 1 | 557.639 | 313.319 | 596.366 | 379.776 | 395.264 |
| 2 | 1857.749 | 1067.018 | 1932.699 | 1347.770 | 1318.526 |
| 3 | 2063.317 | 1165.999 | 2274.462 | 1607.904 | 1374.517 |
| 4 | 3853.943 | 2194.583 | 4203.503 | 2910.398 | 2578.716 |
| 5 | 4943.645 | 2820.119 | 5395.665 | 3786.580 | 3224.728 |
| 6 | 6871.660 | 3890.307 | 6821.618 | 4985.010 | 4735.560 |

Table 5.9 Inter laminar shear stress result comparison for composite blade with and without optimization

| Number of layers | XZ-component stress (MPa) | | YZ-component stress (MPa) | |
|---|---|---|---|---|
| | Before Optimization | After Optimization | Before Optimization | After Optimization |
| 2 | 0.396 | 0.270 | 0.118 | 0.131 |
| 4 | 0.183 | 0.183 | 0.183 | 0.183 |
| 6 | 0.183 | 0.183 | 0.183 | 0.183 |
| 8 | 0.183 | 0.183 | 0.183 | 0.183 |

The stresses induced in the blades before and after optimization are shown in Tabular and graphical form (Tables 5.5, 5.6 and Figures 5.24 through 5.28).Comparison for natural frequency for different matrices before and after optimization are shown in Tables 5.7 to 5.8.The operating frequency is maximum for Carbon epoxy. The inter laminar shear stress for E-glass epoxy before and after optimization is marginally higher in YZ component (Table 5.9).

The first three mode shapes for Aluminium Propeller blade are shown in Figure 5.29 to 5.31.A comparison has been made between metallic and composite Propeller with and without optimization are shown in Figure 5.32 and 5.33.

The first bending frequency for aluminium propeller blade is 557.639 Hz (Figure 5.31), similarly, for first twisting frequency the value is 1857.749 Hz (Figure 5.30) and second bending frequency is 2063.31 Hz (Figure 5.31).These results are also named in Tables 5.7 and 5.8 respectively. The operating frequency is maximum for the carbon epoxy before and after optimization of the propeller blade (Figures 5.32 and 5.33).

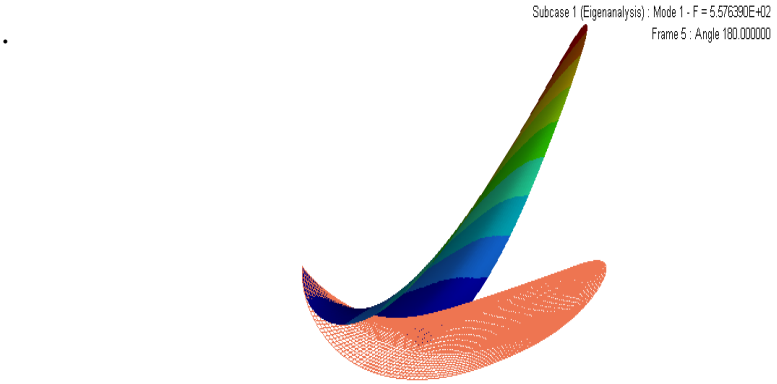


Figure 5.29: First bending mode shape of Aluminium propeller blade

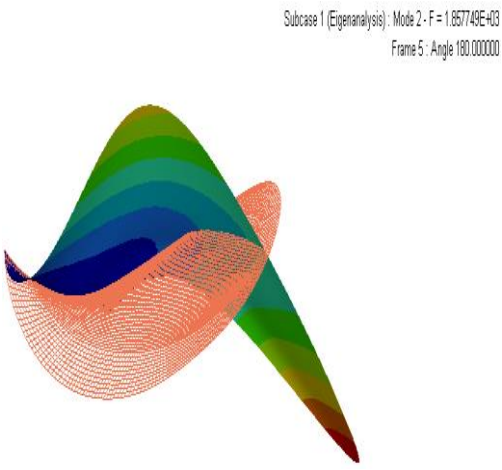


Figure 5.30: First twisting mode shape of Aluminium propeller blade

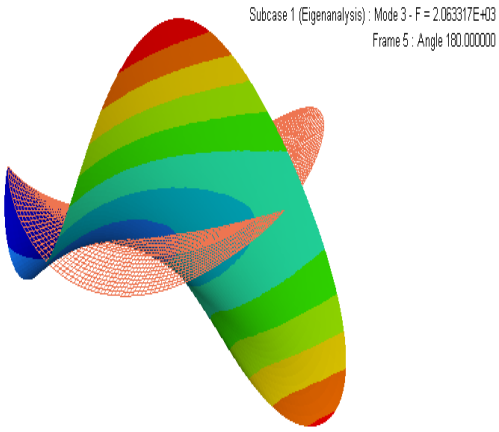


Figure 5.31: Second bending mode shape of Aluminium propeller blade

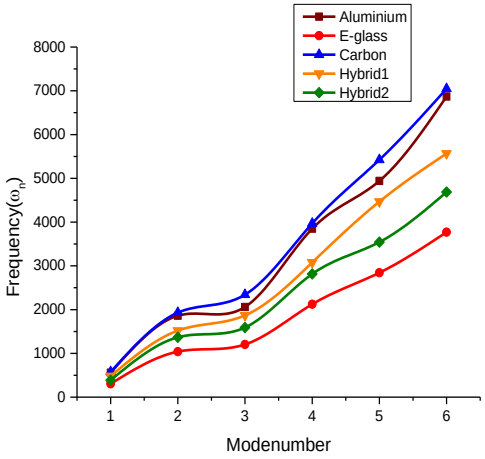


Figure 5.32: Mode number vs Frequency (before optimization)

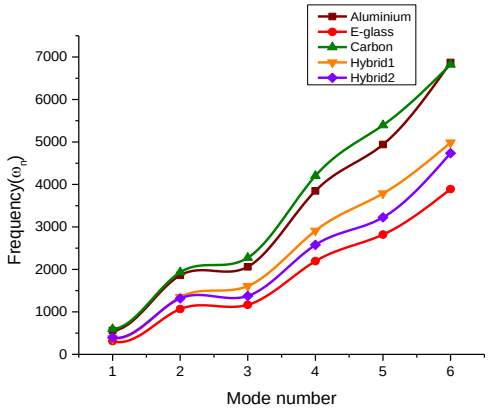


Figure 5.33: Mode number vs Frequency (after optimization)

## 5.5 Conclusions

A methodological procedure for obtaining optimized propeller blade made from composite materials is presented.

1. The phases of optimization stated regarding three steps of the baseline composite are presented. The concept of super ply and ply drop off are incorporated.
2. By stringing these 3 phases of techniques together, the Optistruct software provides a comprehensive and unique process for the design and optimization of composite laminates.
3. The free size optimization for composites allows a true concept level design synthesis of plies. A new ply and stack based modelling technique is employed that simplifies laminate representation and facilitates the ply bundle sizing optimization followed by the ply shuffling optimization which makes the process unique.
4. From the previous design phases, the process is automated and integrated into Hyperworks by generating the input data required for a subsequent phase.
5. Additionally the process also allows for flexibility in case any modifications are to be required. Throughout the design process, manufacturability constraints and behavioral constraints are preserved to arrive at a feasible design and ensure a meaningful process.
6. A sizing optimization is performed for minimum weight. Manufacturing constraints are included in the sizing optimization. Total thicknesses of 0°, +45$^{o}$, -45$^{o}$ and 90$^{o}$ plies are presented. Finally, a ply stacking optimization is performed taking into account the manufacturing constraints.
7. Weight savings of 27% are achieved in the structural load case considered using Hypermesh software. The maximum allowable displacement is kept less than or equal to 0.939mm and Eigenvalue frequencies not less than 550 Hz, are achieved in the final optimized values.

# Chapter 6

# Discussions

The numerical and experimental results presented in Chapter-3, 4 and 5 in response to the corresponding theories have been compared and analysed. The following salient points from the above analysis have been discussed.

## 6.1 Open water characteristics of Marine propeller blade

From the theoretical and numerical analysis as presented in Chapter-3, the following observations are made for the open water characteristics of the marine propeller blade.

1. The open water characteristics of B-series 4 bladed marine propeller are predicted computationally using FLUENT solver and the results obtained are validated by standard B-series data.
2. With varying advanced ratios from 0.5 to 1.3 (see Table 3.10 and Table 3.11) the performance characteristics of propeller stated in terms of J, $K_T$, $K_Q$, as the requirement are determined with varying rotational speed (800 rpm to 2000 rpm) and advanced velocity (2m/s to 6.12m/s).
3. The maximum open water efficiency obtained for computational results is 59.8% (see Table 3.11) for advanced coefficient of 0.743 (with N=23.33rps) and advanced velocity of 6.12m/s. With varying advanced velocity and constant rotational speed, the maximum open water efficiency found to be 60.1% (see Table 3.14) for J=0.822 corresponding $V_a$=4.5m/s and N=15.5rps.
4. The minimum cavitation inception point (min abs pressure $<1.72x10^3$) for Aluminium propeller blade is observed to occur at J=0.422 and rotational speed N=1490 rpm (see Figure 3.25). For this cavitational inception speed, the finite element analysis is performed for determining the deformations and corresponding stresses.

## 6.2 Static analysis of Marine propeller blade

Numerical results have been presented for evaluating the stresses and corresponding deformations induced in the marine propeller in Chapter-4. The results obtained from the Burrill theoretical method for computing the stress is used as a reference to compute and compare the stress and deformations obtained due to thrust and torque applied on propeller blade. The following observations are made from the numerical and theoretical analysis.

1. From Burrill method of maximum stress determination, the maximum stress obtained for the metallic propeller blade is 2442.47 MPa (section 4.8.2). Similarly, the maximum stress induced in the propeller blade due to thrust and torque distribution on propeller blade is 2496.8 MPa (section 4.8.3). The percentage variation between the obtained values of the theoretical and numerical result is about 1.82% which shows that the numerical procedure followed to obtain the stress, and deformations are correct.
2. The maximum deformation for composite propeller blade was found to be around 0.327mm (see Figure 4.26) for all layers which is same as than that of Aluminium propeller i.e. 0.082mm, (see Figure 4.18) which shows that by changing the layup sequence further composite materials can be made much stiffer than Aluminium propeller.
3. Maximum induced von Mises stress for aluminium propeller was found to be 11 MPa (see Figure 4 .19).
4. Interlaminar shear stresses were calculated for composite propeller by incorporating a different number of layers viz. 2,4,6,8 (see Table 4.5) and was found that the percentage variation between 2 and 6 layers was 0.285% along xz planes and 0.452% along yz-axes, which shows that there is strong bonding between the layers and there's no peel-off.

## 6.3 Free vibrational analysis of Marine propeller

From the experimental and the numerical results as presented in Chapter-4, the following observations are made for the dynamic characteristics of propeller blade fabricated with both metallic and composite materials.

## Aluminium Propeller blade

1. From the Eigenvalue analysis, the first critical speed for Aluminium propeller blade using mathematical code, numerical solver ANSYS and Optistruct are 487.09, 671.92 Hz and 676 Hz and experimental is 686.66 Hz (see Table 4.13). The first bending frequency and its corresponding mode shape is shown in the Figure 4.50, and the percentage variation between numerical and experimental values is 1.4%.
2. The illustrations shown in the Figure 4.42 represents the fabricated model of the single propeller blade with hub for experimental and the corresponding Figure 4.43 to Figure 4.44 are the single surface model of the propeller modelled for numerical analysis.
3. The Figures 4.45 are modal data selection for all control points, with all accelerometers 1, 2, 3 placed on the blade. The final synthesized and stabilized frequency response function graphs is shown for 4.46 and 4.47.
4. The free vibration anlysis of the Aluminium propeller blade modelled with shell and solid elements and their comparison with experimental values are shown in Table 4.13.The corresponding mode shapes associated with non dimensional frequencies are shown in the Figures 4.49a, 4.49b, 4.49c.The first mode shape represents the first bending; the second mode shape represents the first twisting and the third mode shape represents the second bending correspondingly.The fourth mode shape represents the second twisting, the fifth mode shape represents the combined bending and twisting, and the sixth mode shape represents the edgewise bending and twisting.

## Composite Propeller blade

1. From the Eigenvalue analysis the first critical speed for E-glass epoxy propeller blade with ply sequence $\left(-45°/45°/90°/0°\right)_s$ using Mathematical code, numerical solver ANSYS and experimental is 319.5 Hz, 415.41Hz and 460.31Hz are showin in Table 4.15.The first bending frequency corresponding its mode shape are shown in the Figure 4.54 and the percentage variation between numerical and experimental values is 1.4%.

2. The illustrations shown in the Figure 4.50 represents the fabricated model of the single propeller blade with hub for experimental.
3. The Figures 4.51 are modal data selection for all control points, with all accelerometers 1, 2, 3 placed on the blade. The final synthesized and stabilized frequency response function graphs is shown for 4.52 and 4.53.
4. The free vibration analysis of E-glass epoxy composite blade modelled with shell and solid elements and their comparison with experimental values are shown in Table 4.15.The non-dimensional frequencies of the E-glass epoxy propeller blade are shown in the Table 4.16.

## 6.4 Optimization of Composite propeller blade

From the numerical results as presented in Chapter-5, the following observations are made for the optimization of composite propeller blade modelled with both hybrid and non-hybrid composites. The entire optimization scheme is represented in 3-way step process whereby stringing these operations together a unique and comprehensive state of the process for design and optimization with incorporation of ply drops and concept of super ply for composite can be achieved.

1. In the initial level of the design phase of optimization for E-glass epoxy material propeller (see Figure 5.4) blade ply bundle sizing is done, with an even distribution of elemental thickness over the entire structure and concept of super ply is used. The manufacturing constraints incorporated in this phase are the volume fraction and the deformation. The load constraints considered are the pressure distribution and hub fixed for all degrees of freedom.
2. The process of the previous design phase is carried over to the second phase of design optimization scheme, (see Figure 5.5) with automatic generation of data for the subsequent phase. The optimization of ply stacking is done in this phase, to take into account of manufacturing constraints. The manufacturing constraints considered in this phase are the minimum weight and Eigen-frequencies.
3. In the final phase of optimization scheme, (see Figure 5.7) an optimal stacking sequence is to be determined from composite shuffling optimization. With the ply sequence carried from composite sizing phase composite plies are shuffled by updating the stack card and the design parameters are preserved.

4. Similar procedure is followed for Carbon epoxy and hybrid composite materials. The optimal stacking sequences after final phase optimization for hybrid and non-hybrid composite materials are as follows.
5. For the balanced sequence $[-45°/45°/90°/0°]_S$ taken as a base reference (see Table 5.1), the final optimal stacking sequence obtained for E-glass epoxy material blade is $[90°/\pm45°/0_4°/\pm45°/90_3°/\pm45_2°/0_2°/\pm45°]$
6. Again the balanced sequence $[-45°/45°/90°/0°]_S$ taken as a base reference (see Table 5.2),the final optimal stacking sequence obtained for Carbon-epoxy material blade is $[0°/\pm45_6°/90_2°/\pm45°/90°/\pm45°/90°]$.
7. Further, the balanced sequence $[-45°/45°/90°/0°]_S$ taken as a base reference (see Table 5.3) the final optimal stacking sequence obtained for Hybrid composite having E-glass epoxy properties applied at $[0°,90°]$ and Carbon epoxy properties applied at $[\pm45°]$ is $[\pm45°/0_3°/\pm45_3°/90_3°/\pm45°/0°]$.
8. For the balanced sequence $[-45°/45°/90°/0°]_S$ taken as a base reference (see Table 5.4) the final optimal stacking sequence obtained for Hybrid composite having E-glass epoxy properties applied at $[\pm45°]$ and Carbon epoxy properties applied at $[0°,90°]$ is $[90_3°/\pm45°/0_2°/\pm45_7°]$.

## 6.5 Effect of Optimized stacking sequence on Strength analysis

### Stress analysis

The effect of optimized stacking sequence obtained from $[-45°/45°/90°/0°]_S$ ply sequence for both hybrid and non-hybrid composite materials resulted in drastic changes in both stress and Eigenvalue analysis compared with Aluminium propeller blade.

1. By using optimized stacking sequence the percentage of weight savings for E-glass epoxy material is 23.40%, for Carbon being 38.71%, for Hybrid composite having E-glass epoxy properties applied at $[0°,90°]$ and Carbon epoxy properties applied at $[\pm 45°]$ is 44.08% and for Hybrid composite having E-glass epoxy properties applied at $[\pm 45°]$ and Carbon epoxy properties applied at $[0°,90°]$ is 24.22%, since the mass of single Aluminium propeller blade is 5.231Kg.
2. The reduced percentage in deformation after optimized stacking sequence for E-glass epoxy material is 2.95%, for Carbon being 1.06%, for Hybrid composite having E-glass epoxy properties applied at $[\pm 45°]$ and Carbon epoxy properties applied at $[0°,90°]$ is 12.28%, where as an increase in deformation is observed for Hybrid composite having E-glass epoxy properties applied at $[0°,90°]$ and Carbon epoxy properties applied at $[\pm 45°]$ is 49.25%.
3. An incremental percentage has been observed in von Mises stress for optimized stacking sequence for all the composite materials in comparisons to Aluminium propeller blade. The increased stress values in percentage are 13.55% for E-glass epoxy, 9.677% for Carbon-epoxy, 9.638% for Hybrid composite having E-glass epoxy properties applied at $[\pm 45°]$ and Carbon epoxy properties applied at $[0°,90°]$ and 32.76% for Hybrid composite having E-glass epoxy properties applied at $[\pm 45°]$ and Carbon epoxy properties applied at $[0°,90°]$.
4. For major Principal stress Carbon-epoxy attained same value of stress before and after optimization ,whereas E-Glass epoxy, Hybrid composites attained slight higher values after optimization, E-glass epoxy about 14.503%, Hybrid composite having E-glass epoxy properties applied at $[\pm 45°]$ and Carbon epoxy properties applied at $[0°,90°]$ about 17.27%, Hybrid composite having E-glass epoxy properties applied at $[\pm 45°]$ and Carbon epoxy properties applied at $[0°,90°]$, about 32.795%.

5. For minor Principal stress E-Glass epoxy attained 26.66% and Hybrid composite having E-glass epoxy properties applied at $[\pm 45°]$ and Carbon epoxy properties applied at $[0°, 90°]$, attained 42.10% reduced value of stress after optimization, whereas Carbon-epoxy and Hybrid composite having E-glass epoxy properties applied at $[\pm 45°]$ and Carbon epoxy properties applied at $[0°, 90°]$ attained 12% and 33.33% increased value of stress after optimization.
6. For stress component along X-axis an increment of 22.30% for E-Glass epoxy,17.85% for Carbon epoxy,40.42% for Hybrid composite having E-glass epoxy properties applied at $[0°, 90°]$ and Carbon epoxy properties applied at $[\pm 45°]$ is attained whereas for Hybrid composite having E-glass epoxy properties applied at $[\pm 45°]$ and Carbon epoxy properties applied at $[0°, 90°]$ got reduction in stress value of 10.71%.
7. For stress component along Y axis a reduction of 3.07% for E-Glass epoxy, 14.01% for Carbon epoxy is achieved whereas for Hybrid composite having E-glass epoxy properties applied at $[0°, 90°]$ and Carbon epoxy properties applied at $[\pm 45°]$ and Hybrid composite having E-glass epoxy properties applied at $[\pm 45°]$ and Carbon epoxy properties applied at $[0°, 90°]$ achieved gain in stress value of 26.31% and 32.43%.
8. For stress component along XY axis a reduction of 35.13% for E-Glass epoxy, 47.91% for Carbon epoxy, 19.35% for Hybrid composite having E-glass epoxy properties applied at $[0°, 90°]$ and Carbon epoxy properties applied at $[\pm 45°]$ is achieved whereas Hybrid composite having E-glass epoxy properties applied at $[\pm 45°]$ and Carbon epoxy properties applied at $[0°, 90°]$ achieved closure value of stress similar to that of before optimization.
9. Taking shear component of stress into consideration increase in stress values of 12.5% for E-glass epoxy and 42.16% for Hybrid composite having E-glass epoxy properties applied at $[\pm 45°]$ and Carbon epoxy properties applied at $[0°, 90°]$ is

obtained whereas reduction in stress value of 5.61% for Carbon epoxy and 21.11% for Hybrid composite having E-glass epoxy properties applied at $[0°,90°]$ and Carbon epoxy properties applied at $[\pm 45°]$ is achieved.

10. Taking the optimized stacking sequence into consideration for E-glass epoxy material the interlaminar shear stress along XZ component is reduced by 31.8% and a marginal increment of 9.92% along YZ component is observed.

## Free Vibration analysis

The vibrational characteristics of marine propeller made of both metallic and fiber reinforced plastics materials of E-Glass epoxy, carbon epoxy and Hybrid are analyzed by using shell type elements. By using the optimized stacking sequence, obtained for these materials their effects on the non-dimensional fundamental frequencies and frequency ratios of the shell type blade have been discussed in detail. Some important observations are noticed in the following line after examining the developed model for different parameters.

1. With E-glass epoxy having $[90°/\pm 45°/0_4°/\pm 45°/90_3°/\pm 45_2°/0_2°/\pm 45°]$ as the optimized stacking sequence in replacement to Aluminum material increase in first bending, first twisting, second twisting, combined bending-twisting, edgewise bending-twisting mode frequencies with 2.5-3.0% are observed (see Table 5.7 and Table 5.8) whereas the second bending and combined bending-twisting mode frequency is reduced by 0.7-3.7%.
2. The replacement of Carbon-epoxy material with an optimized stacking sequence of $[0°/\pm 45_6°/90_2°/\pm 45°/90°/\pm 45°/90°]$ for Aluminium material resulted in increase in first bending, first twisting, and second twisting and combined bending -twisting frequencies with 3-5% are observed, (see Table 5.7 and Table 5.8) whereas second bending mode and edgewise bending-twisting frequencies are reduced by 0.5-3 %.
3. For Hybrid composite with $[\pm 45°/0_3°/\pm 45_3°/90_3°/\pm 45°/0°]$ optimum stacking sequence resulted in a decrease in all modal frequencies about 10-54.5% are observed when compared to before optimization (see Table 5.7 and Table 5.8) .

4. For Hybrid composite with $[90_3° / \pm 45° / 0_2° / \pm 45_7°]$ optimum stacking sequence resulted in an increase in first bending, first twisting and edgewise bending-twisting mode frequencies about 1-2.2% and second bending, second twisting and combined bending-twisting mode frequencies are reduced by 3-13.5% (see Table 5.7 and Table 5.8).

# Chapter 7

# Conclusions and Future Scope of Work

## 7.1 Conclusions

The objectives of the present research work have been outlined in chapter-1. Taking the objectives into consideration as a major factor, theoretical, numerical and experimental analyses have been carried out in chapters 3, 4 and 5. In depth discussions of the numerical and experimental results are presented in chapter 6. From the theoretical, numerical, experimental results and discussions the conclusions drawn are depicted below.

1. The open water characteristics of Aluminum propeller blade are computed using FLUENT solver. These open water characteristics are important which specifies the suitability and applicability of marine propeller for underwater conditions. These characteristics are compared with standard series data.
2. The maximum open water efficiency with varying advanced ratios, rotational speeds, and advanced velocities are evaluated, and the cavitation inception point for a metallic propeller for corresponding rotational speed, and advanced velocity are determined.
3. The maximum stress developed in the propeller blade are determined numerically and compared theoretically with Burrill method of stress determination.
4. The maximum deformations for metallic and composite propeller blade are determined using numerical solver Ansys using shell 181elements.
5. The free vibrational characteristics of both metallic and composite propeller blade are carried out experimentally and numerically using Ansys solver. The non-dimensional frequencies of the propeller in terms of mode shapes are plotted. From the results, it shows that the Aluminium propeller has got higher operating frequencies when compared to the composite propeller with ply sequence $[-45°/45°/90°/0°]_S$.

6. Based on the optimized stacking sequence obtained if an Aluminium propeller blade is to replace with composite material taking the below factors into consideration the following conclusions are drawn.
    a. Taking weight factors into consideration if a propeller blade made of composite material is to be designed the Hybrid composite having E-glass epoxy properties applied at $[0°, 90°]$ and Carbon epoxy properties applied at $[\pm 45°]$ with optimized stacking sequence $[\pm 45° / 0_3° / \pm 45_3° / 90_3° / \pm 45° / 0°]$ has 44.08% of weight savings compared to other composite materials and metallic one.
    b. For a propeller blade made of Aluminium material is to be replaced with composite material for reduced deformations and stress values (which are obtained from CFD pressure distribution) and are to be considered as primary objective functions, Hybrid composite having E-glass epoxy properties applied at $[\pm 45°]$ and Carbon epoxy properties applied at $[0°, 90°]$ with optimized stacking sequence $[90_3° / \pm 45° / 0_2° / \pm 45_7°]$ achieved lower values of deformation and stress values compared to other composite materials.
    c. If the objective function of a composite propeller blade replaced from Aluminium is to operate at higher values of operating frequencies' considered for both bending, twisting, combined bending-twisting and edgewise bending-twisting mode frequencies then Carbon epoxy with optimized stacking sequence $[0° / \pm 45_6° / 90_2° / \pm 45° / 90° / \pm 45° / 90°]$ attained higher values of frequencies.

## 7.2 Future Work

1. More amount of research can be conducted about the refinement of mesh and more particularly an improved way of combining the blade and hub of propeller inside the block. For attaining a close form of results tetrahedral element mesh is replaced with hexahedral elements.

2. Further trials can be conducted over varying advanced velocities and rotational speed in order to have conclusive results in comparison with experimental results. This additional analysis provides more amount of information for enhancement of open water efficiency and distribution of pressure over the blades.
3. By further changing the layup sequence, by proper tailoring composite materials at specified ply angles, varying the number of layers the desired vibration characteristics can be attained for the blade without modifying the shape, deformation and stresses can be further reduced which can result in further optimization of the blade.
4. Using the optimized sequence as a base reference, further CFD analysis can be carried out for hybrid and non-hybrid composites to find out the un-deflected geometry of the marine propeller.

## 7.3 Fabrication Limitations of using Present Method

1. Resin mixing, laminate resin contents, and laminate quality are very dependent on the skills of laminators. Low resin content laminates cannot usually be achieved without the incorporation of excessive quantities of voids.
2. Health and safety considerations of resins. The lower molecular weights of hand lay-up resins generally mean that they have the potential to be more harmful than higher molecular weight products. The lower viscosity of the resins also means that they have an increased tendency to penetrate clothing.
3. Resins need to be low in viscosity to be workable by hand. This generally compromises their mechanical/thermal properties due to the need for high diluent/styrene levels.

# Bibliography

[1] S.Ekinci, “A Practical Approach for Design of Marine Propellers with Systematic Propeller Series,” Brodogradnja, vol. 62, no. 2, pp. 123–129, 2011.

[2] L. C. Burrill, “Calculation of Marine Propeller Performance Characteristics,” Trans North East Coast Inst. Eng. Shipbuild., vol. Vol. 60 , 44 1943.

[3] L.C.Burrill and C. S. Yang, “The Effect of Radial-Pitch Variation on the Performance of a Marine Propeller,” J. Am. Soc. Nav. Eng., vol. 65, no. 4, pp. 732–740, Nov. 1953.

[4] M. Felli, R. Camussi, and F. Di Felice, “Mechanisms of evolution of the propeller wake in the transition and far fields,” J. Fluid Mech., vol. 682, pp. 5–53, Sep. 2011.

[5] A.Mihaela, “Developments in the design of ship propeller,” Sci. Bull. Politeh. Univ. Timisoara Trans. Mech. Univ. Galati, 2005. [17] H. T. KIM and F. STERN, “Viscous flow around a propeller-shaft configuration with infinite-pitch rectangular blades,” J. Propuls. Power, vol. 6, no. 4, pp. 434–444, 1990.

[6] H.Miyata, “Time marching CFD simulation for moving boundary problems,” Proc. 21st Symp. Nav. Hydrodyn., pp. 291–311, 1997.

[7] S. Subhas, V. F. Saji, S. Ramakrishna, and H. N. Das, “CFD analysis of a propeller flow and cavitation,” Int. J. Comput. Appl., vol. 55, no. 16, 2012.

[8] J. Martínez-Calle, L. Balbona-Calvo, J. González-Pérez, and E. Blanco-Marigorta, “An open water numerical model for a marine propeller: A comparison with experimental data,” in ASME 2002 Joint US-European Fluids Engineering Division Conference, 2002, pp. 807–813.

[9] J. B. Brandt and M. S. Selig, “Propeller performance data at low reynolds numbers,” in 49th AIAA aerospace sciences meeting, 2011, pp. 2011–1255.

[10] E. Benini, “Significance of blade element theory in performance prediction of marine propellers,” Ocean Eng., vol. 31, no. 8, pp. 957–974, 2004

[11] F. E. Weick, “Full-Scale Wind-Tunnel Tests on Several Metal Propellers Having Different Blade Forms,” Jan. 1931.

[12] F. E. Weick, “Full Scale Wind Tunnel Tests with a Series of Propellers of Different Diameters on a Single Fuselage,” 1930.

[13] J.E.Kerwin, “Marine Propellers,” Annu. Rev. Fluid Mech., vol. 18, no. 1, pp. 367–403, 1986.

[14] D.T.Valentine, "Reynolds-Averaged Navier-Stokes Codes and Marine Propulsor Analysis," Hydrodyn. Dir. Res. Dev. Rep. Carderock Div. Nav. Surf. Warface Cent. Bethesda MD USA, p. 42, Sep. 1993.

[15] J. E. Kerwin and C. S. Lee, "Prediction of steady and unsteady marine propeller performance by numerical lifting-surface theory," Publ. Soc. Nav. Archit. Mar. Eng., Sep. 1978.

[16] Streckwall, H, "A Method to Predict the Extent of Cavitation on Marine Propellers by Lifting-surface-theory," Int. Symp. Cavitation Sendai Jpn., vol. 1986.

[17] H. T. KIM and F. STERN, "Viscous flow around a propeller-shaft configuration with infinite-pitch rectangular blades," J. Propuls. Power, vol. 6, no. 4, pp. 434–444, 1990.

[18] H.Ghassemi and P. Ghadimi, "Computational hydrodynamic analysis of the propeller–rudder and the AZIPOD systems," Ocean Eng., vol. 35, no. 1, pp. 117–130, 2008.

[19] H.Ghassemi, R. Shademani, and A. Ardeshir, "Hydrodynamic characteristics of the surface-piercing propeller for the planing craft," in ASME 2009 28th International Conference on Ocean, Offshore and Arctic Engineering, 2009, pp. 589–595.

[20] H.Ghassemi, "Hydrodynamic performance of coaxial contra-rotating propeller (CCRP) for large ships," Pol. Marit. Res., vol. 16, no. 1, pp. 22–28, 2009.

[21] H.Ghassemi, M. Ghassabzadeh, and M. G. Saryazdi, "Effect of material on hydro-elastic behaviour of marine propeller by using BEM-FEM hybrid software," Pol. Marit. Res., vol. 20, no. 4, pp. 62–70, 2013.

[22] H.Ghassemi, "The Effect of Wake Flow and Skew Angle on the Ship Propeller Performance."

[23] Y.L.Young, "Fluid–structure interaction analysis of flexible composite marine propellers," J. Fluids Struct., vol. 24, no. 6, pp. 799–818, Aug. 2008.

[24] Y.L.Young, "Hydroelastic behavior of flexible composite propellers in wake inflow," presented at the 16th International Conference on Composite Materials, ICCM-16 - "A Giant Step Towards Environmental Awareness: From Green Composites to Aerospace," 2007.

[25] Y.L.Young and B. R. Savander, "Numerical analysis of large-scale surface-piercing propellers," Ocean Eng., vol. 38, no. 13, pp. 1368–1381, 2011.

[26] P. Dymarski, "Computations of the propeller open water characteristics using the SOLAGA computer program. Predictions of the cavitation phenomenon," Arch. Civ. Mech. Eng., vol. 8, no. 1, pp. 15–25, Jan. 2008.

[27] M.N.Senthil Prakash and V.A. Subramanian, "Simulation of propeller- hull interaction using RANSE solver," Int. J. Ocean Clim. Syst., vol. Vol.1, No.3, 4., pp. 189–203, 2009.

[28] M.N.Senthil Prakash and V.A. Subramanian, "Body force based simulation of propeller hull interaction," 3rd Int. Conf. Ocean Eng. ICOE 2009Chennai, Feb. 2009.

[29] M.N. Senthil Prakash and Subramanian, V.A, "Optimization of Propeller by Coupled VLM and Ranse Solver Method," 7th Int. Conf. HIPER 2010 Fla. USA, Oct. 2010.

[30] H.J.Lin, W. M. Lai, and Y. M. Kuo, "Effects of Stacking Sequence on Nonlinear Hydroelastic Behavior of Composite Propeller Blade," J. Mech., vol. 26, no. 3, pp. 293–298, Sep. 2010.

[31] N.L.Mulcahy, B. G. Prusty, and C. P. Gardiner, "Hydroelastic tailoring of flexible composite propellers," Ships Offshore Struct., vol. 5, no. 4, pp. 359–370, Oct. 2010.

[32] J.P.A.A.Blasques, C. Berggreen, and P. Andersen, "Hydro-elastic analysis and optimization of a composite marine propeller," Mar. Struct., vol. 23, no. 1, pp. 22–38, 2010.

[33] H. N. Das, "CFD Analysis For Cavitation of a Marine Propeller," Sympsium High Speed Mar. Veh., pp. 72–80, 2008.

[34] Das,H.N. and Jayakumar, L.C.P, "Computational prediction and Experimental validation of the Characteristics of a contra rotating propeller," Proc. NRB Semin. Mar. Hydrodyn. Visakhapatnam India, Feb. 2002.

[35] C.N Banerjee, H.N. Das, and B.Srisudha, "Computational analysis and Experimental Validation of Hull Propulsor Interaction For an Autonomous Under water vehicle(AUV)," Proc. Seventh Asian CFD Conferr. Bangalore India, Nov. 2007.

[36] G.V.Krishna, V.F.Saji, H.N Das, and P.K.Panigrahi, "Accoustic Characterstization of a Benchmark Marine propeller using CFD," Proc. Nav. Symp. AccoustcsNSA-2008 VisakhapatnamIndia, Dec. 2008.

[37] V. Krasilnikov, Z. Zhang, and F. Hong, "Analysis of unsteady propeller blade forces by RANS," in First international symposium on marine propulsors smp, 2009, vol. 9.

[38] A. Chattopadhyay, T. R. McCarthy, and C. E. Seeley, "Decomposition-based optimization procedure for high-speed prop-rotors using composite tailoring," J. Aircr., vol. 32, no. 5, pp. 1026–1033, 1995.

[39] N. M. El Chazly, "Static and dynamic analysis of wind turbine blades using the finite element method," Comput. Struct., vol. 48, no. 2, pp. 273–290, 1993.

[40] S. Bernad, R. Susan-Resiga, S. Muntean, and I. Anton, "Numerical analysis of the cavitating flows," Proc. Romanian Acad. Ser. A, vol. 7, 2006.

[41] D. Sridhar, T. V. K. Bhanuprakash, and H. N. Das, "Frictional Resistance Calculations on a Ship using CFD," Int. J. Comput. Appl., vol. 11, no. 5, pp. 24–31, Dec. 2010.

[42] B.Chang, "Application of CFD to P4119 propeller," 22 Nd ITTC Propeller RANSPanel Method Workshop Fr., 1998.

[43] A.Sanchez Caja, "P4119 RANS calculations at VTT," ITTC Propeller RANSPanel Method Workshop Fr., 1998.

[44] F. Salvatore, L. Greco, and D. Calcagni, "Computational analysis of marine propeller performance and cavitation by using an inviscid-flow BEM model," in Second International Symposium on Marine Propulsors, smp, 2011, vol. 11.

[45] K.Kimura, T. Kawamura, Z. Huang, A. Fujii, and T. Taketani, "Study on unsteady cavitating flow simulation around marine propeller using a RANS CFD code.," 2009.

[46] Takashi Kanemaru and Jun Ando, "Numerical Analysis of Steady and Unsteady Sheet Cavitation on a Marine Propeller Using a Simple Surface Panel Method "SQCM," First Int. Symp. Mar. Propulsors Smp'09 Trondheim Nor., Jun. 2009.

[47] W. H. Choong, K. B. Yeo, F. Tamiri, and K. T. K. Teo, "Outboard Marine Propeller Performance Analysis through CFD Modelling," in 2013 UKSim 15th International Conference on Computer Modelling and Simulation (UKSim), 2013, pp. 310–313.

[48] V.H.Arakeri and A. J. Acosta, "Viscous Effects in the Inception of Cavitation on Axisymmetric Bodies," J. Fluids Eng., vol. 95, no. 4, pp. 519–527, Dec. 1973.

[49] V.H.Arakeri, "Viscous effects on the position of cavitation separation from smooth bodies," J. Fluid Mech., vol. 68, no. 4, pp. 779–799, Apr. 1975.

[50] V.H.Arakeri, J. A. Carroll, and J. W. Holl, "A Note on the Effect of Short and Long Laminar Separation Bubbles on Desinent Cavitation," J. Fluids Eng., vol. 103, no. 1, pp. 28–32, Mar. 1981.

[51] J.H.J.Van der Meulen, "A Holographic Study of the Influence of Boundary Layer and Surface Characteristics on Inception and Developed Cavitation on Axisymmetric Bodies.," Proc. 12th Symp. Nav. Hydrodyn. Wash. DC, pp. 443–451, 1998.

[52] J.H.J.Van der Meulen, "Boundary Layer and Cavitation Studies of NACA 16–012 and NACA 4412 Hydrofoils," Proc. 13th Symp. Nav. Hydrodyn. Tokyo Jpn., pp. 195–219, 1980.

[53] K.Randle and P. Bull, "Predictions of the Thrust and Torque Performance for two Propeller Blades Using Computational Fluid Dynamics," 4th Int. Conf. Mar. Hydrodyn. Mar. CFD, Mar. 2005.

[54] W.Wienken, J. Stiller, and A. Keller, "A Method to Predict Cavitation Inception Using Large-Eddy Simulation and its Application to the Flow Past a Square Cylinder," J. Fluids Eng., vol. 128, no. 2, p. 316, 2006.

[55] L.Zhou, Z. Wang, Y. Luo, and G. Peng, "Numerical Simulation of Cavitating Flow in a Francis Turbine," pp. 1193–1197, Jan. 2008.

[56] G. Kuiper, "New developments around sheet and tip vortex cavitation on ships propellers," Httpresolver Caltech Educ. Lect. 007, 2001.

[57] T.Watanabe, T. Kawamura, Y. Takekoshi, M. Maeda, and S. H. Rhee, "Simulation of steady and unsteady cavitation on a marine propeller using a RANS CFD code," in Proceedings of the Fifth International Symposium on Cavitation, Osaka, Japan, 2003.

[58] V. H. Arakeri, "Cavitation inception," Sadhana - Acad. Proc. Eng. Sci., vol. 2, no. MAY, p. 149, 1979.

[59] C. W. Dekanski, M. I. G. Bloor, and M. J. Wilson, "The generation of propeller blade geometries using the PDE method," J. Ship Res., vol. 39, no. 2, pp. 108–116, 1995.

[60] D.w.Taylor, "The Speed and Power and Ships," Washington 1933.

[61] J.E.Conolly, "Strength Of Propellers," Reads Lond. Meet. R. Intuit. Nav. Archit. On, pp. 139–160, Dec. 1960.

[62] T.Sontvedt, "Propeller blade stresses, application of finite element methods," Comput. Struct., vol. 4, no. 1, pp. 193–204, Jan. 1974.

[63] C.S.Lee, Y.J. kim, G.D.Kim, and I.S.Nho, "Case Study On The Structural Failure Of Marine Propeller Blades," pp. 87–98, Jan. 1972.

[64] M.jourdian and J.L.Armand, "Strength Of Propeller Blades-A Numerical Approach," Socity Nav. Archit. Mar. Eng., pp. 201–213, May 1978.

[65] G.H.M.Beek and B.V.,Drunen, "Hub-Blade Interaction In Propeller Strength," Soc. Nav. Archit. Mar. Enginers, pp. 191–194, May 1978.

[66] G. W. Stickle and J. L. Crigler, "Propeller Analysis from Experimental Data," Jan. 1941.

[67] P.Castellini and C. Santolini, "Vibration measurements on blades of naval propeller rotating in water," 1996, vol. 2868, pp. 186–194.

[68] W.J.Colclough and J.G.Russel, "The Development Of A Composite Propeller Blade With A CFRP Spar," Aeronaut. J., pp. 53–57, Jan. 1972.

[69] J.G.Russel, "Use of reinforced plastics in a composite propeller blade," Plast. Polym., pp. 292–296, Dec. 1973.

[70] C. Leyens, F. Kocian, J. Hausmann, and W. A. Kaysser, "Materials and design concepts for high performance compressor components," Aerosp. Sci. Technol., vol. 7, no. 3, pp. 201–210, 2003.

[71] C.-C.Lin and Y.-J. Lee, "Stacking sequence optimization of laminated composite structures using genetic algorithm with local improvement," Compos.Struct.,vol.63, no. 3–4, pp. 339–345, 2004.

[72] G.-F. Lin, "Comparative Stress/Deflection Analyses of a Thick-Shell Composite Propeller Blade," DTIC Document, 1991.

[73] E. praefke, "Contra Rotating Complex Shafting For A Fast Monohull Ferry," Pap. Present. 6th Int. Conf. FAST SEA Transp.

[74] S.Nithiyama, Y. sakamoto, S. Ishida, and M.Oshima, "Development Of Contra Roatating Propeller System For Juno-A 37000-Dwt Class Bulk Carrier," SNAME Trans., vol. vol.98, pp. 27–52, 1990.

[75] S. Timoshenko, Vibration Problems In Engineering. D.Van Nostrand Company INC., 1937.

[76] Timoshenko, Theory of elasticity. Tata McGraw-Hill Education, 2001.

[77] P. F. W. M.Sc, "IX. The transverse vibrations of a rod of varying cross-section," Philos. Mag. Ser. 6, vol. 25, no. 145, pp. 85–106, Jan. 1913.

[78] D.M.Wrinch, "Lateral vibrations of bars of conical type," Proc.Roy.soc.,101, p. 493, 1922.

[79] F.Meyer, "Mathematiche theorieder transersaken schwingungen eines stabes von veranderlichen Querchnite, Ann,derphysik and chemie," vol. 33, p. 661, 1888.

[80] R.L.Sutherland and Goodman, "LE vibration of prismatic bars including rotary inertia and shear deflections," Univof III, 1954.

[81] J.L.Taylor, "Natural vibrational frequencies of flexible rotor blades," Aircr. Engr30, p. 331, 1958.

[82] "Effect of Taper on Uncoupled Natural Frequencies of Cantilever Beams." [Online]. Available: http://www.idr.iitkgp.ac.in/xmlui/handle/123456789/4924. [Accessed: 05-Jun-2016].

[83] R.J.Dunholter, "static displacement and coupled frequencies of a twisted bar," J Aero Sci13, p. 214, 1946.

[84] W.T.White, "An integral equation approach to problems of vibrating beams," JFanklin Inst245, p. 25 and 117, 1948.

[85] R.C.Diprima and G.H.Handleman, "vibration of twisted beams," Q.Appl.math.,12, p. 241, 1954.

[86] W.Carneige, "Experimental determination of center of flexure and center of torsion coordinates of asymmetrical aero foil cross section," JMES 1, p. 241, 1959.

[87] J. C. Houbolt and G. W. Brooks, "Differential equations of motion for combined flapwise bending, chordwise bending, and torsion of twisted nonuniform rotor blades," Jan. 1958.

[88] H.G.Barten, J. A.Sheurenbrand, and D. D.Seheer, "Stress and vibrational analysis of inducer blades using finite element techniques," AIAA Pap., pp. 70–630.

[89] R.Ahmad, R. G.Anderson, and O. C.Zienkiewiez, "Vibration of thick curved shells, with particular reference to turbine blades," J. Strain Anal., vol. No. 5, pp. 200–200, 1970.

[90] M. a. J. Bossak and O. C. Zienkiewicz, "Free vibration of initially stressed solids, with particular reference to centrifugal-force effects in rotating machinery," J. Strain Anal. Eng. Des., vol. 8, no. 4, pp. 245–252, Oct. 1973.

[91] A. Leissa and K. I. Jacob, "Three-dimensional vibrations of twisted cantilevered parallelepipeds," ASME Trans. J. Appl. Mech., pp. 614–618, Sep. 1986.

[92] R. E. Kielb, A. W. Leissa, and J. C. Macbain, "Vibrations of twisted cantilever plates—a comparison of theoretical results," Int. J. Numer. Methods Eng., vol. 21, no. 8, pp. 1365–1380, Aug. 1985.

[93] R.Southwell, and F.Gough,"The free transverse vibration of airscrew blade," Br. ARC Rep. Memo. No 766, 1921.

[94] P. P. Fried mann, and F. Straub, "Application of the finite element method to rotary-wing aero elasticity," J. Am. Helicopter Soc., pp. 36–44, 1980.

[95] N. T. Sivaneri and I. Chopra, "Dynamic stability of a rotor blade using finite element analysis," AIAA J., vol. 20, pp. 716–723, 1982.

[96] D. Thakkar and R. Ganguli, "Induced shear actuation of helicopter rotor blade for active twist control," Thin-Walled Struct., vol. 45, no. 1, pp. 111–121, Jan. 2007.

[97] M. R. M. Crespo Da Silva, "A comprehensive analysis of the dynamics of a helicopter rotor blade," Int. J. Solids Struct., vol. 35, no. 7, pp. 619–635, Mar. 1998.

[98] V. Ramamurti and R. Kielb, "Natural frequencies of twisted rotating plates," J. Sound Vib., vol. 97, pp. 429–449, Dec. 1984.

[99] S. Sreenivasamurthy and V. Ramamurti, "A parametric study of vibration of rotating pre-twisted and tapered low aspect ratio cantilever plates," J. Sound Vib., vol. 76, no. 3, pp. 311–328, Jun. 1981.

[100] A. W. Leissa, J. K. Lee, and A. J. Wang, "Rotating Blade Vibration Analysis Using Shells," J. Eng. Power, vol. 104, no. 2, pp. 296–302, Apr. 1982.

[101] T. Tsuiji, M. Shugyo, and T. Yamashita, "Free Vibration Analysis of Rotating Thin Twisted Plates," Trans. Jpn. Soc. Mech. Eng. Ser. C, vol. 61, no. 592, pp. 4575–4583, 1995.

[102] X. X. Hu and T. Tsuiji, "Free vibration analysis of rotating twisted cylindrical thin panels," J. Sound Vib., vol. 222, no. 2, pp. 209–224, Apr. 1999.

[103] H. Lo, "A nonlinear problem in the bending vibration of a rotating beam," JApplMech TransASME, vol. 19, p. 461, 1952.

[104] W.E.Boyce, R.C.Diprima and G.H.Handleman, Vibrations of rotating beams of constant sections," ProcandUsNatlcongAppl Mech ASME, p. 165, 1954.

[105] M.J.Schilhansl, "Bending frequency of a rotating cantilever beam," J.Appl.Mech.,ASME,25, p. 28, 1958.

[106] G.Hirsch, "Investigation of vibration in bending of rotating turbine blades on non-rigid support," Jahrbuck Wissens ChartGessellsch Luftahrt, p. 174, 1958.

[107] G.Horway, “chord wise and beam wise bending of hinged rotor blades,” J AeroSci 15, p. 497, 1948.

[108] F. Niordson, Vibrations of turbine blades with loose hinge support. Norrköping: Norrköpings Tidningars Aktiebolag, 1954.

[109] C.F.Garland, “The normal modes and vibrations of beams having non collinear elastic and mass axes,” JapplMechTransASME Pa-, vol. 97, 1940.

[110] M. S. Qatu and A. W. Leissa, “Vibration studies for laminated composite twisted cantilever plates,” Int. J. Mech. Sci., vol. 33, no. 11, pp. 927–940, Jan. 1991.

[111] G. S. Bir, “Computerized Method for Preliminary Structural Design of Composite Wind Turbine Blades,” J. Sol. Energy Eng., vol. 123, no. 4, pp. 372–381, Jul. 2001.

[112] A. Kumar, H. Jaiswal, A. Pandey, and P. P. Patil, “Free Vibration Analysis of Truck Transmission Housing based on FEA,” Procedia Mater. Sci., vol. 6, pp. 1588–1592, 2014.

[113] A. D. Otero and F. L. Ponta, “Structural Analysis of Wind-Turbine Blades by a Generalized Timoshenko Beam Model,” J Sol Energy Eng J. Sol. Energy Eng., vol. 132, no. 1, p. 11015, 2010.

[114] L. W. Yu, Zhang Hai-quan, and Zeng lin, “Reliability analysis of bionic wind turbinr blades based on the response surface methodology [J],” J. Sol. Energy Eng., vol. 31, iss. 9, pp. 1204–1208, 2010.

[115] M. Shakeri, M. H. Yas, and M. G. Gol, “Optimal Stacking Sequence of Laminated Cylindrical Shells Using Genetic Algorithm,” Mech. Adv. Mater. Struct., vol. 12, no. 4, pp. 305–312, Jul. 2005.

[116] V. Yıldırım and E. Kıral, “Investigation of the rotary inertia and shear deformation effects on the out-of-plane bending and torsional natural frequencies of laminated beams,” Compos. Struct., vol. 49, no. 3, pp. 313–320, Jul. 2000.

[117] A. A. Khdeir and J. N. Reddy, “Free vibration of cross-ply laminated beams with arbitrary boundary conditions,” Int. J. Eng. Sci., vol. 32, no. 12, pp. 1971–1980, Dec. 1994.

[118] E. F. Crawley, “The Natural Modes of Graphite/Epoxy Cantilever Plates and Shells,” J. Compos. Mater., vol. 13, no. 3, pp. 195–205, Jul. 1979.

[119] J. T.-S. Wang, D. Shaw, and O. Mahrenholtz, “Vibration of rotating rectangular plates,” J. Sound Vib., vol. 112, no. 3, pp. 455–468, Feb. 1987.

[120] D. Shaw, K. Y. Shen, and J. T. S. Wang, “Flexural vibration of rotating rectangular plates of variable thickness,” J. Sound Vib., vol. 126, no. 3, pp. 373–385, Nov. 1988.

[121] S. Kapuria and M. N. Alam, “Efficient layer wise finite element model for dynamic analysis of laminated piezoelectric beams,” Comput. Methods Appl. Mech. Eng., vol. 195, pp. 2742–2760, 2006.

[122] J. Cho and S. Lee, "Propeller blade shape optimization for efficiency improvement," Comput. Fluids, vol. 27, no. 3, pp. 407–419, Mar. 1998.

[123] Charles Dai, Stephen Hambric, Lawrence Mulvihill, Siu Shing Tong, and David Powell, "A Prototype Marine Propulsor Design Tool Using Artificial Intelligence and Numerical Optimization Techniques," SNAME Trans., vol. 102, pp. 57–69, 1994.

[124] R. Latorre and M. Mizina, "Design study for outboard propeller with spoiler," Ocean Eng., vol. 26, no. 8, pp. 727–737, Aug. 1999.

[125] Ki-Han Kim, Michael B. Wilson, Greg P. Platzer, and Eric Bjarrne, "Design and Model Evaluation of a New Propeller for the U.S. Navy's Auxiliary Oiler AO-177 Jumbo Class," SNAME Trans., vol. 98, pp. 53–76, 1990.

[126] W.K. Blake, K. Meyne, J.E. Kerwin, E. Weitendorf, and J. Friesch, "Design of APL C-10 Propeller with Full-Scale Measurements and Observations Under Service Conditions," SNAME Trans., vol. 98, pp. 77–111, 1990.

[127] John.D.Anderson Jr, "Computational Fluid dynamics-The Basis with Applications, Mcgraw-Hill series in Mechanical Engineering | | ISBN 0070016852".

[128] S. Patankar and D. Spalding, "A calculation procedure for heat, mass and momentum transfer in three-dimensional parabolic flows," Int. J. Heat Mass Transf., vol. 15, no. 10, pp. 1787–1806, Oct. 1972.

[129] S.Solomon Raj, and P.Ravinder Reddy, "Design of Hybrid composite marine propeller for improved cavitation," Int. J. Innov. Res. Technol. Sci., vol. ISSN 2321-1156, 2014.

[130] John Carlton, "Marine Propellers and Propulsion, 2nd Edition | | ISBN 9780080549231." .

[131] "KT, KQ and efficiency curves for the Wageningen B-series propellers." [Online]. Available: https://deepblue.lib.umich.edu/handle/2027.42/3557. [Accessed: 03-Jun-2016].

[132] J. Ghose and R. Gokarn, Basic ship propulsion. 2004.

[133] R. Narayanaswami and H. M. Adelman, "Evaluation of the Tensor Polynomial and Hoffman Strength Theories for Composite Materials," J. Compos. Mater., vol. 11, no. 4, pp. 366–377, Oct. 1977.

[134] A. F. Molland, S. R. Turnock, and D. A. Hudson, Ship Resistance and Propulsion: Practical Estimation of Propulsive Power. Cambridge University Press, 2011.

[135] I. M. Daniel and O. Ishai, Engineering Mechanics of Composite Materials. Oxford University Press, 2006.

[136] H. J. Lin and J. F. Tsai, "Analysis of Underwater Free Vibrations of a Composite Propeller Blade," J. Reinf. Plast. Compos., Jan. 2008.

[137] S. Mohamed Nabi and N. Ganesan, “Comparison of beam and plate theories for free vibrations of metal matrix composite pre-twisted blades,” J. Sound Vib., vol. 189, no. 2, pp. 149–160, Jan. 1996.

[138] Y.-J. Kee and J.-H. Kim, “Vibration characteristics of initially twisted rotating shell type composite blades,” Compos. Struct., vol. 64, no. 2, pp. 151–159, May 2004.

[139] D. W. Jensen and E. F. Crawley, “Frequency Determination Techniques for Cantilevered Plates with Bending-Torsion Coupling.,” AIAA J., vol. 22, no. 3, pp. 415–420, 1984.

[140] M. D. Olson and G. M. Lindberg, “Dynamic analysis of shallow shells with a doubly-curved triangular finite element,” J. Sound Vib., vol. 19, no. 3, pp. 299–318, Dec. 1971.

# Appendices

## Appendix-A Matlab code for Free vibration analysis of Propeller

```
% MATLAB codes for Finite Element Analysis
% clear memory
clear all;
colordef white;
clf
% materials
E  = 200e9;     poisson = 0.3;
thickness=1;
I=thickness^3/12;
rho=7850;
% matrix C
% bending part
C_bending=I*E/(1-poisson^2)*...
    [1 poisson 0;poisson 1 0;0 0 (1-poisson)/2];
%Membrane part
C_membrane= E*(thickness)/((1-poisson^2))* ...
   [1  poisson 0; ...
   poisson  1  0; ...
   0  0  (1-poisson)/2];
```

```
    % shear part
    C_shear=thickness*E/2/(1+poisson)*eye(2);
    %Mesh generation
    L  = 20;B=20;
    numberElementsX=10;
    numberElementsY=10;
    numberElements=numberElementsX*numberElementsY;

    [nodeCoordinates, elementNodes] = ...
        rectangularMesh(L,B,numberElementsX,numberElementsY);
    xx=nodeCoordinates(:,1);
    yy=nodeCoordinates(:,2);
    drawingMesh(nodeCoordinates,elementNodes,'Q4','k-');
    axis off
    numberNodes=size(xx,1);

    % GDof: global number of degrees of freedom
    GDof=5*numberNodes;

    % computation of the system stiffness and mass matrices
    [stiffness]=formStiffnessMatrixMindlinQ4(GDof,numberElements
,...
        elementNodes,numberNodes,nodeCoordinates,C_shear,...
        C_bending,C_membrane,thickness,I);

    [mass]=formMassMatrixMindlinQ4(GDof,numberElements,...

elementNodes,numberNodes,nodeCoordinates,rho,thickness,I);

    % % boundary conditions
    [prescribedDof,activeDof,fixedNodeW]=...
    EssentialBC5dof('cfff',GDof,xx,yy,nodeCoordinates,numberNode
s)
    G=E/2.6;
```

```
% V : mode shape
% D : frequency
%
numberOfModes=12;
[V,D] = eig(stiffness(activeDof,activeDof),...
    mass(activeDof,activeDof));
Do = (E*thickness^3)/(12*(1-(poisson^2)));
D=diag(sqrt(D)*L*L*sqrt(rho*thickness/Do));
[D,ii] = sort(D); ii = ii(1:numberOfModes);
VV = V(:,ii);
activeDofW=setdiff([1:numberNodes]',[fixedNodeW]);
NNN=size(activeDofW);

    VVV(1:numberNodes,1:12)=0;
for i=1:12
        VVV(activeDofW,i)=VV(1:NNN,i);
end

NN=numberNodes;N=sqrt(NN);
x=linspace(-L,L,numberElementsX+1);
y=linspace(-B,B,numberElementsY+1);

% drawing Eigenmodes
drawEigenmodes2D(x,y,VVV,NN,N,D)
```

```
%.StiffnessMatrix.....................................
.............
   function [K]=...
    formStiffnessMatrixMindlinQ4(GDof,numberElements,...
    elementNodes,numberNodes,nodeCoordinates,C_shear,...
    C_bending,C_membrane,thickness,I)
 % computation of stiffness matrix
% for Mindlin plate element
 % K : stiffness matrix

K=zeros(GDof);
 % Gauss quadrature for bending part
[gaussWeights,gaussLocations]=gaussQuadrature('complete');

% cycle for element
% cycle for element
for e=1:numberElements
  % indice : nodal condofectivities for each element
  % elementDof: element degrees of freedom
  indice=elementNodes(e,:);
  elementDof=[indice indice+numberNodes
indice+2*numberNodes...
              indice+3*numberNodes indice+4*numberNodes];
  ndof=length(indice);

  % cycle for Gauss point
  for q=1:size(gaussWeights,1)
    GaussPoint=gaussLocations(q,:);
    xi=GaussPoint(1);
    eta=GaussPoint(2);

% shape functions and derivatives
    [shapeFunction,naturalDerivatives]=shapeFunctionQ4(xi,eta)

% Jacobian matrix, inverse of Jacobian,
% derivatives w.r.t. x,y
    [Jacob,invJacobian,XYderivatives]=...

Jacobian(nodeCoordinates(indice,:),naturalDerivatives);

% [B] matrix bending
    B_b=zeros(3,5*ndof);
    B_b(1,ndof+1:2*ndof)  = XYderivatives(:,1)';
    B_b(2,2*ndof+1:3*ndof)= XYderivatives(:,2)';
    B_b(3,ndof+1:2*ndof)  = XYderivatives(:,2)';
    B_b(3,2*ndof+1:3*ndof)= XYderivatives(:,1)';

    % [B] matrix membrane
    B_m=zeros(3,5*ndof);
    B_m(1,3*ndof+1:4*ndof)      = XYderivatives(:,1)';
    B_m(2,4*ndof+1:5*ndof)      = XYderivatives(:,2)';
    B_m(3,3*ndof+1:4*ndof)      = XYderivatives(:,2)';
    B_m(3,4*ndof+1:5*ndof)      = XYderivati
```

```
% stiffness matrix bending
    K(elementDof,elementDof)=K(elementDof,elementDof)+ ...
        B_b'*C_bending*B_b*gaussWeights(q)*det(Jacob);

   %stiffness matrix membrane
   K(elementDof,elementDof)=K(elementDof,elementDof)+ ...
        B_m'*C_membrane*B_m*gaussWeights(q)*det(Jacob);

  end  % Gauss point
end    % element

% shear stiffness matrix

% Gauss quadrature for shear part
[gaussWeights,gaussLocations]=gaussQuadrature('reduced');

% cycle for element
% cycle for element
for e=1:numberElements
  % indice : nodal condofectivities for each element
  % elementDof: element degrees of freedom
  indice=elementNodes(e,:);
  elementDof=[indice indice+numberNodes
indice+2*numberNodes...
              indice+3*numberNodes indice+4*numberNodes];
  ndof=length(indice);

  % cycle for Gauss point
  for q=1:size(gaussWeights,1)
    GaussPoint=gaussLocations(q,:);
    xi=GaussPoint(1);
    eta=GaussPoint(2);
% shape functions and derivatives
    [shapeFunction,naturalDerivatives]=shapeFunctionQ4(xi,eta)

% Jacobian matrix, inverse of Jacobian,
% derivatives w.r.t. x,y
    [Jacob,invJacobian,XYderivatives]=...

Jacobian(nodeCoordinates(indice,:),naturalDerivatives);
% [B] matrix shear
    B_s=zeros(2,5*ndof);
    B_s(1,1:ndof)       = XYderivatives(:,1)';
    B_s(2,1:ndof)       = XYderivatives(:,2)';
    B_s(1,ndof+1:2*ndof)  = shapeFunction;
    B_s(2,2*ndof+1:3*ndof)= shapeFunction;

% stiffness matrix shear
    K(elementDof,elementDof)=K(elementDof,elementDof)+...
        B_s'*C_shear  *B_s*gaussWeights(q)*det(Jacob);
  end  % gauss point
end    % element
```

```
%Mass matrix%
function [M]=...
    formMassMatrixMindlinQ4(GDof,numberElements,...
    elementNodes,numberNodes,nodeCoordinates,rho,thickness,I)

% computation of mass matrix
% for Mindlin plate element

M=zeros(GDof);

% Gauss quadrature for bending part
[gaussWeights,gaussLocations]=gaussQuadrature('complete');

% cycle for element
for e=1:numberElements
  % indice : nodal condofectivities for each element
  indice=elementNodes(e,:);
  ndof=length(indice);

  % cycle for Gauss point
  for q=1:size(gaussWeights,1)
    GaussPoint=gaussLocations(q,:);
    xi=GaussPoint(1);
    eta=GaussPoint(2);

% shape functions and derivatives
  shapeFunction,naturalDerivatives]=shapeFunctionQ4(xi,eta);

% Jacobian matrix, inverse of Jacobian,
% derivatives w.r.t. x,y
    [Jacob,invJacobian,XYderivatives]=...

Jacobian(nodeCoordinates(indice,:),naturalDerivatives);

% [B] matrix bending
    B_b=zeros(3,5*ndof);
    B_b(1,ndof+1:2*ndof)        = XYderivatives(:,1)';
    B_b(2,2*ndof+1:3*ndof)      = XYderivatives(:,2)';
    B_b(3,ndof+1:2*ndof)        = XYderivatives(:,2)';
    B_b(3,2*ndof+1:3*ndof)      = XYderivatives(:,1)';
% [B] matrix membrane
    B_m=zeros(3,5*ndof);
    B_m(1,3*ndof+1:4*ndof)      = XYderivatives(:,1)';
    B_m(2,4*ndof+1:5*ndof)      = XYderivatives(:,2)';
    B_m(3,3*ndof+1:4*ndof)      = XYderivatives(:,2)';
    B_m(3,4*ndof+1:5*ndof)      = XYderivatives(:,1)';
    % mass matrix
    M(indice,indice)=M(indice,indice)+...
        shapeFunction*shapeFunction'*thickness*rho*...
        gaussWeights(q)*det(Jacob);
        M(indice+numberNodes,indice+numberNodes)=...

 M(indice+numberNodes,indice+numberNodes)+...
        shapeFunction*shapeFunction'*I*rho*...
        gaussWeights(q)*det(Jacob);
```

```
    M(indice+2*numberNodes,indice+2*numberNodes)=...
        M(indice+2*numberNodes,indice+2*numberNodes)+...
        shapeFunction*shapeFunction'*I*rho*...
        gaussWeights(q)*det(Jacob);

    M(indice+3*numberNodes,indice+3*numberNodes)=...
        M(indice+3*numberNodes,indice+3*numberNodes)+...
        shapeFunction*shapeFunction'*thickness*rho*...
        gaussWeights(q)*det(Jacob);

    M(indice+4*numberNodes,indice+4*numberNodes)=...
        M(indice+4*numberNodes,indice+4*numberNodes)+...
        shapeFunction*shapeFunction'*thickness*rho*...
        gaussWeights(q)*det(Jacob);
    end  % Gauss point
end    % element


% Shape function%
.....................................................
    function
[shape,naturalDerivatives]=shapeFunctionQ4(xi,eta)

    % shape function and derivatives for Q4 elements
    % shape : Shape functions
    % naturalDerivatives: derivatives w.r.t. xi and eta
    % xi, eta: natural coordinates (-1 ... +1)

    shape=1/4*[ (1-xi)*(1-eta);(1+xi)*(1-eta);
             (1+xi)*(1+eta);(1-xi)*(1+eta)];
    naturalDerivatives=...
           1/4*[-(1-eta), -(1-xi);1-eta,    -(1+xi);
                 1+eta,      1+xi;-(1+eta),   1-xi];

    end % end function shapeFunctionQ4

%Jacobian.m%.....................................................
.........

    function [JacobianMatrix,invJacobian,XYDerivatives]=...
        Jacobian(nodeCoordinates,naturalDerivatives)

    % JacobianMatrix    : Jacobian matrix
    % invJacobian : inverse of Jacobian Matrix
    % XYDerivatives  : derivatives w.r.t. x and y
    % naturalDerivatives  : derivatives w.r.t. xi and eta
    % nodeCoordinates  : nodal coordinates at element level

    JacobianMatrix=nodeCoordinates'*naturalDerivatives;
    invJacobian=inv(JacobianMatrix);
    XYDerivatives=naturalDerivatives*invJacobian;
```

```
%
%GaussQuadrature%.....................................
.............

    function [weights,locations]=gaussQuadrature(option)
    % Gauss quadrature for Q4 elements
    % option 'complete' (2x2)
    % option 'reduced'  (1x1)
    % locations: Gauss point locations
    % weights: Gauss point weights

    switch option
        case 'complete'

        locations=...
          [ -0.577350269189626 -0.577350269189626;
             0.577350269189626 -0.577350269189626;
             0.577350269189626  0.577350269189626;
            -0.577350269189626  0.577350269189626];
        weights=[ 1;1;1;1];

        case 'reduced'

        locations=[0 0];
        weights=[4];
    end

    end  % end function gaussQuadrature
```

# Dissemination

**INTERNATIONAL JOURNALS:**

- M.L.Pavan Kishore, R.K Behera "Free Vibration Characteristics of Metallic Propeller Blade replaced with Composite material Using Finite Element Approach". Applied Mechanics and Materials Vols. 592-594 (2014) pp. 2051-2055.
- M.L.Pavan Kishore, R.K.Behera "Effect of Material Behavior on Dynamic Characteristics Determination of Marine Propeller Blade Using Finite Element Analysis" Proceedia engineering" Elsevier publication 144 ( 2016 ) 767 – 774.

**NATIONAL JOURNALS:**

- M.L.Pavan Kishore, R.K.Behera, Sreenivasulu Bezawada "Structural analysis of NAB Propeller Material" International Journal of Modern Engineering Research (IJMER) Vol. 2, Issue. 5, Sep.-Oct. 2012 pp-3390- replaced with Composite 3397, ISSN: 2249-6645.
- M.L.Pavan Kishore, R.K.Behera "Replacement of Nab Propeller Blade with Composite for Strength Criteria". International Journal of Engineering Science Invention ISSN (Online): 2319 – 6734, ISSN (Print): 2319 – 6726 PP.42-46
- M.L.Pavan Kishore, R.K.Behera, Sreenivasulu Bezawada "Harmonic Analysis of Nab Propeller Replaced with Composite Material" International Journal of Current Engineering and Technology Vol.4, No.2 (April 2014) ISSN 2277 – 4106, P-ISSN 2347 – 5161.
- M.L.Pavan Kishore, R.K Behera "Determination of Effect Of Stacking Sequence On Strength Evaluation Of Composite Propeller Blade" International Journal of Scientific Engineering and Technology (ISSN: 2277-1581)
- M.L.Pavan Kishore, R.K.Behera "Determination of Optimal Stacking Sequence for Modal Characteristics Evaluation of Composite Marine Propeller Blade". Journal of Mechanical Design and Vibration, 2014, Vol. 2, No. 4, 94-101.
- M.L.Pavan Kishore, R.K.Behera "Effect of Pre twist on Free Vibration Characteristics Determination of Metallic Curved Blade Replaced with Composite Material". Journal of Ocean Research, 2014, Vol. 2, No. 1, 11-16.
- M.L.Pavan Kishore, R.K.Behera "Base line study for determination of effect of stacking sequence on Vibration characteristics of composite Propeller Blade" Science Direct Aquatic Proceedia 4 ( 2015 ) 458 – 465.

**INTERNATIONAL CONFERENCES:**

- M.L.Pavan Kishore, R.K.Behera (2013), Replacement of Nab Propeller Blade with Composite for Strength Criteria".Advances in modeling and Analysis of Aerodynamic Systems (AMAAS),NIT Rourkela, Odisha, India,1-2$^{nd}$ March.

- M.L.Pavan Kishore, R.K.Behera , D.Harsha Vardhan (2014) “Free Vibration Analysis of Four Bladed Propeller Using Different Materials” Proceedings of 4th SARC International Conference, 30 March-2014, Nagpur, India, ISBN: 978-93-82702-70-2 88.
- M.L.Pavan Kishore, R.K.Behera, (2014), “Free Vibration Characteristics of Metallic Propeller Blade replaced with Composite material Using Finite Element Approach”, International Mechanical Engineering Congress (IMEC-2014) ”,NIT Tiruchirapalli, Tamilnadu, India,June 13-15 2014.
- M.L.Pavan Kishore, R.K.Behera, (2014) “Determination of Effect Of Stacking Sequence On Strength Evaluation Of Composite Propeller Blade”,19th “International Conference on Hydraulics, water resources, coastal and environmental Engineering(Hydro 2014)”,MANIT Bhopal, Madhya Pradesh, India , 18-20th December,2014.
- M.L.Pavan Kishore, R.K.Behera, (2015) “Base line study for determination of effect of stacking sequence on Vibration characteristics of composite Propeller Blade” International Conference on Water Resources ,Coastal and Ocean Engineering(ICWRCOE- 2015), NIT Surathkal, Karnataka, India,12-14th March 2015.
- M.L.Pavan Kishore, R.K.Behera,(2015) “Effect of Material Behaviour on Dynamic Characteristics Determination of Marine Propeller Blade Using Finite Element Analysis” 12th International Conference on Vibration Problems(ICOVP 2015), IIT Guwahati, India, 14-17th December 2015.

**NATIONAL CONFERENCE:**

- M.L.Pavan Kishore, R.K.Behera , D.Harsha Vardhan (2014) “Free Vibration Analysis of Four Bladed Propeller Using Different Materials” Proceedings of 4th SARC International Conference, 30 March-2014, Nagpur, India, ISBN: 978-93-82702-70-2 88.

**ARTICLES UNDER REVIEW:**

- M.L.Pavan Kishore, R.K.Behera “Numerical Investigation for CFD Simulation of Open Water Characteristics and Cavitation Inception of Marine Propeller Blade” Journal of Maritime Research (under review).

# Index